Turbulence modelling and gravitational-wave data analysis for binary neutron star mergers

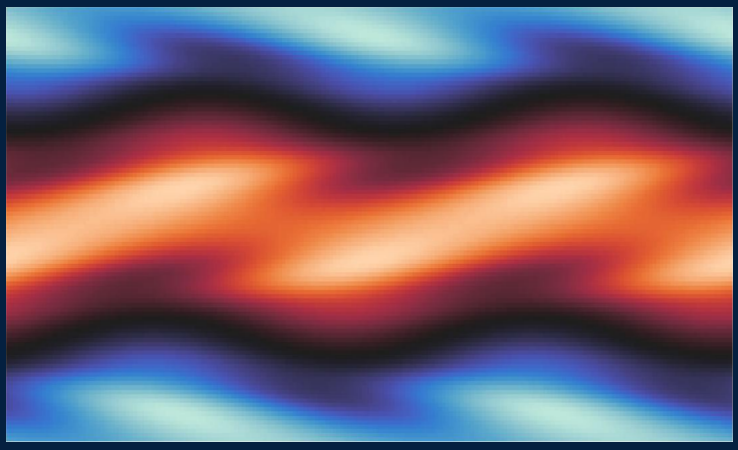

Miquel Miravet Tenés

Directors:

José Antonio Font Roda, Pablo Cerdá Durán

Doctorat en Física codi 3126
Departament d'Astronomia i Astrofísica
Universitat de València

TESI DOCTORAL
Juliol 2024

VNIVERSITAT DE VALÈNCIA

Turbulence modelling and gravitational-wave data analysis for binary neutron star mergers

Miquel Miravet Tenés

Doctorat en Física codi 3126
Departament d'Astronomia i Astrofísica
Universitat de València

TESI DOCTORAL

Directors:
José Antonio Font Roda, Pablo Cerdá Durán

Juliol 2024

Declaració

El Prof. **José Antonio Font Roda**, Catedràtic del Departament d'Astronomia i Astrofísica de la Universitat de València, i el Prof. **Pablo Cerdá Durán**, Professor Titular del Departament d'Astronomia i Astrofísica de la Universitat de València,

CERTIFIQUEN:

Que la present memòria, titulada **Turbulence modelling and gravitational-wave data analysis for binary neutron star mergers**, ha sigut realitzada sota la seua direcció en el Departament d'Astronomia i Astrofísica de la Universitat de València per **Miquel Miravet Tenés**, i constituïx la seua Tesi Doctoral per a optar al títol de Doctor per la Universitat de València una vegada cursats els estudis en el Doctorat en Física.

I perquè així conste, en compliment de la legislació vigent, signem el present certificat.

Burjassot, a 3 de juliol de 2024

Signat: José Antonio Font Roda Pablo Cerdá Duŕan

Als meus pares i al meu germà.
A Marina.

Agraïments

Ja de ben petit no parava de preguntar als meus pares per qualsevol cosa que el meu enteniment no aconseguia explicar.[1] Passats els anys, vaig pensar, ingènuament, que estudiar la carrera de física finalment em donaria la resposta a totes les qüestions que tenia sobre l'Univers que m'envoltava. Evidentment, això no va ser així. Amb la meua curiositat encara insatisfeta, vaig tindre la *meravellosa* idea de començar un doctorat al Departament d'Astronomia i Astrofísica. Malgrat no haver sigut capaç de respondre a eixies preguntes que jo mateix em feia quan tenia uns 12 anys (*Què hi havia abans del Big Bang? Hi existeixen universos paral·lels? Què hi ha dins d'un forat negre?*, i d'altres preguntes típiques dels documentals vespertins de La 2), durant aquestos darrers anys he tingut la fortuna d'estudiar uns dels objectes més interessants de l'Univers: els estels de neutrons. I, d'una manera o d'altra, també he sigut capaç de posar el meu granet de sorra en la comprensió d'aquestos estels tan curiosos.

Hi ha molta gent culpable del fet que estiga, mentre escric aquestes línies, cada vegada més a prop de convertir-me en doctor. En primer lloc, vull agrair de tot cor als meus supervisors, Toni i Pablo, per haver-me guiat i fet costat durant aquestos anys.

Toni, recorde nítidament aquella xarrada que donares al novembre de l'any 2017 sobre ones gravitacionals (encara guarde a la meua habitació el full de l'anunci). Va ser en eixe moment quan vaig saber que volia dedicar-me a estudiar aquestes arrugues de l'espaitemps. Et vull donar les gràcies per haver comptat amb mi quan vaig contactar-te durant l'estiu de l'any 2019 per saber si seria possible realitzar el projecte de fi de màster amb tu, i sobretot per accedir a ser el meu tutor durant aquestos anys de doctorat. Vull aprofitar també per agrair el teu suport quan anava tan perdut quan vaig començar a donar les classes de tutelades al grau. Mai oblidaré els teus comentaris quan em veus amb una

[1] Papà, mamá, vull agrair-vos públicament la vostra paciència.

samarreta de grups com *Pink Floyd*, *Joy Division*, *Queen* o *The Beatles*. Tampoc oblidaré les xarrades matineres al teu despatx en què sempre em convides a seure amb un "Please, take a seat", encara que m'haja quedat plantat en la porta. Sempre, sempre, t'he pogut trobar quan he tingut cap problema, i sempre he trobat el teu suport. Estic molt agraït per la teua proximitat i tots els teus consells, tant científics com personals.

Pablo, te conocí cuando empecé el máster y Toni y yo bajamos a tu despacho (todavía estabas en el primer piso) para discutir los primeros pasos de mi trabajo de fin de máster, que ha degenerado con los años en esta tesis. Ha sido un placer trabajar contigo estos años y empezar un proyecto que tenías en mente desde hacía mucho tiempo y que por fin hemos podido desarrollar. Agradezco tu paciencia cuando entro cada dos por tres en tu despacho para comentarte hasta la mínima chorrada que se me pasa por la cabeza. También recordaré esas charlas en tu despacho que se alargaban más de la cuenta y donde llenaba la pizarra de expresiones ininteligibles. Y es que en muchas de estas ocasiones salía de tu despacho sabiendo algo nuevo que desconocía antes de entrar.

Als dos, gràcies de nou per mostrar-vos sempre disponibles quan necessitava reunir-me amb vosaltres per comentar-vos qualsevol avanç (o problema) en els nostres projectes, i, sobretot, per haver-me ajudat a créixer com a investigador. Espere que açò no siga un acomiadament definitiu i pugam continuar treballant junts en un futur no massa llunyà.

I would also like to thank the referees of this thesis: Juan Antonio Miralles, Martin E. Pessah, Viola Sordini, Roberto De Pietri, Meg Millhouse and Carlos Palenzuela. I am very grateful for the time you spent reviewing this work and for agreeing to be part of this committee.

Quiero también agradecer a Martin y a Milton el haber sido unos actores vitales en el desarrollo de este trabajo. Martin, muchas gracias por haberme dejado *trastear* con tu código y por haber tenido tantísima paciencia cuando no sabía por dónde tirar con las simulaciones. Milton, muchas gracias por haberme ayudado desde el primer momento que pisaste este departamento y por haber tenido tanto interés en trabajar conmigo. Estoy seguro de que haremos muchas cosas juntos en el futuro.

A més, voldria mostrar el meu agraïment a totes les persones del DAA que m'han acompanyat durant aquestos anys. Als meus companys de doctorat: Davide, Fabrizio, Nico, Sergio, Beatrice, Tasos, Marco Cusinato, Peppe, Raimon, Inês, Salva, Marco Molina,..., per haver format part d'una manera o altra d'aquesta experiència. No poden faltar Raquel i Miquel (el bueno), per compartir tants dinars i aguantar les meues *tremendes turres*. Gràcies també al professorat

del Departament: Manel, Vicent, Susana, Juan Antonio, Pepe, Miguel Ángel,..., i, a més a més, vull agrair a Vicent i a José Carlos la seua ajuda durant els meus anys de docència en el grau. Y Álex, gracias por haberme guiado y ayudado tanto estos años, te deseo lo mejor en tu próxima etapa.

Tal com la gent es pot imaginar, la quantitat de paperassa que s'ha de dur a terme durant una tesi és descomunal. Congressos, viatges, docència,..., qualsevol cosa requereix plenar un fum de documents. Afortunadament, Manel, Arancha i Ana fan que aquestes coses siguen molt més fàcils de fer. El DAA no podria tindre millor secretaria sense vosaltres. Sempre és un plaer pujar-hi per demanar-vos qualsevol cosa i que em rebeu amb un somriure d'orella a orella. Sou l'alegria del Departament.

Vull agrair també als meus companys de carrera que començaren amb mi aquesta llarga aventura a la universitat (Jordi, Kike, Raül, Cento, Salva T, Marina, Silvia, Alicia, Cris, Salva M, Javi, Xavo, Pedro, Álvaro, Codina,...). Molts de vosaltres us estareu preguntant com he estat tan boig de seguir encara quatre anys més a Burjassot. Certament, no sé què respondre.

Durant el meu pas per l'institut, vaig tindre la sort de tindre com a professors a persones que van despertar en mi l'amor que ara tinc per la física: Lluís Fillol i Manolo Simón. Gràcies de tot cor per ser els primers en guiar-me en aquest llarg viatge. També vull donar les gràcies a Eulogi Oset, Miquel Portilla, Enric Valor i alguns altres professors per haver contribuït a que tinga un bon record del meus anys a la facultat.

I want to thank all my collaborators, who contributed to the work I am presenting here. Gracias Florencia, por haber empezado conmigo desde cero ese proyecto que no sabíamos cómo iba a terminar. Thank you Roberto for being so helpful, I could learn a lot from you about GW data analysis. I am also very grateful with the Institute for Pure and Applied Mathematics from UCLA for hosting me during the three-month long program and for giving me the opportunity to acquire a wider knowledge about the field of GW astrophysics. Moreover, I was very lucky to meet amazing people there: Simone (*h*sssstia tio!!*), Sushant, Yanyan, Lorena,... and Marco Cavaglià, who has been always supportive and has (patiently) supervised the Machine Learning project during almost two years. I would also like to thank Luciano Rezzolla and Natey Kübler for inviting me to their department to give a seminar about my work.

No puedo pasar por alto los tres meses que pasé de estancia en Copenhague, en el Niels Bohr Institute, trabajando junto a Martin Pessah. Martin, muchísimas gracias por haberme recibido allí y por haberme hecho sentir como en casa. Me siento muy afortunado de haber trabajado contigo y de haber aprendido tanto

de ti en tan poco tiempo. My three months in København were amazing thanks to the very nice people I met there: David, Kai, Gaia, Philip, Marcela, Lorenz, Dan, Chris and Pablo. It is also worthy of mention the Søernes Ølbar, the place where the GW memory project was conceived (and where I had the best afterwork beers).

Gràcies a l'Ajuda per a la Formació de Professorat Universitari (FPU) i les Ajudes Complementàries de Mobilitat per a Estàncies Breus, del Ministeri de Ciència, Innovació i Universitats del Govern d'Espanya (amb referències FPU19/01750 i EST23/00420, respectivament) per haver-me donat els recursos necessaris per a realitzar aquesta tesi. Part dels estudis realitzats durant aquesta tesi es van dur a terme amb el superordinador Lluis Vives (Servei d'Informàtica de la Universitat de València), amb la Xarxa Espanyola de Supercomputació mitjançant l'ús de MareNostrum al Centre de Supercomputació de Barcelona, i amb els recursos computacionals del LIGO Laboratory.

Aquesta tesi no podria haver-se escrit sense els meus amics i la meua família. Malgrat haver-me preguntat en repetides ocasions què hi estava fent (ni jo ho sabia, de vegades) i haver fet l'esforç d'entendre la meua resposta (amb més o menys èxit), sempre estaré agraït pel vostre interés i, sobretot, per la vostra preocupació quan les coses no anaven tan bé. *Stand*, este "ALRIGHT!" va por vosotros. Guille, aquí tienes *esas integrales* por las que tanto preguntas. Andrea, siento no haber podido visitarte este año, me has pillado liado con esto de aquí, pero sabes de sobra que te echo mucho de menos. Menchu, nunca estaré suficientemente agradecido al campus de hidrogeles inteligentes por darme la oportunidad de conocerte. Arturet, Juanan, Raül, Vlis, Lydia, Xavi, Álvaro, Damian,..., a la mayoría os conozco desde hace más de 15 años y tengo la inmensa suerte de teneros todavía en mi vida. Charles, Angy, Lídia, quiero agradeceros en especial a vosotros todo el cariño que me habéis dado durante estos años de altibajos (más altos que bajos, afortunadamente). Sois la familia que he podido elegir. Os quiero mucho.

Tinc molt clar què respondre quan algú em pregunte si em penedisc d'haver dedicat aquestos intensos quatre anys a fer una tesi doctoral. Sens dubte, li diria que no. I la raó principal és que gràcies a aquesta tesi he pogut conéixer a dues persones que portaré sempre amb mi: David i Jose. Xics, no sou conscients de tot el que heu significat per a mi aquestos anys. Heu sigut, literalment, el meu dia a dia, i la raó per la qual m'alçava de matí i anava a treballar amb un somriure. Qui anava a dir el primer dia que vaig entrar per la porta del 3.02. (el millor despatx del món) que hi trobaria dos *tremendos jjjambos* com vosaltres.

David, benvolgut *Davittt*, ja sé que açò ho va dir Jose en els seus agraïments, però permet que ho repetisca. No he conegut mai una persona tan intel·ligent i brillant com tu. Estic segur que aconseguiràs tot el que et proposes i espere que, vages a on vages, la gent aprecie que vals un món. És un orgull ser el teu amic. Trobaré a faltar les sessions matinals d'entreneniment al despatx amb els nostres *cafelitos* (espere que ho estigues llegint amb el to apropiat). I poc es parla del *cardio* que m'has obligat a fer quan he intentat seguir-te pel corredor, perquè eixes camallades que fas són insuperables. Amic, el teu *Mokkos* et trobarà a faltar, però espere que puguem retrobar-nos en aquest Departament al més aviat possible.

Jose, querido *Joselito*, mi socialista favorito. No te puedes imaginar lo mucho que se ha notado tu ausencia en el 3.02. durante este último año. Dice mucho de ti que siempre hagas el esfuerzo de venir a desayunar con nosotros y de que nos veamos un par de veces por semana, ya sea para tomarnos un *combito* o para bebernos una cervecita a la fresca en la plaza de Patraix. Quiero que sepas que nunca olvidaré ese momento en el que me diste un abrazo cuando más lo necesitaba. Tienes un grandísimo corazón[2] y, por muy lejos que estemos el uno del otro, sé que esta amistad va a durar para siempre. Prometo hacerte pronto una visita por tus tierras viguesas, y también por Villanueva de la Cañada, para tomarme un cafecito por 40 céntimos en mi futuro lugar de trabajo (guiño, guiño). Ah, y quiero aprovechar para recordarte que tienes todos tus papeles en mi estantería esperando a que algún día los recojas, porque puede que algún día acaben dentro del patinillo.

Estic també molt agraït amb vosaltres per haver-me donat l'oportunitat de conéixer a Ana i a Josep, les vostres parelles. Crec, sincerament, que teniu la millor companyia i us desitge de bon cor el millor. David, Jose, és una sort enorme tindre al meu costat dues persones com vosaltres. Gràcies per contagiar-me el vostre *quokkisme* i espere també haver-vos contagiat una mica el meu *tremendo maikisme*. Dona igual a on anem, el 3.02. viurà sempre en nosaltres!!!! ↗

Prim (aka *Getita, BC, Jermayolin*), que además de amiga eres (prima) hermana, gracias por haber sido desde el momento en el que nací una compañera inseparable (e insuperable). Danitito, el trotamundos, quien es *su propio jefe*, el mejor comentarista de los partidos del C.F. Pozuelo, que sepas que me siento muy afortunado de tener un primo como tú. Gracias también a Rodri, Pau, Nico, Jorge, Claudia y Pauet, y a todos mis tíos y tías, por componer la familia de la cual estoy tan orgulloso de formar parte. Y es que esta familia no existiría

[2] Y una grandísima piscina que quiero visitar más a menudo.

sin mis yayos, Juan y Amparo. Yayos, gracias por haberme dado muchos de los mejores recuerdos de mi infancia y por haber creado la mejor familia del mundo. Vuestro nieto el (casi) doctor os quiere y os querrá siempre. Y yayo, por cierto, siento decepcionarte, pero esta tesis no me ha dado las respuestas a tus numerosas cuestiones metafísicas. Tendremos que seguir discutiendo largo y tendido sobre esas preguntas todavía sin responder, pero, a partir de ahora, de doctor a doctor.

No m'oblide de la meua tia Filo. Ja sé que no he de treballar tant, com sempre em dius, però pots veure que el treball ha donat fruit, finalment. Tampoc m'oblide dels meus iaios, Pepito i Filo. Mai m'oblide, de fet. El vostre *xiquet fadrí* ja s'ha fet fadrí de veritat. Encara que no hi estigueu, cada vegada que supere cap meta pense en vosaltres. Us estime molt, i us trobe a faltar.

Papà, mamá, Joan, mai podré agrair-vos suficientment tot el que heu fet per mi. Si he arribat fins ací és pel vostre suport incondicional i la vostra paciència extraordinària. Heu confiat sempre en mi, i això és el que m'ha donat forces per aconseguir (quasi) tot el que m'he proposat. Tot el que sóc i el que seré és gràcies a vosaltres. Sou el millor exemple a seguir. I ara, finalment, ja podrem fer-nos eixa cervesseta merescuda en la piscina d'Eslida. Us estime, *pollos*.

Gracias a Rafa, Nuria, Jalo y Raquel, porque después de estos años también formáis parte de mi familia. Y a Raki, Panxa y Kira, por ser mis mejores amigos perrunos.

Y Marina, ni en cientos de páginas podría escribir todo lo agradecido que estoy de poder compartir mi vida contigo. Eres la persona que me ha acompañado en este viaje de cuatro años, y la que me acompañará el resto de mi vida. Has tenido que aguantar muchos momentos no demasiado fáciles y aún así has sido quien ha hecho que siga hasta el final. No te merezco, y no sé si en toda una vida podré hacer todo lo que has hecho por mí. Marina, te quiero. De esta nube no me voy a bajar nunca.

Bé, sé que açò només és el principi i que encara queda camí per recòrrer. Perquè, com deia el meu benvolgut Freddie, *the show must go on!*

Abstract

The plethora of gravitational-wave observations from several astronomical systems is changing our understanding of the Universe at an unprecedented rate. More concretely, the multimessenger observations of binary neutron star mergers have provided important information about matter at extreme densities, the generation of short gamma-ray bursts, the production of heavy elements, and the rate of expansion of the Universe. The understanding of the complex physics involved in this astrophysical scenario has been expanded thanks to the use of numerical simulations. To properly describe these systems, simulations need prohibitive computational resources to account for all the physics of the problem: a realistic equation of state for dense matter, an accurate neutrino transport scheme or the treatment of small-scale turbulence, among other issues. Realistic simulations of binary neutron star mergers can provide gravitational-wave signals that can be directly compared to real detections. The study of the postmerger gravitational-wave signal can put constraints on the equation of state and give information about the dynamics and stability of the merger remnant.

This thesis presents a comprehensive study of the magnetohydrodynamical turbulence triggered by the main instabilities developed during and after the merger of two neutron stars: the Kelvin-Helmholtz instability and the magnetorotational instability. Moreover, this thesis provides several applications of unmodelled reconstructions of binary neutron star postmerger signals, and a new approach to rapidly classify gravitational-wave sources.

The first part of the thesis focuses on the development of a new model for turbulence in binary neutron star mergers. This new model, which consists in solving evolution equations for turbulent energy densities, aims to reproduce the effects of the small-scale physics with moderate resolution. Moreover, this part of the thesis presents a new study of the saturation mechanism of the magnetorotational instability.

The second part of the thesis is dedicated to the analysis of gravitational-wave signals from the postmerger phase of binary neutron star mergers. Due to the stochastic nature of the signal during that phase, unmodelled reconstructions are applied to study the inference of inertial modes and the detectability of differences in the treatment of thermal effects with the equation of state. Furthermore, a new machine learning approach to rapidly classify compact binary sources of gravitational waves is presented. This new scheme aims to provide more faithful information about the gravitational-wave source to perform electromagnetic follow-up observations.

The findings of this thesis enhance our understanding of the instabilities that play a role in binary neutron star mergers by developing turbulence that can have important consequences on the stability of the merger remnant. Moreover, the work on gravitational-wave data analysis has implications for future applications of gravitational-wave astronomy to study the equation of state of neutron star matter, and multimessenger observations of compact binary systems.

Resum

He tingut la fortuna de realitzar la meua tesi doctoral en una època en què la física de la gravitació està esdevenint nombrosos avanços gràcies a la plètora d'observacions d'ones gravitacionals. Aquestes deteccions estan canviant el nostre enteniment sobre l'Univers a un ritme sense precedents. Més concretament, l'observació d'ones gravitacionals de la fusió de dos estels de neutrons, coneguda com GW170817, arran de la subseqüent detecció de radiació electromagnètica al llarg de tot l'espectre (des d'ones de ràdio fins a raigs gamma) va donar lloc a l'era de l'astronomia multi-missatgera. Els estels de neutrons són, després dels forats negres, els objectes més compactes de l'Univers. És per això que el seu estudi pot ajudar a entendre el comportament de la matèria sotmesa a densitats supranuclears. Les observacions de fusions de binàries d'estels de neutrons otorguen l'evidència més directa que les fusions d'objectes estelars compactes, en què al menys un dels components de la binària és un estel de neutrons, són progenitors dels motors que impulsen les explosions de raigs gamma. A més, aquestos events donen un fort suport observacional a les proposicions teòriques que relacionen les fusions d'estels de neutrons amb la nucleosíntesi d'elements pesats. Fins i tot, les fusions de binàries d'estels de neutrons també poden emprar-se per a obtindre una mesura independent del ritme d'expansió de l'Univers (la constant de Hubble).

El nostre enteniment de la física tan complexa involucrada en les fusions d'aquestos estels i també en la consegüent evolució del sistema s'ha expandit considerablement durant les últimes dècades. Açò ha sigut possible gràcies a l'ús de simulacions numèriques. La Relativitat Numèrica és l'eina emprada per a estudiar aquestos sistemes. Tanmateix, l'enorme espai de paràmetres del problema, la seua dimensionalitat i la quantitat de física a tindre en compte limiten el nombre de simulacions que es realitzen. Per a descriure adequadament aquestos escenaris, les simulacions numèriques necessiten emprar una equació d'estat de la matèria realista que incloga efectes tèrmics i altres característiques

microfísiques; un esquema correcte per al transport de neutrins; una resolució suficientment elevada per a capturar turbulència a xicoteta escala, i d'altres fenòmens físics que tenen un paper important i que es discutiran al llarg de la tesi.

Els estels de neutrons

Els estels de neutrons es formen després del col·lapse gravitacional del nucli de ferro d'un estel massiu amb una massa superior a les 10 masses solars, el qual desencadena una explosió de *supernova* de tipus IIb[3]. Malauradament, el mecanisme d'explosió encara no s'entén completament, però es coneix que els neutrins juguen un paper important. Aquestos són expulsats de l'interior de l'estel de neutrons en formació i s'emporten l'energia necessària per reviure l'explosió. El romanent d'aquesta supernova és un proto-estel de neutrons amb una temperatura relativament elevada i que gira ràpidament amb rotació diferencial.

L'estel de neutrons format es refreda amb el temps i perd la seua rotació diferencial inicial, el que duu a una rotació uniforme i de ritme reduït. Aquestos estels de neutrons aïllats i estables estan magnetitzats, i poden presentar els camps magnètics més intensos observats a l'Univers (fins a 10^{16} G). La seua massa es troba al voltant de les dues masses solars i tenen radis d'una desena de quilòmetres, aproximadament. A més, emeten feixos de radiació electromagnètica (en el rang de les ones de ràdio) des dels seus pols magnètics. Arran dels seus períodes estables de rotació, aquestos feixos s'observen com a polsos de radiació quan arriben a la Terra, i van ser identificats per primera vegada per Jocelyn S. Bell fa més de 50 anys.

Les densitats característiques dels estels de neutrons poden arribar fins i tot a valors per damunt de la densitat del nucli atòmic. Açò resulta en una font de pressió (contra la gravetat) que no només és produïda per electrons, sinò també per altres partícules del nucli atòmic i altres d'exòtiques. En aquestes condicions tan extremes, per tant, és necessari que la matèria estiga correctament descrita per l'equació d'estat; és a dir, per la relació entre les variables termodinàmiques. L'evolució dels sistemes binaris d'estels de neutrons i també l'estructura i l'estabilitat dels romanents d'aquestes fusions depenen estretament de l'equació d'estat de la matèria. A més a més, l'equació d'estat té un impacte elevat en l'emissió de neutrins i en les condicions perquè es done la nucleosíntesi d'elements

[3]Un mecanisme de formació alternatiu és el col·lapse induït per acreció d'una nana blanca, que condueix a una supernova de tipus Ia

químics pesats després de la fusió dels estels. Per això, s'han dut a terme molts esforços per a entendre la termodinàmica d'aquestos objectes compactes.

Els estels de neutrons posseeixen un ampli rang de períodes de rotació, des dels mil·lisegons fins als segons. La rotació ve donada per la conservació del moment angular durant el col·lapse del nucli de l'estel progenitor (o durant la col·lisió de dos estels de neutrons que resulta en un romanent estable). En nàixer (o després de la fusió), els estels de neutrons presenten un elevat grau de rotació diferencial, és a dir, diferents parts de l'estel roten a diferents velocitats. En el cas d'un proto-estel de neutrons, aquest hereta el moment angular de l'estel progenitor i, a causa de la reducció dràstica de tamany, la velocitat de rotació és substancialment elevada. En el cas dels romanents de la fusió de dos estels de neutrons, les capes externes dels estels són expulsades en la col·lisió i formen un disc d'acreció al voltant del nucli de l'estel romanent. A més, la rotació diferencial pot excitar diverses inestabilitats i modes d'oscil·lació que emeten radiació gravitatòria i poden amplificar el camp magnètic. Cal afegir que la rotació diferencial augmenta la massa màxima de l'estel a causa de les forces centrífugues que compensen la gravetat. El nou valor de la massa màxima dependrà de l'equació d'estat de la matèria.

Quan els estels de neutrons aïllats evolucionen en el temps i s'estabilitzen, es refreden i el seu període de rotació esdevé molt estable. Aquest període constant és molt útil per mesurar la massa dels estels de neutrons, i també per detectar ones gravitacionals amb molt baixa freqüència ($10^{-9} - 10^{-6}$ Hz). Es pot aprofitar l'estabilitat temporal d'un gran nombre de púlsars galàctics i detectar variacions en el temps d'arribada dels polsos de radiació (en ones de ràdio) a causa de la radiació gravitacional. Aquesta tècnica de detecció s'anomena *Pulsar Timing Array (PTA)*. Les ones gravitacionals caracteritzades per freqüències tan petites poden ser emeses per fonts com el fons de radiació gravitatòria de fusions de forats negres supermassius o fenòmens exòtics de l'Univers primerenc. De fet, ja s'ha anunciat una detecció d'aquest fons estocàstic d'ones gravitacionals.

Quan dos estels de neutrons es troben en un sistema binari, units gravitacionalment, els objectes eventualment col·lisionen. La pèrdua d'energia del sistema a causa de l'emissió de radiació gravitatòria redueix el radi orbital fins que les superfícies dels estels es toquen i els objectes es fusionen. Segons la massa dels components de la binària, entre d'altres, la natura del romanent de la fusió pot variar. Si la massa total del sistema és molt elevada, l'objecte col·lapsarà a un forat negre ràpidament. En canvi, si la massa total no supera un valor crític, l'objecte pot ser un estel de neutrons hipermassiu que romandrà estable durant uns centenars de mil·lisegons fins que col·lapse. L'elevat grau de rotació diferen-

cial i la pressió tèrmica generen el suport centrífug suficient per a contrarrestar la gravetat de l'objecte. Durant el seu breu temps de vida, l'estel hipermassiu pot sofrir diverses oscil·lacions i inestabilititats magnetohidrodinàmiques, a més d'ejectar massa, la qual forma un disc al voltant de l'objecte. El temps de vida del romanent de la fusió, junt amb la seua dinàmica, tenen implicacions importants en l'emissió de radiació electromagnètica i en la producció d'elements pesats. Per desgràcia, tot açò encara no s'entén completament, perquè depén estretament d'un tractament adequat de tota la física involucrada. A banda de necessitar una equació d'estat realista per descriure correctament el comportament de la matèria, els esquemes de transport de neutrins són importants per a estudiar la influència de la pressió tèrmica en l'estabilitat del romanent.

Com ja s'ha mencionant anteriorment, la massa expulsada durant i després de la fusió dels estels pot orbitar al voltant del romanent i formar un disc d'acreció. Aquesta massa pot ser expulsada mitjançant diversos mecanismes a diferents velocitats. Aquest material ejectat és important per a la creació d'elements químics. Nous elements poden ser produïts quan nuclis atòmics s'exposen a fluxos intensos de neutrons. En aquest escenari, la fracció d'electrons és molt petita, el que facilita la captura ràpida d'electrons i la creació d'elements molt pesats. De fet, es pensa que les fusions d'estels de neutrons són l'únic escenari en què es poden formar aquestos elements.

Cal també afegir que les binàries d'estels de neutrons són l'escenari idoni per a les explosions de raig gamma de curta duració. Quan el romanent de la fusió col·lapsa a un forat negre, dolls (ultra)relativistes nodrits per camps magnètics molt intensos són capaços d'emetre aquesta radiació.

Turbulència magnetohidrodinàmica

La turbulència generada durant la col·lisió dels estels de neutrons i durant la fase consegüent és capaç d'amplificar el camp magnètic dels estels diversos ordres de magnitud. Un camp magnètic molt intens pot tindre efectes en la dinàmica del romanent de la fusió, o tindre la capacitat d'impulsar dolls relativistes que podrien explicar certes observacions electromagnètiques. Per exemple, el desenvolupament de la inestabilitat magneto-rotacional en el romanent dona lloc a una redistribució del seu moment angular que en redueix el grau de rotació diferencial, la qual cosa afecta a l'estabilitat de l'objecte i, per tant, a l'emissió multi-missatgera i a la nucleosíntesi d'elements químics.

En escenaris molt dinàmics com les binàries d'estels de neutrons pot existir una transferència d'energia i de moment a través d'un ampli rang d'escales

de longitud, conegut com a rang inercial. Quan açò ocorre, les estructures a gran escala que es trobaven ordenades poden esdevindre una disrupció i formar petites estructures desordenades. L'energia i el moment es transferiran a aquestes escales, on l'energia cinètica es transforma en energia interna, fins que s'arriba a l'escala de dissipació, en què el ritme de transferència d'energia és igual al ritme de dissipació d'energia. El grau de turbulència es quantifica amb el nombre de Reynolds (Re), quantitat que mesura la ràtio entre la major escala del rang inercial i l'escala de dissipació. S'ha comprovat experimentalment que, per tal de considerar un fluid com a turbulent, el seu nombre de Reynolds ha de ser $\mathrm{Re} \gtrsim 1000$. En binàries d'estels de neutrons, aquesta quantitat pot arribar a valors de $10^{15} - 10^{16}$.

La font de turbulència dominant durant la col·lisió dels estels és la inestabilitat de Kelvin-Helmholtz (KH). El salt de velocitat en la interfície entre els dos estels pot produir cisalles a gran escala que activen aquesta inestabilitat. Aquestes cisalles de velocitat produeixen vòrtexs que, al seu torn, formen estructures més petites que poden amplificar el camp magnètic a petites escales diversos ordres de magnitud. La turbulència generada per la inestabilitat de KH decaurà amb el temps quan assolisca les escales dissipatives, ja que no hi ha injecció addicional d'energia cinètica des de les escales grans.

Durant l'evolució del romanent hipermassiu, la inestabilitat magneto-rotacional s'ha vist com el principal mecanisme responsable de produir turbulència magneto-hidrodinàmica i de redistribuir moment angular. Objectes amb rotació diferencial (amb un gradient negatiu de la velocitat angular) i amb camps magnètics dèbils estan subjectes a aquesta inestabilitat. Petites pertorbacions poden créixer exponencialment en forma d'estructures ordenadres i tindre un impacte en el fluid a gran escala. Aquest creixement de les pertorbacions s'atura eventualment arran de mecanismes que no s'entenen completament. Es creu que el desenvolupament d'inestabilitats parasítiques sobre la inestabilitat magneto-rotacional és la causa de la seua saturació. Aquestes inestabilitats secundàries creixen molt ràpidament i trenquen les estructures ordenades, el que dona lloc a un estat turbulent.

Les simulacions numèriques necessiten resoldre l'ampli rang d'escales en què la turbulència es desenvolupa per tal de capturar tota la física involucrada en el problema. Tanmateix, si la resolució espacial no és suficientment elevada, les simulacions potser només capturen una part d'aquest rang d'escales, el que pot resultar en un tractament incorrecte de la física a petita escala i amb conseqüències en totes les escales. En simulacions de fusions de binàries d'estels de neutrons, es necessiten recursos prohibitius per a dur a terme un tractament realista de la microfísica (equació d'estat, transport de neutrins) i

de la turbulència magnetohidrodinàmica. Per tant, és convenient dissenyar un model que siga capaç de capturar la física a petita escala i el desenvolupament de la turbulència amb una resolució moderada. Encara que aquest model de turbulència no siga correcte en escales molt petites, ha de ser capaç de capturar la física quan s'aplica a les escales característiques del problema.

Per tal de simular fusions d'estels de neutrons, les simulacions numèriques es realitzen en el context de la relativitat general. La inclusió de models per a turbulència pot significar la modificació de les equacions de la magnetohidrodinàmica (que descriuen la dinàmica del fluid magnetitzat) amb termes efectius que representen l'efecte de les escales no resoltes. En relativitat general, aquesta modificació de les equacions de moviment ha de retindre la seua covarància. Per tant, l'aplicació d'aquestos models ha de fer-se amb cura. Durant les últimes dècades, diversos models de turbulència s'han proposat en simulacions de fluids relativistes. En molts casos, les variables turbulentes es relacionen amb les quantitats resoltes per la simulació mitjançant relacions fenomenològiques que introdueixen certs factors que han de ser calibrats amb simulacions locals de control.

Simulacions de binàries d'estels de neutrons amb aquestos models han pogut reproduir amb èxit l'amplificació turbulenta del camp magnètic a petita escala, pròpia de la inestabilitat de KH. S'han comparat els resultats amb simulacions d'elevada resolució, i s'ha comprovat que es pot assolir la mateixa amplificació només utilitzant la meitat de la resolució emprada en simulacions sense models de turbulència. A més a més, l'aplicació d'un terme efectiu de viscositat en l'equació del moment és capaç de reproduir el transport de moment angular generat per la inestabilitat magneto-rotacional i dur a l'estel romanent de la fusió a un estat de rotació uniforme.

Un nou model per a la turbulència en binàries d'estels de neutrons

La major part d'aquestos anys l'he dedicada al desenvolupament d'un nou model de turbulència que siga capaç de reproduir l'evolució de les energies cinètiques turbulentes de les inestabilitats magnetohidrodinàmiques més importants en les fusions de dos estels de neutrons: la inestabilitat de KH i la inestabilitat magneto-rotacional. El model, que té un fort caràcter fenomenològic, es basa en equacions d'evolució per a les energies cinètiques turbulentes lligades a les inestabilitats del problema. En el Capítol 2, presente la versió del model per a la inestabilitat magneto-rotacional. Tal com he dit anteriorment, inestabilitats secundàries (les parasítiques) són les encarregades de saturar el creixement de la inestabilitat principal. Per tant, en aquest cas, la versió del meu model consta

de dues equacions que es troben lligades. Les equacions són hiperbòliques i diferencials, amb un terme de flux i termes font que contenen quantitats obteses a partir d'estudis analítics de la inestabilitat. La inestabilitat parasítica s'alimenta de la principal, i el terme de creixement de l'equació per a la energia parasítica és directament proporcional a l'energia de la inestabilitat magneto-rotacional, i al seu torn és el terme font negatiu en l'equació d'evolució de l'energia turbulenta de la inestabilitat primària. La dissipació en energia interna es veu reflectida en el sistema d'equacions amb un terme font negatiu a l'equació per a la inestabilitat parasítica. La resolució d'aquestes dues equacions diferencials permet reproduir el creixement exponencial i súper-exponencial (per al cas parasític) de les densitats d'energia turbulentes i la seua consegüent saturació.

Aquestes quantitats es poden relacionar amb els termes que s'han d'afegir a les equacions de la magnetohidrodinàmica, els tensors de tensió turbulents, i que representen els efectes de la dinàmica a petita escala. La relació es duu a terme mitjançant uns factors de proporcionalitat que, per simplicitat, es consideren constants en espai i temps. Els coeficients que s'apliquen a l'energia turbulenta de la inestabilitat magneto-rotacional són analítics i es basen en arguments físics, mentre que els coeficients parasítics s'han de calibrar amb simulacions de control.

En el Capítol 3, presente la versió del model de turbulència per a la inestabilitat KH. En aquest cas, el model és prou més simple. Només consta d'una equació per a la densitat d'energia turbulenta, i té la mateixa estructura que l'equació per a la densitat d'energia parasítica. Això és així perquè, en el context de magnetohidrodinàmica ideal (amb viscositat i resistivitat nul·les), les inestabilitats parasítiques que saturen la inestabilitat magneto-rotacional són de tipus KH. En aquest cas, però, el terme de creixement ve donat pel salt en velocitat característic de la interfície entre els dos estels. Mitjançant simulacions numèriques en caixes, he pogut testar el model i també calibrar els coeficients de proporcionalitat que relacionen la densitat d'energia turbulenta amb els tensors turbulents que apareixen en les equacions de moviment del fluid.

Per a ambdues versions del model, i amb l'ajuda de les simulacions numèriques de control, s'ha observat que el model és capaç de donar una estimació dels tensors de tensió turbulents del mateix ordre de magnitud que el cas en què la turbulència es pot resoldre. De fet, al Capítol 4 es presenten simulacions numèriques d'un estel de neutrons magnetitzat amb rotació diferencial. En aquestes condicions, s'espera que la inestabilitat magneto-rotacional es desenvolupe si s'empra la resolució espacial necessària. Per tant, després d'introduir en el codi numèric les equacions d'evolució de les energies turbulentes de la inestabilitat magneto-rotacional i la parasítica, s'han realitzat simulacions amb baixa resolució, la

qual, en principi, no permet observar el desenvolupament de la inestabilitat. No obstant això, la inclusió del model en les simulacions dona lloc al transport de moment angular que s'espera arran del desenvolupament de la inestabilitat. Per contra, com s'esperava, en simulacions que no contenen el model no s'observa aquest efecte. En aquestes simulacions només s'han afegit els tensors turbulents en l'equació del moment del fluid, però si es vol estudiar l'amplificació del camp magnètic s'hauria de modificar també l'equació d'inducció per al camp magnètic. Investigacions amb lleugeres modificacions del model es faran en el futur pròxim per a estudiar aquest altre tret característic de la inestabilitat magneto-rotacional. A més, la implementació d'una formulació covariant del model és necessària per dur a terme simulacions numèriques en relativitat general.

La saturació de la inestabilitat magneto-rotacional

Al Capítol 5 s'investiga, mitjançant un estudi analític de les equacions magneto-hidrodinàmiques, l'evolució dels modes parasítics que s'encarreguen de saturar la inestabilitat magneto-rotacional. Aquest tipus d'estudi ja s'havia realitzat amb anterioritat, però en aquest cas moltes simplificacions s'han relaxat i s'ha pogut obtenir resultats més realistes que concorden més amb resultats de simulacions numèriques locals capaces de resoldre la inestabilitat. En aquest Capítol s'ha estudiat el creixement súper-exponencial d'una gran quantitat de modes parasítics amb diferents amplituds inicials. S'ha observat que els modes que creixen més ràpidament assoleixen la mateixa amplitud que la inestabilitat magneto-rotacional (és a dir, la saturació) quan aquesta és més d'un ordre de magnitud major que el camp magnètic vertical inicial, tal i com s'observa en treballs numèrics. A més, els resultats d'aquest treball suggereixen una petita modificació del meu model de turbulència presentat al Capítol 2, ja que aquest tractament més realista de les inestabilitats parasítiques ha permés observar que el seu creixement és, en realitat, més lent del que s'esperava.

Anàlisi de senyals d'ones gravitacionals de binàries d'estels de neutrons

Les fusions de binàries d'estels de neutrons són fonts principals de radiació gravitatòria. La detecció de senyals d'ones gravitacionals de fusions de binàries d'estels de neutrons ens permet acarar els resultats obtesos mitjançant simulacions numèriques amb les observacions i inferir paràmetres físics de la font (que es troben codificats en el senyal). Simulacions mostren que el senyal emés en aquest sistema és molt sensible a l'equació d'estat de la matèria. A més,

l'espectre de freqüències del romanent de la fusió mostra l'excitació de modes d'oscil·lació en l'estel. És per això que una anàlisi curosa d'aquestos trets podria donar informació inestimable de la física dels estels de neutrons.

El senyal d'ones gravitacionals reflecteix la dinàmica del sistema. Durant la fase en què els dos estels s'apropen l'un a l'altre, abans de col·lisionar, l'amplitud i la freqüència del senyal augmenten. En aquesta fase, l'emissió d'ones gravitacionals està ben aproximada per expansions analítiques i semi-analítiques. L'efecte de marea a causa del tamany finit de l'estel de neutrons es troba gravat en l'ona gravitacional, ja que canvia l'evolució de la seua fase. Aquestes deformacions de marea depenen molt de l'equació d'estat i poden ser descrites per un paràmetre conegut com a deformació de marea. Aquest paràmetre, junt amb les masses de la binària i la seua ràtio, són els paràmetres que dominen en l'ona gravitacional durant aquesta fase anterior a la fusió. La rotació dels estels i l'eccentricitat del sistema juguen un paper secundari. Arran dels events GW170817 i GW190425, detectats per la col·laboració LIGO, Virgo i KAGRA (LVK) i que es corresponen amb les dues úniques fusions de binàries d'estels de neutrons observades fins ara, hi existeixen estimacions reals d'aquest paràmetre de deformació de marea. Amb el valor obtingut de la deformació de marea, i amb el de la massa efectiva de la binària, va ser possible obtindre una estimació del valor del radi de l'estel de neutrons més massiu del sistema. Açò es va dur a terme mitjançant relacions universals independents de l'equació d'estat, construïdes amb nombroses simulacions numèriques.

Durant la fase posterior a la fusió dels estels de neutrons, l'energia emesa en ones gravitacionals és considerablement major que durant la fase prèvia a la col·lisió, i la freqüència característica del senyal es troba en el rang dels kHz. Aquesta part del senyal és més difícil de descriure i té una natura certament estocàstica, a causa de la interacció de diferents efectes tals com turbulència, camps magnètics intensos, radiació de neutrins o inestabilitats hidrodinàmiques. A més, ja hem vist que dur a terme simulacions realistes d'aquesta fase de la fusió és una tasca molt complicada. En conseqüència, és també difícil extraure senyals d'ones gravitacionals realistes que es puguen emprar per a futures deteccions. L'espectre de les ones gravitacionals emeses durant els primers mil·lisegons després de la col·lisió es troba caracteritzat per un pic principal que es correspon amb el mode fonamental quadrupolar d'oscil·lació de l'estel. La localització d'aquest pic és sensible a l'equació d'estat. Més concretament, simulacions numèriques han permés determinar que el pic està estretament correlacionat amb la deformació de marea. Variacions en l'equació d'estat poden produir una varietat significant d'espectres d'ones gravitacionals amb diferents posicions dels

pics de freqüència. És per això que l'ús de relacions quasi-universals que enllacen aquesta freqüència amb propietats de l'estel de neutrons romanent ha fet que l'espectroscopia d'ones gravitacionals esdevinga un camp de recerca molt actiu per a estudiar l'equació d'estat d'aquestos objectes. Cal afegir que hi poden existir pics secundaris relacionats amb diferents modes d'oscil·lació estelars.

Mentre el romanent evoluciona, aquest s'estabilitza i l'amplitud del senyal d'ona gravitacional disminueix, i les freqüències del senyal també evolucionen amb el temps. Eventualment, el romanent pot col·lapsar a un forat negre, i l'emissió de radiació gravitacional s'atura sobtadament.

La tècnica emprada per inferir els paràmetres físics de sistemes de binàries d'estels de neutrons durant la fase prèvia a la col·lisió és, en anglés, el *matched filtering*. Aquest mètode permet identificar senyals soterrats en soroll del detector mitjançant la correlació de les dades amb models generats a partir de mil·lions de mostres d'ones gravitacionals teòriques. A més, aquesta tècnica permet estimar paràmetres astrofísics de les fonts d'ones gravitacionals. Malauradament, el senyal posterior a la fusió dels estels és molt més difícil de detectar, perquè el seu rang de freqüències característic no és òptim per als detectors actuals. A causa del nombre limitat de simulacions numèriques d'aquesta fase de la fusió, no és possible produir un nombre suficient d'ones gravitacionals sintètiques per dur a terme el *matched filtering*. Una alternativa a aquesta tècnica és la recerca no modelada de senyals. Malgrat ser un mètode menys eficient, permet reconstruir la fase posterior a la col·lisió i extraure informació de l'espectre d'ones gravitacionals.

Reconstruccions no modelades dels senyals de romanents hipermassius

Al Capítol 7 presente una aplicació d'aquesta recerca no modelada de senyals gravitacionals. Els romanents hipermassius, després d'unes quantes desenes de mil·lisegons, quan el mode quadrupolar dominant es relaxa, poden esdevindre inestabilitats convectives que exciten els anomenats modes inercials, els quals presenten freqüències i una amplitud menors que les del mode quadrupolar. L'estudi, mitjançant la reconstrucció no modelada dels senyals extrets de simulacions numèriques i injectats en soroll dels detectors, mostra que aquestos modes no es poden detectar pels observatoris d'ones gravitacionals actuals (LIGO, Virgo i KAGRA), però sí per futurs detectors (Cosmic Explorer i Einstein Telescope), els quals tenen una sensitivitat deu vegades major que la dels actuals. La detecció d'aquestos modes i la caracterització dels seus pics a l'espectre d'ones gravitacionals poden donar informació addicional de l'equació d'estat, a més d'una visió més profunda de l'estructura interna d'aquestos romanents hipermassius. Les

freqüències característiques dels modes inercials potser estiguen relacionades amb paràmeters físics de l'estel de neutrons. Açò podria comprovar-se mitjançant la realització de simulacions numèriques amb diverses equacions d'estat que permeten construir relacions quasi-universals. Per desgràcia, es necessiten escales de temps prou elevades per excitar aquestos modes, la qual cosa pot limitar la producció d'aquestes simulacions.

A banda d'aquest treball, al Capítol 8 he avaluat la possible identificació d'efectes tèrmics en romanents de fusions d'estels de neutrons mitjançant, de nou, reconstruccions no modelades de senyals d'ones gravitacionals. Quan el romanent hipermassiu es forma, la temperatura no es pot negligir i s'ha de tindre en compte en les simulacions numèriques. La forma d'introduir aquestos efectes en les simulacions és a través de l'equació d'estat. Dos enfocaments diferents s'empren actualment: l'enfocament híbrid, computacionalment menys costós però, al seu torn, menys realista, i l'ús d'equacions d'estats tabulades, computacionalment més costoses però que incorporen efectes tèrmics d'una manera més realista. En aquest Capítol, reconstruccions de senyals injectats en soroll mostren que les freqüències de l'espectre característiques del mode fonamental quadrupolar són diferents entre els dos enfocaments, i que aquestes diferències poden ser detectades a distàncies considerables per futurs detectors. La distància màxima de detectabilitat depén de l'equació d'estat considerada.

Classificació a temps real de fonts d'ones gravitacionals amb un nou mètode bayesià

Actualment, la col·laboració LVK es troba en el seu quart període d'observació (O4). Al llarg dels anys, la sensitivitat dels detectors ha millorat, i açò ha resultat en un increment substancial de les deteccions d'ones gravitacionals. En aquest nou període d'observació es realitza aproximadament una detecció al dia, i s'espera que açò augmente en els pròxims períodes d'observació. Aquest fet pot afectar els mètodes tradicionals emprats per la detecció de senyals i l'estimació de paràmetres. Doncs, l'ús de tècniques de intel·ligència artificial en l'astrofísica d'ones gravitacionals està esdevenint un increment considerable. Les seues aplicacions són increïblement diverses. En l'anàlisi de dades d'ones gravitacionals, la intel·ligència artificial pot completar els bancs de mostres emprats en *matched filtering*, ajudar en cerques d'events i accelerar l'estimació de paràmetres de les fonts dels senyals.

Al Capítol 9 s'explora una de les possibles aplicacions de la intel·ligència artificial en el camp de l'astrofísica d'ones gravitacionals. Hi presente un nou esquema per a classificar en temps real senyals d'ones gravitacionals provinents de

binàries d'objectes compactes. Aquest mètode empra les masses i els paràmetres de rotació estimats pels algoritmes de detecció per oferir probabilitats que la font de radiació gravitatòria tinga un estel de neutrons i, si escau, hi haja matèria romanent després de la col·lisió de la binària. Aquestes mètriques venen donandes per dos algoritmes supervisats de classificació, anomenats *Random Forest* (RF) i *K-Nearest Neighbours* (KNN), els quals han sigut entrenats sobre conjunts enormes de dades i una gran varietat d'equacions d'estat.

La novetat presentada en aquest Capítol és l'ús d'una tècnica bayesiana per calcular probabilitats més realistes a partir dels resultats dels algoritmes de classificació. Aquest esquema ofereix informació més directa i interpretable que pot ser d'utilitat per a la comunitat astronòmica, ja que ajudaria a donar una resposta ràpida per realitzar observacions en l'espectre electromagnètic, en el cas en què hi haguera un romanent que emetera aquest tipus de radiació. A més, aquest mètode es pot aplicar a altres propietats dels senyals gravitacionals detectats pels observatoris LVK. Per exemple, podria donar la probabilitat que una de les components de la binària es trobe en el buit de massa dels estels de neutrons. Com els estels de neutrons tenen una massa màxima (al voltant d'unes 2.5 masses solars), i forats negres amb masses inferiors a 5 masses solars rarament s'han observat, hi existeix un buit de massa entre l'estel de neutrons més massiu i el forat negre més lleuger mai observats. Trobar objectes dins d'aquesta regió crítica podria donar-nos informació molt important. Si hi es troba un estel de neutrons, aquesta observació posaria restriccions molt fortes en l'equació d'estat de la matèria densa. Alternativament, si es detecta un forat negre en aquesta regió, això tindria un fort impacte en el nostre enteniment de les explosions de *supernova*, les quals són el mecanisme de formació dels forats negres de massa estelar.

Altres treballs

A banda dels treballs en què he sigut l'autor principal, els quals ja han estat resumits, he participat en diversos projectes amb un paper més secundari. A l'Apèndix A, explique de manera resumida els projectes en què he estat involucrat i la meua contribució a aquestos. Dos d'aquestos treballs consisteixen en l'estudi dels efectes de la matèria fosca en la dinàmica i l'estabilitat dels estels de neutrons. Aquesta matèria fosca pot representar-se mitjançant partícules bosòniques molt lleugeres que només interactuen gravitacionalment amb la matèria fermiònica que constitueix els estels de neutrons.

El primer projecte consisteix en l'estudi de l'impacte que pot tindre un núvol de matèria fosca constituït per partícules bosòniques en l'estabilitat d'un estel de neutrons que, aïllat, és inestable a la *inestabilitat de barra*. Quan un estel amb rotació diferencial gira amb molta velocitat, pot patir una deformació en forma de barra. Aquesta inestabilitat, relacionada amb un cert mode d'oscil·lació de l'estel, excita l'emissió d'ones gravitacionals. En aquest treball, trobàrem que l'addició de matèria fosca (mitjançant l'acoblament del potencial del camp bosònic a les equacions d'Einstein) pot alterar aquesta inestabilitat, i excitar diferents modes d'oscil·lació i, fins i tot, estabilitzar l'estel. Aquest efecte depén de la massa del núvol bosònic i de la mateixa partícula de matèria fosca.

El segon projecte relacionat amb l'efecte de la matèria fosca en estels de neutrons pretén estudiar l'efecte de l'axió, una partícula bosònica amb un potencial característic, en la configuració d'equilibri dels estels de neutrons. Quan es troben aïllats, els estels de neutrons tenen configuracions estables per a certs valors de la seua massa i el seu radi. En afegir aquest camp bosònic, vam trobar que hi poden existir més configuracions d'equilibri, és a dir, que es poden trobar estels de neutrons estables per a més combinacions de masses i radis, segons també quins valors tinguen els paràmeters que descriuen el camp de l'axió.

Per últim, durant la meua estada al Niels Bohr Institute vaig realitzar un projecte secundari que consistia en l'estudi dels efectes de la memòria d'ones gravitacionals en el fons còsmic de microones. La memòria d'ones gravitacionals és un efecte de la relativitat general que ocorre quan una ona provoca un canvi persistent en la posició relativa de parells de masses. Aquest efecte pot generar-se a causa de la col·lisió de binàries massives de forats negres, entre d'altres. En aquest projecte vam descobrir que l'efecte de memòria pot provocar fluctuacions en la temperatura del fons còsmic de microones, perquè pot alterar la longitud d'ona dels fotons mitjançant un procés de camí aleatori. Aquestes fluctuacions, malauradament, són de molt baixa magnitud, i els observatoris actuals ho tenen molt difícil per detectar-les.

List of publications

- **Assessment of a new sub-grid model for magnetohydrodynamical turbulence. I. Magnetorotational instability**. **Miquel Miravet-Tenés**, Pablo Cerdá-Durán, Martin Obergaulinger and José A. Font. *MNRAS*, Volume 517, Issue 3, pp. 3505–3524, November 2022. DOI: 10.1093/mnras/stac2888.

- **Assessment of a new sub-grid model for magnetohydrodynamical turbulence. II. Kelvin–Helmholtz instability**. **Miquel Miravet-Tenés**, Pablo Cerdá-Durán, Martin Obergaulinger and José A. Font. *MNRAS*, Volume 527, Issue 1, pp. 1081–1092, October 2023. DOI: 10.1093/mnras/stad3237.

- **Effective angular momentum transport in differentially rotating neutron stars**. **Miquel Miravet-Tenés**, Martin Obergaulinger, Milton Ruiz, Pablo Cerdá-Durán and José A. Font. To be submitted. 2024.

- **The saturation of the magnetorotational instability – revisited**. **Miquel Miravet-Tenés** and Martin E. Pessah. To be submitted. July 2024.

- **Prospects for the inference of inertial modes from hypermassive neutron stars with future gravitational-wave detectors**. **Miquel Miravet-Tenés**, Florencia L. Castillo, Roberto De Pietri, Pablo Cerdá-Durán and José A. Font. *Phys. Rev. D*, Volume 107, Issue 10, pp. 103053, May 2023. DOI: 10.1103/PhysRevD.107.103053.

- **Identifying thermal effects in neutron star merger remnants with model-agnostic waveform reconstructions and third-generation detectors**. **Miquel Miravet-Tenés**, Davide Guerra, Milton Ruiz, Pablo Cerdá-Durán and José A. Font. January 2024. Submitted to *Phys. Rev. D*.

- **Bayesian real-time classification of multi-messenger electromagnetic and gravitational-wave observations**. Marina Berbel, **Miquel Miravet-Tenés**, Sushant Sharma Chaudhary, Simone Albanesi, Marco Cavaglià, Lorena Magaña Zertuche, Dimitra Tseneklidou, Yanyan Zheng, Michael W. Coughlin and Andrew Toivonen. *Class. Quantum Grav.*, Volume 41, Issue 8, pp. 085012, April 2024. DOI: 10.1088/1361-6382/ad3279.

- **Impact of ultralight bosonic dark matter on the dynamical bar-mode instability of rotating neutron stars**. Fabrizio Di Giovanni, Nicolás Sanchis-Gual, Davide Guerra, **Miquel Miravet-Tenés**, Pablo Cerdá-Durán and José A. Font. *Phys. Rev. D*, Volume 106, Issue 4, pp. 044008, August 2022. DOI: 10.1103/PhysRevD.106.044008.

- **Fermion-axion stars: Static solutions and dynamical stability**. Fabrizio Di Giovanni, Davide Guerra, Simone Albanesi, **Miquel Miravet-Tenés**, Dimitra Tseneklidou. *Phys. Rev. D*, Volume 106, Issue 8, pp. 084013, October 2022. DOI: 10.1103/PhysRevD.106.084013.

- **Gravitational Wave Memory Imprints on the CMB from Populations of Massive Black Hole Mergers**. Lorenz Zwick, David O'Neill, Kai Hendriks, Philip Kirkeberg and **Miquel Miravet-Tenés**. April 2024. Submitted to *Astron. Astrophys.*.

Contents

Nomenclature

Acronyms / Abbreviations

ADM	Arnowitt–Deser–Misner
ANN	artificial neural network
ASD	amplitude spectral density
BBH	binary black hole
BH	black hole
BNS	binary neutron star
BSSN	Baumgarte-Shapiro-Shibata-Nakamura
CBC	compact binary coalescence
CCSN	core-collapse supernova
CE	Cosmic Explorer
CFL	Courant-Friedrichs-Lewy
CFS	Chandrasekhar-Friedman-Schutz
CI	credible interval
CMB	Cosmic Microwave Background
CNN	convolutional neural network
cWB	Coherent Wave Burst
DL	deep learning

DNS direct numerical simulations

EM electromagnetic

EOB effective one-body

EOS equation of state

ET Einstein Telescope

FAR false alarm rate

FFE force-free electrodynamics

FFT fast Fourier transform

FPR false positive rate

GCN General Coordinates Network

GPR Gaussian process regression

GRB gamma-ray burst

GR General Relativity

GRMHD general-relativistic magnetohydrodynamics

GW gravitational wave

GWM gravitational-wave memory

GWTC Gravitational-wave Transient Catalog

HLLE Harten, Lax, Van Leer, Einfeldt

HLL Harten-Lax-van Leer

HLV Hanford-Livingston-Virgo

HMNS hypermassive neutron star

IMBH intermediate-mass black hole

ISCO innermost stable circular orbit

karoo KarooGP

KHI Kelvin – Helmholtz instability

KNN KNeighborClassifier

LES large-eddy simulations

LIGO Laser Interferometer Gravitational-Wave Observatory

LVC LIGO and Virgo Collaboration

LVK LIGO, Virgo, and KAGRA

MCMC Markov Chain Monte Carlo

MDC Mock Data Challenge

MHD magnetohydrodynamics

MInIT MHD-instability-induced-turbulence

ML machine learning

MMA multi-messenger astronomy

MP monotonicity-preserving

MRFF mean rest fluid frame

MRI magnetorotational instability

NICER Neutron star Interior Composition Explorer

NR Numerical Relativity

NSBH neutron star-black hole

NS neutron star

O2 second observing run

O3 third observing run

O4 fourth observing run

O5 fifth observing run

PI parasitic instability

PN post-Newtonian

PNS protoneutron star

PPM Piecewise Parabolic Method

PSD power spectral density

PTA pulsar timing array

PT phase transition

QPOs quasi-periodic oscillations

RF random forest

RJMCMC reversible jump Markov chain Monte Carlo

RMNS remnant massive neutron star

ROC Receiver Operating Characteristic

SFS sub-filter scale

sGRBs short gamma-ray bursts

SNR signal-to-noise ratio

SN supernova

TOV Tolman-Oppenheimer-Volkoff

TPR true positive rate

WD white dwarf

WENO weighted essentially non-oscillatory

CHAPTER 1

Introduction

I have been extremely fortunate to do my PhD thesis during a period where a lot of progress is being made in the field of gravitational astrophysics. The first ever detection of a gravitational wave (GW) signal occured during the first day of my Bachelor degree, and the subsequent observations stimulated me to start my research career in this direction. Plenty of new GW signals from a wide variety of astrophysical sources which are still invisible to us are awaiting to be detected.

We are in a golden era of astrophysics where a plethora of new GW observations is changing our understanding of the Universe at an unprecedented rate [Abbott et al. 2016a, Abbott et al. 2019a, Abbott et al. 2021c, Abbott et al. 2024, Abbott et al. 2023b]. In particular, the seminal observations of GWs from binary neutron star (BNS) merger GW170817, along with the subsequent observation of electromagnetic (EM) radiation across the entire spectrum (from radio waves to gamma rays), spurred the era of multimessenger astronomy [Abbott et al. 2017b, Abbott et al. 2017e, Abbott et al. 2017c]. Multimessenger observations of BNS mergers provide the most direct evidence that stellar compact mergers, where at least one of the binary companions is a neutron star (NS), are progenitors of the central engines that power gamma-ray bursts (GRBs) [MacFadyen and Woosley 1999]; they give strong observational support to theoretical proposals linking BNS mergers with production sites for r-process nucleosynthesis and kilonovae [Eichler et al. 1989, Li and Paczynski 1998, Metzger et al. 2010a]; they can be used as standard sirens to give an independent measure of the expansion of the Universe [Schutz 1986, Nissanke et al. 2010, Abbott et al.

2017a], and put tight constraints on the equation of state (EOS) of matter at supranuclear densities (see, e.g., Oertel et al. 2017 and references therein).

Our understanding of the complex physics and dynamics involved in BNS mergers and in their postmerger evolution has significantly expanded in the last few decades. This has been possible thanks to the use of numerical simulations, ever larger and more accurate in terms of computational resources and more sophisticated in terms of input physics. Numerical Relativity (NR) is the tool which is employed to study these systems (see Paschalidis [2017], Baiotti and Rezzolla [2017], Duez and Zlochower [2019], Shibata and Hotokezaka [2019], and Ciolfi [2020b] for recent reviews). The huge parameter space of the problem, its dimensionality, and the amount of physics involved limit the number of simulations. To properly describe these systems, numerical simulations need to employ realistic EOS that include thermal effects and other microphysical features; a proper transport scheme for neutrinos; large enough resolution to capture small-scale turbulence, and more other physics that play a role and will be further discussed in the following sections.

Therefore, the description of the long-term evolution of the postmerger phase for generic initial conditions remains poorly constrained [Siegel et al. 2013, Shibata and Hotokezaka 2019, Ciolfi 2020b]. As a result, linking the results of simulations with the data from multimessenger observations of BNS mergers, short gamma-ray bursts (sGRBs) and kilonovae, is still to a large extent an ongoing task.

1.1 Neutron stars

NSs are ideal astrophysical laboratories for testing matter at extreme conditions and provide connections between astrophysics, nuclear physics and particle physics. The extreme densities reached in their core ($\sim 10^{14}$ g/cm^3) can result in matter dominated by exotic particles and phenomena such as superfluidity and superconductivity. They also possess the most intense magnetic fields in the Universe (with strengths up to 10^{16} G in some cases) and can rotate at very high frequencies, reaching rotational frequencies of several kHz. Due to their high compactness, General Relativity (GR) must be taken into account to properly describe their equilibrium structure. Their typical mass and radius, which can be determined by the Tolman-Oppenheimer-Volkoff (TOV) equations (under spherical symmetry and neglecting magnetic fields) together with a realistic relation between the thermodynamic variables (EOS), are of the order of 1.5 $M_\odot$ and ~ 12 km, respectively.

1.1.1 **Formation**

NSs are born after the gravitational collapse of the iron core of a massive star with a mass $M \geq 10\ M_{\odot}$, which triggers a core-collapse supernova (CCSN) explosion[1]. The explosion mechanism is still not fully understood, but neutrinos can play an important role in the absence of rapid rotation, leading to neutrino-driven explosions [Bethe and Wilson 1985, Burrows and Lattimer 1987]. Neutrinos leak out from the hot interior of the protoneutron star (PNS), carrying away the energy needed to revive the (accretion) shock. A small fraction of the emitted neutrinos is absorbed, heating the surrounding gas. This provokes that the stalled shock, which has lost energy as it progressed radially ourwards, revives and the supernova explosion sets. The energy released in this explosion is of the order of 10^{51} erg. Due to the diverse CCSN progenitors, PNSs can be born with different rotation rates. For progenitors with rapid rotation (with rotation frequencies in the range of several Hz), the amplification of the magnetic field can in fact drive the explosion, resulting in magnetorotational explosions [Kuroda et al. 2020, Obergaulinger and Aloy 2021, Powell et al. 2023]. The PNS remnant is born with rotation frequencies of the order of ~ 1 kHz and amplified magnetic field strengths of $\sim 10^{14}$ G. In this scenario, a collimated outflow can be produced, being a candidate r-process site. Moreover, the energy explosions can be higher than the neutrino-driven mechanism, reaching values of $\sim 10^{52}$ erg.

The PNS is born with an initially large temperature of order 50 MeV and a radius of around 100 km. It is lepton rich and consists of an unshocked core with low entropy and high density, surrounded by a transition region and a shocked envelope with lower density and higher entropy. The neutrinos in the inner region are trapped, but the outer envelope is not opaque to neutrinos. Less than a second after core bounce, the outer envelope cools down and contracts, decreasing its entropy. After several minutes, the NS cools down to temperatures lower than 1 MeV, and thermal effects become negligible [Burrows and Lattimer 1986, Keil and Janka 1995, Keil, Janka, and Mueller 1996, Prakash et al. 1997, Pons et al. 1999]. In some cases, the PNS may not survive this early evolution, collapsing instead to a black hole (BH). This might be due to the fact that the accretion pushes the PNS above the maximum mass supported gravitationally (fallback supernova, e.g., Chan et al. 2018), or if the shock is never revived and the mass goes into forming a BH (failed supernova, e.g., Nadezhin 1980). If the failed supernova occurs for a rotating progenitor, the collapsing mass can circularise into an accretion disc around the BH. This disc can be neutrino-cooled

[1] An alternative formation mechanism for NSs is the accretion-induced collapse of a white dwarf (WD) [Nomoto 1982] that leads to a Type Ia supernova.

if it is formed deep enough. This system, known as *collapsar* [Woosley 1993], can give rise to a relativistic jet, powering a long-duration gamma-ray burst (lGRB) [Woosley and Bloom 2006].

The stable PNS continues cooling down and reaches uniform rotation due to a combination of spin-down mechanisms and viscosity. These isolated stable NSs can be relatively highly magnetised ($B \sim 10^{10} - 10^{15}$ G) and emit beams of EM radiation (in the radio range) out of their magnetic poles. Due to their stable rotational periods, these beams are observed as pulses of radiation when they arrive to Earth, and were first identified by Jocelyn S. Bell more than 50 years ago [Hewish et al. 1968] as pulsating stars (PSR B1919+21). That is why NSs that spin rapidly and are magnetised are also known as *pulsars*.

1.1.2 **Structure**

NSs are only surpassed by BHs as the most known compact objects in the Universe. They span a wide range of density regimes [Lattimer and Prakash 2004], from densities comparable to those of the WDs to values above the nuclear density, $\rho_{\rm nuc}$ ($\sim 10^{14}$ g/cm^3). Figure 1.1 shows the surface and internal layers of a NS. These objects possess a very thin atmosphere of a few centimeters and an envelope with a negligible amount of mass, but both play a key role in the formation of the photon spectrum and in the transport of thermal energy from the star. The envelope is followed by an outer crust with a mass density similar to a WD ($\rho \sim 10^7$ g/cm^3), where nuclei (mainly $^{56}_{26}$Fe) are in a lattice and the electron degeneracy pressure dominates. As density increases, the dominant nuclei achieve a neutron excess with a mass number $A \sim 200$, which is impossible to reproduce in terrestrial laboratories. When density overcomes the neutron drip threshold at $\rho \approx 4.3 \times 10^{11}$ g/cm^3 (resulting in a null neutron chemical potential), free nucleons coexist with nuclei, resulting in a neutron fluid that dominates over nuclei. In the transition to the NS core, nuclei are close together and the lattice transforms into a continuous phase in which matter has a different dimensionality (from 3D nuclei to 1D slabs) and coexists with multidimensional voids. This is known as the nuclear pasta phase and happens when the mass density is close to the nuclear density, $\rho_{\rm nuc} \sim 10^{14}$ g/cm^3. When $\rho \approx \rho_{\rm nuc}$, the lattice dissolves entirely and matter in the core consists of free nucleons, electrons and neutrinos that are created and trapped within. Above nuclear density, the Fermi energy is so high that even nucleons become relativistically degenerate, and neutrons and protons interact to form exotic particles such as pions (forming Bose-Einstein condensates), kaons and hyperons, leading to a

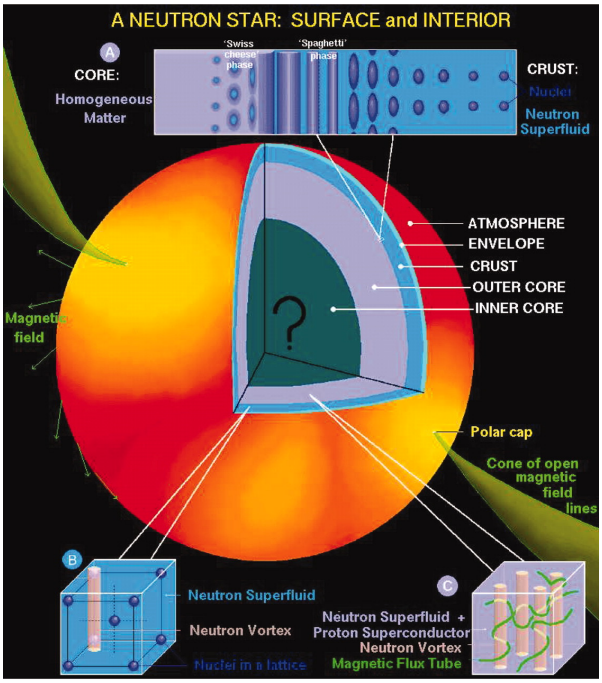

Figure 1.1 Surface and internal regions of a NS. The upper bar shows the geometric matter transitions between the crust and the core. In the bottom, superfluid aspects of the crust (left) and the core (right) are depicted. From Lattimer and Prakash 2004. Reprinted with permission from AAAS.

region of coexisting hadronic and deconfined quark matter [Glendenning 1992, Alford 2001], characterised by superfluidity and superconductivity.

1.1.3 **Equation of state**

The characteristic supranuclear densities of NSs lead to a source of pressure (to balance gravity) that is not only produced by electrons, but mostly by nucleons and other exotic particles. Therefore, the EOS must correctly describe matter at such extreme conditions (see, e.g., Glendenning 1997, Klähn et al. 2006).

The evolution of BNS systems and also the structure and stability of the resulting remnants are highly dependent of the EOS. Moreover, the EOS has a high impact in the neutrino emission and the conditions for the r-process nucleosynthesis to happen during the BNS postmerger phase [Ruffert, Janka, and Schaefer 1996, Ruffert et al. 1997]. Furthermore, very high densities are reached as well in CCSNe [Kotake, Sato, and Takahashi 2006, Burrows and Vartanyan 2021] and in the resulting PNS, and the treatment of matter can

have a strong influence in the further evolution of the PNS [Prakash et al. 1997, Pons et al. 1999]. This is the reason why there have been strong efforts to constrain the thermodynamics of these compact objects (see, e.g., Lattimer 2012 and Oertel et al. 2017 for reviews and references therein).

1.1.3.1 *Theoretical approaches to build an equation of state*

The number of parameters used to build an EOS depends on the equilibrium conditions. For a cold and charged-neutral NS in β-equilibrium, the EOS can be parametrised solely with the baryonic number density, n_B. In this case, an EOS given in terms of the pressure and the energy density can close the system of hydrodynamic equations and determine global properties of the star such as the masses and radii. However, in PNSs and BNS mergers β-equilibrium is not achieved, and temperature effects are not negligible. This makes the temperature and the electron fraction, Y_e, additional parameters of the EOS. The EOSs that cover ranges of temperature and charge fractions that are characteristic of NSs can be used in numerical simulations which can lead to results that can be contrasted with astrophysical observations [Lattimer and Prakash 2007, Steiner, Lattimer, and Brown 2010, Fortin et al. 2016]. Such EOSs should also include a description of nonuniform matter at subsaturation densities where nuclei appear, and a description of homogeneous matter at supranuclear densities [Oertel et al. 2017]. Relatively high temperatures achieved in CCSNe and BNS mergers favor the appearance of additional particles apart from electrons, nuclei and nucleons, e.g., hyperons [Oertel, Fantina, and Novak 2012] or pions [Peres, Oertel, and Novak 2013]. Moreover, phase transitions to quark matter might be included [Nakazato, Sumiyoshi, and Yamada 2008, Sagert et al. 2009].

There exist different *ab initio* methods to build a NS EOS that start from "realistic" few-body interactions to face the many-body problem [Fetter and Walecka 2003, Guardiola 1998, Müther and Polls 2000, Lee 2009, Baldo and Burgio 2012]. An alternative to the *ab initio* methods are the so-called phenomenological approaches which employ effective interactions with less complexity. Phenomenological EOSs can be seen as purely parametric mean-field models in which a parametrised functional is fitted to microscopically motivated EOSs [Nambu and Jona-Lasinio 1961a, Nambu and Jona-Lasinio 1961b, Chodos et al. 1974, Bender, Heenen, and Reinhard 2003]. Thus, these models are very useful to apply in astrophysical simulations (see e.g. Read et al. 2009 for piecewise polytrope fits and Alford 2001 for the application of a linear fit for quark matter). All these approaches deal with particle interactions and treat the many-body problem of a variety of subatomic particles in different ways. The complexity of the

EOS models can vary, going from single-parameter, barotropic EOSs, i.e. polytropic EOS [Tooper 1965], to hadronic EOS [Heiselberg and Hjorth-Jensen 2000, Haensel, Potekhin, and Yakovlev 2007] and strange quark EOS [Glendenning 1997, Gondek-Rosińska et al. 2000].

1.1.3.2 *Observational constraints on the equation of state: masses and radii*

Presently, NS masses probably represent the most reliable observational constraint on the EOS of compact stars. Masses can be accurately measured from radio binary pulsars [Manchester and Taylor 1977], in which a pulsar is orbiting around another NS, a WD or a main-sequence star. The extraordinary stability of the pulsar period allows for accurate timings of the binary orbits. The measure of the Doppler shift permits inferring the orbital velocities and the total mass of the binary can be deduced. The maximum NS mass is an important quantity useful to rule out candidates for NS EOS. The pulsars observed in PSR J1614-2230 [Demorest et al. 2010] and PSR J0348+0432 [Antoniadis et al. 2013], with masses of $1.928 \pm 0.017\ M_\odot$ and $2.01 \pm 0.04\ M_\odot$, respectively, are the most massive pulsars measured with relatively high precision, constraining considerably the parameter space of the EOS (see Figure 1.2). Moreover, the detection of some relativistic effects facilitates the measurements of each component mass. The Shapiro delay [Shapiro 1964] yields a slower propagation of the pulsar radiation due to a deep gravitational well, compared to flat spacetime. Moreover, an orbiting pair of NSs emit GWs that carry away angular momentum and energy from the system, shrinking the orbits. This effect was first observed in the Hulse-Taylor binary pulsar, PSR B1913+16, becoming a strong proof of GR [Lorimer 2008]. Years later, the Shapiro delay was observed with relatively high precision in the binary pulsar PSR B1534+12 [Stairs et al. 2002]. The masses of the pulsar PSR J0737-3039 [Lyne et al. 2004] have also been determined to impressive accuracy employing this method. Masses can also be measured for NSs that accrete matter from a stellar companion in the so-called X-ray binaries, but with a higher uncertainty and in a model-dependent way [Falanga et al. 2015], since the companion's light curve needs to be modelled.

The methods employed to measure NS radii possess higher uncertainties. There are proposed methods based on thermal X-ray and optical luminosities of isolated and quiescent NSs [Guillot et al. 2013, Potekhin 2014]; type-I X-ray bursts, i.e., the expansion of the thermal photosphere [Galloway and Lampe 2012, Poutanen et al. 2014]; the observation of quasi-periodic oscillations (QPOs) in accreting NSs [Schaab and Weigel 1999], or the detection of GWs from NS mergers [Bauswein et al. 2017]. Several past observations suggested that $R \gtrsim 10$

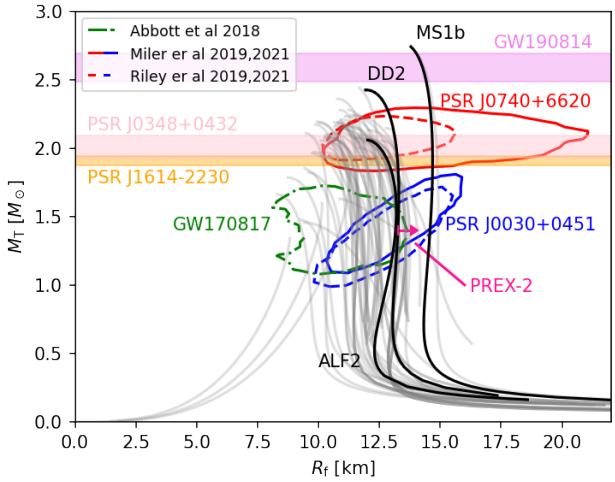

Figure 1.2 Gravitational mass and circumferential radius for different EOSs including the observational constraints (95% confidence levels) from GW observations (LIGO-Virgo), EM detections (NICER or XMM-Newton), and mass measurements of two high-mass pulsars (radii not measured). The PREX-2 1σ lower limit on the radius for a 1.4 $M_\odot$ NS is also included. Figure reprinted with permission from Di Giovanni et al. 2022. Copyright (2022) by the American Physical Society.

km, but the accuracy was much worse than for the mass measurements. Luckily, the Neutron star Interior Composition Explorer (NICER) mission [Gendreau et al. 2012, Gendreau et al. 2016], installed on the International Space Station and launched on 2017, has already measured the massess and radii of two pulsars, PSR J0030+0451 [Miller et al. 2019, Riley et al. 2019] and PSR J0740+6620 [Miller et al. 2021, Riley et al. 2021], with a determination of their radii with $\sim 10\%$ uncertainty ($13.02^{+1.24}_{-1.06}$ km [Miller et al. 2019] and $13.7^{+2.6}_{-1.5}$ km [Miller et al. 2021], respectively, and $12.71^{+1.14}_{-1.19}$ km [Riley et al. 2019] and $12.39^{+1.30}_{-0.98}$ km [Riley et al. 2021]). In addition, the recent observations of GWs emitted by a BNS merger have put additional constraints on the EOS by inferring values for the masses and radii of the component NSs. This will be covered with more detail in Section 1.4.

From different EOS candidates, one can build theoretical mass-radius relations that can be compared with real measurements of masses and radii of NSs. The EOSs with a maximum mass below the heaviest NSs found are excluded. In Figure 1.2 some mass-radius relations are depicted for several EOS candidates. Real measurements from pulsar observations or GW signals put constraints in the validity of the EOSs, as shown by the highlighted regions in the figure. Some models can also be excluded by causality (speed of sound > speed of light), finite

pressure and GR. The theoretical existence curves in Figure 1.2 are obtained by solving the TOV equation and hence assume spherical symmetry.

1.1.4 **Rotating neutron stars**

NSs have a wide range of rotational periods, ranging from milliseconds to several seconds (see, e.g., Paschalidis 2017 for a review). Rotation is driven by angular momentum conservation during the collapse of their progenitors' core (or during a BNS merger that results in a stable NS remnant). Initially differentially and fast-rotating NSs can spin down over time due to various mechanisms, such as viscosity, magnetic-field braking [Spitzer 1978], gravitational radiation (driven by the mass quadrupole term; Papaloizou and Pringle 1978) and by emission of particles like neutrinos [Mikaelian 1977].

Newly born NSs and merger remnants possess a relatively high degree of differential rotation, i.e., different parts of the star rotate at different rates. In the case of PNSs, the star inherits the angular momentum of the progenitor star, and due to the drastic reduction in size, it spins substantially fast. Also, differential rotation rises due to the collapse of the core. In the case of BNS merger remnants, they rotate very rapidly due to the conservation of angular momentum from the merging stars. As we will see in Section 1.2, the outer layers of the stars are disrupted during merger and form an accretion disc around the core of the merger remnant. This may depend on the binary mass ratio. For a high enough value, no tidal disruption is expected. Differential rotation can drive various instabilities and oscillation modes, e.g., r-modes, emitting gravitational radiation, and amplify the magnetic field due to a dynamo process. Furthermore, it can increase the maximum mass of the star due to the strong centrifugal forces that balance gravity. The value of the new threshold mass is dictated by the EOS. Efforts have been made to build NS models with realistic rotational profiles and EOSs, so that tighter constraints can be placed on the maximum mass of rotating NSs (e.g., Stergioulas and Friedman 1995, Nozawa et al. 1998, Hanauske et al. 2017, Iosif and Stergioulas 2022, Cassing and Rezzolla 2024).

Isolated NSs that have cooled down, i.e., pulsars, have a remarkably stable rotational period. This constant period is very helpful to measure the mass of the NS, as discussed in Section 1.1.3, and to detect very low-frequency GWs ($10^{-9} - 10^{-6}$ Hz). By exploiting the temporal stability of numerous galactic pulsars across the sky by continuously monitoring the radio signals, variations in the arrival time of pulses due to gravitational radiation can be detected. This detection technique is called *pulsar timing array (PTA)* [Hobbs et al. 2010]. GWs with these small frequencies can come from sources such as the GW

background from supermassive BH mergers or exotic phenomena in the early Universe. Indeed, a detection of this stochastic GW background has already been claimed [Agazie et al. 2023].

1.1.4.1 *Quasi-normal oscillation modes*

General linear perturbations of the energy density in a TOV NS can be written as a sum of quasi-normal modes, labelled by the indices (l, m) that come from the spherical harmonics. The angular dependence is given by Legendre polynomials, and their time dependence is oscillatory, with a certain frequency. Oscillations (or pulsations) can be excited after a core collapse or during the BNS early postmerger phase [Imamura, Friedman, and Durisen 1985, Managan 1985, Ipser and Lindblom 1990, Moenchmeyer et al. 1991, Zwerger and Mueller 1997], among other scenarios. They can be a source of gravitational and high-energy radiation in isolated NSs, and can give further information on the EOS [Font et al. 2001, Dimmelmeier, Stergioulas, and Font 2006, Gaertig and Kokkotas 2011, Krüger et al. 2021]. The main pulsation modes in relativistic NSs have been classified in three different classes: the *polar modes*, which are analogous to the pulsations of a Newtonian fluid and are slowly damped (f-modes, p-modes, g-modes); the *axial and hybrid* modes, which are associated to the rotation of the star, are degenerate with zero frequency in nonrotating stars (*inertial* modes, r-modes), and the *spacetime modes*, analogous to the quasi-normal modes of a BH (w-modes). Rotation impacts the modes of a nonrotating NS [Stergioulas and Friedman 1998, Font et al. 2002]. The degeneracy in the index m is broken and nonaxisymmetric modes arise. Also, prograde modes (with $m < 0$) are different from the retrograde modes ($m > 0$). In general, the frequencies of prograde modes increase, while those from retrograde modes decrease when the rotation rate increases.

For further details about the different types of oscillation modes see, e.g., McDermott, van Horn, and Hansen 1988, Andersson and Kokkotas 1998, Kokkotas and Schmidt 1999.

1.1.4.2 *Nonaxisymmetric instabilities*

At birth or during accretion, NSs that rotate rapidly can be subject to several nonaxisymmetric instabilities that affect their spin rate and dynamical evolution. A star with a high enough rotation rate (for ratios of the rotational kinetic energy T to the gravitational potential energy W, $\beta \equiv T/|W| \geq 0.27$) will undergo a dynamical instability known as the bar-mode instability [Houser,

Centrella, and Smith 1994, Shibata, Baumgarte, and Shapiro 2000, Shibata and Sekiguchi 2005, Baiotti et al. 2007]. This instability will deform the star into a nonaxisymmetric (bar) shape due to centrifugal forces. Differentially rotating ellipsoids can also develop spiral arms when β is much larger than the threshold value. Such configuration will lead to a strong GW emission in the range of kHz and also to mass ejection. It has also been observed that relativistic effects decrease the critical value of β for dynamical bar formation, in post-Newtonian simulations [Saijo et al. 2001] and in full GR [Manca et al. 2007, Löffler et al. 2015]. The bar-mode instability can also develop for low values of the β parameter, i.e., slower rotation rates. If the star possess a high degree of differential rotation, it can be dynamically unstable against the bar-mode deformation [Centrella et al. 2001, Ott et al. 2005]. To study this instability, both hydrodynamic (e.g., Cerdá-Durán, Quilis, and Font 2007, Corvino et al. 2010, De Pietri et al. 2014, Shibagaki et al. 2020) and magnetohydrodynamic (MHD) (e.g., Camarda et al. 2009, Fu and Lai 2011) simulations have been performed. Figure 1.3 displays snapshots at different times of the rest-mass density of a differentially rotationg NS prone to the bar-mode instability. The different row represent models with different vertical magnetic field strengths (from top to bottom, $B_z = \{10^{14}, 4 \times 10^{15}, 10^{16}\}$ G). The instability develops for low enough initial magnetic fields (top row), but it can be suppressed for higher values (lower panels). In the next Subsection, the role of magnetic fields in NSs is discussed in more detail.

Highly differentially rotating NSs can also become unstable to the dynamical one-arm (spiral) instability. It was discovered in Newtonian hydrodynamic simulations by Centrella et al. 2001. The one-arm instability consists in the displacement of the maximum density of the NS from its core. This phenomenon results in the stellar core orbiting around the centre of mass with an almost constant frequency. This deformation leads to a time variation of the quadrupole moment that results in the emission of GWs. It is still unclear how this instability arises, despite numerous studies. Simulations by Saijo and Yoshida 2006, Ou and Tohline 2006 and Corvino et al. 2010 argue that the one-arm instability is excited near the corotation radius, i.e., the radius at which the local angular velocity of the fluid and the angular frequency of the unstable mode match. This is also the case for the bar-mode instability [Cerdá-Durán, Font, and Dimmelmeier 2007, Passamonti and Andersson 2015]. Both the bar-mode and the one-arm instabilities arise in dynamical scenarios where highly differentially rotating NSs form. Simulations have shown the emergence of the one-arm (spiral) instability in CCSNe [Ott et al. 2005, Kuroda, Takiwaki, and Kotake 2014, Shibagaki et al.

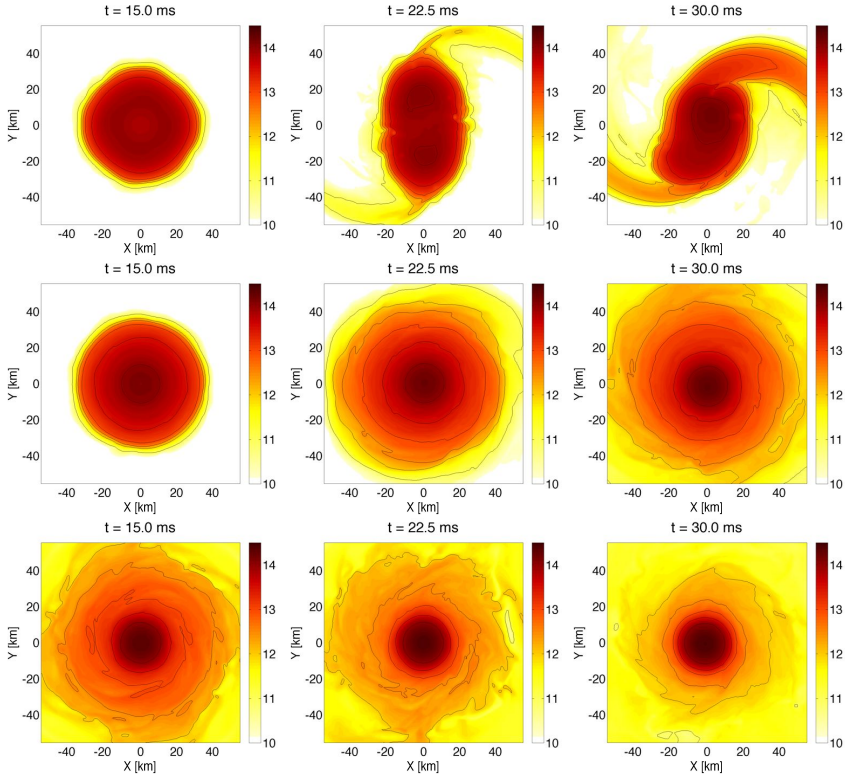

Figure 1.3 Snapshots of the rest mass density at different times, for three differentially rotating NS models with different initial vertical magnetic fields. From top to bottom, $B_z = \{10^{14}, 4 \times 10^{15}, 10^{16}\}$ G. For sufficiently low magnetic fields, the bar-mode instability can develop (top panels). However, if the initial magnetic field is strong enough, the instability can be supressed (middle and bottom panels). Figure reprinted with permission from Franci et al. 2013. Copyright (2013) by the American Physical Society.

2020, Takiwaki, Kotake, and Foglizzo 2021] and in the hypermassive NS formed after a BNS merger [Paschalidis et al. 2015, East et al. 2016, Radice, Bernuzzi, and Ott 2016, Xie et al. 2020].

At lower rotation rates, the star can undergo the so-called Chandrasekhar-Friedman-Schutz (CFS) instability [Chandrasekhar 1970, Friedman and Schutz 1978], which arises from the coupling between its rotation and its oscillation modes. An oscillating mode that is retrograde for a corotating observer has a negative angular momentum (compared to the unperturbed star), but if the mode is prograde for a distant observer, this will remove angular momentum from the star and the angular momentum will increase its negative value. This results in a loss of angular momentum via gravitational radiation, until the

oscillation mode becomes stable as the star spins down. Some inertial modes and the r-modes are generically unstable to the CFS instability.

In this context, it is worthy of mention the r-mode instability [Andersson 1998, Andersson, Kokkotas, and Stergioulas 1999, Andersson and Kokkotas 2001]. The r-modes possess frequencies of the same order of magnitude as the rotation frequency of the NS. They are caused by the Coriolis force generated by the rotation, and they involve the motion of fluid elements primarily in the axial direction. The r-modes are unstable due to the GW emission for all rotating NSs, regardless their rotation rate.

Another nonaxisymmetric instability that rotating stars can undergo is the viscosity-driven instability [James 1964], which breaks the circulation of the fluid. It is not as generic in rotating NSs as the CFS instability, since it strongly depends on the stiffness of the EOS [Skinner and Lindblom 1996, Bonazzola, Frieben, and Gourgoulhon 1998] and it is supressed by relativistic effects [Shapiro and Zane 1998, Gondek-Rosińska and Gourgoulhon 2002]. This instability is associated with the regions where viscosity is more significant, in the NS's outer layers, and is characterised by the shearing motion between fluid layers.

1.1.5 **Magnetic fields in neutron stars**

Magnetic fields play a crucial role in shaping the properties and behaviour of NSs. Even though NSs have some of the strongest magnetic fields in the Universe (with surface values ranging from 10^8 to 2×10^{13} G in pulsars), the magnetic field energy densities are too small in comparison with the total energy density of the fluid. This is the reason why the presence of magnetic fields is often ignored in numerical studies. Nevertheless, magnetic fields with moderate strengths might affect the stability of the star without altering its bulk properties. In addition, there exists a class of NSs that possess stronger magnetic fields (up to $\sim 10^{15}$ G), the so-called *magnetars* [Kouveliotou et al. 1998], which experience powerful phenomena due to their intense magnetic field [Bocquet et al. 1995]. Moreover, initially weak magnetic fields can undergo a significant amplification due to the appearance of dynamo processes triggered by fluid instabilities.

1.1.5.1 *Observational constraints*

The measurement of the NS period and its time variation allows estimating the magnitude of the magnetic field. As mentioned earlier in Subsection 1.1.1, NSs spin down during their evolution, and magnetic fields are responsible for that. The stellar period and its time evolution are strongly linked to the magnetic field

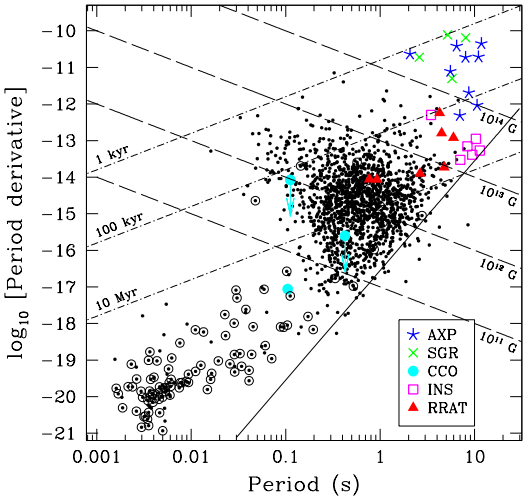

Figure 1.4 $P - \dot{P}$ diagram for 1704 objects. The black dots correspond to 1674 rotation-powered pulsars (RPPs), and the different colors represent other classes of NSs: 9 Anomalous X-ray Pulsars (AXP, blue crosses), 5 Soft Gamma Repeaters (SGRs, green crosses), 3 Central Compact Objects (CCOs, cyan circles), 6 Isolated NSs (INSs, magenta squares), and 7 Rotating Radio Transients (RRATs, red triangles). The open circles stand for binary systems. Lines of constant magnetic field, B, (dashed) and pulsar age, τ, (dash-dotted) are provided. The solid line in the figure is a "death line", below which RPPs' radio emission shuts off. Figure reproduced with permission from Kaspi 2010.

strength. Magnetic fields in NSs have been measured in both isolated and binary systems. In Lorimer 2008, 20 known isolated millisecond pulsars observed in the Galactic disc are displayed. They possess magnetic fields of about $B \sim 10^{10}$ G. Moreover, observations of eccentric ($e > 0.05$) binary pulsars not located in globular clusters indicate that the magnetic field at the stellar surface is in the range of $B \sim 10^{9.7} - 10^{12.6}$ G. Figure 1.4 shows a $P - \dot{P}$ diagram (period vs period time derivative) of observed NSs, including lines of constant magnetic field and pulsar ages. The higher the magnetic field strength, the higher the period time derivative (actually, $B \propto (P\dot{P})^{1/2}$).

However, the magnetic field also decays through ambipolar diffusion and Ohmic dissipation. In addition, the Hall effect, i.e., the decoupling of electrons from protons, rearranges the magnetic field in the star. As the magnetic field decays, the spin down is reduced, until eventually the field is too weak to change the spin period anymore. Viganò et al. 2013 found that an initial magnetic field of 3×10^{12} G can be reduced by a factor ~ 2 in a timescale of 5×10^5 yr. This means that, close to the merger time of a BNS system ($t \sim 10^7 - 10^9$ yr, Lorimer

2008), the magnetic field might be $\sim 3-4$ orders of magnitude lower than its initial value.

1.1.5.2 *Magnetic field structure and magnetosphere*

Generally, magnetised NSs possess magnetic fields with poloidal and toroidal components. In the former, magnetic field lines emerge from one magnetic pole of the NS and converge at the opposite pole of the star, resulting in a somewhat dipolar configuration. Stars with stationary purely poloidal magnetic fields must be uniformly rotating, and the current is purely toroidal [Carter 1973]. On the other hand, poloidal currents can generate purely toroidal magnetic fields in ideal MHD [Oron 2002, Frieben and Rezzolla 2012], and the toroidal field can also emerge if the field is not axisymmetric. However, a mixed magnetic field configuration seems to be more stable [Braithwaite and Spruit 2006]. If the star is differentially rotating, a toroidal component will arise from the wound-up poloidal field. The interplay between differential rotation and magnetic fields can have important consequences for the stability of the NS: magnetic braking of the differential rotation, dynamo effects that amplify the magnetic field and the development of the magnetorotational instability (MRI), which plays a crucial role in the evolution of PNSs and BNS postmerger remnants.

The NS magnetic field interacts with charged particles in the stellar magnetosphere, with important implications in high-energy phenomena, shaping the EM emission of the star. To treat the magnetic field outside the star, i.e., decoupled from the fluid, ideal MHD is no longer valid, since it assumes that the bulk fluid and embedded magnetic field are constrained to move together. One would need to employ Maxwell's equations for force-free electrodynamics (FFE) (or even vacuum) exteriors together with ideal MHD for the star's interior. The development of resistive schemes in general-relativistic magnetohydrodynamics (GRMHD) simulations of NSs is an ongoing field of research. There are several works in special relativity of aligned and oblique rotators (rotating magnetic dipoles) to study stationary pulsar magnetospheres using FFE [e.g., Contopoulos, Kazanas, and Fendt 1999, Spitkovsky 2006, Kalapotharakos, Contopoulos, and Kazanas 2012, Kalapotharakos et al. 2012, Contopoulos, Kalapotharakos, and Kazanas 2014, Mahlmann and Aloy 2022], without including the NS interior. These simulations have brought important results, e.g., the proof of the stationary configuration of the magnetosphere or the computation of the spin-down–Poynting–luminosity.

There have also been several efforts to go beyond ideal MHD in the context of special-relativistic [e.g., Palenzuela et al. 2009, Wright and Hawke 2020] and dynamical GR spacetimes [e.g., Andersson 2012, Andersson et al. 2022,

Palenzuela 2013, Dionysopoulou et al. 2013, Paschalidis and Shapiro 2013, Pétri 2016, Carrasco, Palenzuela, and Reula 2018]. In the context of the EM emission of (non)rotating collapsing NSs, it has been found that the Poynting luminosity of nonrotating and rotating models scales with the square of the initial magnetic field strength at the pole, with an increase of $\approx 20\%$ of the rotating cases with respect to the nonrotating models [Lehner et al. 2012]. For the case of rotating pulsars, Palenzuela 2013 showed (using the FFE solution for an aligned dipole field) that the spin-down luminosity differs by 20% from the flat spacetime case, due to GR and other effects. Later, Ruiz, Paschalidis, and Shapiro 2014 presented a more systematic study, providing relations that link the spin-down luminosity with the star rotation and compactness, using the technique from Paschalidis and Shapiro 2013 to match the ideal MHD interior with the force-free limit.

In addition to the global magnetic field structure, NSs also have magnetic fields anchored in their solid crust (crustal magnetic fields) [Gil, Melikidze, and Geppert 2003, Pons and Geppert 2007, Gourgouliatos, De Grandis, and Igoshev 2022]. They influence the nonuniform surface temperature [Pons et al. 2002, Geppert, Küker, and Page 2004] and can explain the fact that old pulsars show no significant magnetic field decay over their lifetime [Hartman et al. 1997, Regimbau and de Freitas Pacheco 2001]. Moreover, depending on their relative strength, a rapid decay of the crustal dipolar field could have observable influence on the pulsar's spin down.

1.1.5.3 *Magnetic field amplification*

Although magnetic fields in isolated NSs are usually not strong enough to have a significant impact in the stellar dynamics, they can be amplified due to hydrodynamic turbulence triggered by fluid instabilities. The interplay between the fluid velocity and the magnetic field lines leads to dynamo mechanisms that can arise from different processes and transport angular momentum from the NS interior to the exterior layers (see, e.g., Brandenburg and Subramanian 2005 for a review). There exist several mechanisms that amplify magnetic fields in newly born PNSs and in BNS merger remnants: differential rotation, convection and other mechanisms related to turbulence.

The wind-up process of the magnetic field, also called the Ω-dynamo [Obergaulinger, Aloy, and Müller 2006, Obergaulinger et al. 2006, Cerdá-Durán, Font, and Dimmelmeier 2007], consists in the transformation of the poloidal magnetic field into a toroidal field while rotational kinetic energy is extracted from differential rotation. Several instabilities undergone by the toroidal field can

transform it back into a poloidal magnetic field, closing the dynamo mechanism. In PNSs, these instabilities are driven by either lepton gradients which result in the so-called *neutron-finger instability* [Bruenn and Dineva 1996], or by the *convective instability* driven by negative entropy gradients [Keil and Janka 1995, Keil, Janka, and Mueller 1996, Pons et al. 1999, Miralles, Pons, and Urpin 2000, Raynaud et al. 2020]. In these cases, the α-effect, i.e., the twisting of the magnetic field lines due to the effect of the star's rotation in convective regions, is the one that closes the dynamo [Thompson and Duncan 1993, Wheeler et al. 2000, Bonanno, Urpin, and Belvedere 2005, Masada, Takiwaki, and Kotake 2022, Reboul-Salze et al. 2022].

There exist other instabilities that can act in convectively stable regions. The Tayler instability [Tayler 1973] was proposed by Spruit 1999 and confirmed by numerical simulations [Braithwaite 2006a, Braithwaite 2006b, Barrère et al. 2022, Margalit et al. 2022] as a mechanism that closes the Ω-dynamo. It is a kink instability that destroys the toroidal field by transforming it into a poloidal field. Therefore, the Ω-dynamo needs to generate the toroidal field component faster than its destruction due to the Tayler instability. Saturation will be reached when both timescales are similar. For typical magnetic field strengths in PNS progenitors, the Tayler instability is found to be inefficient in amplifying the magnetic field in short timescales, but it can become important on longer timescales where the $\alpha - \Omega$-dynamo acts. Figure 1.5 depicts and schematic representation of this dynamo process.

The MRI [Chandrasekhar 1960, Balbus and Hawley 1991, Balbus and Hawley 1992], which will be further discussed in more depth in Section 1.3, is another process that is able to amplify the magnetic field in differentially rotating PNSs and BNS merger remnants [Akiyama et al. 2003, Obergaulinger et al. 2009, Rembiasz et al. 2016a, Guilet et al. 2022, Reboul-Salze et al. 2022]. It is a shear instability that generates turbulence and amplifies arbitrary weak magnetic fields, which results in the redistribution of angular momentum inside the star. In the process, axisymmetric channel flows are formed [Goodman and Xu 1994] and the amplification saturates due to the channel destruction by nonaxisymmetric parasitic instabilities [Goodman and Xu 1994, Pessah and Goodman 2009, Rembiasz et al. 2016b]. The difficulties to numerically capture the fastest growing mode of the MRI because of the large resolution needed in 3-dimensional simulations makes this instability an issue that nowadays is still under study.

Magnetic fields also have an impact in the evolution of hydrodynamic instabilities. For example, Camarda et al. 2009 performed Newtonian MHD simulations

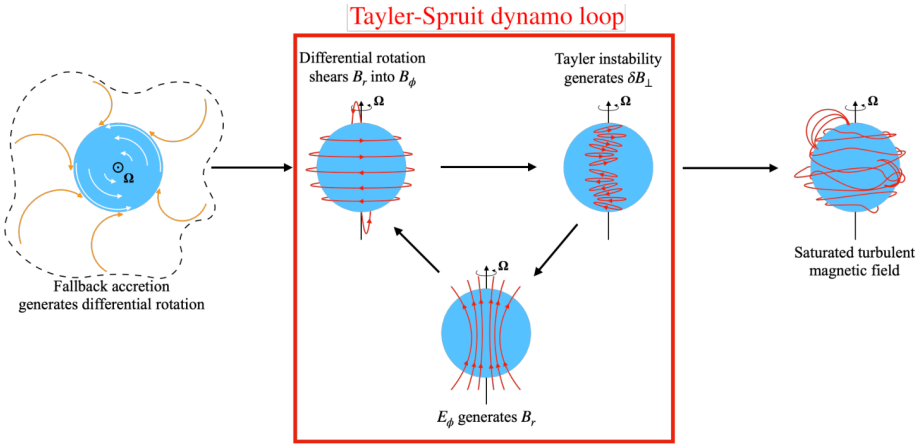

Figure 1.5 Pictorial representation of the Tayler-Spruit dynamo action. In the left panel, the fallback accretion (orange arrows) generates differential rotation, $\Omega(r)$ in the star. In the middle panel, the differential rotation generates a toroidal magnetic field, B_ϕ, from the radial component, B_r, by shearing. The Tayler instability generates an electromotive force E_ϕ (due to a nonaxisymmetric perpendicular magnetic field, $\delta B_\perp$) that in turn arises a radial magnetic field. The right panel shows the saturated turbulent magnetic field. Figure reproduced with permission from Barrère et al. 2022.

of differentially rotating NSs prone to the bar-mode instability, and found that magnetic fields seem to not have a very significant effect in realistic configurations. However, the most extreme cases were able to suppress growth of the bar mode. In addition, Franci et al. 2013 studied the effects of magnetic fields on the development of the dynamical bar-mode instability in GRMHD simulations. The authors found that if an initial purely poloidal field confined inside the NS is strong enough ($B \gtrsim 10^{16}$ G), it can suppress the instability completely, whereas weak fields have negligible impact on the instability (see Figure 1.3). Moreover, Muhlberger et al. 2014 showed that magnetic fields can suppress the development of the low-β type bar-mode instability.

1.2 Binary neutron star mergers: an overview

BNS mergers are very dynamical astrophysical events that can be observed through different astronomical signatures (EM, neutrino and gravitational radiation). In order to properly study and model what happens in a BNS merger, many physical aspects need to be taken into account: nuclear physics to build realistic EOSs and study the nucleosynthesis likely triggered after the merger; particle physics to include neutrinos, and GRMHD to capture the evolution of the fluid and the magnetic field in a curved spacetime. Mergers that involve

NSs can be of two different types: neutron star - black hole (NSBH) mergers, where one of the components is a BH, and BNS mergers, in which both compact objects are NSs. In the former case, the NS will (likely) be disrupted by the BH, leading to a BH as a merger remnant. Depending on the binary mass ratio (and also the NS compactness and the BH spin), the BH might be surrounded by an accretion disc subject to MHD instabilities and dynamical outflows could be triggered, or alternatively the NS will be totally absorbed by the BH, leaving no matter behind. In the following, I focus on the latter case, BNS mergers, which can show a wider variety of postmerger scenarios.

1.2.1 **Stages of a binary neutron star merger**

As stated in Section 1.1.1, NSs are born mostly from the core-collapse explosion of massive progenitor stars. When two of these stars are bound together in a binary system, they can end up in a compact object binary. In order to merge within one Hubble time, they need to be close enough. This requires a common-envelope stage [Bhattacharya and van den Heuvel 1991], in which one component collapses into a NS first and is enveloped by the second component during its supergiant phase, which collapses later to another NS[2]. This is thought to be the standard formation channel for BNS systems. However, they can also form dynamically, when the stars are formed separately but become gravitationally bound when they come close to each other. This happens in globular clusters where the stellar density is higher.

1.2.1.1 *Inspiral phase*

Once the binary system is formed, the two NSs orbit around each other. Both stars lose energy due to GW emission, leading to an orbital decay that makes them inspiral towards one another. During this phase, the NSs can be treated as cold ($T = 0$) and the evolution of the binary system can be well-described by post-Newtonian (PN) expansions [Blanchet 2006], where the stars are treated as point particles (see Section 1.4).

The major part of the lifetime of the system happens during this phase, lasting about $10^7 - 10^9$ yr for most Galactic systems analysed [Kalogera et al. 2001, Lorimer 2008], and only during the late inspiral (from hours to minutes before the merger) the binary becomes unstable. The stars become tidally deformed and the orbital trajectory is affected [Kochanek 1992]. The tidal

[2]One of the components (or both) can collapse to a BH and form binary black hole (BBH) or NSBH systems, but we are focusing on BNS mergers.

deformation of the NSs strongly depends on the EOS, and more precisely on its stiffness. This effect can be observed through the inspiral GW signal, which will be covered in Section 1.4, and serves to put constraints on the EOS of NS matter.

There have also been few studies about the EM emission during the inspiral phase, known as *precursor emission* [Fernández and Metzger 2016]. If one of the stars is magnetised, the orbital motion induces a current along the magnetic field lines that connect both stars. The resulting voltage powers EM emission that becomes more intense as the stars get closer to each other. This phenomenon is known as magnetospheric interaction [Hansen and Lyutikov 2001, Lai 2012, Palenzuela et al. 2013]. Furthermore, it is worth mentioning the driving of a crust-core interface mode (crustal fracture model or crust-shattering flares) that can lead to shattering of the NS crust [Tsang et al. 2012, Tsang 2013]. This resonant excitation could be a source of GRB precursor emission.

1.2.1.2 *Dynamical phase*

The system enters the *merger* or *dynamical phase* when the stars plunge together. To properly study the physics involved during this phase, full NR simulations are needed. The stars are supposed to be irrotational before merger, since gravitational emission circularises the orbits, and when they touch each other there exists a discontinuity in velocity at the interface between the stars. This velocity jump triggers the Kelvin – Helmholtz instability (KHI), which leads to the formation of vortices and turbulent motion that can result in a substantial amplification of the magnetic field, growing up to equipartition with the kinetic energy of the turbulent field, i.e., $B \sim 10^{16}$ G [Kiuchi et al. 2015, Ruiz et al. 2016, Ciolfi et al. 2019, Aguilera-Miret, Viganò, and Palenzuela 2022, Kiuchi et al. 2024]. Due to the tidal deformation (gravitational torques) of the NSs in the late inspiral, matter can be expelled (dynamical ejecta) in a timescale of ≤ 10 ms and form a disc around the merger remnant [Rezzolla et al. 2010, Rosswog 2013, Radice et al. 2016, Radice et al. 2018, Shibata and Hotokezaka 2019]. Typical mass fractions of the discs observed in simulations are of the order of $10^{-3} - 10^{-2}\ M_\odot$. The total mass and the mass ratio of the binary, and the stiffness of the EOS determine the total amount of ejected mass. Also, thermal energy is generated from shock heating [Metzger et al. 2010b, Bauswein, Goriely, and Janka 2013] at the interface between the stars.

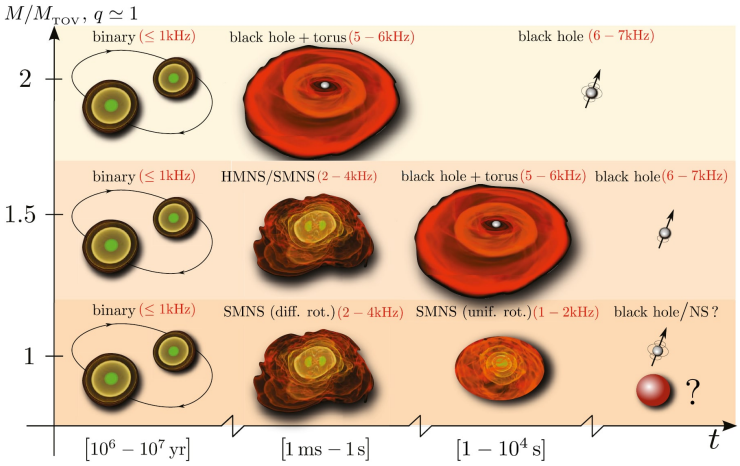

Figure 1.6 Schematic view that illustrates the different stages of an equal-mass BNS merger for different initial total masses of the system M in terms of the maximum mass of a TOV (nonrotating) star, $M_{\rm TOV}$. The top row shows a rapid collapse to a BH surrounded by an accretion disc (very massive binary); the middle row shows a delayed collapsed of the postmerger remnant star, and the bottom row depicts the formation of a supermassive NS that eventually yields a nonrotating neutron star or collapses to a BH. The characteristic frequencies of the emitted GWs are highlighted in red. Figure reprinted with permission from Baiotti and Rezzolla 2017. Copyright (2017) by IOP Publishing Ltd.

1.2.1.3 *Postmerger phase*

After merger, the system settles down into a new configuration. The outcome of the merger strongly depends on the total mass of the system (see, e.g., Piro, Giacomazzo, and Perna 2017, Bernuzzi 2020 and Sarin and Lasky 2021 for reviews). Figure 1.6 is a schematic view of possible BNS merger outcomes as a function of the total mass of the system. For very massive progenitors (the threshold mass will depend on the EOS), the remnant will be gravitationally unstable and suffer a *prompt collapse* to form a spinning BH surrounded by an accretion disc within few milliseconds after the merger. The mass of the accretion disc depends on the EOS, but, as previously stated, it does not exceed 10^{-2} $M_\odot$ [Hotokezaka et al. 2013, Ruiz and Shapiro 2017, Shibata and Hotokezaka 2019].

Postmerger remnants with masses $M_{\rm rem} \leq 1.2 M_{\rm TOV}$ will survive for more than a second [Falcke and Rezzolla 2014, Ravi and Lasky 2014]. These stars are known as *supramassive* when their mass is above the TOV threshold, but still below the maximum mass for uniformly rotating NSs, which is very insensitive to the EOS [e.g., Komatsu, Eriguchi, and Hachisu 1989]. The *supramassive* remnant will be stable against gravity until there is a loss of angular momentum

that spins down the star, due to X-ray emission or magnetic braking [Faber and Rasio 2012], with a lifetime between seconds and hours. Alternatively, remnant massive neutron stars (RMNSs) with masses below $M_{\rm TOV}$ are stable.

If the total mass of the binary is somewhat larger ($M_{\rm rem} \geq 1.2 M_{\rm TOV}$), the system may go through a short-lived phase in which a transient postmerger object forms, a so-called hypermassive neutron star (HMNS), supported against gravitational collapse by rapid differential rotation and thermal pressure[3]. These remnants have larger masses compared to stationary nonrotating NSs (TOV solutions with mass $M_{\rm TOV}$), and their maximum mass depends on the EOS [Baumgarte, Shapiro, and Shibata 2000, Shibata et al. 2006, Bauswein, Baumgarte, and Janka 2013, Piro, Giacomazzo, and Perna 2017, Weih, Most, and Rezzolla 2018, Espino and Paschalidis 2019]. The HMNS survives several tens (or even hundreds) of milliseconds, even though this is not completely understood, undergoing several oscillations and (magneto)hydrodynamical instabilities, and eject mass that forms a disc around the star. Both the rotational profile and the disc mass depend on the EOS [Kastaun and Galeazzi 2015] and the mass ratio of the binary system [Bernuzzi 2020] (see next Subsection). These RMNSs, apart from differentially rotating, are characterised by strong magnetic fields (up to $B \sim 10^{16}$ G), which have undergone a turbulent amplification during (KHI) and after the merger (MRI) [e.g., Anderson et al. 2008, Liu et al. 2008, Kiuchi et al. 2014, Kiuchi et al. 2015, Palenzuela et al. 2015, Kawamura et al. 2016]. Once support against gravity by rapid rotation and neutrino pressure lessens, the remnant eventually collapses to a BH. Damping of differential rotation comes from magnetic and viscous dissipation, i.e., angular momentum transport, that may arise from instabilities such as the MRI.

The lifetime of the remnant is still poorly understood, since it strongly depends on an adequate treatment of all the physics involved. The turbulent magnetic field amplification produced during and (few tens of ms) after the merger plays an important role on the stability of the remnant, but it requires very high resolutions to be captured (see Section 1.3). Moreover, faithful neutrino transport schemes are needed to study the influence of thermal pressure on the stability of the RMNS several tens of ms after merger (the neutrino-cooling timescale) [Kaplan et al. 2014]. The lifetime of the remnant also depends on the remnant mass, but in every case there will be a period of strong differential rotation just after the merger. The remnant's lifetime, together with its dynamics and evolution, have important implications in the EM and kilonova emission

[3]Temperatures in BNS mergers can go up to 80 MeV and the inclusion of thermal effects in the EOS is needed.

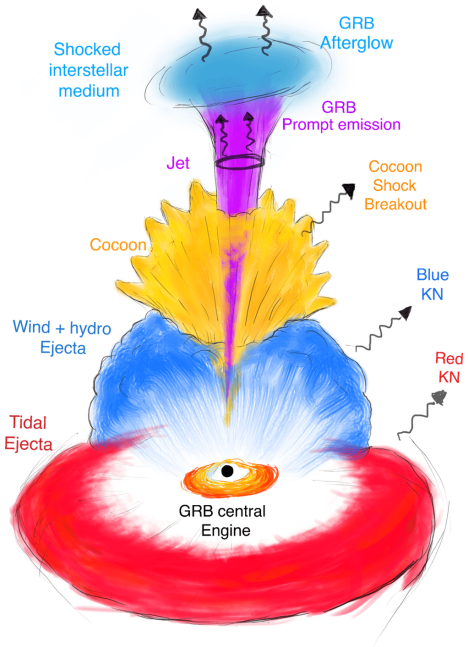

Figure 1.7 Artistic representation of the BNS/NSBH postmerger scenario, after the formation of an accretion disc around the remnant. The red component denotes the tidal dynamical ejecta, the blue component the ejecta from the disc, the purple component refers to the jet and the yellow component corresponds to the heated matter from the jet, i.e., cocoon. The components of the figure are not scaled proportionally for artistic purposes. Figure reproduced with permission from Ascenzi et al. 2021.

that trigger the r-process nucleosynthesis [Fernández and Metzger 2016, Metzger 2019].

1.2.2 **Mass ejecta and electromagnetic emission**

During and after a BNS merger mass can be lost through many different channels and on different timescales. The material ejected during the merger phase is collectively called *dynamical ejecta*. As mentioned before, the dynamical ejecta in BNS mergers has two components: shock-heated material from the interface between the stars and mass ejected in tidal tails (e.g., Bauswein, Goriely, and Janka 2013, Radice et al. 2018, Shibata and Hotokezaka 2019). For NSBH mergers, however, only the latter can occur [Shibata and Taniguchi 2011, Foucart et al. 2017] when the NS is tidally disrupted and not swallowed by the BH [Foucart, Hinderer, and Nissanke 2018]. The quantity of mass ejected by dynamical outflows ranges from 10^{-4} $M_\odot$ to 10^{-2} $M_\odot$, depending on the stiffness of the EOS and the binary total mass and mass ratio. For stiff EOSs,

the velocity of the NSs at merger is relatively small because the minimum orbital separation is large (they have larger radii). This results in a small dynamical ejecta mass. For a large total mass of the system, the shock heating efficiency and kinetic energy of the remnant star can be high, leading to a large dynamical ejecta. Moreover, for smaller mass ratios ($q \equiv m_2/m_1$, being m_1 the larger mass) the dynamically ejected mass is observed to be larger (for $q \lesssim 0.8$) the dynamical ejecta mass can be $M_{\rm ej} \gtrsim 0.005\ M_\odot$. The eccentricity of the orbit also impacts the mass of the ejecta, being larger for eccentric mergers [East and Pretorius 2012].

The composition and velocity of the dynamical ejecta is key for the predictions of the EM emission after merger, and for nucleosynthesis calculations as well. The composition, i.e., the electron fraction Y_e of the ejecta, strongly depends on the neutrino treatment, but it can present values as low as $Y_e \sim 0.1$ [Bernuzzi 2020]. As a word of caution, an accurate neutrino transport scheme is still not available, and a strong effort is being made in this direction, being the Monte Carlo [Foucart et al. 2020] and the gray two-moment (M1) [Thorne 1981, Shibata et al. 2011, Wanajo et al. 2014] schemes the state-of-the art approaches. On the other hand, the ejecta velocity is very sensitive to the stiffness of the EOS [Radice et al. 2018] and numerical treatment of magnetic fields. In addition, the characteristic velocities of dynamical ejecta have values of $\sim 0.1 - 0.3c$ [Hotokezaka et al. 2013, Sekiguchi et al. 2016, Radice et al. 2018], and the asymptotic velocities can reach values of $\sim 0.8c$.

Part of the mass ejected during and after merger can orbit around the remnant, forming an accretion disc (see Setiawan, Ruffert, and Janka 2006, Fujibayashi et al. 2020, Fernández, Foucart, and Lippuner 2020, among others). As for the RMNS before the collapse, gravity is balanced by centrifugal acceleration and thermal pressure, which determines the geometrical thickness of the disc. Mass from the disc can be ejected as wind (disc outflow) by several mechanisms that act on different timescales: the Lorentz force [Blandford and Znajek 1977], which acts on a timescale of few ms and needs a poloidal magnetic field; neutrino absorption [Ruffert, Janka, and Schaefer 1996, Just et al. 2022], acting during several tens of ms[4] [Metzger and Fernández 2014], and *thermal* ejection, due to viscous (turbulent) heating and nuclear recombination, active on longer timescales ($t \sim 100$ ms) [Metzger, Piro, and Quataert 2009]. The latter mechanism becomes dominant as neutrino cooling shuts down. It has been observed that $10 - 40\%$ of the initial mass of the disc can be ejected [Fernández and Metzger 2013, Just

[4]This mechanism is important for HMNS, but sub-dominant for a BH, since the neutrino fraction is smaller in that case.

et al. 2015, Fujibayashi et al. 2020] on a timescale of a few seconds. This mass ejecta coming from the remnant's disc is known as *secular ejecta*. The electron fraction of the material is around $Y_e \sim 0.2 - 0.4$, being higher in discs around NS remnants rather than BHs, but generally less neutron rich than the dynamical ejecta. The velocity of the disc ejecta is significantly slower than the dynamical ejecta, with speeds up to $\lesssim 0.2c$ [Bernuzzi 2020]. Figure 1.7 displays an artistic representation of the mass ejection and the associated EM emission during the BNS/NSBH postmerger phase.

Flashes of gamma rays of cosmological origin, with energies of the order of $10^{50} - 10^{53}$ erg, have been observed since the late 1960s. These so-called GRBs (see Piran 2004 for a review) are classified into *long* and *short* [Kouveliotou et al. 1993]. The former last several tens of seconds and might be caused by the collapse of very massive stars [Narayan, Paczynski, and Piran 1992, Hjorth et al. 2003, Woosley and Bloom 2006]. The latter ones only last less than a second. BNS mergers are the candidate scenario for these sGRBs [Rezzolla et al. 2011, Murguia-Berthier et al. 2017], but what is the formation mechanism of a GRB jet? Numerical simulations have revealed that magnetic fields in HMNS remnants have a complex topology, since dipolar fields are destroyed at merger, tangling the magnetic field [Kiuchi et al. 2014]. In GRMHD simulations of BNS mergers where the remnant collapses to a BH, magnetically-powered jets can be obtained (see, e.g., Kiuchi et al. 2014, Ruiz et al. 2016, Combi and Siegel 2023, and Dionysopoulou, Alic, and Rezzolla 2015 for an application of resistive-MHD). These jets can break out the slower mass ejecta, depending on their power, the opening angle and the quantity of ejected mass [Kawamura et al. 2016]. Figure 1.8 depicts several snapshots of a BNS merger simulation where a jet is launched. Magnetic field lines are rearranged after merger, while an accretion disc is formed around the remnant BH. Current studies are exploring the possibility that long-lived NS remnants, in addition to accreting BHs, could power ultrarelativistic GRB jets (since generally they do not fulfil the conditions for the Blandford-Znajek mechanism) [Ciolfi 2020a, Bamber et al. 2024].

1.2.3 **Kilonovae: r-process nucleosynthesis**

The production of heavy elements in astrophysical processes has been an active field of research since the 1950s when Burbidge et al. 1957 first formulated the theory of cosmic nucleosynthesis. There exist several scenarios where this phenomenon occurs: Big Bang nucleosynthesis, low-mass stars (s-processes), high-mass stars (formation of α elements) and explosive nucleosynthesis, forming elements beyond the iron peak via r-processes. I will focus here on the latter.

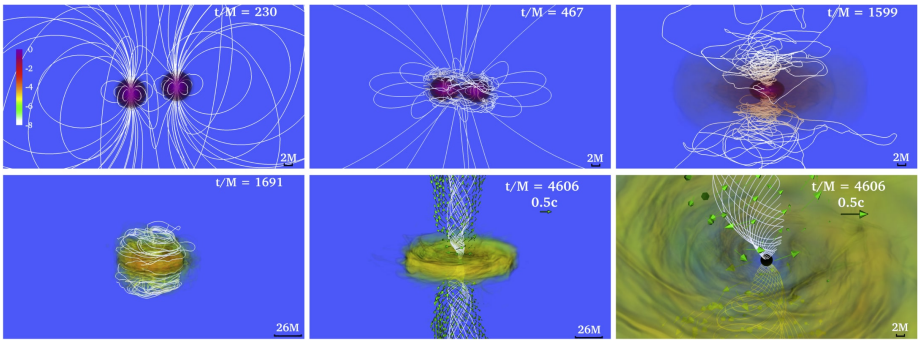

Figure 1.8 Snapshots of the formation of a jet after a BNS merger. The rest-mass density is normalised to its initial value and the magnetic field lines are represented by white lines. In the last two bottom panels, an incipient jet is launched, and the arrows indicate plasma velocities. Figure reproduced from Ruiz et al. 2016 by permission of the AAS.

New elements can be produced by exposing nuclei to intense neutron fluxes. This results in a competition between neutron capture (n-capture), the inverse process, and β-decay, where a neutron transforms into a proton by the emission of an electron accompanied by an antineutrino. The final composition depends on the timescale of the n-capture and the β-decay time. A high flux of neutrons generates heavier nuclei, becoming more unstable, until a nucleus for which decay is faster than n-capture is reached. This process can involve nuclei located far away from the valley of stability, but β-decay is responsible for leading back to stable nuclei with higher mass number A.

Heavy elements with mass numbers above the iron's ($A \gtrsim 56$) cannot be produced in stellar interiors, but they can be synthesised during a supernova (SN) explosion. Neutrino-driven winds in CCSNe favour the formation of heavy elements during the late explosion, when the postshock wave is propagating outwards. However, SN simulations have shown that the electron fraction is around $0.4 - 0.5$, too large to allow for rapid neutron captures, i.e., r-processes, that lead to very heavy elements ($A \gtrsim 120$). In contrast, BNS mergers lead to mass ejecta with smaller electron fractions, making them perfect candidate sites for r-processes [Freiburghaus, Rosswog, and Thielemann 1999].

In order to compute nucleosynthesis from the ejecta in simulations, it is typical to use passive tracer particles that sample the ejecta in mass [Wu et al. 2016]. The thermodynamic trajectory in time generated by each particle can be used as input to a nuclear reaction network. The ejecta components of BNS mergers will have different contributions to nucleosynthesis. Tidal dynamical ejecta (present in NSBH and BNS mergers) preserves a very low electron fraction

($Y_e \sim 0.05$ from cold NS matter) and expands quickly, making it ideal for the production of heavy elements [Roberts et al. 2017]. The shocked dynamical ejecta, only present in BNS mergers, suffers from some reprocessing by neutrinos, reducing the quantity of neutrons [Zappa et al. 2023]. On the other hand, the secular outflow from the disc also undergoes significant neutrino reprocessing, leading to a broad distribution of Y_e in the disc [Curtis et al. 2023]. The computed abundances of very heavy elements in numerical simulations present a good agreement with solar abundances and seem to be robust for different EOSs and mass ratios [Radice et al. 2018].

The material dominated by heavy elements undergoes radioactive decay emitting EM radiation in the optical and infrared bands. This emission is known as *kilonova*[5] [Li and Paczynski 1998, Metzger et al. 2010a]. The Lanthanides produced in the dynamical ejecta (which is very neutron rich) decay emitting near-infrared radiation that lasts for ~ 1 week, due to the higher opacity than iron-group elements (e.g., Kasen, Badnell, and Barnes 2013, Fontes et al. 2015, Tanaka et al. 2020). However, there is also a contribution from the disc outflow that is more isotropic. The leading portion of the ejecta encounters a low optical depth, resulting in a thermal transient that peaks in a timescale of ∼hours. The lifetime of the RMNS plays an important role here. If the HMNS is long-lived, the emitted neutrinos can increase the electron fraction so that no Lanthanides are produced, the optical depth is low and results in a radiation that peaks at optical wavelengths. On the other hand, if there is a rapid collapse to a BH, the electron fraction will remain low and the disc outflows will be neutron rich, leading to a similar emission to that from the dynamical ejecta [Metzger and Fernández 2014]. Therefore, the kilonova has an *early* blue (optical) and a *red* (infrared) component depending on the mass ejection mechanism and the neutrino absorption. There may exist a late-time radio transient, generated by the interaction between subrelativistic ejecta and the interstellar medium. This accelerates particles, leading to synchrotron emission [Nakar and Piran 2011, Hotokezaka et al. 2016]. The timescale of this transient has been predicted to be between years and decades [Balasubramanian et al. 2022].

The multimessenger event GW170817[6] [Abbott et al. 2017d], which was observed and well localised by both Advanced Laser Interferometer Gravitational-Wave Observatory (LIGO) and Advanced Virgo interferometers, allowed to follow-up EM observations from γ-rays to radio waves [Abbott et al. 2017e]. An

[5] Metzger et al. 2010a used this nomenclature for the first time, since the EM transient peaked at a luminosity 10^3 higher than a typical nova.

[6] The detection of SN1987A [Hirata et al. 1987] on Feb 23 1987 is considered to be the first multimessenger event, as it was observed in EM and neutrinos.

unusually weak GRB coming from the binary merger localization (GRB 170817A) was detected by Fermi [Goldstein et al. 2017] and INTEGRAL [Savchenko et al. 2017] satellites. Moreover, a near-infrared counterpart (AT2017gfo) was discovered and monitored [Cowperthwaite et al. 2017, Tanvir et al. 2017]. This observation provides strong support to the connection between sGRBs, r-process nucleosynthesis and BNS mergers.

1.3 Turbulence in binary neutron star mergers

As previously discussed, the redistribution of angular momentum in the HMNS remnant has important effects on the stability of the object and therefore on the subsequent multimessenger emission and the r-process nucleosyntesis. The suppression of differential rotation in the star is operated by turbulence. It can be driven by the Kelvin – Helmholtz (KH) instability during the late inspiral and merger phases or by the MRI in the postmerger phase. Before describing these MHD instabilities, it is important to understand what *turbulence* means (for reviews, see, e.g., Brandenburg and Subramanian 2005, Radice and Hawke 2024).

In very dynamical scenarios such as BNS mergers there can exist transfer of energy and momentum across a wide range of length scales (known as inertial range). When this happens, the ordered large-scale structures from the fluid can become disrupted and form disordered small-scale structures. The kinetic energy and momentum will be transferred to smaller scales, where kinetic energy is converted into internal energy, until the dissipation scale is reached. This is the scale at which the energy transfer rate is balanced by the viscous energy dissipation rate. The so-called inertial forces are developed in this direct cascade to smaller scales. The degree of turbulence in a physical system is quantified by the (dimensionless) Reynolds number (Re), which measures the ratio between the largest scale of the inertial range and the dissipation scale where the turbulent cascade ends. It has been shown experimentally that flows with $\mathrm{Re} \gtrsim 1000$ become turbulent [Frisch 1995]. Typical values of Re in a BNS merger are $\mathrm{Re} \sim 10^{15} - 10^{16}$ [Radice and Hawke 2024]. Moreover, magnetic stresses can have an influence in the development of turbulence. Magnetic tension can drive anisotropic turbulence and there can exist an inverse cascade due to dynamo action that creates large-scale magnetic fields. In addition to the redistribution of angular momentum in the BNS merger remnant, turbulence may rapidly and strongly amplify the magnetic field during and after the merger. A very strong

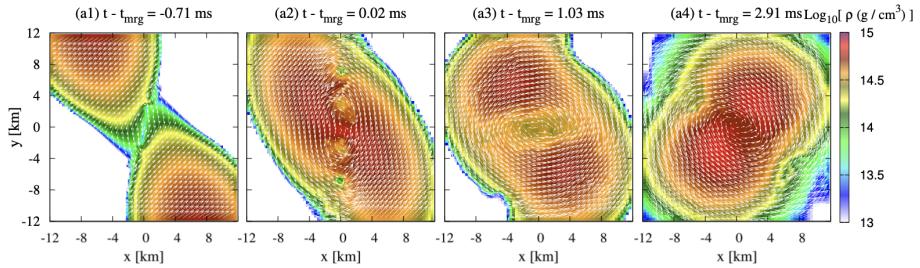

Figure 1.9 Snapshots of the merger of two NSs, represented by the rest-mass density, giving rise to the KHI. The white arrows represent the velocity fields. The velocity shear produces vortices that can lead to the amplification of the small-scale magnetic field. Figure reprinted with permission from Kiuchi et al. 2015. Copyright (2015) by the American Physical Society.

magnetic field might be able to power jets and drive (ultra)relativistic outflows that could explain EM observations.

1.3.1 **Kelvin – Helmholtz instability**

In the interface between the two NSs the jump in velocity can produce large-scale shears in the fluid that drive the KH instability [Chandrasekhar 1961, Miura and Sato 1978, Miura and Pritchett 1982]. These velocity shears produce large-scale vortices which in turn develop into smaller structures that can amplify the small-scale magnetic field several orders of magnitude. Figure 1.9 depicts snapshots of the rest-mass density from a GRMHD simulation from Kiuchi et al. 2015, at the moment at which two NSs merge. The velocity jump in the interface between both stars leads to the formation of vortices, which are represented by white arrows.

The typical wavelength of the unstable modes is the width of the shear layer. This marks the initial value of the inertial range of scales. Moreover, the growth rate of the instability, which indicates how rapid the magnetic field amplification can be, scales with the velocity jump over the shear layer width [Miura and Pritchett 1982]. Turbulence will decay in time as it reaches the dissipative scales, since there is no more energy and momentum injection from large scales.

Local box simulations show that magnetic fields need to be initially very weak ($B \lesssim 10^{13}$ G) to develop a turbulent state (e.g., Ryu, Jones, and Frank 2000, Obergaulinger, Aloy, and Müller 2010). Otherwise, the magnetic field dominates the dynamics, leading to a slower deceleration of the shear flow and a more pronounced alignment of the flux and vorticity tubes. Once turbulence is developed, the weak magnetic field can reach amplitudes $3-4$ orders of magnitude above its initial value. In order to prove this in *global* GRMHD

simulations, prohibitive resolutions are needed to capture the inertial range of scales. A few such simulations with very high spatial resolution show the amplification of the magnetic field [Kiuchi et al. 2015, Kiuchi et al. 2018, Kiuchi et al. 2024]. However, a model for turbulence would be needed for simulations with modest resolution.

1.3.2 **Magnetorotational instability**

The MRI [Velikhov 1959, Chandrasekhar 1960] has been suggested as the mechanism that drives MHD turbulence and redistributes angular momentum in astrophysical discs orbiting around compact objects [Balbus and Hawley 1991, Balbus and Hawley 1998]. Weakly magnetised accretion discs [Shakura and Sunyaev 1973, Lynden-Bell and Pringle 1974] (in the absence of further destabilising effects such as entropy or composition gradients), can be unstable to the MRI when there is a negative radial gradient in the angular velocity. The onset conditions of the MRI can be fulfilled in PNSs (e.g., Cerdá-Durán et al. 2008, Obergaulinger et al. 2009) and BNS postmerger remnants (e.g., Fernández et al. 2019, Kiuchi et al. 2024).

Due to the relevance of the MRI in several astrophysical scenarios, a lot of effort has been made in trying to understand the physics of the instability and the resulting turbulent state. Seed perturbations can grow exponentially on timescales close to the rotational period. These perturbations take the form of channel modes, which are pairs of vertically stacked layers in which the velocity and the magnetic fields have radial and azimuthal components of alternating polarity, i.e., with alternating sign. The size of the channels is proportional to the magnetic field strength and inversely proportional to the rotation frequency and density. For studies that explore the linear growth of the stability, see, e.g., Pessah, Chan, and Psaltis 2006b, Pessah, Chan, and Psaltis 2007, Pessah and Chan 2008, Lesaffre, Balbus, and Latter 2009. From these modes, the joint contribution of the magnetic (Maxwell) stress tensor and kinetic (Reynolds) stress tensor leads to the transport of angular momentum from the inner parts of the disc to its outskirts. Moreover, the growth of the magnetic stresses results in an exponential amplification of the magnetic field. The growth of the instability will eventually terminate, resulting in the breakdown of the channels into small-scale turbulence.

The mechanism responsible for the saturation of the MRI and thus the factor by which seed perturbations are amplified is not yet fully understood. Goodman and Xu 1994 presented an explanation based on parasitic instabilities (PIs) that was further developed with local linear (and weakly nonlinear) analyses

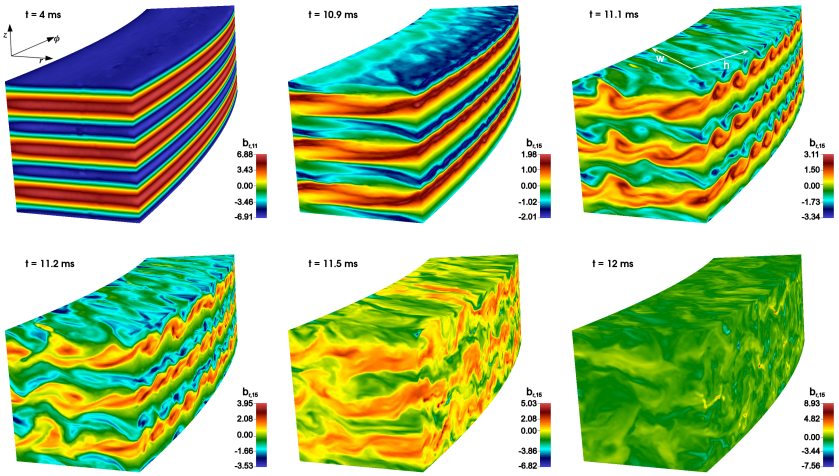

Figure 1.10 Spatial distribution of the radial component of the magnetic field (generated by the MRI), for different times. Initially, the magnetic field forms shear layers that are eventually disrupted, leading to a turbulent state at which the magnetic field amplitude saturates. Figure reproduced with permission from Rembiasz et al. 2016b (Figure 6).

by Umurhan, Menou, and Regev 2007, Lesaffre, Balbus, and Latter 2009, Latter, Lesaffre, and Balbus 2009, Latter, Fromang, and Gressel 2010, Pessah and Goodman 2009 and Pessah 2010, among others. This model provides a physical mechanism that explains the termination of the MRI and the subsequent nonlinear regime. The laminar channel flows can be unstable against PIs that can be of KH or tearing-mode (TM) type, depending on the value of the kinematic viscosity and resistivity, i.e. non-ideal effects. At the beginning of the exponential growth of the MRI, the effect of the PIs is negligible, since they grow much slower than the primary instability. Nevertheless, the growth rate of the PIs is proportional to the amplitude of the MRI modes, which grow exponentially in time. This means that, at some point, the PIs start growing much faster than the MRI modes, and they eventually disrupt the channel modes and saturate the main instability, leading to a turbulent regime. The predictions made by these analytical approaches have been tested by several numerical MHD simulations [Latter, Lesaffre, and Balbus 2009, Latter, Fromang, and Gressel 2010, Longaretti and Lesur 2010, Murphy and Pessah 2015, Rembiasz et al. 2016b, Rembiasz et al. 2016a, Hirai et al. 2018]. However, there are still some discrepancies between the analytical predictions and the numerical results. Figure 1.10 shows snapshots at different times of the radial component of the magnetic field, from three-dimensional MHD box simulations by Rembiasz et al.

2016b. Initially, the field is distributed in laminar channel flows, but eventually these channels are disrupted, and a turbulent state is achieved in which the amplitude of the field saturates.

1.3.3 Sub-grid modelling and large-eddy simulations of binary neutron star mergers

Numerical simulations need to resolve the wide range of scales in which turbulence develops if one wants to capture all the physics involved in the problem. The so-called direct numerical simulations (DNS) aim to do that. Nevertheless, if the resolution is not large enough, simulations may only capture part of the range of scales, leading to an incorrect treatment of the small-scale physics that can have important consequences in all scales. In simulations of BNS mergers, extremely high computational resources are needed in order to account for a realistic treatment of the microphysics (EOS, neutrino transport), non-ideal effects and turbulence. Therefore, it is fairly convenient to devise a model able to capture small-scale physics and the development of turbulence while sidestepping computationally prohibitive DNS. Even though the model for turbulence might not be correct in very small scales, it can capture the proper physics when applied to the characteristic scales of the problem. The simulations that employ this approach are known as *large-eddy simulations (LES)*.

A way to see how the small-scale fields impact on the dynamics of the bulk flow is to apply the mean-field formalism [Krause and Rädler 1980] to the MHD equations. One can separate between resolved and unresolved contributions of the velocity and magnetic fields by applying a filtering operation in space (or time). If we assume that the behaviour is solved for a certain lengthscale l, we can introduce a filter that acts on that scale. The residual between filtered and unfiltered fields will be the turbulent contribution. By introducing this decomposition in the MHD equations, which are nonlinear, and after applying the filtering operation to the equations, additional terms with products of turbulent quantities, i.e., turbulent stresses, will appear. The goal of turbulence modelling is to find a closure relation for the fluctuations that allow to express them in terms of resolved quantities.

In the context of GR, the closure needs to retain the covariance of the equations of motion. The filtering operation can break this covariance and problems may arise with the averaging of the Lorentz factor. Several discussions have been made, e.g, in Celora et al. 2021, Celora et al. 2024, to keep the covariance by adding an observer with the 4-velocity of the flow and applying

the averaging procedure in its rest frame, so that the metric and covariant derivatives are not affected.

During the last decades, several closure relations, also called *sub-grid closures*, have been proposed as models for turbulence in numerical simulations of relativistic flows. Smagorinsky 1963 presented a simple model for Newtonian flows that relates the turbulent velocity with the shear of the mean flow. It introduces an effective turbulent viscosity the value of which needs to be provided. A way to find the optimal value is to calibrate it with control box simulations. The presence of *calibration constants* in such phenomenological models is common. Radice 2017, Radice 2020 extended this model to GR and applied it to BNS merger simulations. In those works, the turbulent viscosity is defined as the coupling between a mixing length (close to the MRI wavelength) and the local sound speed.

Giacomazzo et al. 2015 introduced a sub-grid term in the induction equation for the vector potential to study the turbulent magnetic field amplification during the merger phase, where the KH instability takes place. The closure is inspired by the mean-field dynamo theory [Krause and Rädler 1980], where the sub-grid source term in the induction equation is proportional to the large-scale magnetic field (or vector potential). A similar model has been introduced by Most 2023, who employs a new approach to the MRI-driven $\alpha\Omega$ dynamo [Parker 1955, Reboul-Salze et al. 2022] for GRMHD simulations. Also recently, Aguilera-Miret, Viganò, and Palenzuela 2022 and Palenzuela et al. 2022 performed GRLES with the so-called gradient model [Leonard 1975, Carrasco, Viganò, and Palenzuela 2020, Viganò et al. 2020]. This agnostic model makes use of the Taylor series approximation (or gradient) of the fields to obtain an expression for the turbulent terms. There is a factor that depends on the filtering kernel that relates the sub-grid terms to the size of the kernel. More information about the Newtonian form of this model is provided in Chapter 2. Moreover, there have been some works that developed sub-grid models based on the application of machine learning (ML) techniques, such as deconvolutional neural networks [Yuan, Xie, and Wang 2020], or physics-informed ML to treat turbulence in CCSN simulations [Karpov et al. 2022].

The use of LES has allowed exploring with more depth the effects of small-scale turbulence in BNS merger simulations. In the past, several works did not manage to capture the magnetic field amplification triggered during the merger [Baiotti, Giacomazzo, and Rezzolla 2008, Giacomazzo, Rezzolla, and Baiotti 2011]. However, with the use of very high spatial resolutions ($\Delta x \sim 10$ m), it has been possible to capture the turbulent dynamo from the KH instability

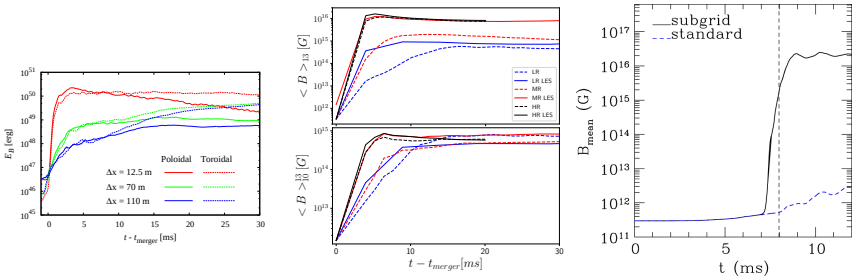

Figure 1.11 Left panel: Exponential amplification of the magnetic energy due to the KHI in a GRMHD simulation of a BNS merger with no sub-grid models. Very high resolution is needed ($\Delta_x = 12.5$ m) to obtain a correct saturation amplitude. Figure reprinted with permission from Kiuchi et al. 2018. Copyright (2018) by the American Physical Society. Middle panel: Magnetic field amplification due to the KHI from another GRMHD simulation, employing the gradient sub-grid model. The same saturation amplitude is reached using a high-resolution run without the model and a mid-resolution run with the sub-grid approach. Figure reprinted with permission from Palenzuela et al. 2022. Copyright (2022) by the American Physical Society. Right panel: Comparison between a GRLES and a standard simulation. The GRLES approach allows the magnetic field to be amplified several orders of magnitude, in contrast to the standard simulation, in which turbulence is not captured. Figure reproduced by permission of the AAS from Giacomazzo et al. 2015.

without the use of LES [Kiuchi et al. 2015, Kiuchi et al. 2018, Kiuchi et al. 2024]. Promising results were obtained by Giacomazzo et al. 2015 with the application of a mean-field dynamo sub-grid model, reaching magnetic field amplitudes of 10^{16} G. More convergent results were shown by Aguilera-Miret, Viganò, and Palenzuela 2022, Palenzuela et al. 2022, where they performed GRLES with the gradient sub-grid model. Those simulations confirmed that weak small-scale magnetic fields can be amplified up to 10^{16} G. It is worth noting that in Palenzuela et al. 2022 the same value of the field amplitude was obtained with a high-resolution simulation without the sub-grid model and also with a mid-resolution LES, showing convergence. Figure 1.11 shows how the magnetic field is amplified due to the KHI in different simulations. The left panel depicts an effective amplification with GRMHD simulations with very high spatial resolution ($\Delta x = 12.5$ m) and no sub-grid approaches [Kiuchi et al. 2018]. The middle panel, however, depicts a GRLES approach with the gradient model [Palenzuela et al. 2022]. The same saturation amplitude is achieved by performing a high-resolution simulation and by using half the spatial resolution with the sub-grid model. In the right panel, the mean-field dynamo developed by Giacomazzo et al. 2015 allows the mean magnetic field to be amplified several orders of magnitude. Aguilera-Miret, Viganò, and Palenzuela 2022 also found that the amplification seems to be independent of the initial magnetic field (as long as it is weak enough). Furthermore, Aguilera-Miret et al. 2023 also

observed an inverse cascade of the magnetic field at later times after merger, leading to an amplification of the large-scale field, which is characteristic from a turbulent dynamo. Very recently, Kiuchi et al. 2024 have found strong evidence for a $\alpha\Omega$-dynamo in the postmerger remnant from GRMHD simulations with extremely high resolution ($\Delta x = 12.5$ m, with no sub-grid models), showing the expected inverse cascade triggered by the MRI.

Duez et al. 2004 studied angular momentum transport in postmerger remnants by performing hydrodynamical axisymmetric evolutions of differentially rotating NSs built with a *j-constant* law for the rotation profile [Eriguchi and Mueller 1985]. Further MHD simulations by Siegel et al. 2013 confirmed the qualitative findings of Duez et al. 2004, in which viscosity appeared due to magnetic and kinetic turbulent stresses. More recently, the GRLES calculations of Radice et al. 2018, Duez et al. 2020 showed that viscosity drives the NSs to a uniform rotation, leading to the collapse of those models with mass above the uniformly rotating limit. Nevertheless, it has been found that the rotational profile of RMNS remnants is considerably different to the *j-constant* one. The maximum rotational frequency is located far from the centre of the star, at densities below 10^{13} g/cm^3, and the inner core is slowly rotating [Shibata and Sekiguchi 2005, Kastaun and Galeazzi 2015, Kastaun et al. 2017]. Since the angular momentum is lower at the center, the effective viscosity from the MRI can rise the rotational velocity in the inner core, increasing the degree of differential rotation of the star and therefore delaying the collapse [Radice 2017]. Several examples of such rotational profiles from HMNSs can be found in, e.g., Hanauske et al. 2017, Iosif and Stergioulas 2022, Cassing and Rezzolla 2024.

The impossibility of DNS to cover all the range of scales where turbulence develops makes the use of LES a good effective approach. Their application has confirmed the magnetic field amplification triggered by the KH instability and the $\alpha\Omega$ dynamo, and the angular momentum transport arising from the MRI. However, the additional parameters that these models introduce may have an effect on the physics of the problem, and one needs to be careful with preserving covariance in GR simulations [Celora et al. 2021]. Substantial work needs to be done in this field to provide further insight on the role of turbulence in the evolution and stability of the merger remnant and the subsequent observational EM and GW signatures, along with the computation of the mass ejecta that plays a key role in r-process nucleosynthesis.

1.4 Gravitational waves from neutron star mergers

BNS mergers are prime sources of gravitational radiation. The detection of GW signals from BNS mergers allows confronting the results obtained through numerical simulations and to infer physical parameters of the source (encoded in the waveforms). Simulations show that the GWs emitted in BNS mergers are very sensitive to the EOS of NS matter. Moreover, their postmerger spectra show the excitation of oscillation modes in the RMNS remant. A careful analysis of these features may yield invaluable information on NS physics.

1.4.1 Extracting information from the gravitational-wave signal

Gravitational waveforms reflect the dynamics of the system. During the inspiral phase, the amplitude and frequency of the GW signal increase as the objects come close to each other. This part of the signal is known as the *chirp signal*. At this stage, the GW emission is well approximated by analytical and semi-analytical expansions. The effect of tides due to the finite size of the NS is imprinted in the waveform, changing its phase evolution [Hinderer et al. 2016]. Such tidal deformations of the stars strongly depend on the EOS[7], but are very difficult to extract from the waveform separately for each binary component, and they can be described by the tidal deformability parameter. In PN waveforms, the dominant tidal parameter (also known as the *effective tidal deformability*, $\tilde{\Lambda}$), which corresponds to the mass-weighted averaged tidal deformability, appears and can be extracted from GW observations of the inspiral phase, together with the chirp mass, $M_{\rm chirp}$, of the binary. The masses, their ratios, and the tidal deformability, i.e., the EOS, are the dominant parameters in the inspiral waveform. The spin (although the stars are slowly rotating before merger) and the binary eccentricity (relevant when the systems are formed via dynamical capture) might add minor corrections to the signal. Also, the possible influence of magnetic fields in the inspiral waveform has also been studied [Giacomazzo, Rezzolla, and Baiotti 2009], and it is unlikely to be detected by current detectors for realistic premerger field strengths (only detectable for unrealistically large values, $B \sim 10^{17}$ G).

The tidal deformability of NSs can take values between $\mathcal{O}(100)$ and $\mathcal{O}(1000)$, depending on the EOS and the stellar mass. By fixing the individual NS mass, the deformability can change by a factor ~ 10 according to the choice of the EOS. A large value of the tidal parameter corresponds to a less compact star that is easily deformable, which has a *soft* EOS. On the other hand,

[7] In particular, they depend on the pressure gradients inside the star.

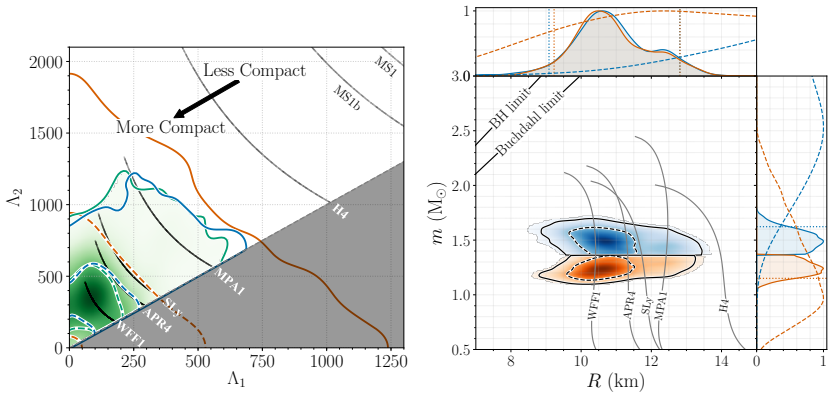

Figure 1.12 Left: Marginalised posterior probability for the tidal deformabilities of the two component stars of GW170817. The green area shows the posterior computed using EOS-insensitive relations. The solid (dashed) lines represent the 50% (90%) credible levels of the posteriors, given by different relations. The grey dashing stands for the unphysical region where $\Lambda_2 < \Lambda_1$ (being 1 the primary mass), and some values of the tidal parameters for different EOSs appear as black lines. Right: Marginalised posterior for the mass m and radius R of each of the component stars of GW170817, obtained from EOS-insensitive relations. The blue (orange) color represents the more (less) massive component. The grey lines show some mass-radius relations for several EOSs and in the top left corner there are lines denoting the Schwarszchild BH and Buchdahl limits. The plots at the sides depict one-dimensional posteriors. Figures reproduced with permission from Abbott et al. 2018a. Copyright (2018) by the American Physical Society.

lower values of the tidal deformability indicate the existence of a *stiff* EOS. There have been actual estimates of the tidal deformability from the analysis of the two BNS mergers detected by the LIGO, Virgo, and KAGRA (LVK) Collaboration, GW170817 [Abbott et al. 2017d] and GW190425 [Abbott et al. 2020b]. For GW170817, the statistical uncertainties made it only possible to set an upper limit for the mass-weighted tidal deformability, $\tilde{\Lambda} < 800$ [Abbott et al. 2017d], which excludes several stiff EOSs. From this detection, there have been numerous estimates and constraints on EOSs on the basis of the bounds on $\tilde{\Lambda}$ (see Figure 1.12 and, e.g, Abbott et al. 2018a, Zhang, Li, and Xu 2018, Lim and Holt 2018, Abbott et al. 2019b, Landry and Essick 2019). In the case of GW190425, the upper limit for $\tilde{\Lambda}$ was 1200 for low-spin priors.

With the inferred value of the tidal deformability and the chirp mass, it was possible to also infer the radius of the primary NS, i.e., the more massive one. For a primary mass $m_1 = 1.4\ M_\odot$, the inferred radius was $R_{1.4} \approx 12$ km. This was found thanks to EOS-insensitive (quasi-universal) relations, built from a large set of simulations employing various EOSs [Yagi and Yunes 2017, Chatziioannou, Haster, and Zimmerman 2018, De et al. 2018, Raithel, Özel, and Psaltis 2018]. At merger, it was found by Read et al. 2013 that the instantaneous GW frequency

is well correlated with the tidal deformability and the NS compactness. By employing an extended set of EOSs, the authors presented EOS-insensitive relations between this frequency at the peak amplitude and the compactness and tidal parameter.

As previously discussed, the postmerger phase is characterised by the formation of a RMNS remnant that eventually collapses to a BH. The energy emitted in GWs is considerably larger than in the inspiral phase, and the characteristic frequency of the signal is in the range of kHz. This part of the waveform is more difficult to model than the inspiral signal and has a somewhat stochastic nature. This is due to the interplay of different effects such as turbulence, strong magnetic fields, neutrino radiation, viscosity or hydrodynamical instabilities. In addition, this challenges the possibility of performing realistic numerical simulations and therefore extract accurate GW signals that could be employed for detection purposes (e.g., Breschi et al. 2019, Breschi et al. 2022). In fact, the Computational Relavity (CoRe) database[8] [Dietrich et al. 2018, Gonzalez et al. 2023] is a collaborative effort to produce a catalog of NR simulations of compact binaries.

The GW spectrum of the early postmerger phase (up to $t - t_{\rm merg} \approx 30$ ms) is characterised by a main peak, f_2, that corresponds to the fundamental quadrupolar ($m = 2$) mode of oscillation of the star [Zhuge, Centrella, and McMillan 1994, Ruffert, Janka, and Schaefer 1996]. The location of this peak is sensitive to the EOS, and it is around $\sim 2 - 4$ kHz, e.g., Takami, Rezzolla, and Baiotti 2015. Numerical simulations have allowed determining that this peak is tightly correlated with the tidal deformability and also with the radius of a NS with mass 1.6 $M_\odot$ [Bauswein et al. 2012, Hotokezaka et al. 2013]. This quasi-universal relation was explained by Bernuzzi, Dietrich, and Nagar 2015, who noticed that for a large tidal deformability, the tidal interaction during the inspiral is more attractive, leading to a merger at lower frequencies. The remnant star is consequently less bound and more extended, resulting in a lower frequency of its fundamental mode. Variations on the EOS can produce a significant variety of postmerger GW spectra with different peak locations. Figure 1.13 shows the diversity of postmerger waveforms that can be obtained for different EOSs and initial masses. The use of quasi-universal, EOS-insensitive, relations to link this frequency with NS properties has turned GW spectroscopy into a very active field of research to constrain the EOS of NS matter (see e.g. Baiotti, Giacomazzo, and Rezzolla 2008, Stergioulas et al. 2011, Bauswein et al. 2012, Bauswein and Stergioulas 2015, Hotokezaka et al. 2013, Takami, Rezzolla, and Baiotti 2014,

[8] http://www.computational-relativity.org

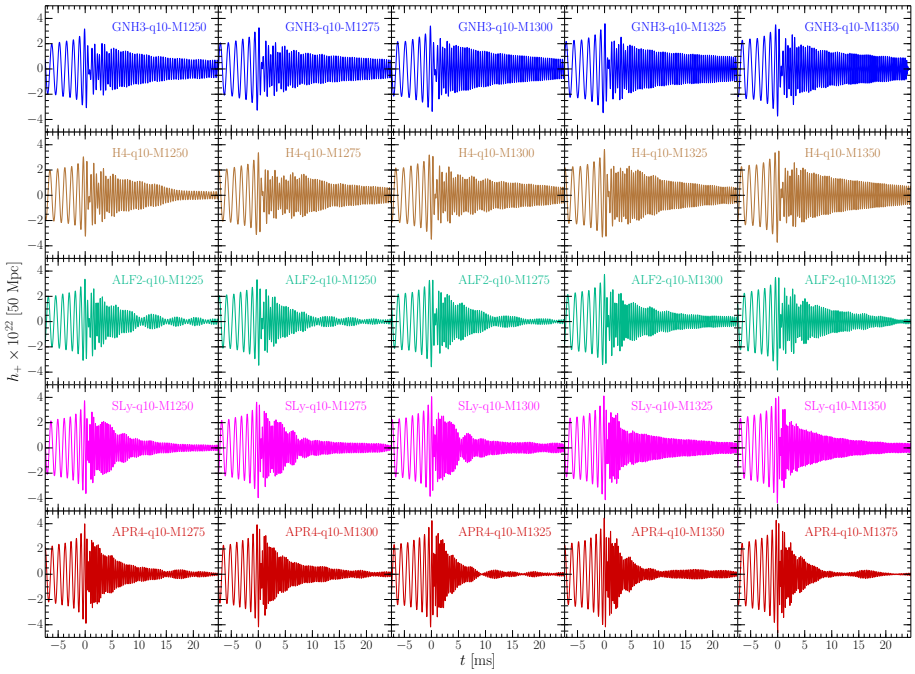

Figure 1.13 Several gravitational waveforms for equal-mass BNS mergers. Each row refers to a different EOS, while each column stands for a certain initial mass. Figure reprinted with permission from Takami, Rezzolla, and Baiotti 2015. Copyright (2015) by the American Physical Society.

Takami, Rezzolla, and Baiotti 2015, Bernuzzi et al. 2014, Bernuzzi, Dietrich, and Nagar 2015, Clark et al. 2016, De Pietri et al. 2016, De Pietri et al. 2020). There may exist secondary peaks in the GW postmerger spectrum that are related to different oscillation modes of the star. For example, the one-arm instability (see Section 1.1) can imprint a frequency peak at about half the value of the main f_2, but its amplitude is considerably lower compared to the main peak, making it more difficult to detect.

As the remnant evolves it stabilises and the amplitude of the GW signal decreases, while the frequencies evolve in time [Rezzolla and Takami 2016, Maione et al. 2017, De Pietri et al. 2020]. At a certain point, the remnant may collapse to a BH, and the GW emission suddenly stops. As collapse approaches, the star loses angular momentum by emitting gravitational radiation, which lowers the waveform amplitude as the remnant becomes more axisymmetric and compact (e.g, Maione et al. 2017). The frequency of the quadrupolar mode increases when the collapse gets closer.

Postmerger densities can become incredibly large, beyond twice nuclear saturation density. For lower values, the NS (hadronic) EOS is expected to describe the star realistically enough. However, in the postmerger phase matter in the core may undergo phase transitions (PTs) to, for example, deconfined quark matter. The appearance of quarks considerably softens the EOS. The eventual observation of NSs with similar masses and different tidal deformabilities might be an evidence of transitions to quark matter. This phenomenon would have an imprint in the GW emission from the postmerger remnant star (see e.g. Bauswein et al. 2019, and Mondal et al. 2023 for the detectability of PTs). After some milliseconds, the increased quark fraction in the core can change the quadrupole moment and therefore change the value of f_2. In fact, a method to detect a PT would consist in comparing the main frequency peak measured in the postmerger with the one inferred from the tidal deformability via quasi-universal relations. The latter would be unaffected by the PT, since the tidal deformability is measured during the inspiral. In addition, the stability lifetime of the RMNS can be modified by PTs, and the formation of a quark core can trigger neutrino bursts that can power GRBs [Cheng and Dai 1996, Bombaci and Datta 2000]. The existence of PTs is also due to the relatively high temperatures reached. The treatment of thermal effects in the EOS is an issue that will be further discussed in Chapter 8.

It is also worthy of mention the convexity of the EOS. For non-convex EOSs, the sound speed can be non-monotonic with the number density and the evolution of the remnant can lead to significant differences in the GW emission [Rivieccio et al. 2024]. Indeed, these differences can be of the same order of those provoked by PTs, despite those not being included in the EOS description.

1.4.2 Data analysis of postmerger gravitational waves

The observation and analysis of GW170817, the first GW signal from a BNS merger, has allowed to put constraints on the EOS by measuring the effective tidal deformability from the inspiral phase. The second BNS merger observation, GW190425, did not further improve previous constraints [Dietrich et al. 2020].

The technique employed to infer the parameters of BNS systems during the inspiralling phase is *matched filtering* [Abbott et al. 2020a]. This method is able to identify signals buried in the detector noise by correlating the data with precomputed templates made of a large sample (of the order of millions) of theoretical waveforms. Matched filtering is not only used for detection of modelled sources. By performing Bayesian analyses, it is also possible to infer astrophysical parameters of the sources using the templates. The synthetic

inspiral waveforms (also known as approximants) that are commonly used to create the database are analytical PN expansions (for reviews, see Blanchet 2006, Blanchet 2014, Futamase and Itoh 2007, Schäfer and Jaranowski 2018 and references therein), effective one-body (EOB) approaches [Buonanno and Damour 1999, Buonanno and Damour 2000, Damour et al. 2008, Damour and Nagar 2010] and the `Phenom` models [Ajith et al. 2007]. So far, three classes of 4th-order PN methods have been employed to compute the dynamics of BNS systems: the Hamiltonian approach [Damour, Jaranowski, and Schäfer 2014], the Fokker-action approach [Bernard et al. 2017, Bernard et al. 2018], and effective field theories [Foffa et al. 2017, Levi 2020]. The EOB models reduce the binary system to a single effective particle under an effective potential. They combine results from PN theory and strong-field effects such as scattering. There exist two big families of EOB models for spinning BH binaries: one developed in, e.g., Barausse and Buonanno 2011, Taracchini et al. 2012, Taracchini et al. 2014, Pan et al. 2014, Babak, Taracchini, and Buonanno 2017, and another employed in, e.g., Damour 2001, Damour et al. 2008, Damour, Iyer, and Nagar 2009, Damour and Nagar 2009, Damour and Nagar 2014. These models differ in the choice of several degrees of freedom that arise in the EOB theory, such as the functional form for the potentials. Tidal effects have been included in different ways to study NS binaries [Ho and Lai 1999, Baiotti et al. 2010, Damour and Nagar 2010, Bernuzzi et al. 2012, Steinhoff et al. 2016]. The `Phenom` approaches approximate waveforms by calibrating them to NR using analytical or semi-analytical expressions. Alternatively, they can be obtained through the "hybridisation" of waveforms from NR simulations and PN approximations. By incorporating finite size effects of NSs, the approximants used for BH binaries can be augmented with a tidal description. A commonly used phenomenological approximant for BNS is `NRTidal` [Dietrich, Bernuzzi, and Tichy 2017], and the newest version `NRTidalv2` [Dietrich et al. 2019]. Another phenomenological waveform model recently developed can be found in Kawaguchi et al. 2018. The analyses of GW170817 employed different waveform models, named `TaylorF2, IMRPhenomD_NRTidal, IMRPhenomPv2_NRTidal` and `SEOBNRv4_ROM_NRTidal`. A recent line of work is the use of surrogate models [Field et al. 2014, Varma et al. 2019], which allow the fast computation of waveforms in the frequency domain. These models have been shown to reach an accuracy comparable to NR, and can be useful to perform a parameter space sampling, with direct use in parameter estimation pipelines. Surrogate models for BNS signals can be found in, e.g., Lackey et al. 2017,

Lackey et al. 2019. For further details about approximants of BNS waveforms, see Dietrich, Hinderer, and Samajdar 2021 and references therein.

Unfortunately, the postmerger GW signal is more challenging to detect, because its characteristic frequencies lay in the range of several kHz, resulting in a smaller signal-to-noise ratio (SNR) for present-day observatories. Therefore, only sources located at very close distances (≈ 30 Mpc) can have a detectable postmerger signal [Clark et al. 2016, Chatziioannou et al. 2017, Tsang, Dietrich, and Van Den Broeck 2019]. In addition, the only way to produce realistic waveforms of this stage is via numerical simulations, which is not an easy task. The large amount of physics involved makes simulations very computationally expensive, and it is not possible to build large template banks for matched-filtering applications. To rapidly build postmerger waveform templates, ML techniques have been employed to fit synthetic signals with numerical waveforms [Easter et al. 2019, Whittaker et al. 2022].

An alternative to matched-filtering techniques are generic unmodelled searches. Although less efficient than matched filtering, unmodelled analyses properly reconstruct the postmerger signal and extract information from the GW spectrum depending on the SNR (see, for example, Clark et al. 2016, Klimenko et al. 2016, Chatziioannou et al. 2017, Tsang, Dietrich, and Van Den Broeck 2019). Two model-agnostic searches were performed for the postmerger signal of GW170817 [Abbott et al. 2017]: Coherent Wave Burst (cWB) [Klimenko et al. 2016] and BayesWave [Cornish and Littenberg 2015, Littenberg and Cornish 2015]. The former algorithm consists on searches of coherent excess power in wavelet transformations, while the latter employs Bayesian inference, reconstructing the waveform with a linear superposition of sine-Gaussian wavelets. Even though neither method found any postmerger signal in GW170817 [Abbott et al. 2017, Abbott et al. 2019b], they placed upper limits on the total energy emitted in GWs.

Future GW detectors such as Einstein Telescope [Punturo et al. 2010, Hild et al. 2011] and Cosmic Explorer [Evans et al. 2021] will be a factor ten more sensitive than current detectors in the range of high-frequency postmerger signals, increasing the horizon detection distance by roughly the same factor. Model-agnostic waveform reconstructions would be able to provide GW spectra that could be used to infer physical properties of the star via quasi-universal relations, and give information about the oscillation modes of the RMNS remnant.

1.4.3 Use of machine learning techniques for gravitational-wave data analysis

The rate of detections in the current LVK's fourth observing run (O4) is almost one per day, and it is expected to increase in the next observing runs. This may affect traditional approaches for signal detection and parameter estimation. Therefore, the use of ML techniques in GW astrophysics is experiencing a rapid increase. Their plausible applications are incredibly diverse. In GW data analysis, ML can help complete template banks, aid searches and speed-up parameter estimation (see Huerta et al. 2019, Cuoco et al. 2021 for reviews and references therein).

As previously mentioned, waveform surrogate models are used to cover certain regions of the parameter space. Such models can be built with ML regression techniques, such as Gaussian Process Regression [Easter et al. 2019]. Moreover, ML algorithms such as convolutional neutral networks are also employed to search for (BBH) GW signals, with sensitivity comparable to matched filtering [Gabbard et al. 2018, George and Huerta 2018, Álvares et al. 2021, Boudart and Fays 2022]. Indeed, it has been found that ML GW searches are competitive on simulated data, but they struggle when handling real noise and long-duration data [Schäfer et al. 2023]. Moreover, ML techniques can provide a rapid inference of source properties. These methods are likelihood-free, autoregressive normalising flows which give results comparable to traditional Markov Chain Monte Carlo (MCMC) methods [Green, Simpson, and Gair 2020]. For example, [Gabbard et al. 2022] showed that conditional variational autoencoders perform full parameter estimation of GW150914 in ~ 1 s. Finally, another application of ML to GW astrophysics is the real-time classification of compact binary sources with supervised algorithms [Chatterjee et al. 2020]. A rapid characterisation of the nature of the system is crucial for the success of multimessenger observations.

1.4.4 My involvement in the Virgo Collaboration

The Virgo Collaboration[9] was founded in 1993 with the goal of building a GW interferometer in Europe. It was first built in 2003, and underwent several major upgrades which culminated with the Advanced Virgo detector [Acernese et al. 2015]. The Virgo Collaboration joined efforts with the LIGO Scientific Collaboration in 2007, when they signed a MoU to jointly analyse the GW data and publish the results. Currently, the fourth Observing Run is ongoing, jointly with the Japanese KAGRA detector [KAGRA Collaboration et al. 2019]. During the previous three Observing Runs, 90 GW events were identified by

[9] https://www.virgo-gw.eu

the Advanced LIGO and Advanced Virgo detectors. Most of those events were identified as BBH mergers, but two detected sources were regarded as BNS mergers, GW170817 and GW190425. In July 2016, the Valencia Virgo Group[10] joined the Virgo Collaboration. This group is based in the Departament d'Astronomia i Astrofísica of the Universitat de València. I became a member of the group when I started my PhD thesis, by November 2020. During this period, I was involved in several *service work* activities and I participated quite actively in the Collaboration.

My *service work* activities were diverse. During the first year, I joined the GstLAL team to help perform searches of sub-solar mass compact objects during the 03b run. In addition, I translated into Spanish several science summaries and press notes from the Collaboration. Once O4 started, I participated in several Rapid Response Team (RRT) shifts. The RRT is a joint LVK effort to support multimessenger searches by providing timely supervision and human vetting of the signal alerts. As Level-0 shifter, I had the role of responding in low latency to all significant candidate alerts during my shifts[11]. Furthermore, I took part in the Parameter Estimation ROTA team. My work there consisted in monitoring the online parameter estimation analyses of real candidate events. If the run failed or the candidate event required further analyses, I manually launched and monitored additional runs.

In February 2022, I was elected co-chair of the Virgo Early Career Scientists (VECS) group. During the mandate, which lasted one year, I organised monthly meetings together with my co-chair and other activities that were useful to the early-career community. For example, we organised job fairs and different activities during the Virgo weeks and LVK meetings. We also forwarded job vacancies and information about tutorials or talks that were interesting to young researchers. Moreover, we prepared a joint project with the Outreach team called "Women of Virgo". It consisted in interviewing women working for Virgo and getting to know their experience in their scientific careers. In summer 2022, the new Virgo bylaws were approved, and I took part of the discussions to modify the bylaws that involved early-career scientists. Currently, I am involved in the rewriting of a draft of the new bylaws, a task that has been assigned to the VECS group.

During these almost four years, I attended periodically the meetings of the Extreme Matter group and I also presented there my works on sub-grid

[10] https://www.uv.es/virgogroup/index.html

[11] And I was lucky enough to retract a compact binary merger candidate and sign off a real one!

modelling (Chapters 2 and 3) and data analysis of GW postmerger signals (Chapters 7 and 8). In addition, while I was working on the project about real-time classification of compact binary coalescence (CBC) events (see Chapter 9), I discussed the results with the EM-bright group and gave a presentation to this group and the EM-follow up group as well.

Moreover, all the publications submitted during the thesis have undergone the internal review of the LVK Collaboration before being submitted to the scientific journals.

1.5 Outline

This thesis is organised as follows:

PART I.- Turbulence modelling (Chapters 2, 3, 4 and 5). In this first block, which can be considered the main part of the thesis, I discuss the work related to the analysis and modelling of MHD turbulence in the context of BNS mergers. In the first two chapters, I present a new sub-grid model for MHD turbulence generated by the MRI (Chapter 2) and the KH instability (Chapter 3). By comparing its performance with the output of local DNS, I assess the validity of this model. In Chapter 4, I present preliminary results from the application of the sub-grid model into numerical simulations of differentially rotating isolated NSs. In Chapter 5, I perform a local linear analysis to study the saturation of the MRI by PIs, relaxing some assumptions made in previous works. Finally, I dedicate Chapter 6 to summarise the main conclusions of this part and discuss future work useful to improve the current version of my sub-grid model and implement it in upcoming simulations.

PART II.- Analysis of gravitational-wave signals (Chapters 7, 8 and 9). This second part contains all the work I performed in the context of data analysis of GW signals from NS mergers. Chapters 7 and 8 explore the capability of reconstructing BNS postmerger waveforms and extract information from the recovered GW spectra, focusing on the inference of inertial modes (Chapter 7) and the identification of thermal effects (Chapter 8). Chapter 9 comprises the application of ML algorithms to classify compact binary sources using a Bayesian approach. In Chapter 10, I summarise the conclusions of this second part and I present future applications of the methods I employed.

Appendices. In the Appendices A, I present a summary of the research works that I have co-authored during my thesis. In Appendices A.1 and A.2, I show my contribution to the study of the impact of bosonic matter on the dynamics and stability of NSs. The work in Appendix A.1 consists in the analysis of the impact of ultralight bosonic particles in the development of the bar-mode instability in NSs, while in Appendix A.2 I present a study of the stability of configurations of fermion-axion stars. Furthermore, in Appendix A.3 I give a brief summary of a project about the impact of the gravitational-wave memory (GWM) effect from populations of massive BH mergers on the temperature of the Cosmic Microwave Background (CMB).

Part I

Magnetohydrodynamical turbulence in neutron stars

CHAPTER 2

Assessment of a new sub-grid model for magnetohydrodynamical turbulence – I. Magnetorotational instability

This Chapter was originally published in: **Miquel Miravet-Tenés**, Pablo Cerdá-Durán, Martin Obergaulinger and José A. Font. *Assessment of a new sub-grid model for magnetohydrodynamical turbulence. I. Magnetorotational instability. MNRAS*, Volume 517, Issue 3, pp. 3505–3524, November 2022. DOI: 10.1093/mnras/stac2888. *Reproduced with permission.*

2.1 Introduction

As discussed in the Introduction of this thesis, numerical simulations are an essential tool to study systems involving NSs, such as BNS mergers. However, the huge parameter space of the problem, its dimensionality, and the amount of physics involved limit the number of simulations. Therefore, the description of the long-term evolution of the postmerger phase for generic initial conditions remains poorly constrained [Siegel et al. 2013, Shibata and Hotokezaka 2019, Ciolfi 2020b]. As a result, linking the results of simulations with the data from multimessenger observations of BNS mergers, sGRBs and kilonovae, is still to a large extent an ongoing task. A key aspect of the riddle is the fate of the postmerger HMNS remnant whose lifetime can be strongly affected by a number

of physical effects. Among the most significant ones is the turbulent amplification of the magnetic field occurring throughout the process, from the late inspiral (via instabilities such as the KHI) to well inside the postmerger phase (via the MRI or magnetic winding). The presence of intense magnetic fields of $\mathcal{O}(10^{15})$ G has important consequences in the dynamics of the postmerger remnant. The turbulence generated by the MRI is probably the dominant process transporting angular momentum in the HMNS. The efficiency of this process is directly related with the timescale in which the BH forms and it leaves an imprint in the emitted GWs. Moreover, turbulent and convective dynamos could amplify the magnetic field and generate large-scale structures (dipole fields) that seem to favour the formation of jets and sGRBs.

Nevertheless, as discussed in Section 1.3, current numerical simulations are unable to resolve the scales at which turbulence develops with enough accuracy. Steps to overcome this limitation have been taken through direct numerical MHD simulations[1] with very high resolution. However, as these simulations are computationally very expensive (involving $\sim \mathcal{O}(10)$ million CPU hours) it is currently not possible to perform a systematic study of the magnetorotational evolution of BNS merger remnants.

An alternative way to DNS is to use sub-grid models [Smagorinsky 1963, Leonard 1975, Müller and Carati 2002, Ogilvie 2003, Giacomazzo et al. 2015, Radice 2017, Radice 2020]. This allows performing relatively modest numerical simulations, in terms of resolution, by combining them with a model that describes the small-scale dynamics, smaller than the computational grid. Sub-grid models have found applications in astrophysics (e.g. in stellar evolution [Charbonneau 2013]) as well as in other fields of physics (e.g. meteorology [Müller and Scherer 2005]) and engineering (e.g. aerodynamics [Ekman et al. 2020]). The specific case of magnetised fluids comes with its own challenges, mostly related to the problem of the emergence of inverse cascades. The majority of studies in this context have dealt with solar and stellar dynamos [Charbonneau 2013]. In the last few years there have been attempts to use sub-grid models in GR based on simple approaches [Giacomazzo et al. 2015, Radice 2017, Shibata, Kiuchi, and Sekiguchi 2017, Shibata, Fujibayashi, and Sekiguchi 2021, Viganò et al. 2020]. Pioneering LES of BNS mergers have already been performed using some of those models [Viganò et al. 2020, Palenzuela et al. 2022, Aguilera-Miret, Viganò, and Palenzuela 2022].

[1] Although strictly speaking the term *direct numerical simulation* should be used exclusively for simulations in which all scales are resolved without the necessity of sub-grid models, here we use the term in a loose way to refer to simulations without sub-grid models, even if not all scales are resolved.

In this Chapter we take first steps towards the development and testing of new approaches for sub-grid models for MHD and compare our proposal with current procedures based on the gradient sub-grid model [Viganò, Aguilera-Miret, and Palenzuela 2019, Carrasco, Viganò, and Palenzuela 2020]. We restrict ourselves to the case of high conductivity and density, for which we have high Reynolds numbers and the fluid approximation is valid; this is precisely the case of interest for BNS mergers. The gradient model, based on the Taylor expansion and the inverse function theorem, is widely used nowadays due to the fact that it does not rely on any phenomenological assumption. We first introduce sub-grid modelling with the α-β dynamo approach from Parker [1955] [see Krause and Rädler 1980, for details] and perform an a-priori test of the gradient model by comparing the outcome of the model and the data from an in-box MRI simulation. The same numerical data is used to assess our new proposal. The sub-grid model we put forward in this work is based on the proportionality relations between the components of the turbulent stress tensors. We devise evolution equations for the turbulent energy densities [Pessah and Goodman 2009, Pessah 2010, Rembiasz et al. 2016b] that make it straightforward to model the stress tensors in terms of the energy densities of the MRI and the PIs. The form of the evolution equation depends on the physics of the particular instability under consideration, which, in the case of this work will be the MRI. A performance comparison between our model and the gradient sub-grid model of Carrasco, Viganò, and Palenzuela 2020 is done by computing the L_2 relative error norm for different filter sizes and grid resolutions.

This Chapter is organised as follows: in Section 2.2 we discuss the mean-field formalism used to separate numerically resolved quantities from the small-scale turbulent ones. Next, in Section 2.3 we show a direct application of the mean-field formalism to the induction equation with the determination of the α and β dynamo coefficients, and present the basis of both, the gradient sub-grid model and our new model. In Section 2.4 we briefly describe the MRI simulation we use to carry out our testing of the new sub-grid method and the model comparison. The results of the various tests are also reported in this section. Finally, our conclusions are summarised in Section 2.5. Some equations in the Chapter contain indices with Latin characters. Those are spatial and hence take values from 1 to 3. Unless stated otherwise we use geometrised units by setting $G = c = 1$, and the magnetic permeability is also set to $\mu_0 = 1$, corresponding to a Gaussian or Heaviside-Lorentz unit system [see Jackson 1975].

2.2 Mean-field MHD

2.2.1 Newtonian MHD equations

The mathematical framework for our study is Newtonian MHD whose equations we review in this section. The MHD equations stem from the result of applying the Navier-Stokes and the Maxwell equations to an electrically conducting fluid (or plasma). The equations couple the different dynamical variables of the plasma, such as the fluid velocity, the gas pressure, the mass density and the magnetic field. A Newtonian approach can be applied when the plasma velocity is not relativistic. A common further simplification is to consider the ideal MHD case where the fluid has an infinite electric conductivity, $\sigma \to \infty$. In this case Ohm's law reduces to

$$E_i = -\epsilon_{ijk} v_j B_k \,, \tag{2.1}$$

where ϵ_{ijk} is the 3-dimensional Levi-Civita symbol. This means that the electric field $\boldsymbol{E}$ is completely determined by the magnetic field $\boldsymbol{B}$ and the fluid velocity $\boldsymbol{v}$. Therefore, by inserting Eq. (2.1) into Faraday's law

$$\boldsymbol{\nabla} \times \boldsymbol{E} = -\frac{\partial \boldsymbol{B}}{\partial t}, \tag{2.2}$$

one obtains the induction equation:

$$\frac{\partial \boldsymbol{B}}{\partial t} = \boldsymbol{\nabla} \times (\boldsymbol{v} \times \boldsymbol{B}). \tag{2.3}$$

If we use the expansion of the curl of the vector product

$$\boldsymbol{\nabla} \times (\boldsymbol{v} \times \boldsymbol{B}) = \boldsymbol{v}(\boldsymbol{\nabla} \cdot \boldsymbol{B}) - \boldsymbol{B}(\boldsymbol{\nabla} \cdot \boldsymbol{v}) + (\boldsymbol{B} \cdot \boldsymbol{\nabla})\boldsymbol{v} - (\boldsymbol{v} \cdot \boldsymbol{\nabla})\boldsymbol{B}, \tag{2.4}$$

along with the solenoidal condition of the magnetic field, $\boldsymbol{\nabla} \cdot \boldsymbol{B} = 0$, one can rewrite the induction equation as

$$\partial_t B^i + \partial_j (v^j B^i - v^i B^j) = 0 \,. \tag{2.5}$$

This is the first equation of the MHD system. The remaining equations follow immediately from the equations of mass continuity, the Euler equation, and the energy equation. The final set of MHD equations can be cast in the following conservation form:

$$\partial_t \boldsymbol{F}^0 + \partial_j \boldsymbol{F}^j = 0 \,, \tag{2.6}$$

where vector $\boldsymbol{F}^0 \equiv \boldsymbol{C}$ is the state vector, whose components are the following conserved quantities

$$\boldsymbol{C} = \begin{bmatrix} \rho \\ N^i \\ U \\ B^i \end{bmatrix}, \tag{2.7}$$

which correspond to the mass density, the momentum density, the energy density, and the magnetic field, respectively. The vectors $\boldsymbol{F}^j$ are the fluxes along spatial direction j,

$$\boldsymbol{F}^j \equiv \begin{bmatrix} N^j \\ T^{ji} \\ S^j \\ D^{ji} \end{bmatrix} = \begin{bmatrix} \rho v^j \\ \rho v^i v^j - B^i B^j + \delta^{ij}\left[p + B^2/2\right] \\ v^j\left[U + p + B^2/2\right] - (v_k B^k) B^j \\ v^j B^i - v^i B^j \end{bmatrix}, \tag{2.8}$$

where p is the thermal pressure and $B^2 = B^i B_i$.

The fluxes are written in terms of the *primitive quantities*, $P = \{\rho, v^i, \varepsilon, B^i\}$, where ε is the specific internal energy. One can express the conserved fields $\boldsymbol{C}$ in terms of the primitive ones[2]:

$$N^i = \rho v^i, \tag{2.9a}$$

$$U = \rho(\varepsilon + v^2/2) + B^2/2\,. \tag{2.9b}$$

2.2.2 **Foundations of mean-field MHD**

The aim of this work is to employ the mean-field MHD formalism to the previous equations. In this approach a filter is applied to all variables both in space and time, over certain characteristic (small) length to compute mean quantities. Any variable can then be decomposed into a mean and a fluctuating (turbulent) component of zero mean. Thus, the MHD equations can be written in terms of mean quantities (resolved scales in numerical simulations) and of the average of combinations of the fluctuations (unresolved scales). A sub-grid model provides a closure relation between the two terms that allows us to write the system of equations as a closed system amenable to be solved numerically.

Given any field $\boldsymbol{A}$, the corresponding mean field will be denoted by $\overline{\boldsymbol{A}}$, defined to be the expectation value of $\boldsymbol{A}$ in an ensemble of identical systems. The averages that will be used in the MHD equations can be both spatial or temporal. Hence, the averaging operator will be defined following Charbonneau

[2]Note that the mass density and the magnetic field are both primitive and conserved fields.

2013 as either

$$\overline{\boldsymbol{A}} = \frac{1}{V}\int_V \boldsymbol{A}(t,\boldsymbol{x})\, d^3\boldsymbol{x}\,, \tag{2.10}$$

for a spatial average in a scale of order λ (having thus a volume $V \propto \lambda^3$), or

$$\overline{\boldsymbol{A}} = \frac{1}{\tau}\int_\tau \boldsymbol{A}(t,\boldsymbol{x})\, dt\,, \tag{2.11}$$

for a time average in a timescale τ. Moreover, the average can be performed over different realisations of a simulation. We denote by $\boldsymbol{A}'$ the difference between the original field and the mean field,

$$\boldsymbol{A}' = \boldsymbol{A} - \overline{\boldsymbol{A}}\,. \tag{2.12}$$

We will refer to it as the *fluctuating field*. The above decomposition can be physically interpreted as follows: the field $\boldsymbol{A}$ is characterised by a slowly varying component, $\overline{\boldsymbol{A}}$, which varies on a large spatial (temporal) scale L (T) and is properly resolved, plus a rapidly fluctuating part, $\boldsymbol{A}'$, which varies on a much smaller (shorter) scale, l (t), and represents the effect of the unresolved dynamics. Therefore, the average operation is computed over an intermediate spatial (temporal) scale λ (τ): $l \ll \lambda \ll L$ ($t \ll \tau \ll T$).

It is useful to consider the following relations, known as the Reynolds averaging relations [Krause and Rädler 1980],

$$\begin{gathered} \boldsymbol{A} = \overline{\boldsymbol{A}} + \boldsymbol{A}', \qquad \overline{\overline{\boldsymbol{A}}} = \overline{\boldsymbol{A}}, \qquad \overline{\boldsymbol{A}'} = 0, \\ \overline{\boldsymbol{A}+\boldsymbol{C}} = \overline{\boldsymbol{A}} + \overline{\boldsymbol{C}}, \qquad \overline{\overline{\boldsymbol{A}}\,\overline{\boldsymbol{C}}} = \overline{\boldsymbol{A}}\,\overline{\boldsymbol{C}}, \qquad \overline{\overline{\boldsymbol{A}}\,\boldsymbol{C}'} = 0, \end{gathered} \tag{2.13}$$

holding for any given fields $\boldsymbol{A}$ and $\boldsymbol{C}$.

Since the average of the fluctuating part is zero, the only possible terms related to the fluctuating part in the mean-field equations are the mean of combinations of two fluctuating variables. For this work, we consider only fluctuations of the velocity ($\boldsymbol{v}'$) and of the magnetic field ($\boldsymbol{B}'$), and neglect the fluctuations of density ($\rho' = 0$) and internal energy ($\epsilon' = 0$). This is similar to the work of Ogilvie [2003] that considers the incompressible shearing sheet case [Goldreich and Lynden-Bell 1965]. The incompressible case is also a very good approximation for the particular case of the MRI (see Goodman and Xu 1994 and the discussion in Rembiasz et al. 2016a) With these considerations, the fluctuating part in the equations can be written in terms of the following tensors:

$$M_{ij} = B_i' B_j', \tag{2.14a}$$

$$R_{ij} = v_i' v_j', \tag{2.14b}$$

$$F_{ij} = v'_i B'_j - v'_j B'_i \,, \tag{2.14c}$$

namely, the Maxwell, Reynolds and Faraday stress tensors, respectively, as defined in Ogilvie 2003. From their definitions, it follows that the Maxwell and Reynolds tensors are symmetric, while the Faraday stress tensor is antisymmetric. These objects naturally appear when performing the averaging of the MHD equations, which have the form [Ogilvie 2003]

$$\partial_t \widetilde{\boldsymbol{F}}^0 + \partial_j \widetilde{\boldsymbol{F}}^j = \boldsymbol{S}(\overline{R}_{ij}, \overline{M}_{ij}, \overline{F}_{ij}) \,, \tag{2.15}$$

where quantities with tilde refer to identical functional expressions as Eqs. (2.7) and (2.8), but for the mean quantities $\overline{\boldsymbol{B}}$ and $\overline{\boldsymbol{v}}$ instead of $\boldsymbol{B}$ and $\boldsymbol{v}$. Note that $\widetilde{\boldsymbol{F}}^0 \neq \overline{\boldsymbol{F}}^0$ and $\widetilde{\boldsymbol{F}}^j \neq \overline{\boldsymbol{F}}^j$. The source term $\boldsymbol{S}$ is a function of the mean stresses. Its value for some particular cases can be found, e.g., in Krause and Rädler 1980 or Ogilvie 2003. The general case is not of direct interest for this work and will be presented elsewhere. In Eq. (2.15) only quadratic terms, $\mathcal{O}(\boldsymbol{A}'^2)$, have been considered, and higher order terms have been neglected. This should be a good approximation if $|\boldsymbol{A}'|^2 \ll |\overline{\boldsymbol{A}}|^2$.

2.3 Sub-grid models

We now turn to discuss some sub-grid models that have already been used in previous works, along with the new model we propose in this Chapter.

2.3.1 α-β dynamo mean-field model

Let us start by filtering the induction equation given in Eq. (2.3). First, we express the fields in terms of resolved and unresolved parts:

$$\frac{\partial}{\partial t}(\overline{\boldsymbol{B}} + \boldsymbol{B}') = \boldsymbol{\nabla} \times \left[(\overline{\boldsymbol{v}} + \boldsymbol{v}') \times (\overline{\boldsymbol{B}} + \boldsymbol{B}')\right] . \tag{2.16}$$

Averaging the previous expression leads to:

$$\frac{\partial}{\partial t}\overline{\boldsymbol{B}} = \boldsymbol{\nabla} \times \left(\overline{\boldsymbol{v}} \times \overline{\boldsymbol{B}}\right) + \boldsymbol{\nabla} \times \left(\overline{\boldsymbol{v}' \times \boldsymbol{B}'}\right) , \tag{2.17}$$

where we have made use of $\overline{\boldsymbol{B}'} = \overline{\boldsymbol{v}'} = 0$ and $\overline{\overline{\boldsymbol{v}} \times \boldsymbol{B}'} = \overline{\boldsymbol{v}' \times \overline{\boldsymbol{B}}} = 0$. Note that Eq. (2.17) is the same as Eq. (2.3) but written in terms of filtered quantities and with an extra term. Also note that the contribution $\overline{\boldsymbol{v}' \times \boldsymbol{B}'}$ comes from nonlinearity. Therefore, we define the turbulent electromotive force as:

$$\xi \equiv \overline{\boldsymbol{v}' \times \boldsymbol{B}'} \,. \tag{2.18}$$

The α-β dynamo mean-field model provides a closure equation for ξ expressed in terms of the mean quantities. It assumes statistical homogeneity, steadiness and isotropy for $\boldsymbol{v}'$. Due to the homogeneity of $\boldsymbol{v}'$, the electromotive force will only change with position as far as the mean magnetic flux density and the spatial derivatives do. Furthermore, due to the isotropy of $\boldsymbol{v}'$, any quantity derived from it must be rotation-invariant, and the only vector that does so is the zero-vector. Therefore, there is no contribution of $\boldsymbol{v}'$ to the vector structure of ξ. Additionally, it assumes that $\overline{\boldsymbol{B}}$ depends so weakly on time and position that ξ can be represented by $\overline{\boldsymbol{B}}$ and its first spatial derivatives. Under these assumptions, the turbulent electromotive force has to fulfil

$$\xi_i = \alpha_{\mathrm{d}\ ij}\overline{B}^j - \beta_{\mathrm{d}\ ij}(\boldsymbol{\nabla}\times\overline{B})^j, \tag{2.19}$$

where α_{d} and β_{d} are the so-called dynamo coefficients that depend on the turbulent velocity field, $\boldsymbol{v}'$ [Charbonneau 2013, Reboul-Salze et al. 2021]. This equation can be used as a closure relation that allows us to express Eq. (2.17) solely in terms of resolved quantities ($\overline{\boldsymbol{B}}$, $\overline{\boldsymbol{v}}$).

In the numerical simulations of MRI of Reboul-Salze et al. 2021 no correlation was found between the electromotive force from Eq. (2.19) and the mean current $\overline{J} = -\boldsymbol{\nabla}\times\overline{B}$. Therefore, one could simplify equation (2.19) to

$$\xi_i = \alpha_{\mathrm{d}\ ij}\overline{B}^j\,. \tag{2.20}$$

This closure relation is one of the sub-grid models we test in this work. The interested reader is addressed to Krause and Rädler 1980 and Reboul-Salze et al. 2021 for further information.

2.3.2 **Gradient sub-grid model**

The gradient sub-grid model [Leonard 1975, Müller and Carati 2002] has recently received attention in compressible MHD studies, in particular to investigate magnetic-field amplification in BNS mergers [Viganò, Aguilera-Miret, and Palenzuela 2019, Carrasco, Viganò, and Palenzuela 2020, Viganò et al. 2020, Aguilera-Miret et al. 2020, Palenzuela et al. 2022, Aguilera-Miret, Viganò, and Palenzuela 2022]. In this model one does not need to assume a phenomenological form for the sub-filter-scale terms as it simply relies on the Taylor expansion of the fluxes of the MHD equations, Eq. (2.8), expressed in terms of the primitive variables.

We start by writing the primitive fields P in terms of the conserved ones, Eq. (2.7), by computing $\widetilde{P}^l \equiv g^l(\overline{\boldsymbol{C}})$. Here, the "$\sim$" symbol over a given field means that this field is expressed in terms of filtered quantities. In our case,

the primitive variables will be thus functions of the filtered conserved fields. Therefore, we obtain the following expression when applying a filter over the MHD equations:

$$\partial_t \overline{C}^l + \partial_j \overline{F}^{j,l} = 0\,, \tag{2.21}$$

where index "j" represents the spatial directions and index "l" represents the fields of each set of quantities. We next express the fluxes in terms of $\widetilde{P}(\overline{\boldsymbol{C}})$, which leads to:

$$\partial_t \overline{C}^l + \partial_j F^{j,l}(\widetilde{P}) = \partial_j \tau_{\mathrm{F}}^{j,l}\,. \tag{2.22}$$

The term on the right-hand side is the sub-filter scale (SFS) tensor,

$$\tau_{\mathrm{F}}^{j,l} \equiv F^{j,l}(\widetilde{P}) - \overline{F^{j,l}(P)}\,, \tag{2.23}$$

and there will be one for each flux. In order to express these tensors only in terms of the filtered variables and their derivatives, one performs a Taylor expansion to first order in η (which is related to the filter size) of $\overline{\boldsymbol{F}^{j,l}(P)}$ around $\overline{P}$

$$\overline{F^{j,l}(P)} \simeq F^{j,l}(\overline{P}) + \eta\left(\nabla^2 F^{j,l}(\overline{P}) - \frac{dF^{j,l}}{d\overline{P}^m}\nabla^2\overline{P}^m\right)\,, \tag{2.24}$$

and then expand around $\widetilde{P}$

$$F^{j,l}(\overline{P}) \simeq F^{j,l}(\widetilde{P}) + \eta\frac{dF^{j,l}}{d\widetilde{P}^m}\left(\nabla^2\widetilde{P}^m - \frac{d\widetilde{P}^m}{d\overline{C}^n}\nabla^2\overline{C}^n\right)\,, \tag{2.25}$$

where the indices (l, m, n) denote the spatial components of fields. By the inverse function theorem we are able to express the primitive variables, P, in terms of the conserved ones, $\widetilde{P} = P(\overline{C})$ (the full procedure is outlined in Carrasco, Viganò, and Palenzuela 2020). Finally, we can re-express the SFS tensors from Eq. (2.23) in the form

$$\tau_{\mathrm{F}}^{j,l} = -\eta\nabla\frac{dF^{j,l}}{d\overline{C}^n}\cdot\nabla\overline{C}^n\,. \tag{2.26}$$

This is the closure relation of the gradient sub-grid model. It relates the contribution of the dynamics from the smaller scales to the filtered variables and their derivatives. The SFS tensor in Eq. (2.26) is proportional to the filter size, i.e., the typical scale of the simulation, given by the numerical resolution. The accuracy of the derivatives of the filtered variables depends on the numerical method used to compute them and also on the resolution of the simulation. Therefore, the model is expected to perform better for higher resolutions and also for smaller sizes of the filter [Carrasco, Viganò, and Palenzuela 2020].

The filtered version of the MHD system in terms of the conserved variables $\overline{C}^m$ reads:

$$\partial_t \overline{\rho} + \partial_j N^j(\widetilde{P}) = \partial_j \tau^j_{\rm N}, \tag{2.27a}$$

$$\partial_t \overline{N}^i + \partial_j T^{ji}(\widetilde{P}) = \partial_j \tau^{ji}_{\rm T}, \tag{2.27b}$$

$$\partial_t \overline{U} + \partial_j S^j(\widetilde{P}) = \partial_j \tau^j_{\rm S}, \tag{2.27c}$$

$$\partial_t \overline{B}^i + \partial_j D^{ji}(\widetilde{P}) = \partial_j \tau^{ji}_{\rm D}\,. \tag{2.27d}$$

These equations have the same form as Eq. (2.22) and the non-negligible contribution of the smaller scales appears in the form of source terms in the right-hand side of the equations. Thanks to the closure relation for the SFS tensors given by Eq. (2.26), the source terms can be computed with the derivatives of the fluxes with respect to the conserved variables. Their final expressions are:

$$\tau^j_{\rm N} = -\eta \nabla \frac{d\overline{N}^j}{d\overline{C}^m} \cdot \nabla \overline{C}^m = 0\,, \tag{2.28a}$$

$$\begin{aligned}\tau^{ji}_{\rm T} = -\eta \nabla \frac{dT^{ji}}{d\overline{C}^m} \cdot \nabla \overline{C}^m = \eta \Big[&- 2\overline{\rho} \nabla \widetilde{v}^i \cdot \nabla \widetilde{v}^j + 2 \nabla \widetilde{B}^i \cdot \nabla \widetilde{B}^j - \\ &- \delta^{ji} \big[\nabla \frac{d\widetilde{P}}{d\overline{\rho}} \cdot \nabla \overline{\rho} + \nabla \frac{d\widetilde{P}}{d\widetilde{\varepsilon}} \cdot \nabla \widetilde{\varepsilon} - \frac{2}{\overline{\rho}} \frac{d\widetilde{P}}{d\widetilde{\varepsilon}} \nabla \overline{\rho} \cdot \nabla \widetilde{\varepsilon} + \nabla \overline{B}_k \cdot \nabla \overline{B}^k - \\ &- \frac{1}{\overline{\rho}} \frac{d\widetilde{P}}{d\widetilde{\varepsilon}} \big(\overline{\rho} \nabla \widetilde{v}_k \cdot \widetilde{v}^k + \nabla \overline{B}_k \cdot \nabla \overline{B}^k \big) \big] \Big]\,,\end{aligned} \tag{2.28b}$$

$$\begin{aligned}\tau^j_{\rm S} = -\eta \nabla \frac{d\overline{S}^j}{d\overline{C}^m} \cdot \nabla \overline{C}^m = \eta \Big[&- 2 \big[\nabla \widetilde{\Theta} \cdot \nabla \widetilde{v}^j + \big(\overline{B}^j \overline{B}_k \nabla \widetilde{v}^k - \\ &- \widetilde{\Theta} \nabla \widetilde{v}^j \big) \cdot \nabla (\ln \overline{\rho}) - \overline{B}^j \nabla \overline{B}_k \cdot \nabla \widetilde{v}^k - \nabla (\widetilde{\boldsymbol{v}} \cdot \overline{\boldsymbol{B}}) \cdot \nabla \overline{B}^j \big] + \\ &+ \widetilde{v}^j \big[\nabla \frac{d\widetilde{P}}{d\overline{\rho}} \cdot \nabla \overline{\rho} + \nabla \frac{d\widetilde{P}}{d\widetilde{\varepsilon}} \cdot \nabla \widetilde{\varepsilon} - \frac{2}{\overline{\rho}} \frac{d\widetilde{P}}{d\widetilde{\varepsilon}} \nabla \overline{\rho} \cdot \nabla \widetilde{\varepsilon} + \nabla \overline{B}_k \cdot \nabla \overline{B}^k - \\ &- \frac{1}{\overline{\rho}} \frac{d\widetilde{P}}{\widetilde{\varepsilon}} \big(\overline{\rho} \nabla \widetilde{v}_k \cdot \widetilde{v}^k + \nabla \overline{B}_k \cdot \nabla \overline{B}^k \big) \big] \Big]\,,\end{aligned} \tag{2.28c}$$

$$\begin{aligned}\tau^{ji}_{\rm D} = -\eta \nabla \frac{dD^{ji}}{d\overline{C}^m} \cdot \nabla \overline{C}^m = -2\eta \big[&\nabla \widetilde{v}^i \cdot \nabla \overline{B}^j - \nabla \widetilde{v}^j \cdot \nabla \overline{B}^i + \\ &+ \big(\overline{B}^i \nabla \widetilde{v}^j - \overline{B}^j \nabla \widetilde{v}^i \big) \cdot \nabla (\ln \overline{\rho}) \big]\,,\end{aligned} \tag{2.28d}$$

where $\widetilde{\Theta} \equiv \overline{U} + \widetilde{p} + \overline{\boldsymbol{B}}^2/2$. The derivatives of $\widetilde{p}$ with respect to the mass density and the specific internal energy can be obtained using the EOS.

As we show below in Section 2.4, to assess the method we will employ the SFS tensors given by Eqs. (2.28) to results of in-box MRI numerical simulations, comparing their values with those computed using Eq. (2.23).

2.3.3 **MHD-instability-induced-turbulence (MInIT) mean-field model**

In the previous sections we have shown that the sub-grid-scale terms that arise from averaging the MHD equations can be modelled in terms of averaged variables. For the gradient sub-grid model, the SFS terms represent the sub-grid contributions of the fluxes (cf. Eq. (2.23)). In fact, those terms have been obtained by taking gradients of the derivatives of the fluxes with respect to the conserved variables (see Eq. (2.26)).

In our new model the goal is similar, i.e., we want to express the contributions of the sub-grid scales in terms of resolved quantities that evolve over large enough scales so that their evolution can be captured by numerical simulations. Ogilvie 2003 proposed a mean-field model based in the computation of the evolution equations for the mean stresses of the form

$$(\partial_t + \overline{v}_k \partial_k)\overline{M}_{ij} - \overline{M}_{ik}\partial_k \overline{v}_j - \overline{M}_{jk}\partial_k \overline{v}_i = S_{ij}^{(M)}, \tag{2.29}$$

$$(\partial_t + \overline{v}_k \partial_k)\overline{R}_{ij} - \overline{R}_{ik}\partial_k \overline{v}_j - \overline{R}_{jk}\partial_k \overline{v}_i = S_{ij}^{(R)}, \tag{2.30}$$

where $S_{ij}^{(M)}$ and $S_{ij}^{(R)}$ are functions depending on the averages of combinations of three fluctuating variables (e.g., $\overline{v_i v_j b_k}$ ...), and could be approximated by a closure relation. The left-hand side consists of an advective term and a term accounting for the "stretching" by gradients of the mean velocity. Ogilvie 2003 considered only the particular case of $\overline{F}_{ij} = 0$ but, in the most general case, this quantity should fulfil analogous equations.

One could try to find a general closure for the system of equations proposed by Ogilvie 2003 (or a generalisation of this system) but this approach is in general complicated, and the number of additional equations to be solved is significant (12 equations just for the independent components in Eqs. (2.29) and (2.30)). Instead of this general approach, we aim at providing a sub-grid model that resolves turbulence induced by MHD instabilities. The most relevant MHD instabilities developed during BNS mergers are the MRI and the KHI. In this Chapter we focus on modelling the former deferring to the following Chapter the treatment of the latter.

The MRI has been studied through numerical simulations by a number of authors (see references in the Introduction). Here we consider the semi-global simulations of Rembiasz et al. 2016b and use those as part of our tests and model calibration in the next sections. The simulations are discussed in detail in Section 2.4.1 below. Fig. 2.1 displays the time evolution of the stress tensor components in one such simulation. All three tensors evolve in a qualitatively similar way. On top of the initial conditions (a differentially rotating fluid with a

vertical magnetic field) the instability grows exponentially developing nonlinear channel flows. Those are eventually disrupted leading to the termination of the exponential growth. After termination, the fluid settles into a turbulent state in which stresses are approximately constant (in a statistical sense). This behaviour can be understood by the PI theory [Goodman and Xu 1994, Pessah and Goodman 2009]. In this model, the channel flows, which are exact solutions of the nonlinear incompressible MHD equations [Goodman and Xu 1994, Pessah and Chan 2008], are disrupted by secondary (parasitic) instabilities growing in time. In the case of high Reynolds numbers those PIs are of KH type, and their growth rate depends on the exponentially growing shear, leading to a super-exponential growth. As the energy of the PI becomes comparable to that of the channel flows (MRI energy), those are disrupted and the balance between the two instabilities settles the system into a turbulent state. Rembiasz et al. 2016b were able to measure the PI energy and its super-exponential growth, and tested the validity of the termination criterion giving strong support to the PI theory.

Fig. 2.1 compares the different stresses for a particular numerical simulation with an estimation of the energy densities of the MRI, $e_{\rm MRI}$, and of the PI, $e_{\rm PI}$ (see next section for definitions). The general trend is that, up to some constants, $e_{\rm MRI}$ and $e_{\rm PI}$ are good tracers of the evolution of all stresses. Similar behaviour is observed in all the simulations analysed. This motivates the development of a mean-field model based upon evolution equations for $e_{\rm MRI}$ and $e_{\rm PI}$ so that the stresses can be computed from these quantities using calibrated constants (closure relation). In the next four subsections we discuss the MRI and PI and provide the details of the two ingredients (closure relations and energy density equations) that conform the *MHD-instability-induced-turbulence (MInIT) mean-field model*, the main subject of this work.

2.3.3.1 *MRI theory*

We consider a rotating fluid with a magnetic field with non-zero vertical component[3]. We also consider the case of high Reynolds and magnetic Reynolds numbers (effectively ideal MHD for MRI fluctuations). In this case, the general dispersion relation for the modes of wave-like perturbations is [Balbus 1995, Obergaulinger et al. 2009]:

$$(\hat{\gamma}^2 - \hat{k}^2)^2 - (\hat{\gamma}^2 - \hat{k}^2)(\hat{\omega}_{\rm G}^2 + \hat{\omega}_{\rm R}^2 + 4\cos^2\theta_k) - 4\hat{k}^2\cos^2\theta_k = 0\,, \qquad (2.31)$$

[3]By "vertical" it must be understood the component of the magnetic field parallel to the rotational axis, i.e. along the z-direction of the cylindrical coordinate system (r, ϕ, z).

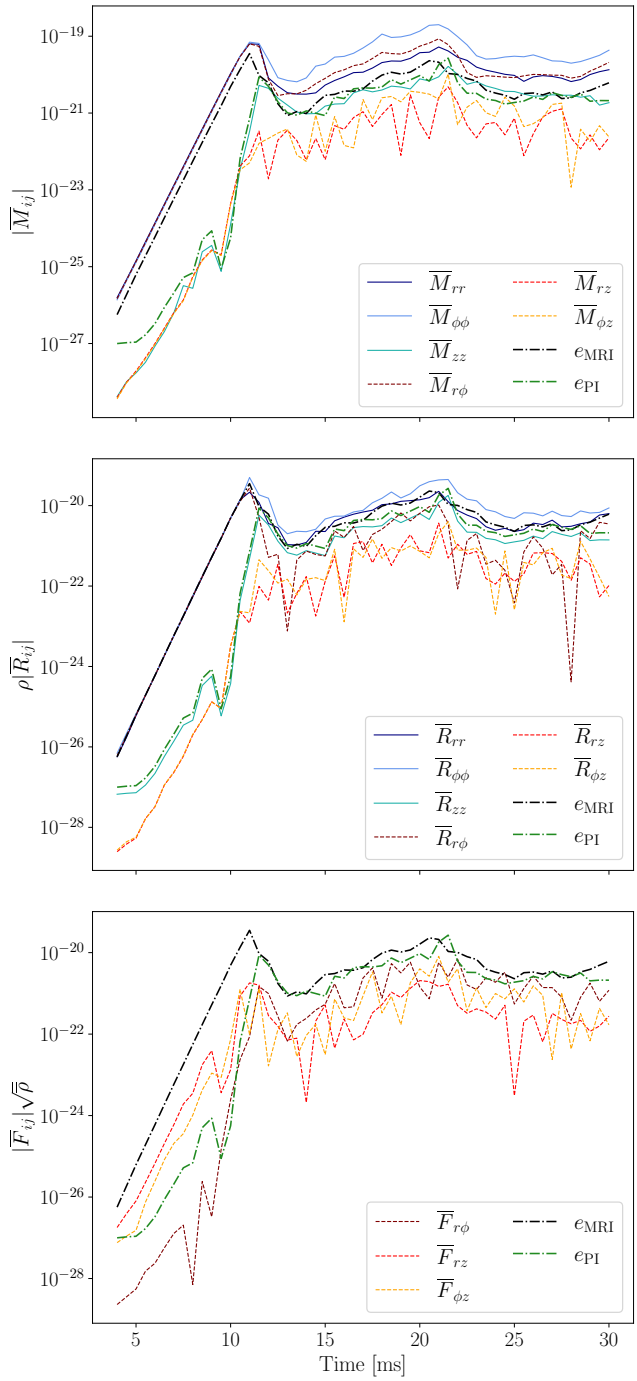

Figure 2.1 Evolution of the Maxwell (top), Reynolds (middle) and Faraday (bottom) stress tensors computed from the numerical data of the simulation MRI-H1 performed by Rembiasz et al. [2016b]. The dash-dotted black and green lines represent the energy densities of the stresses associated with the MRI and PI, respectively.

where θ_k is the angle between the wavevector $\mathbf{k}$ and the vertical axis, $\hat{\omega}_{\mathrm{G,R}}$ are dimensionless frequencies related to buoyancy terms and differential rotation, respectively, and $\hat{\gamma} = \gamma/\Omega$ is the dimensionless growth rate of the mode, normalised by the rotational profile

$$\Omega = \Omega_0 \Big(\frac{r}{r_0}\Big)^{-q}, \tag{2.32}$$

with Ω_0 being the angular velocity at the characteristic radius r_0 and

$$q = -\frac{\mathrm{d}\ln\Omega}{\mathrm{d}\ln \mathrm{r}}, \tag{2.33}$$

corresponding to the rotational shear. In Eq. (2.31) we introduce $\hat{k} = \mathbf{k}\cdot\mathbf{c}_{\mathrm{A}}/\Omega$, where $\mathbf{c}_{\mathrm{A}}$ is the Alfvén speed.

Now, let us focus on the case without buoyancy effects ($\hat{\omega}_{\mathrm{G}} = 0$). In this case, the fastest growing mode has a vertical wavevector [Rembiasz et al. 2016b]:

$$k_{\mathrm{MRI}} \equiv k_{\mathrm{crit}} = \sqrt{1 - \frac{(2-q)^2}{4}}\,\frac{\Omega}{c_{\mathrm{Az}}}, \tag{2.34}$$

where $c_{\mathrm{Az}} = \overline{B}_z/\sqrt{\rho}$ is the vertical component of the Alfvén velocity and is given by the initial magnetic field amplitude in the vertical direction. Thus, the expression of $\hat{k}$ is simplified for the fastest growing mode to

$$\hat{k}_{\mathrm{MRI}} = \sqrt{1 - \frac{(2-q)^2}{4}}\,. \tag{2.35}$$

For the fastest growing mode the perturbations lie on the $r\phi$ plane and therefore $\theta_{k,\mathrm{crit}} = 0$. This implies that the dispersion relation given by Eq. (2.31) leads to the following growth rate of the MRI:

$$\gamma_{\mathrm{MRI}} = \frac{q}{2}\Omega, \tag{2.36}$$

which is constant in time.

Goodman and Xu 1994 demonstrated that this kind of perturbative solutions are not only solution of the linearised MHD equations but also of the full nonlinear equations in the incompressible limit, giving rise to channel flows. During this phase of exponential growth channel modes are characterised very accurately by its perturbation velocity and magnetic field, which we identify as $\boldsymbol{v}'$ and $\boldsymbol{B}'$, fulfilling the next properties in the ideal MHD case [c.f. Pessah and Chan 2008]

$$\boldsymbol{v}' = v_0 \left(\hat{\boldsymbol{r}} + \hat{\boldsymbol{\phi}}\right) \sin(kz)\, e^{\gamma t}, \tag{2.37}$$

$$\boldsymbol{B}' = B_0 \left(\hat{\boldsymbol{r}} - \hat{\boldsymbol{\phi}}\right) \cos(kz)\, e^{\gamma t}, \tag{2.38}$$

where γ and k refer to the fastest growing mode and v_0 and B_0 are the velocity and magnetic field channel-flow amplitudes which are related by

$$\frac{B_0}{\sqrt{\rho}} = \sqrt{\frac{4-q}{q}}\, v_0 \,. \tag{2.39}$$

Note that $\overline{\boldsymbol{B}'^2} = B_0^2\, e^{2\gamma t}$ and $\overline{\boldsymbol{v}'^2} = v_0^2\, e^{2\gamma t}$. These expressions allow us to write the contribution of the MRI channel flows to all the stresses in terms of v_r':

$$\overline{R}_{rr}^{\rm MRI} = \overline{R}_{\phi\phi}^{\rm MRI} = \overline{R}_{r\phi}^{\rm MRI} = \overline{v_r' v_r'}\,, \tag{2.40}$$

$$\overline{R}_{rz}^{\rm MRI} = \overline{R}_{\phi z}^{\rm MRI} = \overline{R}_{zz}^{\rm MRI} = 0\,, \tag{2.41}$$

$$\overline{M}_{rr}^{\rm MRI} = \overline{M}_{\phi\phi}^{\rm MRI} = -\overline{M}_{r\phi}^{\rm MRI} = (4/q-1)\,\rho\,\overline{v_r' v_r'}\,, \tag{2.42}$$

$$\overline{M}_{rz}^{\rm MRI} = \overline{M}_{\phi z}^{\rm MRI} = \overline{M}_{zz}^{\rm MRI} = 0\,, \tag{2.43}$$

$$\overline{F}_{ij}^{\rm MRI} = 0\,, \tag{2.44}$$

where we have used that $\overline{\sin^2(kz)} = \overline{\cos^2(kz)} = 1/2$ and $\overline{\sin(kz)\cos(kz)} = 0$ when averaging over the appropriate length scale (larger than $\lambda_{\rm MRI}$). The contribution of the MRI channel flows to the (kinetic) energy density is then just

$$e_{\rm MRI} = \frac{1}{2}\,\rho\,{\rm Tr}\Big(\overline{\boldsymbol{R}}^{\rm MRI}\Big) = \frac{1}{2}\rho\left(\boldsymbol{R}_{rr}^{\rm MRI} + \boldsymbol{R}_{\phi\phi}^{\rm MRI}\right) = \rho\,\boldsymbol{v_r'}\boldsymbol{v_r'}\,. \tag{2.45}$$

We can now define the next proportionality constants between the different (MRI) stresses and the MRI energy density:

$$\alpha_{ij}^{\rm MRI} \equiv \frac{\overline{M}_{ij}^{\rm MRI}}{e_{\rm MRI}}\,, \tag{2.46}$$

$$\beta_{ij}^{\rm MRI} \equiv \frac{\rho\,\overline{R}_{ij}^{\rm MRI}}{e_{\rm MRI}}\,, \tag{2.47}$$

$$\gamma_{ij}^{\rm MRI} \equiv \frac{\sqrt{\rho}\,\overline{F}_{ij}^{\rm MRI}}{e_{\rm MRI}}\,, \tag{2.48}$$

whose values can be computed directly from the expressions above

$$\alpha_{rr}^{\rm MRI} = \alpha_{\phi\phi}^{\rm MRI} = -\alpha_{r\phi}^{\rm MRI} = 4/q - 1\,, \tag{2.49}$$

$$\alpha_{rz}^{\rm MRI} = \alpha_{\phi z}^{\rm MRI} = -\alpha_{zz}^{\rm MRI} = 0\,, \tag{2.50}$$

$$\beta_{rr}^{\rm MRI} = \beta_{\phi\phi}^{\rm MRI} = \beta_{r\phi}^{\rm MRI} = 1\,, \tag{2.51}$$

$$\beta_{rz}^{\rm MRI} = \beta_{\phi z}^{\rm MRI} = -\beta_{zz}^{\rm MRI} = 0\,, \tag{2.52}$$

$$\gamma_{ij}^{\rm MRI} = 0\,. \tag{2.53}$$

For the case with buoyancy ($\hat{\omega}_{\rm G} \neq 0$) the expressions for $k_{\rm MRI}$ and $\gamma_{\rm MRI}$ become more complex, but can still be computed from the mean quantities [see

Obergaulinger et al. 2009]. Similarly, the coefficients $\alpha_{ij}^{\rm MRI}$, $\beta_{ij}^{\rm MRI}$ and $\gamma_{ij}^{\rm MRI}$ will have a different dependence. In this work we focus on the particular case without buoyancy, but a priori nothing prevents to extend this approach to the most general case.

2.3.3.2 *Parasitic instabilities*

In the high Reynolds and magnetic Reynolds number regime, the dominant parasitic mode is of the KH type and develops along the MRI velocity channel [Pessah and Goodman 2009]. It is characterised by a wavenumber for the fastest growing parasitic mode [Pessah 2010]

$$k_{\rm PI} = 0.59\, k_{\rm MRI}\,, \tag{2.54}$$

and a corresponding growth rate

$$\gamma_{\rm PI} = 0.45\, k_{\rm PI}\, v_0 e^{\gamma_{\rm MRI} t} = \sigma\, k_{\rm MRI}\, v_0 e^{\gamma_{\rm MRI} t}\,, \tag{2.55}$$

with $\sigma = 0.27$. Note that, since the growth rate depends on the amplitude of the channel flow, $v_0 e^{\gamma_{\rm MRI} t}$, the PI will grow super-exponentially. Using the channel mode expressions we can relate $v_0\, e^{\gamma t}$ to $e_{\rm MRI}$ and rewrite the PI growth rate as

$$\gamma_{\rm PI} = \sigma\, k_{\rm MRI} \sqrt{\frac{2\, e_{\rm MRI}}{\rho}}\,. \tag{2.56}$$

Since parasitic modes grow on top of the channel modes, the velocity and magnetic field perturbations can be decomposed as

$$\boldsymbol{v}' = \boldsymbol{v}'^{\rm MRI} + \boldsymbol{v}'^{\rm PI} \quad , \qquad \boldsymbol{B}' = \boldsymbol{B}'^{\rm MRI} + \boldsymbol{B}'^{\rm PI}\,. \tag{2.57}$$

The averaged Reynolds stress will then be

$$\overline{R}_{ij} = \overline{R}_{ij}^{\rm MRI} + \overline{R}_{ij}^{\rm PI} + \overline{v_i^{\rm MRI} v_j^{\rm PI}} + \overline{v_i^{\rm PI} v_j^{\rm MRI}}\,. \tag{2.58}$$

If we consider that MRI and PI modes are spatially uncorrelated, the last two terms in the previous equation can be dropped. Alternatively, we could absorb these two terms into the definition of $\overline{R}_{ij}^{\rm PI}$, since they are zero when no PI modes are present. In either case we can decompose the averaged Reynolds stress into a component coming from the MRI (already computed in the previous section) and a component coming from the PI. Similar arguments can be made for the Maxwell and Faraday stresses leading to the decomposition

$$\overline{\boldsymbol{R}} = \overline{\boldsymbol{R}}^{\rm MRI} + \overline{\boldsymbol{R}}^{\rm PI} \quad , \quad \overline{\boldsymbol{M}} = \overline{\boldsymbol{M}}^{\rm MRI} + \overline{\boldsymbol{M}}^{\rm PI} \quad , \quad \overline{\boldsymbol{F}} = \overline{\boldsymbol{F}}^{\rm PI}\,. \tag{2.59}$$

The (kinetic) energy density of the parasitic modes can be computed as

$$e_{\rm PI} = \frac{1}{2}\,\rho\,{\rm Tr}\Big(\overline{\boldsymbol{R}}^{\rm PI}\Big) = \frac{1}{2}\,\rho\,\left(\overline{R}^{\rm PI}_{rr} + \overline{R}^{\rm PI}_{\phi\phi} + \overline{R}^{\rm PI}_{zz}\right)\,. \tag{2.60}$$

The role of the PI is to disrupt the channel flows generating turbulence. To simplify our model we assume that the turbulence generated by the PI is isotropic, meaning that all diagonal components of $\overline{R}^{\rm PI}_{ij}$ are equal. Under this condition

$$e_{\rm PI} = \frac{3}{2}\rho\,\overline{R}_{zz}\,, \tag{2.61}$$

where we have used that $\overline{R}^{\rm PI}_{zz} = \overline{R}_{zz}$ because $\overline{R}^{\rm MRI}_{zz} = 0$. Additionally, the isotropy condition allows us to rewrite Eq. (2.45) in terms of the Reynolds stress, instead of only the MRI components, as

$$e_{\rm MRI} = \frac{1}{2}\rho\left(\overline{R}_{rr} + \overline{R}_{\phi\phi} - 2\overline{R}_{zz}\right)\,. \tag{2.62}$$

Eqs. (2.61) and (2.62) can be used to estimate the energy density in both types of instabilities in numerical simulations, as in the case of Fig. 2.1. We have to keep in mind that this estimator is not perfect and its application to numerical simulations may lead to artefacts in some cases (see discussion in Rembiasz et al. [2016b] and Rembiasz et al. [2016a] for details).

2.3.3.3 *Closure relation*

Now that we understand that the different stresses depend on $e_{\rm MRI}$ and $e_{\rm PI}$ we can aim at building a phenomenological relation between the two energy densities. An important assumption we make is that the proportionality coefficients do not depend explicitly on time and position, only through their dependence of mean field variables. This means that the stress tensors will have the same time dependence as the energy densities $e_{\rm MRI}$ and $e_{\rm PI}$ as long as the mean quantities are constant. We hence propose the next closure relation:

$$\overline{M}_{ij}(t,\boldsymbol{r}) = \alpha^{\rm MRI}_{ij}\,e_{\rm MRI}(t,\boldsymbol{r}) + \alpha^{\rm PI}_{ij}\,e_{\rm PI}(t,\boldsymbol{r})\,, \tag{2.63a}$$

$$\overline{R}_{ij}(t,\boldsymbol{r}) = \frac{1}{\overline{\rho}(t,\boldsymbol{r})}\left(\beta^{\rm MRI}_{ij}\,e_{\rm MRI}(t,\boldsymbol{r}) + \beta^{\rm PI}_{ij}\,e_{\rm PI}(t,\boldsymbol{r})\right)\,, \tag{2.63b}$$

$$\overline{F}_{ij}(t,\boldsymbol{r}) = \frac{\gamma^{\rm PI}_{ij}}{\sqrt{\overline{\rho}(t,\boldsymbol{r})}}e_{\rm PI}(t,\boldsymbol{r})\,, \tag{2.63c}$$

where the factors involving the mass density are added in order to make the coefficients dimensionless. For the MRI coefficients we use the ones derived for the MRI channel modes, Eqs. (2.49)-(2.53). We note that the diagonal components of $\beta^{\rm PI}_{ij}$ could be determined from Eq. (2.61) and the isotropy condition, resulting in $\beta^{\rm PI}_{ii} = 2/3$. The value of off-diagonal components depends on the correlations

between different components of the velocity entering on the averages but are constrained to be $|\beta_{ij}^{\rm PI}| \leq 2/3 (i \neq j)$. However, we prefer to keep $\beta_{ij}^{\rm PI}$ as a free parameter of the theory, together with $\alpha_{ij}^{\rm PI}$ and $\gamma_{ij}^{\rm PI}$. These coefficients can be calibrated using numerical simulations and their values are discussed in the next sections.

2.3.3.4 *Evolution equations of the MRI and PI energy densities*

The last step is to obtain evolution equations for the PI and MRI energy densities. From their definitions, Eqs. (2.61) and (2.62), the mean-field continuity equation and Eq. (2.30) (neglecting the stretching terms) we obtain equations of the form

$$\partial_t e_{\rm MRI} + \partial_i (\overline{v}_i \, e_{\rm MRI}) = S^{\rm (MRI)} \,, \tag{2.64}$$

$$\partial_t e_{\rm PI} + \partial_i (\overline{v}_i \, e_{\rm PI}) = S^{\rm (PI)} \,, \tag{2.65}$$

i.e., a set of balance laws for both energy densities, with some complicated sources that include both the effect of the MRI and the PI. The stretching terms could be kept and expressed in terms of $e^{\rm MRI}$ and $e^{\rm PI}$ using the coefficients $\beta_{ij}^{\rm MRI}$ and $\beta_{ij}^{\rm PI}$. However, this adds unnecessary complication for the purpose of this work (stretching is irrelevant for the simulations that we discuss in the next sections) and would make the equations non-conservative.

A closed and simple form for the source terms can be justified taking into account some information we derived in the last few subsections, namely: i) the amplitude of MRI channel flows grows exponentially with a growth rate $\gamma_{\rm MRI}$ and hence $e_{\rm MRI}$ grows with a rate of $2\gamma_{\rm MRI}$ during the initial phase; ii) The same happens for $e_{\rm PI}$, but with a growth rate $2\gamma_{\rm PI}$; iii) The PI draws energy from $e_{\rm MRI}$ whenever both energy densities are comparable, quenching the growth of the MRI channels and leading to saturation; iv) Finally, the PI generates turbulence in which larger vortices are broken in smaller ones in a turbulent cascade until the physical dissipation scale is reached where dissipation occurs. At this small scale, kinetic (and magnetic) energy is transformed into thermal energy [see, e.g., Landau and Lifshitz 1987, chapter III]. Taking all these considerations into account we propose the next set of equations for the evolution of MRI and PI energy densities:

$$\begin{aligned} \partial_t e_{\rm MRI} + \partial_i (\overline{v}_i e_{\rm MRI}) &= 2\,\gamma_{\rm MRI}\, e_{\rm MRI} - 2\,\gamma_{\rm PI}\, e_{\rm PI} \,, & (2.66) \\ \partial_t e_{\rm PI} + \partial_i (\overline{v}_i e_{\rm PI}) &= 2\,\gamma_{\rm PI}\, e_{\rm PI} - S_{\rm TD} \,. & (2.67) \end{aligned}$$

The growth rates $\gamma_{\rm MRI}$ and $\gamma_{\rm PI}$ are given in Eqs. (2.36) and (2.56), respectively. The set of equations represents the energy flow in systems unstable to

MRI. Firstly, the term $2\,\gamma_{\rm MRI} e_{\rm MRI}$ draws energy from the averaged quantities to generate MRI channel flows, increasing the MRI energy. Secondly, the term $2\,\gamma_{\rm PI}\,e_{\rm PI}$ acts as an energy sink for $e_{\rm MRI}$; this energy is transferred in a conservative way to the equation for $e_{\rm PI}$, where it acts as a source. Finally, the quantity $S_{\rm TD}$, representing the turbulent energy dissipation at the end of the Kolgomorov cascade, transfers energy back to the averaged quantities in terms of thermal (internal) energy.

In order to solve Eq. (2.67) one also needs an expression for the turbulent energy density dissipation term, $S_{\rm TD}$. In Section 33 of Landau and Lifshitz 1987 there is an estimate for the energy dissipation rate per unit mass, $\epsilon = S_{\rm TD}/\rho$. It is shown that

$$\epsilon \propto v_\lambda^3/\lambda\,, \tag{2.68}$$

where λ corresponds to the size of the turbulent eddy (the order of magnitude of the distances over which changes in velocity can be appreciated) and v_λ is the speed of the turbulence in spatial scales $\sim \lambda$. In the inertial range of scales (Kolmogorov cascade) the flux of energy to smaller scales should be constant across the range of wave vectors and then ϵ should not depend on λ [Landau and Lifshitz 1987]. Since the turbulence we are now considering is developed by the PI, v_λ could be estimated from $e_{\rm PI}$ as

$$v_\lambda \propto \sqrt{\frac{e_{\rm PI}}{\rho}}\,. \tag{2.69}$$

It is possible to demonstrate that this velocity corresponds to the scale with the largest eddy size fitting within the filter size used to perform the averages. According to Kolgomorov's theory, the kinetic energy spectrum scales as $E(k) \propto \epsilon^{2/3} k^{-5/3}$. If we compute the energy in the inertial range of k fitting within a certain volume (e.g., the volume used to average the MHD equations) we obtain:

$$E_{\rm V} = \int_{k_{\rm min}}^{k_{\rm max}} E(k) dk \propto \int_{k_{\rm min}}^{k_{\rm max}} \epsilon^{2/3} k^{-5/3} dk\,, \tag{2.70}$$

where the integral is computed between $k_{\rm min} = 1/\lambda$ (corresponding to the size of the volume considered, which corresponds to the size λ of the largest eddy fitting the volume) and $k_{\rm max}$ (size of the smallest scale, i.e., the dissipation scale). Since we are considering the case with large Reynolds number, $k_{\rm max} \gg k_{\rm min}$, and the integral results in

$$E_{\rm V} \propto \epsilon^{2/3} k_{\rm min}^{-2/3} = (\epsilon\lambda)^{2/3} \propto v_\lambda^2\,, \tag{2.71}$$

where we have used Eq. (2.68) to express the integral in terms of the velocity.

This means that the bigger scales contribute more to the value of $e_{\rm PI}$, where $e_{\rm PI} = E_{\rm V}/{\rm V}$, and justifies the use of Eq. (2.69). In this case, we interpret that $e_{\rm PI}$ is essentially related to the minimum value between the minimum wavelength of the modes of the MRI and the size of the filter. If all the excited modes of the instability are resolved (i.e., the minimum wavelength of the instability is larger than the filter size), λ will be equal to the size of the filter, Δ_f. However, if the scales of the instability are not resolved, the PI should be described by the scale of the instability, which is $\lambda_{\rm MRI}$. Therefore we assume

$$\lambda = \min[\Delta, \lambda_{\rm MRI}]\,. \tag{2.72}$$

Eqs. (2.68) and (2.69) allow us to give an expression for the energy dissipation rate per unit mass

$$\epsilon \propto \frac{1}{\lambda}\Big(\frac{e_{\rm PI}}{\rho}\Big)^{3/2}\,, \tag{2.73}$$

which can be used to estimate the turbulent energy density dissipation rate

$$S_{\rm TD} = \rho\epsilon = C\frac{e_{\rm PI}^{3/2}}{\sqrt{\rho}\lambda}\,, \tag{2.74}$$

where C is a dimensionless constant.

The interpretation of this constant C can be understood by studying Eq. (2.67) at the saturation point $t_{\rm sat}$, i.e. when $\partial_t e_{\rm PI} = 0$. At this maximum, the right-hand side of Eq. (2.67) vanishes and it is possible to compute the ratio of PI to MRI energy

$$\frac{e_{\rm PI}(t_{\rm sat})}{e_{\rm MRI}(t_{\rm sat})} = \frac{8\sigma^2}{C^2}\lambda^2 k_{\rm MRI}^2 = \frac{8\sigma^2}{C^2}\frac{\Omega^2\lambda^2\rho}{\overline{B}_z^2}\left(q - \frac{q^2}{4}\right). \tag{2.75}$$

Therefore, the value of C is directly related to the ratio of PI to MRI energy in the saturated state.

2.4 Results

2.4.1 Box simulations

We test the different sub-grid models discussed in the previous sections using a subset of the three-dimensional, semi-global MRI simulations of Rembiasz et al. 2016b. The simulation domain is a section of a cylindrical annulus with a size of 1 km × 4 km × 1 km in the radial direction, ϕ (i.e., rotational direction), and z direction, respectively. The five models we use are summarised in Table 2.1 and they correspond to simulations with different grid resolutions

NAME	$\overline{B}_{0z}$ [10^{13} G]	Resolution ($r \times \phi \times z$)	Box size [km]	$\lambda_{\rm MRI}$ [km]	Zones per channel
MRI-L1	4.6	$60 \times 240 \times 60$	$1 \times 4 \times 1$	0.333	20
MRI-M1	4.6	$76 \times 304 \times 76$	$1 \times 4 \times 1$	0.333	25
MRI-H1	4.6	$100 \times 400 \times 100$	$1 \times 4 \times 1$	0.333	33
MRI-H2	3.45	$100 \times 400 \times 100$	$1 \times 4 \times 1$	0.25	25
MRI-H3	2.76	$100 \times 400 \times 100$	$1 \times 4 \times 1$	0.2	20

Table 2.1 This table reports the different MRI simulations from Rembiasz et al. [2016b] used to test the sub-grid models discussed in this work. The simulations differ in the numerical resolution and in the initial magnetic-field strength. Note that $\lambda_{\rm MRI}$ is not uniform throughout the computational domain, but varies by $\approx 20\%$.

and initial magnetic-field strength. The dynamics of the plasma is governed by the Newtonian visco-resistive MHD equations and the simulations were performed using the Aenus code [Obergaulinger 2008]. While the resistivity and the shear and bulk viscosities of the simulations are non-zero, they are sufficiently small so as not to affect the growth rates of the MRI and the KHI, the latter acting as the PI terminating the growth of the MRI. Therefore, all the three sub-grid models described in Section 2.3 can in principle be used with these simulations.

The total pressure consists of a polytropic part and a thermal part [Dimmelmeier 2001], $P = P_{\rm p} + P_{\rm th}$, where $P_{\rm p}$ reproduces the pressure exerted by a degenerate electron gas while $P_{\rm th}$ models a finite-temperature correction. The total pressure is

$$P = P_{\rm p} + P_{\rm th} = K\rho^{\gamma} + (\gamma_{\rm th} - 1)\rho\Big(\varepsilon - \rho^{\gamma-1}\frac{K}{\gamma - 1}\Big)\,, \tag{2.76}$$

where ε is the specific internal energy, $K = 4.8974894 \times 10^{14}$ (in cgs units), $\gamma = 1.31$ and $\gamma_{\rm th} = 1.5$. This is a good representation of the EOS at the sub-nuclear densities considered in the simulations.

The initial conditions for the simulations approximate the equatorial layer of an MRI-unstable surface layer of a PNS, which are similar to the postmerger configuration of a BNS merger. We use a differential rotation profile $\Omega(r) \propto r^{-q}$ (see Eq. (2.32)), with $\Omega_0 = 1824$ s^{-1}, a characteristic radius (center of the box) $r_0 = 15.5$ km and a rotational shear $q = 1.25$. The structure of the layer was chosen such as to maintain hydrostatic equilibrium, i.e., balance between the gravitational force of the star, the gas pressure, and the centrifugal force, and marginal convective stability, i.e., a flat pseudo-entropy ($s = P/P_{\rm p}$) profile. This results in a central density of $\rho_0 = 1.83 \times 10^{-15}$, that corresponds to 2.47×10^{13} g cm^{-3}, typical of the regions developing MRI in PNSs and BNS mergers [Rembiasz et al. 2016b]. The initial magnetic field has only a uniform vertical component B_{0z}. Compared to the internal or rotational energy of the

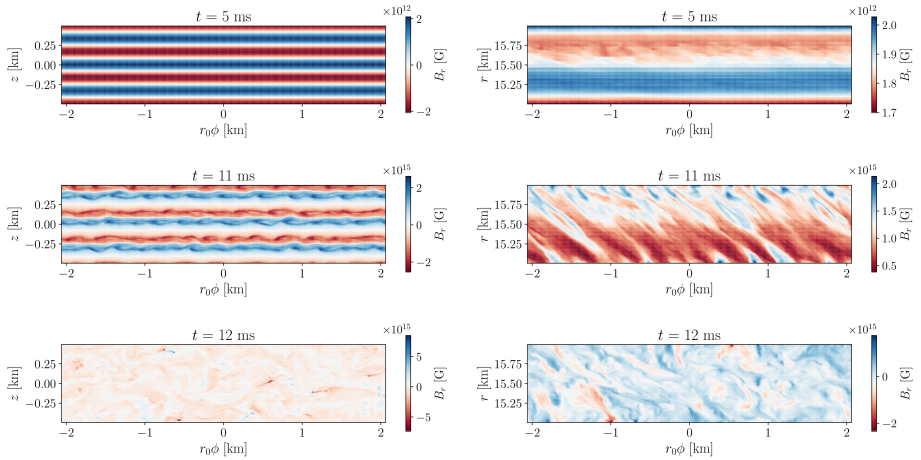

Figure 2.2 Cuts of the radial component of the magnetic field for the simulation MRI-H1, at the $z\phi$ plane (left column) and at the $r\phi$ plane (right column). The rows show different times of the simulation, $t = \{5, 11, 12\}$ ms. The MRI sets in from a layered distribution of B_r ($t = 5$ ms), grows exponentially ($t = 11$ ms) until it saturates and reaches an isotropic and turbulent configuration ($t = 12$ ms).

gas, the magnetic field is weak. In all 5 models, the most unstable MRI channel modes have a wavelength of $\lambda_{\rm MRI} \leq 0.333\,{\rm km}$. This scale is resolved by at least 20 grid cells, which means that the MRI growth rate is numerically close to convergence [see Rembiasz et al. 2016c].

2.4.1.1 *Global quantities.*

The onset, growth and termination of the MRI can be observed by monitoring the evolution of different quantities. Fig. 2.2 displays cuts on the $z\phi$ plane (left) and on the $r\phi$ plane (right) of the radial component of the magnetic field, B_r, for the simulation MRI-H1 at three different times. Shortly after the start of the simulation (5 ms, upper panels) channel modes appear triggered by the applied initial perturbations and the magnetic field exponentially grows from 10^{12} G to 10^{15} G (middle panels), point at which parasitic KH instabilities start to be visible. Eventually the field saturates and a turbulent configuration is reached after $t \approx 12$ ms (bottom panels). The upper right panel of Fig. 2.2 shows that the magnetic field (and similarly all other variables) is not completely smooth in the radial direction. As mentioned before, this is an artefact of the boundary conditions discussed in Rembiasz et al. 2016a. The artefact is related to the use of the so-called shearing disc boundary condition in the radial direction; this approximate treatment of the radial boundaries is necessary because there is

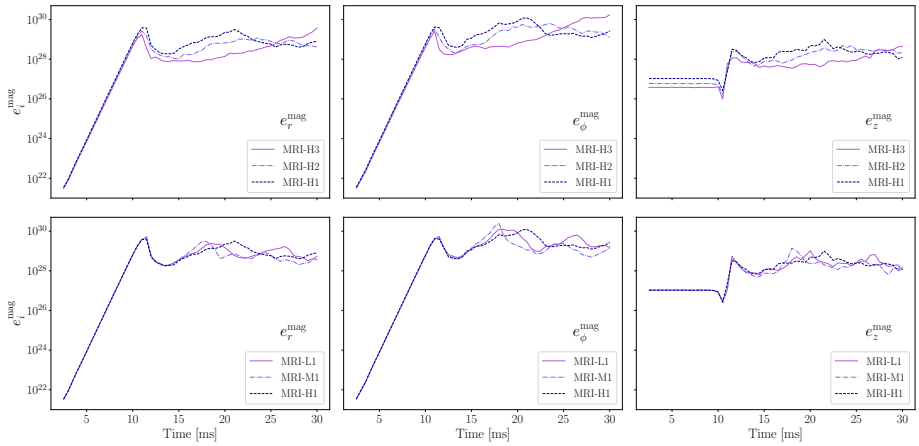

Figure 2.3 Time evolution of the averaged magnetic energy density components, radial (left), azimuthal (centre), and vertical (right), in cgs units. The top panels correspond to simulations with the same resolution but different initial magnetic field strength. The bottom panels depict results for different resolutions but the same value of the initial magnetic field (cf. Table 2.1).

radial dependence of background quantities that does not allow for the use of periodic-like (shearing box) conditions. This limits our ability to compute $e_{\rm PI}$ from the simulation which, in turn, affects the computation of the coefficients for the MInIT sub-grid model (see discussion in Sections 2.3.3.2, 2.4.4.2 and 2.4.4.3).

Fig. 2.3 shows the time evolution of the contribution of each component to the total averaged magnetic energy density

$$\overline{e}_i^{\rm mag} = \frac{\overline{B_i^2}}{2}\,, \tag{2.77}$$

for different resolutions and initial magnetic fields. No important differences are found between the simulations. All cases plotted show that the MRI grows at the same rate and saturates at roughly the same level. Moreover, the amplification of the magnetic field is similar for the three components of the magnetic field. Note that the growth of the vertical component, shown in the right column of the figure, is shorter because the initial magnetic field points in this direction.

Furthermore, Fig. 2.4 shows the time evolution of the contribution of each component to the total averaged kinetic energy for the same simulations shown in Fig. 2.3. The expression for each component is

$$\overline{e}_i^{\rm kin} = \frac{1}{2}\overline{\rho v_i^2}\,. \tag{2.78}$$

The only non-vanishing component of the initial velocity field is the azimuthal one. This component remains nearly constant during the whole simulation

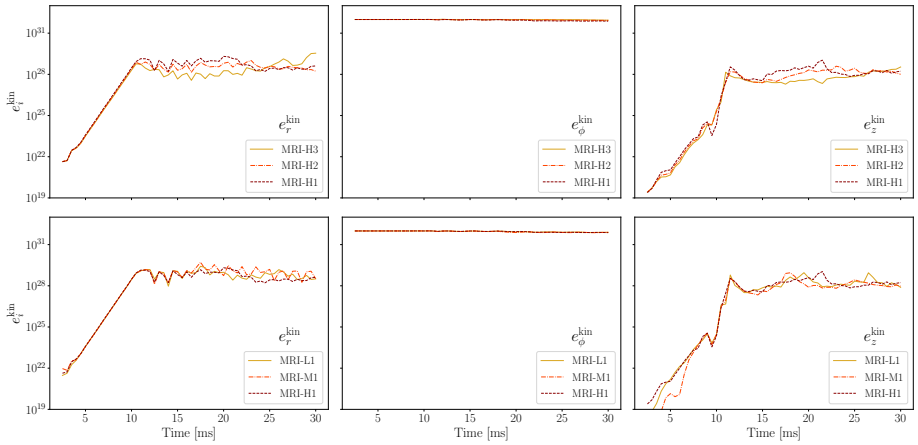

Figure 2.4 Time evolution of the averaged kinetic energy density components, in cgs units. As in Fig. 2.3, we display from left to right the radial, azimuthal and vertical components. Again, the top panels correspond to simulations with different initial magnetic field strength and the bottom panels to simulations with different grid resolution.

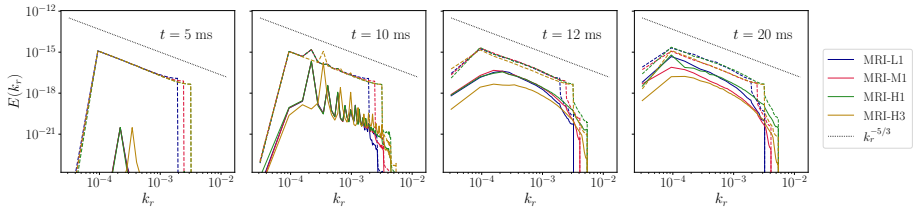

Figure 2.5 Spectra of the magnetic (solid lines) and kinetic (dashed lines) energies for different MRI simulations. As time increases, the magnetic energy tends to even the kinetic energy, specially at smaller scales, where equipartition is reached after $t \approx 12$ ms.

(middle panel) whereas the radial and vertical components grow exponentially until they saturate again at $t \approx 12$ ms. No remarkable differences are found among the 5 simulations.

A way to see how the magnetic field is amplified during the MRI is via the energy spectra. This is shown in Fig. 2.5 at three representative times. Equipartition between kinetic and magnetic energies is reached faster at smaller scales (higher k). Towards the end of the simulations, at $t \approx 20$ ms, the two energies tend towards equipartition at all scales. The simulation with higher resolution, MRI-H1, reaches equipartition at small scales earlier than the rest, while the simulation with the smallest initial magnetic field, MRI-H3, is the slowest to reach a high value of the magnetic field at large scales.

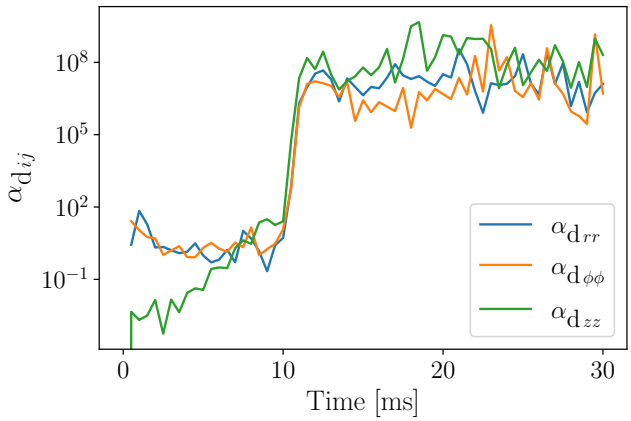

Figure 2.6 Time evolution of the diagonal components of the α-dynamo coefficient, computed from simulation MRI-H1. After an exponential growth, all components reach a similar value at saturation.

2.4.2 **Determination of the α-dynamo coefficient**

Our numerical simulations can also be employed to obtain the dynamo coefficients α_{d} and β_{d}. Here we use Eq. (2.20) to compute α_{d} assuming that this coefficient is constant inside the simulation box (remember the discussion in Section 2.3.1 to neglect the computation of β_{d}). In Fig. 2.6 we show the time evolution of the α_{d} coefficient, computed as the average over the azimuthal direction and evaluated at the center of the rz plane. There is an initial stage at which all diagonal components are nearly constant, except for $\alpha_{\mathrm{d}\,zz}$, which starts at a much lower initial value. At $t \approx 10$ ms, all components grow exponentially for a short time. This is followed by a saturation phase where all components reach a similar and almost constant level. This result supports the use of the α_{d} coefficient as a scalar. However, setting a constant value for this coefficient *at all times* of a simulation could lead to wrong results, specially during the phase in which the exponential growth occurs. This is the reason why we search for a sub-grid model able to deal with temporal evolutions and capture all different stages of the development of turbulence.

2.4.3 **Averaging procedure**

One important aspect to test the different sub-grid models is to have a proper definition of what we mean by average, a procedure that is performed using a filter. There are different filters that can be used to obtain the mean component of a turbulent field. For example, Carrasco, Viganò, and Palenzuela 2020 present

the Gaussian filter, which is used in the formal development of the gradient model. It has nice mathematical properties, but it is not used in the a-priori tests. Alternatively, in the a-priori comparison the authors perform an average over S_f^3 cells, using the so-called box filter. In this work we also use a box filter. Each filter size is labelled by the quantity $S_f = \Delta_f/\Delta$, where Δ is the size of the cell of the direct numerical simulation and Δ_f is the filter size. In the case of the box filter, Δ_f corresponds to the size of the box, which contains S_f cells per dimension. Thus, a filtered quantity is the mean value in a domain with size Δ_f for each direction. Note that even though our simulations used cylindrical coordinates, the filtering operation will be performed over a domain with equal length per dimension, since we need a unique value for the filter size, Δ_f. In fact, in our case the cell size Δ is different for each direction, namely $\Delta r = \Delta z \neq r\Delta\phi$, and therefore the filter size will also be different for each direction, Δ_f^i, giving the same value of S_f in the three directions.

The box filter is characterised by the following normalized kernel [Carrasco, Viganò, and Palenzuela 2020]:

$$F_i(|r_i - r_i'|) = \begin{cases} 1/\Delta_f & \text{if } |r_i - r_i'| \leq \Delta_f^i/2\,, \\ 0 & \text{if } |r_i - r_i'| > \Delta_f^i/2\,, \end{cases} \tag{2.79}$$

for each dimension. The three-dimensional kernel will be

$$F(|\boldsymbol{r} - \boldsymbol{r}'|) = \prod_i^3 F_i(|r_i - r_i'|)\,. \tag{2.80}$$

As mentioned before, our simulations use cylindrical coordinates (r, ϕ, z) and therefore Δ is different for each side of a numerical cell. However, this is not an issue for the box filter where the filter has the same shape as the grid cell Δ. In fact, box-filtered data can be regarded as data from a simulation with lower resolution, i.e., using effectively bigger cells than the actual ones in the simulation.

2.4.4 **Numerical implementation and calibration of the MInIT model**

2.4.4.1 *Energy density evolution equations in the MInIT model*

In order to apply the MInIT model one has to integrate numerically Eqs. (2.66) and (2.67) in time, starting with appropriate initial values at $t = 0$, $e_{\mathrm{MRI}}(0)$ and $e_{\mathrm{PI}}(0)$ (initial conditions are discussed in Section 2.4.4.3). For the box simulation considered in this work, the average velocity $\overline{\boldsymbol{v}}$ only has non-zero ϕ component. In principle, the advective term in the ϕ direction should therefore be considered. However, since the simulation has periodic boundary conditions in

the ϕ direction, any spatial average over the whole simulation box (or involving averages over ϕ) will be independent of whether this advection was actually performed or not. Even if we use a filter of size Δ_f, the result will be independent of this advection term, at least in a statistical sense, as long as we construct the final quantities as averages of filtered quantities at different places in the whole box. Therefore, we will not consider the advection term for the calibration and tests performed in this work.

The second consideration is the calculation of the coefficients in the right-hand side of Eqs. (2.66) and (2.67). Those coefficients depend on the mean quantities ρ, $\overline{B}$ and $\overline{v}$, the latter through the values of Ω and q. There are small differences in the values of these quantities across the box, and even within the filter region.

Finally, we need a numerical procedure to integrate numerically Eqs. (2.66) and (2.67). This system of partial differential equations is in general stiff because it involves the exponential and super-exponential growth of the quantities. Therefore, care has to be taken in the time integration. We use the *Strang splitting* method [Strang 1968] to solve them.

Given the initial conditions of the box simulation, which provide the average values of ρ, $\overline{B}$ and $\overline{v}$, and all calibrated coefficients of the MInIT model (see next two sections), the integration of the equations directly provide a model for the whole simulation, as long as the average values do not change, which is approximately true in our box simulations. The result the model yields can then be compared with that from the numerical simulation to assess its accuracy.

2.4.4.2 *Calibration of the PI coefficients of the MInIT model*

The free coefficients $\alpha_{ij}^{\rm PI}$, $\beta_{ij}^{\rm PI}$ and $\gamma_{ij}^{\rm PI}$ appearing in the closure relations of the MInIT model can be computed from Eqs. (2.63) by averaging the stresses in space and time over the whole box of the simulation and a representative simulation time. In order to avoid initial transients that appear in some tensor components during the growth phase (an artefact of the boundary conditions discussed in Rembiasz et al. 2016a) we only average at times after saturation ($t \gtrsim 12$ ms). The main problem at early times is that $e_{\rm PI}$ has a small value and any small boundary effect produces a large uncertainty in its estimation, introducing a large error in the coefficients. After saturation $e_{\rm PI}$ becomes comparable to $e_{\rm MRI}$ and the small boundary errors become negligible.

The estimated values of the coefficients that we obtain are reported in Table 2.2. We find that the diagonal components of $\alpha_{ij}^{\rm PI}$ and $\beta_{ij}^{\rm PI}$ are all positive, with $\alpha_{rr}^{\rm PI}$ and $\beta_{\rm rr}$ being compatible with zero. The $r\phi$ component for both

Table 2.2 Numerical estimation of the PI coefficients of the closure relations of the MInIT model. The uncertainties (standard deviation) arise from both the time and the spatial averages of the stress tensors used to calculate the coefficients. Simulation MRI-H1 was used to compute the coefficients reported here. Statistically similar coefficients were obtained when used other simulations.

	$\alpha_{ij}^{\mathrm{PI}}$	β_{ij}^{PI}	$\gamma_{ij}^{\mathrm{PI}}$
rr	0.5 ± 1.2	0.08 ± 0.55	-
$\phi\phi$	7 ± 3	1.2 ± 0.8	-
zz	0.8 ± 0.4	0.7 ± 0.3	-
$r\phi$	-1.4 ± 1.5	-0.8 ± 0.6	0.10 ± 0.81
rz	0.06 ± 0.34	0.03 ± 0.18	0.02 ± 0.29
ϕz	-0.1 ± 0.4	0.07 ± 0.26	-0.10 ± 0.51

the Maxwell and Reynolds stresses is consistent with a non-zero value, as expected, since it is responsible for the transport of angular momentum in the radial direction. However, the other non-diagonal values are much smaller and consistent with zero. Regarding the assumption of isotropy in the PI, the expectation is to have $\beta_{ii}^{\mathrm{PI}} = 2/3$ and $|\beta_{ij}^{\mathrm{PI}}| \leq 2/3$ for $i \neq j$ (see Section 2.3.3.2). All coefficients estimated are compatible with these predictions within 2-σ uncertainties. We observe significant differences among the values of different off-diagonal terms: while the rz and ϕz components are practically zero, the $r\phi$ is close to the upper limit of 2/3 and negative. This indicates strong anti-correlations between the r and ϕ components of $\boldsymbol{v}'$ and at the same time low correlation with the z component. This is understandable if the PI (of KH type) develops on top of the channel flows, in a vertical plane forming an angle of $\pi/4$ with the radial direction. This breaks the assumption of isotropy in some sense by establishing a preferred direction. However, it does not affect the assumptions in Section 2.3.3.2.

By averaging over the whole box and time (for $t \gtrsim 12$ ms) of the simulation, we are assuming that there are no statistical spatial or temporal variations in the averaging domain and all samples (points and times) are representative of the same quantity we want to measure. In the spatial case, the radial variations of the initial conditions, which are preserved in the averaged quantities during the simulation, are sufficiently small to be neglected. In order to understand the temporal behaviour we show in Figs. 2.7 and 2.8 the diagonal and non-diagonal components of the coefficients, respectively, computed only from spatial averages, as a function of time. The shaded regions in these figures represent the standard deviation that arises from the average in space of the stresses over the whole box. Comparing with the values from Table 2.2, one can see that the change of the

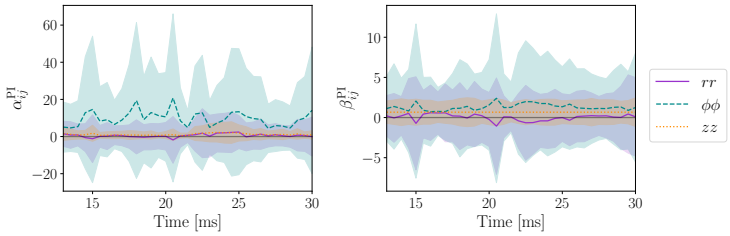

Figure 2.7 Time evolution of the diagonal components of the α^{PI} and β^{PI} coefficients. The shadows represent the standard deviation that arises from the average over the whole simulation box. Note that the values of each component are consistently time-independent.

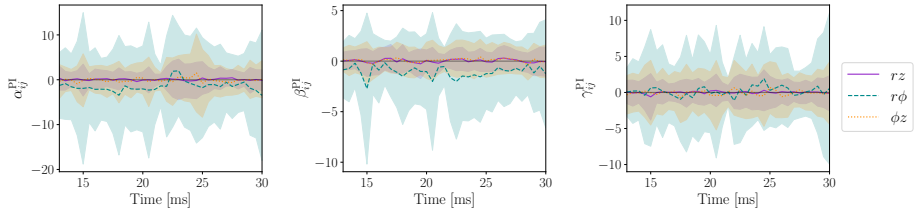

Figure 2.8 Time evolution of the non-diagonal components of the α^{PI}, β^{PI} and γ^{PI} coefficients. As in Fig. 2.7, the shadows represent the standard deviation that arises from the average over the whole simulation.

coefficients is larger in space than in time, since the uncertainty from Table 2.2 is smaller. Indeed, the coefficients oscillate in time around an approximately constant value.

2.4.4.3 *Optimization of the C parameter of the MInIT model*

After fixing the PI coefficients of the closure model, we still have three free parameters that need to be fixed, the dimensionless constant C, Eq. (2.74), and the initial values of the energy densities, $e_{\mathrm{MRI}}(0)$ and $e_{\mathrm{PI}}(0)$. Of these three parameters, only C is truly a free parameter of the MInIT model. The other two depend on the particular physical system. One could in principle take those two values directly from the simulation. However, the boundary-condition errors mentioned in the previous section introduce large uncertainties in $e_{\mathrm{MRI}}(0)$ and $e_{\mathrm{PI}}(0)$, which are in general small quantities. Hence, we keep these two quantities as free parameters to be fitted from the simulation. Instead of $e_{\mathrm{PI}}(0)$, we use the ratio $K_0 = e_{\mathrm{PI}}(0)/e_{\mathrm{MRI}}(0)$ as free parameter. The initial value of e_{MRI} determines the time at which saturation is reached, t_{sat}. The ratio K_0 gives the maximum value of e_{MRI} at $t = t_{\mathrm{sat}}$, and the value of C determines the energy density attained at the saturation regime.

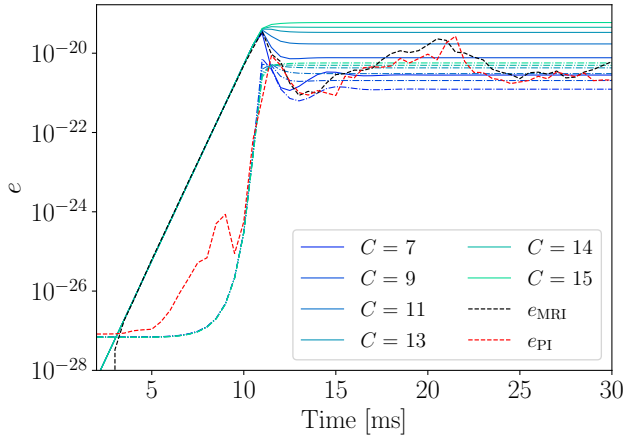

Figure 2.9 Time evolution of $e_{\rm MRI}$ (solid lines) and $e_{\rm PI}$ (dash-dotted lines) using the MInIT model for different values of the free parameter C. The black and red dashed lines show the data from the simulation MRI-H1. We show results only for $K_0 = 1000$ and $e_{\rm MRI}(0) = 7 \times 10^{-31}$ as no significant differences are found for other choices.

In practice, out of the three parameters only C produces changes in the model outcome. We have found that there are no significant changes in the time evolution of $e_{\rm MRI}$ and $e_{\rm PI}$ for values of K_0 and $e_{\rm MRI}(0)$ sampled in the range $K_0 \in [10, 1000]$ and $e_{\rm MRI}(0) \in [2 \times 10^{-31}, 5 \times 10^{-30}]$. Thus, in practice it is sufficient to use sufficiently small values for these initial quantities (e.g. $K_0 = 1000$ and $e_{\rm MRI}(0) = 7 \times 10^{-31}$) since the energy densities grow exponentially and super-exponentially during the development of the instability. Fig. 2.9 shows the evolution of $e_{\rm MRI}$ and $e_{\rm PI}$ for different values of C using the MInIT model. While at saturation $e_{\rm MRI}$ and also $e_{\rm PI}$ do depend on the value of C, there is no such dependence during the growth phase.

Our goal is to find the optimal value of C that minimises the differences between the results of the direct numerical simulation and our model. To estimate these differences we use the L_2 norm (relative error) defined as

$$L_2 = \sqrt{\frac{1}{2}\sum_i (x_{\rm s}^i - x_{\rm m}^i)^2 \left(\frac{1}{\sum_j (x_{\rm s}^j)^2} + \frac{1}{\sum_j (x_{\rm m}^j)^2} \right)}, \tag{2.81}$$

where $x_{\rm s}^i$ are the data from the numerical simulation, and $x_{\rm m}^i$ are the data from the model. To obtain a relative error in Eq. (2.81) we normalise its value to the harmonic mean between the average value of $x_{\rm s}^i$ and $x_{\rm m}^i$. Expressed in this way, L_2 will be large when $x_{\rm s}$ and $x_{\rm m}$ differ considerably (several orders of magnitude) and will be smaller than unity when $x_{\rm s}^i = x_{\rm m}^i + \delta$, with $\delta \ll 1$. Having values

Table 2.3 Optimal values of the parameter C that minimise the L_2-norm of the Maxwell and Reynolds stress tensors. The last column reports the mean values of the two, for different filter sizes.

Optimal values of the C parameter			
	Maxwell	Reynolds	Mean
$S_f = 40$	$8.2^{+0.9}_{-0.9}$	$8.5^{+0.6}_{-0.9}$	$8.3^{+0.7}_{-0.9}$
$S_f = 50$	$8.5^{+0.9}_{-0.6}$	$8.8^{+0.6}_{-0.9}$	$8.6^{+0.7}_{-0.7}$
$S_f = 60$	$8.8^{+0.9}_{-0.6}$	$8.8^{+0.9}_{-0.9}$	$8.8^{+0.9}_{-0.7}$

with the same order of magnitude will give $L_2 \sim 1$. The optimal value of C is obtained by minimizing the relative error from Eq. (2.81) with C as a free parameter, using the stress tensors as our data. The $x^i_{\rm m}$ set is composed by the stress tensors computed with the α, β and γ coefficients and the evolved stress energy densities, $e_{\rm MRI}(t)$ and $e_{\rm PI}(t)$. On the other hand, the $x^i_{\rm s}$ set consists of the stress tensors directly obtained by the filtering of the output of a numerical simulation and the application of Eq. (2.14). Moreover, we only consider the saturation part of the simulation ($t > 12$ ms), which is where parameter C plays an important role (see Fig. 2.9).

In order to have a proper statistical error in the computation of the L_2 norm, we need an ensemble of points on which to compute the norm. A way to obtain reliable results with this procedure is to apply the box filter of Eq. (2.79) over a reasonably large number of grid cells, in our case $10 \times 10 \times 10$ cells located in the center of the box. The filter size must be large enough so that $\Delta_f > \lambda_{\rm MRI}$, where $\lambda_{\rm MRI}$ is the wavelength of the fastest growing mode of the instability. Using a filter smaller than the fastest growing mode would capture different modes which would lead to different values for the growth rates. From Table 2.1 we see that the size of the box is at least 3 times larger than $\lambda_{\rm MRI}$ in the r and z directions and 12 times larger in the angular direction. Depending on the resolution, $\lambda_{\rm MRI}$ will be a certain number of times larger than the size of the computational cell, Δ. In the highest resolution simulation, MRI-H1, $\lambda_{\rm MRI} = 33.3\Delta$. Thus, a filter of size $S_f = \Delta_f/\Delta = 40$ leads to $\Delta_f = 1.2\lambda_{\rm MRI}$. For completeness, we also apply two more box filters with sizes $S_f = 50$ and $S_f = 60$. We do this for all resolutions since all these filter sizes satisfy $\Delta_f > \lambda_{\rm MRI}$. In addition, for the simulations MRI-L1 and MRI-M1 we also use $S_f = 30$. However, for the simulation MRI-L1, $S_f = 60$ yields a filter equal to the size of the box and, thus, this filter is not used for that simulation. Given this, the scales in which the PIs are developed will be represented by $\lambda_{\rm MRI}$ since $\Delta_f > \lambda_{\rm MRI}$, and Eq. (2.74) will have $\lambda = \lambda_{\rm MRI}$.

We calculate the L_2-norm by applying Eq. (2.81) to the modelled and simulation-based stresses. More specifically, we obtain the L_2-norm for each time iteration by making the summation in Eq. (2.81) over the spatial points and all the components of the stresses, in order to give more weight to the larger components, and then we compute the root mean square of the result over time. Table 2.3 reports the values of C that minimise the L_2-norm for the Maxwell and Reynolds stress tensors[4] for different filter sizes, using the highest-resolution simulation, MRI-H1. The upper and lower bounds indicate 10% variations in the minimised L_2-norm. The last column reports the mean value of C. It slightly grows with the size of the filter, but all values fit inside the different confidence intervals. Averaging over the filter sizes, we obtain

$$C_{\rm opt} = 8.6 \pm 0.8\,. \tag{2.82}$$

The same constant is used even when applying the model to other simulations with different resolution.

2.4.5 **Test of the sub-grid models: an a-priori test**

2.4.5.1 *Preliminaries*

After calibrating the coefficients of the MInIT model we turn next to assess the performance of our new sub-grid model compared to the gradient model. This will be done through a so-called a-priori test. This consists in applying a filtering operation (see Section 2.4.3) to data from a numerical simulation and compute from these data the corresponding terms of the sub-grid model to test. This allows for a quantitative comparison with the terms computed by the analytical model, e.g., using Eqs. (2.23) for the gradient model or Eqs. (2.63) for our sub-grid model.

A way to check the goodness of a model is to compute the L_2-norm between the data from the simulation and that from the model (see Eq. (2.81)). We note that Carrasco, Viganò, and Palenzuela 2020 used the so-called Pearson correlation coefficient instead of the L_2-norm as the metric to assess the quality of the gradient sub-grid model. This coefficient, however, turned out not to be suitable for the assessment of our model. While the Pearson coefficient measures the linear correlation between two sets of data, it is not necessary for a model to have a strong linear correlation in order to fit well to data. The goal of the MInIT sub-grid model is not to have tight correlations in the evolution

[4]We do not use the Faraday stress tensor because all its components are much smaller than the ones from the other stresses.

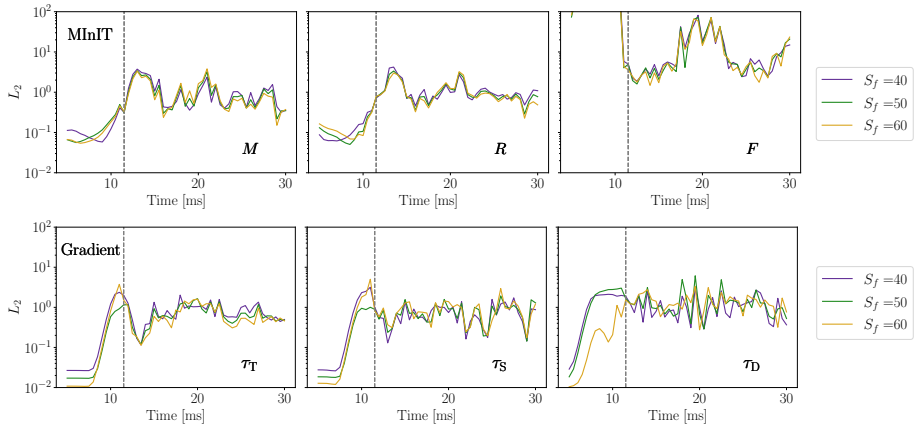

Figure 2.10 Time evolution of the L_2-norm for both the MInIT model (top panels) and the gradient model (bottom panels), using simulation MRI-H1. The vertical dashed lines signal the saturation time of the instability. For the MInIT model, the L_2-norm is below ~ 5 for the Maxwell and Reynolds stress tensors while for the Faraday stress is around 10 after saturation. Similar values are found for the SFS tensors of the gradient model for all cases.

of the different quantities but to provide a representation that is statistically representative of the different quantities on average. For this reason, we resort here to the L_2-norm metric for the model assessment.

2.4.5.2 *A-priori test of the models*

In the a-priori test we compute the L_2-norm of the difference between the numerical data, $x^i_{\rm s}$, and the data obtained with the evolution equations of the model, $x^i_{\rm m}$. This is similar to what we did in Section 2.4.4.3, but now we make use of the whole simulation, i.e., considering the growth phase of the instability as well. As before, we only apply filters with size $\Delta_f > \lambda_{\rm MRI}$ since we are considering the fastest growing mode of the instability. Filter sizes $S_f = 40$, 50 and 60 will be also employed in the test of the gradient model to do a comparison between both models.

Fig. 2.10 shows the values of the L_2-norm for both models before the time-average is performed. The top row corresponds to the MInIT sub-grid model while the bottom row depicts the results of the gradient model. In all the plots in the figure we ignore the first 2 ms of the simulations in order to get rid of initial transients. As the figure shows, the values of the L_2-norm are below ~ 5 at most times and for the two sub-grid models, except for the Faraday stress tensor from the MInIT model which reaches values larger than 10^2 during the initial growth phase. For both models the largest values of the L_2-norm are attained during

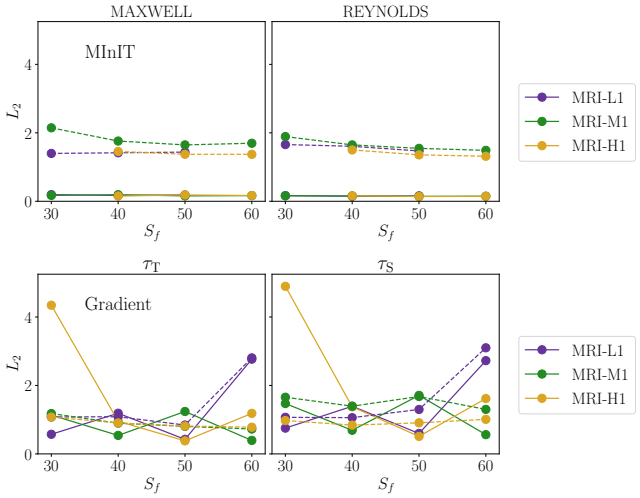

Figure 2.11 L_2-norm of the Maxwell and Reynolds stress tensors of the MInIT model (top row) and of the $\tau_{\rm T}$ and $\tau_{\rm S}$ SFS tensors of the gradient model (bottom row) for different filter sizes, computed over space and time-averaged. Solid (dashed) lines correspond to the initial exponential growth (saturation) of the instability. Colours correspond to simulations with different resolutions, as indicated in the legend.

the saturation phase, as expected. For the MInIT model the coefficients $\alpha^{\rm MRI}$, $\beta^{\rm MRI}$ and $\gamma^{\rm MRI}$ are analytical and match almost perfectly the simulation-based stresses during the exponential growth. In this phase they dominate because $e_{\rm MRI} \gg e_{\rm PI}$. At saturation $e_{\rm PI} \sim e_{\rm MRI}$, and thus the calibrated coefficients $\alpha^{\rm PI}$, $\beta^{\rm PI}$ and $\gamma^{\rm PI}$ also play a role.

In Figs. 2.11 and 2.12 we depict the L_2-norm computed over space and averaged in time by means of the root-mean-square for each filter size. Solid lines correspond to the initial exponential growth of the instability and dashed lines to the saturation phase. As in Fig. 2.10, the top row of both figures depicts the values obtained for the MInIT model and the bottom row those

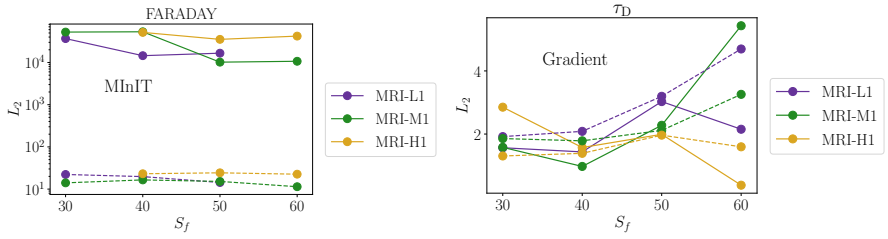

Figure 2.12 As Fig. 2.11 but for the Faraday stress tensor of the MInIT model (top row) and the $\tau_{\rm D}$ SFS tensor of the gradient model (bottom row).

of the gradient model. For the quantities reported in Fig. 2.11 (Maxwell and Reynolds stress tensors and $\tau_{\rm T}$ and $\tau_{\rm S}$ SFS tensors) we find that the values of the L_2-norm are $\mathcal{O}(1)$ for both sub-grid models. This indicates that the two models fit well the data of the simulations, i.e., model and data differ by less than an order of magnitude from each other. In Fig. 2.12 we show the special case of the Faraday stress tensor and its analogue tensor ($\tau_{\rm D}$) computed with the gradient model. The L_2-norm of the Faraday tensor reaches values larger than 10^4 during the growth phase due to the artefacts already discussed in Section 2.3.3.2, since the components of this tensor are exclusively given by $e_{\rm PI}$. After saturation, the L_2-norm of the Faraday stress tensor decreases to values of $\mathcal{O}(10)$. Correspondingly, the values attained by the $\tau_{\rm D}$ SFS tensor of the gradient model are of $\mathcal{O}(1)$.

Figs. 2.11 and 2.12 exhibit that the MInIT model shows almost no dependence on the filter size, for all stress tensors. If anything, the norm is even slightly smaller for larger filters. Moreover, simulations with different resolutions yield almost the same values of the norm. [5] On the other hand, for the gradient model the behaviour of the norm with the filter size is markedly different. In most cases, in particular for low-resolution simulations, the norm of the SFS tensors increases with filter size. This is consistent with the results reported by Carrasco, Viganò, and Palenzuela 2020 who, for the case of the KHI, found a similar behaviour for the Pearson coefficient for different filter sizes.

2.5 Discussion and conclusions

Time-dependent, DNS of astrophysical systems (and in other fields too) have limitations to capture the dynamics at all scales of interest. In particular, the correct description of the development of turbulence at small scales is a challenge for current grid-based simulations which typically suffer from insufficient resolution. Instabilities such as the MRI and the KHI play a major role in the amplification of weak magnetic fields of the postmerger remnant of BNS mergers. Its correct modelling is paramount for reliable estimates of the lifetime of a HMNS and of the multimessenger observational signatures thereof. Linking the results of simulations with the wealth of new data from multimessenger observations of BNS mergers, sGRBs, and kilonovae, is still an ongoing task.

Despite continuous progress in the computational front, with ever more efficient and accurate numerical methods and treatment of physical processes, it is

[5] Simulations with even finer resolutions than the ones employed in this work would be needed to determine whether there could be an actual dependence on resolution.

still not feasible to reproduce all physical effects involved in certain astrophysical scenarios through DNS. An alternative to these computationally expensive simulations are the so-called sub-grid models, which try to deal with the effects of the small scales in terms of the resolved scales, with modest resolution. In this Chapter we have assessed different sub-grid models using three-dimensional box simulations of the MRI [Rembiasz et al. 2016b].

The first model we have tested is the α, β-dynamo model. This is a fairly simple (and limited) model that applies several assumptions to reproduce the dynamo effect arising in the induction equation for the magnetic field. We have found that once the flow is fully turbulent, the different components of the α-dynamo reach a similar constant value. However, setting a constant value for this coefficient throughout the development of turbulence would not work as it would not capture properly the exponential growth of the instability.

The second sub-grid model we have tested is the gradient model. Some recent studies of BNS mergers have implemented this model [e.g. Palenzuela et al. 2022] with promising outcomes – the turbulent amplification of the magnetic field obtained with the model is similar to that obtained with DNS using twice the resolution. The gradient sub-grid model is simulation agnostic as no physical or phenomenological assumption is made since its closure relation to model the sub-filter-scale tensors is based on the Taylor expansion and the inverse function theorem. Thus, this model is universal for any kind of astrophysical scenario, and it is not limited by the physical properties of the problem.

The focus of this Chapter has been to present and assess a new sub-grid model, the MInIT mean-field model. The main appeal of the MInIT model is that it is physically motivated as it is based on the time evolution of the turbulent stress tensors and their relationship with the turbulent energy density of the MRI and of the PIs. By considering a simple linear dependence between the tensors and the energy densities, the model only needs two partial-differential evolution equations for the energies to compute all quantities. These equations take into account the effect of the PIs that saturate the growing turbulence, and also their dissipation at the end of the Kolmogorov cascade, which makes the turbulent stresses to exponentially grow up to a saturation value. The equations also take into account the growth rate of the (fastest growing mode of the) MRI and also of the PI as functions of resolved quantities.

Once the evolution equations are solved, the turbulent stress tensors are obtained by using the constant coefficients that link them to the energy densities. Those are obtained from control numerical simulations and they are found to be almost equal for the range of resolutions and initial magnetic fields considered

in this work. While these coefficients seem therefore universal (at least for simulations of the same type of instability, but see the discussion below) due to the isotropy and homogeneity that arise from the turbulent dynamics, further studies with different initial configurations may be needed to confirm this. We note that, contrary to the gradient sub-grid model, in our new model no spatial derivatives need to be computed and most quantities used in the evolution equation are global parameters of the simulation that we have control on.

The MInIT sub-grid model has been assessed through an a-priori test, i.e., using data from a DNS and applying a filtering operation to compare the filtered data with that given by the model. We have used the L_2-norm (relative error) as our metric to quantify the comparison, obtaining values below ~ 5 for most cases. This means that the data from the simulation and the modelled stresses do not differ more than one order of magnitude. An order-of-magnitude agreement is certainly an achievement for such a simple model and should be sufficient for its use in complex numerical simulations where even larger uncertainties arise from the modelling of many of the physical ingredients (e.g., EOS or neutrino transport). Since the Faraday tensor is in average compatible with zero, the large relative errors observed in the Faraday tensor for the MInIT model should in principle not be a problem for the applicability of the model to global simulations, where its effect on the dynamics would be small. However, given the possible role of the Faraday tensor in the formation of large-scale dynamos, future studies and extensions of the MInIT model could focus on a better description of this component.

Moreover, no dependence on the filter size or the length scale of the unresolved scales has been found, as opposed to the gradient model in which the L_2-norm (slightly) increases with the filter size, particularly for low-resolution simulations. For an ideal sub-grid model, there should not be a dependence on the filter size or on the typical length of sub-grid scales, and it should also properly work in the limit $S_f \to \infty$. This limit represents the case in which the filter is applied to fully resolved simulations, i.e., with "infinite" resolution. We have also observed that the MInIT model behaves consistently for simulations with different resolutions and initial magnetic fields, as those have yielded similar values of the L_2-norm of the stress tensors.

In its comparison with the gradient model, the MInIT model seems to perform with comparable accuracy (except for the Faraday tensor discussed above). This comparison is however unfair and, despite the appearances, different things are being tested and compared. For the case of the MInIT model, the only required information from the simulation is the initial value of the mean quantities, and

from those, the rest of the evolution of predicted. This process mimics the case of its application to global simulations in which the only information known is the average values at grid cells and all the dynamics at sub-grid scales should be modelled. In numerical simulations of the MRI, if the grid cell size is not sufficiently small the instability will not be captured and turbulence will not develop (or will do it at a slower rate). The MInIT model allows us to model MRI in this sub-grid scales and the development of turbulent stresses even if resolution is not sufficient. In opposition, the test for the gradient model uses the time evolution of the average quantities over the filter size (not only the initial values). Since the MRI is well resolved in the simulation, the mean quantities evolve in time and the prediction of the gradient model follows this evolution. If only the initial values were provided to the gradient model, the model would catastrophically fail to predict the growth of the MRI. Somehow, the gradient model needs that the MRI is minimally resolved, and only then is capable of describing the turbulence at even lower scales. Therefore, a better statement for the comparison between both model is that the MInIT model is capable of achieving similar results than the gradient model with less information from the simulation. This may imply that in global simulations the MInIT model may need a lower resolution to achieve the same results that the gradient model. However, this should be tested in the future.

The theoretical framework developed in this work can be applied to different astrophysical systems. Resolving the MRI is a subject of interest across different areas of astrophysics, specially in the modelling of magnetised discs at all scales, e.g., discs around compact objects, protostellar and proto-planetary discs, and those systems could benefit of this model. However, extrapolating the calibrated coefficients obtained in this work to other situations should be handled with care. In particular, our model assumes a regime in which the Reynolds number is large, the magnetic field is not dominant, and turbulence is approximately incompressible. If these conditions are fulfilled, our theoretical arguments suggest that the coefficients could be used outside the range explored here, although proper testing and re-calibration would be encouraged. If some of those conditions do not hold, the coefficients may have different values and/or additional dependencies. Our most immediate aim is to assess the possible universality of the model when applied to a different kind of instability (e.g., the KHI) as well as to further improve the model by a deeper investigation of the relationship between the stress tensors and the turbulent energy densities (see next Chapter).

Applications envisaged include the study of magnetic-field amplification in PNSs following a CCSN and in HMNS resulting from BNS mergers. Sub-grid models as the one reported here can greatly help DNS by properly capturing the magnetic-field amplification at small scales which has potential implications on the lifetime and dynamics of highly magnetised astrophysical compact objects. For this purpose, our MInIT model should be seen as a complex and time-dependent sub-grid model that acts as a closure model. Using this time-dependent closure in combination with an augmented system of MHD equations, similar to the one proposed by Ogilvie 2003, global simulations should be possible in a similar fashion to LES.

CHAPTER 3

Assessment of a new sub-grid model for magnetohydrodynamical turbulence – II. Kelvin–Helmholtz instability

This Chapter was originally published in: **Miquel Miravet-Tenés**, Pablo Cerdá-Durán, Martin Obergaulinger and José A. Font. *Assessment of a new sub-grid model for magnetohydrodynamical turbulence. II. Kelvin–Helmholtz instability. MNRAS*, Volume 527, Issue 1, pp. 1081–1092, October 2023. DOI: 10.1093/mnras/stad3237.

3.1 Introduction

In the previous Chapter I presented a new sub-grid model based on the proportionality relations between the components of the turbulent stress tensors and the evolution of a turbulent kinetic energy density. This new model, dubbed MInIT (for *MHD-instability-induced-turbulence*), is assessed in Chapter 2 in the particular case of the MRI. It is found that MInIT captures the development of turbulent stresses even if the numerical resolution of the MRI simulations is not sufficient. In the current work we continue the study initiated in Chapter 2 by assessing MInIT in the context of the KHI. The results reported in this Chapter indicate that our sub-grid model performs as satisfactorily as its MRI version, yielding order-of-magnitude accurate predictions of the Maxwell and

Reynolds turbulent stresses attained in box numerical simulations of the KHI. Together with the findings of Chapter 2 the present investigation increases our confidence in our new sub-grid model before we develop a GR formulation that can be employed for actual BNS merger simulations, which are envisaged in our short-term plan.

The Chapter is organised as follows: in Section 3.2 we show the basis of the MInIT model applied to the KHI. Next, in Section 3.3 we describe the box numerical simulations of the KHI we use to carry out our testing of the sub-grid model. The results of the various tests are also reported in this section. Finally, our conclusions are summarised in Section 3.4.

3.2 MHD-instability-induced-turbulence (MInIT) mean-field model for KHI

Following Chapter 2 we aim at prescribing an evolution equation for the energy density stored in KHI-induced turbulence, that can be used to estimate the different stresses appearing in the mean-field Eqs. (2.15). The drivers of the KHI are large-scale shears present in the bulk motion of the fluid (in the case of BNS mergers this happens particularly during the merger) that induce a turbulent cascade. The main difference with the MRI is that in that case turbulence is driven by shear flows occurring at small unresolved scales. Therefore, to model the KHI we do not worry about tracking the energy in the shear itself (as we did in Chapter 2) but only in the turbulent part. This results in a model that is somewhat simpler than the MRI model described in Chapter 2.

To build the KHI MInIT model we need three ingredients: the growth rates of the KHI computed in terms of the averaged quantities, an evolution equation for the turbulent energy density, and a closure model to compute the stresses in terms of this energy density. We address these three items next.

3.2.1 KHI growth rates

The growth rate of the KHI in a magnetised fluid was studied by Miura and Pritchett 1982 as a function of the sound Mach number, $M_{\rm s} = v/c_{\rm s}$, the Alfvén Mach number, $M_{\rm A} = v/v_{\rm A}$, and the relative orientation of the velocity and the magnetic field. In the case of a magnetic field parallel to the velocity field, the fastest growing mode appears at the limit of zero magnetic field ($M_{\rm A}^{-1} = 0$). For a flow with $M_{\rm s} = 1$, the fastest growing mode has a wavenumber (parallel to the

velocity) and growth rate

$$k_{\rm KH} \approx 0.4/a_l\,, \qquad \gamma_{\rm KH} \approx 0.14\frac{v}{a_l}\,, \tag{3.1}$$

respectively, where $2v$ here is the variation of the velocity across the shear and a_l is the characteristic scale length of the variation of the velocity in this region. The wavelength of this unstable mode is thus

$$\lambda_{\rm KH} = \frac{2\pi}{k_{\rm KH}} \approx 15.8 a_l. \tag{3.2}$$

For higher magnetic fields both the normalised growth rate ($\gamma_{\rm KH}\frac{a_l}{v}$) and the wavenumber decrease, but as long as the magnetic field is subdominant ($M_{\rm A} > 1$), both quantities do not differ much from the maximum values. The normalised growth rate increases with decreasing sound Mach number $M_{\rm s}$ (about a 20% increase for half the sound Mach number), and increases with increasing Alfvén Mach number $M_{\rm A}$.

As noted by Miura and Pritchett 1982 similar conclusions hold if the magnetic field is transversal to the velocity field. In particular, the growth rates for the transversal case are not larger than for the parallel case when comparing their values for the same Mach numbers. The shape of the shear used for the analysis may also affect the exact values of the growth rates [see Chandrasekhar 1961, for the unmagnetised case] but not their order-of-magnitude. Therefore, for a fluid with a non-dominant magnetic field and $M_{\rm s} \sim 1$ we expect the above numbers to be adequate order-of-magnitude estimates. This is the case for the numerical setup used in the simulations in this work.

3.2.2 **Evolution equation of the KH energy density**

We define the turbulent kinetic energy density in the KHI as

$$e_{\rm KH} = \frac{1}{2}\,\rho \sum_{i=1}^{3} \overline{R}_{ii}\,. \tag{3.3}$$

Following Chapter 2 we can write the evolution equation for this turbulent energy density as

$$\partial_t e_{\rm KH} + \partial_i(\overline{v}_i\, e_{\rm KH}) = S^{\rm (KH)}\,, \tag{3.4}$$

where $S^{\rm (KH)}$ is a source term that acts as a generator and sink of the turbulent energy density. As in our previous work with the MRI, we neglect the stretching terms, which are irrelevant and add unnecessary complication to this work, and would also make the equations non-conservative (see Chapter 2 for more details).

A closed and simple form for the source terms can be justified taking into account some information we derived in the last few subsections, namely: i) the KH channel flows grow exponentially with a growth rate $\gamma_{\rm KH}$ and therefore $e_{\rm KH}$ will grow with $2\gamma_{\rm KH}$; ii) the vortices from the turbulence are broken into smaller ones in a turbulent cascade until dissipation occurs at the physical dissipation scale, where the small scale, kinetic and magnetic energies transform into thermal energy [see, e.g., Landau and Lifshitz 1987, chapter III]. Considering these points, the evolution equation for the KH energy density becomes

$$\partial_t e_{\rm KH} + \partial_i(\overline{v}_i e_{\rm KH}) = 2\,\gamma_{\rm KH}\, e_{\rm KH} - S_{\rm TD}\,, \tag{3.5}$$

where $\gamma_{\rm KH}$ is the growth rate discussed in the previous section. This equation shows the energy flow in a KH-unstable system. The first term in the right-hand side, $2\,\gamma_{\rm KH} e_{\rm KH}$ takes energy from the large-scale quantities, which increases the turbulent energy. The quantity $S_{\rm TD}$ represents the turbulent energy dissipation at the end of the Kolgomorov scale, which dissipates the kinetic (and magnetic) energy into thermal (internal) energy, and is transferred back to the large-scale quantities.

Concerning the Kolgomorov term, we are using the same expression obtained in Chapter 2, which was proposed following the arguments in Section 33 of Landau and Lifshitz 1987, namely

$$S_{\rm TD} = C\frac{e_{\rm KH}^{3/2}}{\sqrt{\rho}\lambda_{\rm KH}}\,, \tag{3.6}$$

where C is a constant that can be calibrated from numerical simulations (see next sections).

In a practical application of the MInIT model one would have a sheared velocity profile that is covered by a number of grid points and one would want to model the sub-grid scale. In practice this means that, depending on the resolution, the KHI could already be partially resolved. However, it is unlikely that the full turbulent cascade is resolved by the simulation, given the extremely large Reynolds numbers of the astrophysical applications considered (e.g., BNS mergers). Therefore, the shear leading to the sub-grid turbulence can be either large-scale shear present in the simulations (e.g., the shear produced at the merger of two NSs), or that generated by eddies of the resolved turbulence of the simulation (e.g., large-scale vortexes produced by KHI in the aforementioned large-scale shear). One characteristic of Kolgomorov-type turbulence, such as the one produced by the KHI (at least in the unmagnetised case) is that the energy flux towards lower scales is constant across wave numbers and proportional to v^3/a_l [Landau and Lifshitz 1987], where v is here the velocity of the vortex

at each scale a_l. One can consider that vortices at each scale break up into smaller-scale vortices due to KHI that arises from the shear produced by those vortices. One can estimate the scaling of the vortex velocity, wavelength, and growth rate of the KHI as

$$v \propto (a_l)^{1/3}\,, \qquad \lambda_{\rm KH} \propto a_l\,, \qquad \gamma_{\rm KH} \propto (a_l)^{-2/3}. \tag{3.7}$$

Since by increasing the grid resolution of the simulation one resolves smaller scales a_l, the KHI at sub-grid scales has larger growth rates but, at the same time, $S_{\rm TD}$ becomes larger as well. The amount of energy density in turbulence in the fully turbulent case can be estimated by making the right-hand side of Eq. (3.5) equal to zero, which implies a zero growth of the instability. This yields an estimated value of

$$e_{\text{ KH, fully turbulent}} \propto (a_l)^{2/3}. \tag{3.8}$$

The implication is that increasing grid resolution leads to a smaller amount of turbulent energy density in the sub-grid model, as one would expect. This scaling relation can be tested in numerical simulations as shown below in Section 3.3.2. We also note, however, that as the resolution is increased the differential equations to be solved become increasingly stiff, from the numerical point of view.

3.2.3 **Closure relation**

The main assumptions of the closure relation used for the MInIT model in Chapter 2 is that the different stress tensors are proportional to the turbulent kinetic energy density and that the proportionality coefficients do not depend explicitly on time and position, which implies that the stress tensors have the same time dependence as $e_{\rm KH}$. The closure relation between the turbulent energy density, $e_{\rm KH}$ and the stresses is the following:

$$\overline{M}_{ij}(t,\boldsymbol{r}) = \alpha_{ij}^{\rm KH}\, e_{\rm KH}(t,\boldsymbol{r})\,, \tag{3.9a}$$

$$\overline{R}_{ij}(t,\boldsymbol{r}) = \frac{1}{\overline{\rho}(t,\boldsymbol{r})}\beta_{ij}^{\rm KH}\, e_{\rm KH}(t,\boldsymbol{r})\,, \tag{3.9b}$$

$$\overline{F}_{ij}(t,\boldsymbol{r}) = \frac{\gamma_{ij}^{\rm KH}}{\sqrt{\overline{\rho}(t,\mathbf{r})}} e_{\rm KH}(t,\boldsymbol{r})\,, \tag{3.9c}$$

where the factors involving the mass density in the last two equations are added in order to make the coefficients dimensionless. These coefficients are calibrated using numerical simulations and their values are discussed in the next sections.

Table 3.1 List of KHI simulations. The middle column depicts the initial value of the magnetic field for all our KHI box simulations. The number of cells for the low, medium, and high resolution simulations is reported in the last column. The size of each side of the box is $L = 1$ and the characteristic width of the shear layer is $a_l = 0.01$.

NAME	$\overline{B}_{x0}$	$N^3_{\rm cells}$
KH-L1	3×10^{-4}	128^3
KH-L2	1×10^{-3}	128^3
KH-L3	3×10^{-2}	128^3
KH-M1	3×10^{-4}	256^3
KH-M3	3×10^{-2}	256^3
KH-H1	3×10^{-4}	512^3
KH-H2	1×10^{-3}	512^3
KH-H3	3×10^{-2}	512^3

3.3 Results

3.3.1 KHI box simulations

To calibrate and test the performance of the model we perform a series of box simulations of the KHI displaying turbulence. We consider a periodic (in all directions) three-dimensional Cartesian box of size L^3, with $L = 1$. The initial fields are similar to the ones employed by Carrasco, Viganò, and Palenzuela 2020:

$$\rho = \rho_0 + \rho_1 \tanh\left(\frac{|y| - y_\pm}{a_l}\right), \tag{3.10a}$$

$$v_x = v_{x0}\,\mathrm{sgn}(y)\tanh\left(\frac{|y| - y_\pm}{a_l}\right) + \delta v_x\,, \tag{3.10b}$$

$$v_y = \delta v_y\,\mathrm{sgn}(y)\exp\left\{\frac{(|y| - y_\pm)^2}{\sigma_y^2}\right\}, \tag{3.10c}$$

$$v_z = v_{z0}\,\mathrm{sgn}(y)\exp\left\{\frac{(|y| - y_\pm)^2}{\sigma_z^2}\right\} + \delta v_z\,, \tag{3.10d}$$

$$B_x = \overline{B}_{x0}, \quad B_y = 0, \quad B_z = 0\,, \tag{3.10e}$$

$$p = p_0\,. \tag{3.10f}$$

These initial conditions describe two shear layers located at $y = y_\pm$. The values considered in our simulations are $y_\pm = \pm 0.25$, $\rho_0 = 1.5$, $\rho_1 = 0.5$, $v_{x0} = v_{z0} = 0.5$, $p_0 = 1$ and $a_l = 0.01$, where a_l is the characteristic width of the shear layer. The parameters $\sigma_y^2 = 0.01$ and $\sigma_z^2 = 0.1$ are the scale of the initial velocity perturbation in the y-direction and the profile of v_z, respectively. The value

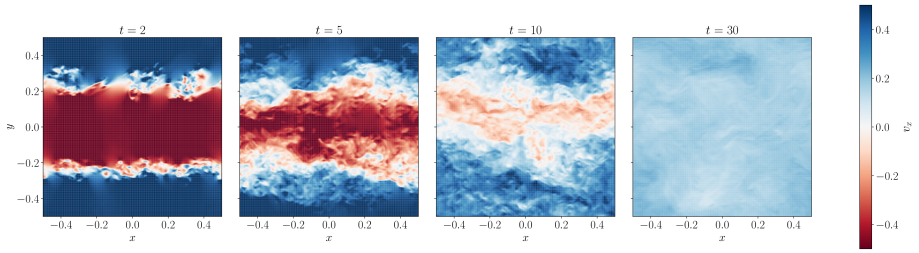

Figure 3.1 Slices of the x-component of the velocity field at the xy-plane for the simulation KH-M1. The panels show different times of the simulation, $t = \{2, 5, 10, 30\}$. The KHI sets in from a shear layer configuration and reaches an isotropic and turbulent configuration at late times ($t = 30$).

of $\overline{B}_{x0}$ is a free parameter that we change for the different simulations. The specific values are reported in Table 3.1. The sound Mach number, $M_s = v_0/c_s$, is fixed to unity in all the simulations. The initial data are perturbed by seeding small random perturbations in velocity, δv_i, with amplitudes of 10^{-3}. We note that this is different to the sinusoidal perturbations used in Carrasco, Viganò, and Palenzuela 2020. We consider an ideal gas EOS,

$$p = (\Gamma - 1)\rho\epsilon\,, \tag{3.11}$$

with $\Gamma = 4/3$.

We evolve these initial conditions using the Aenus code [Obergaulinger 2008] which solves the ideal MHD equations in its conservative form using finite-volume methods. All the simulations were performed using the Harten-Lax-van Leer (HLL) flux formula [Harten, Lax, and Leer 1983], a monotonicity-preserving (MP) reconstruction of 5^{th} order and a 3^{rd} order Runge-Kutta time integrator [Shu and Osher 1988].

The general qualitative behaviour of the simulations can be seen in Figure 3.1. This figure displays a selection of slices in the xy plane of the x-component of the velocity field, v_x, for the simulation KH-M1 at four different times. At the beginning of the simulation there are two shear layers which separate regions with $v_x \approx \pm 0.5$. Once the instability sets in, vortices develop on these shears and a turbulent isotropic state is reached. The process progressively smooths and finally erases the initial shear by transporting linear momentum in the y direction. Figure 3.2 shows similar slices at the same snapshots but for the y-component of the velocity. It is apparent that at early times v_y is characterised by localised perturbations that later merge into a more extended region from $t = 5$ onwards.

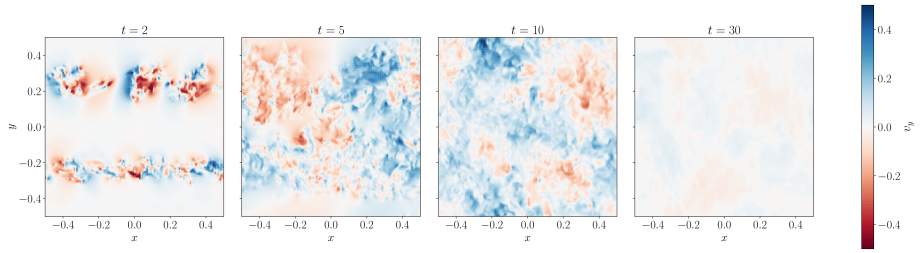

Figure 3.2 Slices of the y-component of the velocity field at the xy-plane for the simulation KH-M1. From left to right the selected times correspond to $t = \{2, 5, 10, 30\}$.

Figure 3.3 shows the time evolution of the contribution of each magnetic-field component to the total averaged magnetic energy density

$$\overline{e}_i^{\mathrm{mag}} = \frac{\overline{B_i^2}}{2}\,, \tag{3.12}$$

for different grid resolutions and initial magnetic field strength $\overline{B}_{x0}$. The saturation level of the turbulent magnetic field depends on the two of them. At low resolution (128^3 cells, blue curves) we find a monotonic increase with the initial field strength (the three values used for the field strength can be distinguished by a different type of line, as indicated in the caption). Keeping the initial field fixed, the energy of the final turbulent field increases when doubling the resolution to the intermediate grid of 256^3 cells. A subsequent twofold increase of the resolution to the finest grid of 512^3 cells, however, does not change the results by the same degree. Therefore, at this resolution, we approach a state in which the differences between weak and strong initial fields are small. For the case of model KH-H3, with the largest initial magnetic field of the models surveyed, $\overline{B}_{x0} = 3 \times 10^{-2}$, the saturated magnetic energy in the x-direction is more than an order of magnitude larger than the energy of the rest of the simulations, with lower initial magnetic fields.

Correspondingly, Figure 3.4 shows the time evolution of the contribution of each component of the kinetic energy to the total averaged value of this quantity for the same simulations shown in Fig. 3.3. The expression for each component is

$$\overline{e}_i^{\mathrm{kin}} = \frac{1}{2}\overline{\rho v_i^2}\,. \tag{3.13}$$

Leaving aside the small effect introduced by the initial random perturbations, the only non-vanishing components of the initial velocity field are v_x and v_z (left and right panels, respectively). These components remain nearly constant during the evolutions (and so do e_x^{kin} and e_z^{kin}). However, the e_y^{kin} component

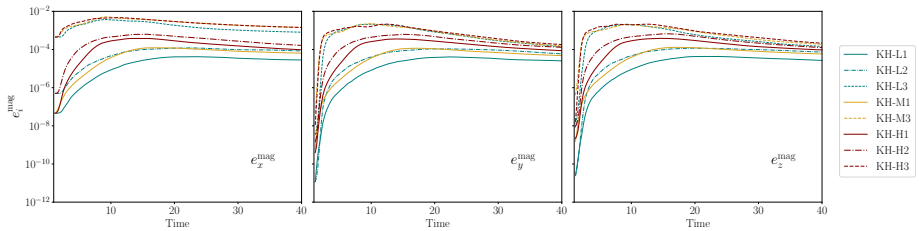

Figure 3.3 Time evolution of the x, y, and z components of the averaged magnetic energy density. Curves with different colors correspond to different grid resolutions, as indicated by the legend on the right (see also Table 3.1). Solid, dash-dotted, and dashed lines correspond to $\overline{B}_{x0} = 3 \times 10^{-4}$, 1×10^{-3} and 3×10^{-2}, respectively.

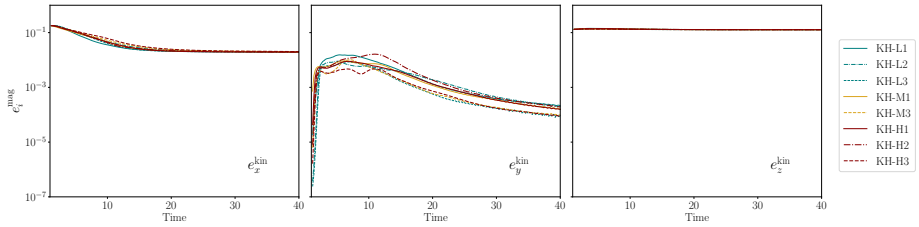

Figure 3.4 Time evolution of the x, y, and z components of the averaged kinetic energy density. As in Fig. 3.3, the colors represent different gird resolutions and the various line styles correspond to different initial magnetic field strengths B_{x0}.

(middle panel) grows exponentially during the early phase of the evolution to saturate and then slowly decrease. No constant state has yet been reached by the end of our simulations. This behaviour of e_y^{kin} is due to the transport of linear momentum across the shear in the y direction. This leads to the mixing of the positive and negative parts of the velocity field which results in the decrease of the velocity components shown in Fig. 3.2, while conserving the initially (almost) zero linear momentum. No remarkable qualitative differences are found among the simulations. It is worth stressing that the y-component of the kinetic energy achieves a lower value for stronger initial magnetic fields, regardless of the resolution.

In Figure 3.5 we depict five snapshots of the evolution of the kinetic energy spectra for different grid resolutions. The spectra were calculated in the same way as in Simon, Hawley, and Beckwith 2009. One can see that the inertial range of the spatial scales, parallel to the Kolmogorov slope $\propto k^{-5/3}$ (dashed line), goes from scales smaller than the characteristic scale of the initial shear (vertical line) to scales at which there is dissipation into internal energy. The red shaded region represents the interval of scales for which we employ box filters

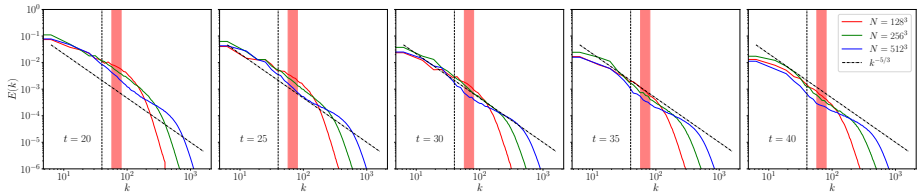

Figure 3.5 Snapshots of the kinetic energy spectra for different gird resolutions (corresponding to models KH-L1, KH-M1, and KH-H1 in Table 3.1). The dashed line corresponds to the Kolgomorov slope $k^{-5/3}$. The red shaded region shows the range in which box filters are applied. All of them are located inside the inertial range of spatial scales. The vertical black line refers to the wavenumber of the initial shear, $k_{\rm KH}$.

(see below), ensuring that we are inside the inertial range. As expected, as the grid resolution increases, the dissipation scales become smaller.

3.3.2 **Averaging procedure**

Our aim is to compare the numerical box simulations with the MInIT model in order to calibrate its free coefficients. In this procedure the KHI box simulations play the role of the true solution of the ideal MHD equations (although it should always be kept in mind that the accuracy of the numerical solution does depend on the finite numerical resolution and on the order of the numerical method). Using the true solution we perform averages over a certain length scale in order to achieve a separation between the large-scale (averaged) features and the small (turbulent) scales that we want to test with MInIT. Given that the result of the simulation does not depend on the sub-grid model itself, this procedure provides an a-priori test of the model. On the other hand, a-posteriori tests would involve performing the simulations with the MInIT model coupled to the dynamics. Those go beyond the scope of the current Chapter and will be presented elsewhere.

The averaging procedure that we use consists in a box filter, identical to the one we employed in Chapter 2. We perform the average over S_f^3 cells, where $S_f = \Delta_f/\Delta$ labels each filter size, Δ is the size of the cell of the DNS, and Δ_f is the filter size. Note that Δ_f is related to the scale λ defined in Section 2.2. Following Carrasco, Viganò, and Palenzuela [2020] we characterise the box filter with the following normalised kernel,

$$F_i(|r_i - r_i'|) = \begin{cases} 1/\Delta_f & \text{if } |r_i - r_i'| \leq \Delta_f^i/2\,, \\ 0 & \text{if } |r_i - r_i'| > \Delta_f^i/2\,, \end{cases} \tag{3.14}$$

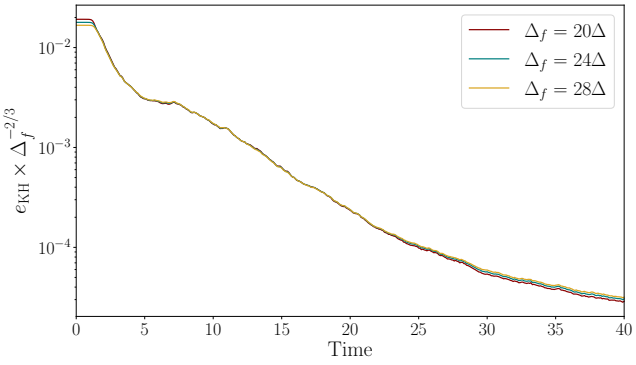

Figure 3.6 Time evolution of the quantity $e_{\rm KH}\Delta_f^{-2/3}$ for the simulation KH-M1 and for different averaging lengths Δ_f.

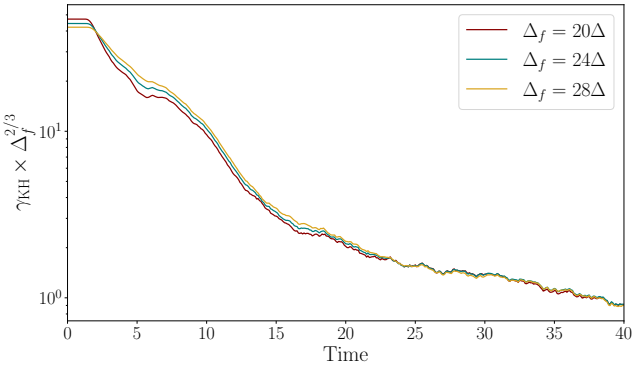

Figure 3.7 Same as Fig. 3.6 but for the quantity $\gamma_{\rm KH}\Delta_f^{2/3}$.

for each dimension i. The three-dimensional kernel is thus

$$F(|\boldsymbol{r} - \boldsymbol{r}'|) = \prod_i^3 F_i(|r_i - r_i'|)\,. \tag{3.15}$$

As a first application of this filter we test the validity of Eq. (3.8) that predicts that the kinetic energy density in the sub-grid scales for fully developed turbulence depends on the filter size Δ_f. Figure 3.6 shows the evolution of $e_{\rm KH}\Delta_f^{-2/3}$ during the entire evolution of simulation KH-M1 for three filter sizes. We observe that this quantity is almost independent of Δ_f, even at early times. At late times ($t \gtrsim 20$) small deviations become more visible. Those could be related to the fact that, since the turbulent cascade is not fully resolved down to the dissipation scale, the smallest scale is only a factor ~ 10 smaller than the averaging scale. Therefore, the assumption that there is a large separation

of scales, used in the derivation of Eq. (3.8), starts being compromised. This results in a small deficit in the turbulent energy density due to the unresolved scales. In addition, in Figure 3.7 we depict the evolution of $\gamma_{\rm KH}\Delta_f^{2/3}$ for the same resolution and filter sizes. According to Eq. (3.7) this quantity should also be independent of the filter size. As the figure shows, during the turbulent phase of the simulation ($t \gtrsim 20$) the scaling holds precisely.

3.3.3 Numerical implementation and calibration of the MInIT model

3.3.3.1 *Energy density evolution equations in the MInIT model*

In order to apply the MInIT model one has to integrate numerically Eqs. (3.5) in time, starting with appropriate initial values at $t = 0$, $e_{\rm KH}(0)$. Those initial conditions are discussed in Section 3.3.3.3 below. For our KHI simulations the average velocity $\overline{\boldsymbol{v}}$ is almost zero for the x component, since both signs cancel out when averaging over the entire box (and taking both sides of the shear layers). Likewise, the averaged component in the y direction is also zero since we only consider random perturbations for this component. The only non-zero component will be $\overline{v}_z$, and we should therefore consider the advective term in this direction. However, since the simulations have periodic boundary conditions in the z direction, any spatial average along this direction will be independent of the advection. Therefore, for the same reason as in Chapter 2, we can safely neglect the advection term for the tests in this work.

We perform our analysis in points centered at the shear layers of the initial conditions, $y_\pm = \pm 0.25$, points where we compute all averaged quantities. Performing the analysis in multiple points in the xz-plane (and different times) allow us to build more statistics for our results. Additionally, we compute auxiliary averages centered in $y_\pm \pm \Delta_f$, that allow us to evaluate y derivatives at the shear. These different averages mimic the coarse numerical cells that one would have in simulations using the sub-grid model. They are used to compute the quantities needed in the model, in particular the growth rate and the KHI length scale needed for the turbulent source term given by Eq. (3.6).

For the growth rate of the turbulent energy density, $\gamma_{\rm KH}$, we assume the values discussed in Section 3.2.1 obtained from Miura and Pritchett 1982 (see Eq. (3.1)). To evaluate this rate we need information from the simulation about the value of the velocity jump of the shear and of the characteristic length scale a_l. Those values are known for the initial conditions, but they are significantly modified as the simulation proceeds. Hence, a way of evaluating the rate is to substitute the term v/a_l by $\partial_y v_x$ in Eq. (3.1). Note that for the initial data this

yields exactly $\partial_y v_x = v_{x0}/a_l$. Numerically, the partial derivative is evaluated using centered finite differences to the coarse grid cells defined above,

$$\gamma^{\rm num}_{{\rm KH},\pm} \approx A_\gamma \partial_y v_x \approx A_\gamma \frac{\bar{v}_y(y_\pm + \Delta_f) - \bar{v}_y(y_\pm - \Delta_f)}{2\Delta_f}\,, \tag{3.16}$$

and then averaged for different points in the xz plane and over the $\pm$ shears to obtain a single value of $\gamma_{\rm KH}$. Note that instead of using the same numerical constant as in Eq. (3.1) we use a generic constant A_γ. This constant should be close to 0.14 according to Miura and Pritchett 1982 but, since it may depend on the exact conditions at the shear (see Section 3.2.1), we leave it free at first; its value is discussed in the next sections.

Regarding the Kolgomorov term from Eq. (3.5), the wavelength of the instability is discussed in Section 3.2.1 following the work of Miura and Pritchett 1982 (see Eq. (3.2)), and is proportional to the shear length scale a_l. Since we only want to model shears at the lower possible scale (see discussion in Section 3.2.2) we assimilate the value of a_l in the estimation of $\lambda_{\rm KH}$ to simply Δ_f. Therefore, in practice Eq. (3.2) is evaluated as

$$\lambda_{\rm KH} \approx 15.8\Delta_f\,. \tag{3.17}$$

Finally, we use the *Strang splitting* method [Strang 1968] to solve Eq. (3.5), since this partial differential equation is generally stiff, due to the exponential growth of the quantities.

3.3.3.2 *Calibration of the coefficients of the model*

We compute the coefficients $\alpha^{\rm KH}_{ij}$, $\beta^{\rm KH}_{ij}$ and $\gamma^{\rm KH}_{ij}$ that appear in Eqs. (3.9) similarly as it was done in Chapter 2, where the stress tensors were obtained by averaging over the whole box and over a representative time of the simulation. In the KHI case we perform averages over smaller boxes, with size similar to the wavelength of the unstable mode (Eq. (3.2)), since we assume that we are able to resolve this initial fastest growing mode. After that, we obtain a single value of the coefficients by averaging over all the boxes of size $\approx \lambda_{\rm KH}$. One of the assumptions of the MInIT model is the proportionality between the different stresses and $e_{\rm KH}$ (see Section 3.2.3), which also implies a proportionality among the different stresses themselves. Fig. 3.8 shows that this proportionality is actually only achieved at later times in the simulation, when turbulence is fully developed. For early times the components of the Reynolds stress that involve v_x start from large values and do not have an exponential growth, due to the fact that this component represents the shear that is decreasing with time. Therefore,

Table 3.2 Time average of the coefficients of the closure equations of our model, Eqs. (3.9). The uncertainty arises from both the time average of the coefficients themselves and the spatial average of the stress tensors used to calculate the coefficients.

	$\alpha_{ij}^{\rm KH}$	$\beta_{ij}^{\rm KH}$	$\gamma_{ij}^{\rm KH}$
xx	0.7 ± 0.3	0.74 ± 0.05	-
yy	0.64 ± 0.18	0.64 ± 0.03	-
zz	0.64 ± 0.19	0.61 ± 0.04	-
xy	-0.01 ± 0.03	-0.01 ± 0.03	-0.010 ± 0.017
xz	-0.02 ± 0.03	-0.041 ± 0.035	-0.01 ± 0.03
yz	-0.026 ± 0.025	-0.02 ± 0.03	-0.008 ± 0.015

we will only consider late simulation times ($t > 20$) for our calculations. This might be regarded as a limitation of the model. However, this drawback only affects during very short transients, since the exponential growth happens on a very short timescale compared to the duration of the simulation.

The estimated values of the coefficients that we obtain are reported in Table 3.2. These values are the average of those corresponding to simulations KH-H1 and KH-H2. The initial magnetic field strength of the run KH-H3 is so large that the magnetic energy dominates over the kinetic energy, and the results differ considerably from the other two cases. We believe that this is not the regime we are interested in, in the context of BNS mergers, since magnetic fields are small (10^{10} - 10^{12} G) when the merger occurs [Lorimer 2008]. Therefore, we compute the coefficients using only the simulations with lower initial magnetic field. We find that the diagonal components of $\alpha_{ij}^{\rm KH}$ and $\beta_{ij}^{\rm KH}$ are all positive. All non-diagonal components of the stresses are much smaller than the diagonal ones, and most of them are also compatible with zero.

By averaging over space and time (for $t \gtrsim 20$), we are assuming that there are no statistical spatial or temporal variations in the averaging domain and all samples (points and times) are representative of the same quantity we want to measure. We depict the temporal behaviour of the coefficients in Figs. 3.9 and 3.10 for the diagonal and non-diagonal components of the coefficients, respectively, computed only from spatial averages. The shaded regions in both figures represent the standard deviation from the spatial average of the stress tensors. The coefficients almost do not change in time (except $\alpha_{ij}^{\rm KH}$), and the uncertainty comes from their spatial variability. The diagonal $\alpha_{ij}^{\rm KH}$ coefficients have larger uncertainties due to their increase in time (see Fig. 3.9). This increase is due to the fact that the turbulence is decaying (and the turbulent kinetic energy goes down) while the turbulent magnetic energy slowly increases up to equipartition with the kinetic component.

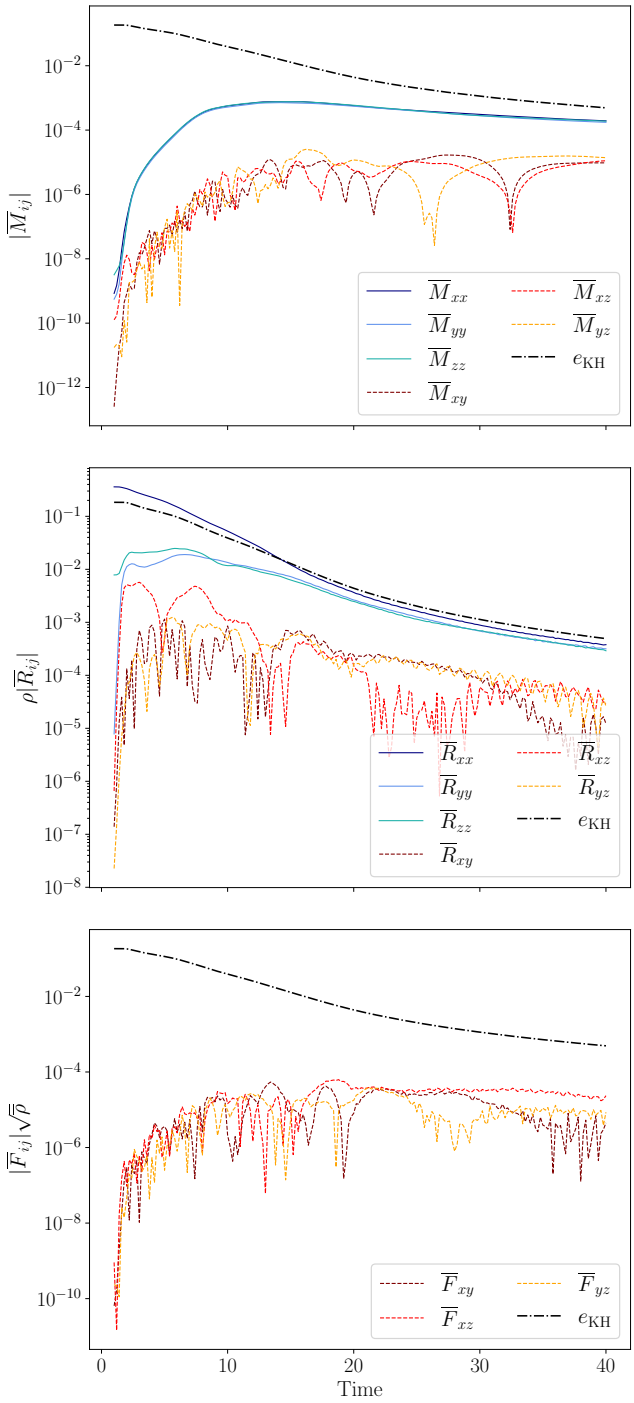

Figure 3.8 Time evolution of the components of the Maxwell (top), Reynolds (middle) and Faraday (bottom) stress tensors for the simulation KH-H1. The Reynolds and the Faraday stress tensors include factors with the mass density to have the same dimensions that e_{KH}.

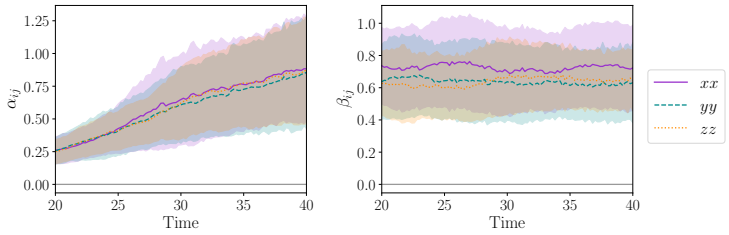

Figure 3.9 Time evolution of the diagonal components of the α^{KH} and β^{KH} coefficients from simulation KH-H1. The shadows represent the standard deviation that arises from the average over the whole simulation box. Note that the values of each component are consistently time-independent when considering late times.

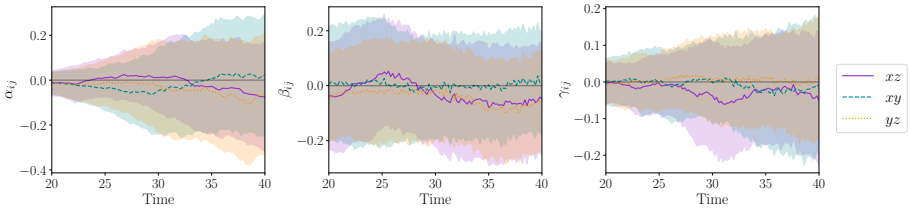

Figure 3.10 Time evolution of the non-diagonal components of the α^{KH}, β^{KH} and γ^{KH} coefficients. As in Fig. 3.9, the shadows represent the standard deviation that arises from the average over the whole simulation.

3.3.3.3 *Optimisation of the C and A_γ parameters of the model*

After the values of the coefficients of the closure relations have been obtained we still need to fix the values of two additional free parameters: the dimensionless constant C from Eq. (3.6) and the factor A_γ from Eq. (3.16). From Eq. (3.1) we already know that we can estimate $A_\gamma = 0.14$. However, before adopting this particular value, we explore the dependence of our results with other possible values for this constant. To do so we compare in Fig. 3.11 the time evolution of e_{KH} as computed directly from the simulation KH-H1 with its value computed

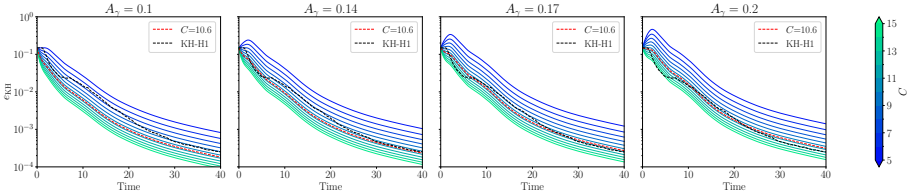

Figure 3.11 Time evolution of e_{KH} (solid lines) using the MInIT model for different values of constants C and A_γ. The black dashed line shows the data from the simulation KH-H1 and the red dashed line highlights the case with the optimal value for C.

Table 3.3 Optimal values of the parameter C that minimise the L_2-norm of the Maxwell and Reynolds stress tensors for different filter sizes. The last column reports the mean values of the two.

Optimal values of the C parameter			
	KH-H1	KH-H2	MEAN
$S_f = 40$	9.3 ± 1.5	8.3 ± 1.5	8.8 ± 1.5
$S_f = 48$	10.7 ± 1.5	9.3 ± 1.5	10.0 ± 1.5
$S_f = 56$	11.7 ± 1.5	10.3 ± 1.5	11.0 ± 1.5

from the MInIT model for different values of C and A_γ. Our goal is to find the optimal values of these two constants matching the evolution given by the simulation. Fig. 3.11 shows that for a wide range of values of A_γ it is always possible to find a value of C that yields an evolution of $e_{\rm KH}$ close to the simulation values. Therefore, given the weak dependence of the results with A_γ we fix it to the value discussed in Section 3.2.1, i.e. $A_\gamma = 0.14$ and proceed with the optimization for C alone.

To optimise the value of C, we minimise the differences between the results from the DNS and our model. These differences are estimated using the L_2 (relative error) norm,

$$L_2 = \sqrt{\frac{1}{2}\sum_i (x^i_{\rm s} - x^i_{\rm m})^2 \left(\frac{1}{\sum_j (x^j_{\rm s})^2} + \frac{1}{\sum_j (x^j_{\rm m})^2} \right)}, \tag{3.18}$$

where $x^i_{\rm s}$ are the data from the numerical simulation, and $x^i_{\rm m}$ are the data from the model. As in Chapter 2 we sum over all spatial values and components of the Maxwell and Reynolds stress tensors for each time iteration, and then we compute the root mean square over time to obtain a single value. We do not consider the Faraday stress tensor components because their values are considerably lower than those of the other stresses. The resulting optimal value is:

$$C_{\rm opt} = 10.6 \pm 1.5\,. \tag{3.19}$$

The upper and lower bounds indicate 10% variations of the minimised L_2-norm. It is worth noting that this value is fully compatible with the one we obtained for the MRI case in Chapter 2. Our final single value of $C_{\rm opt}$ has been obtained after averaging over different filter sizes using both the KH-H1 and KH-H2 simulations. For the same reason of Section 3.3.3.2 the simulation KH-H3 was discarded in the calibration of C. The filter sizes used span from $\Delta_f = 40\Delta$ to $\Delta_f = 70\Delta$, an interval which is inside the inertial range of scales. Table 3.3 reports the optimal values of C for different filter sizes. The sizes

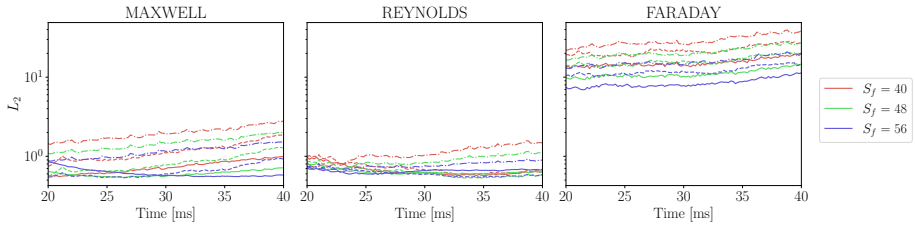

Figure 3.12 A-priori test of the MInIT model: time evolution of the L_2-norm of the Maxwell (left), Reynolds (middle), and Faraday (right) stresses. The norm represents the difference between the quantities computed from the model and the ones from the output of the simulations, as shown in Eq. (3.18). We use data from simulations KH-H1 (solid lines), KH-H2 (dashed lines) and KH-H3 (dash-dotted lines). The L_2-norm is ~ 1 for the Maxwell and Reynolds stress tensors while it is ~ 10 for the Faraday tensor.

that we use are also valid for the simulations with lower resolution, since they correspond to scales inside the inertial range in these cases too.

3.3.4 **An a-priori test of the model**

To close our investigation we next present an a-priori test of our MInIT model for the KHI, paralleling what we did in Chapter 2 for the MRI. To do so we compute the L_2-norm of the difference between the numerical data, $x^i_{\rm s}$, and the data obtained with the evolution equations of the model, $x^i_{\rm m}$, using the optimised coefficients. Figure 3.12 shows the time evolution of the norm for the three stress tensors and different filter sizes, for the simulations with the highest resolutions.

In the cases with the lowest initial magnetic fields (simulations KH-H1 and KH-H2) the L_2-norm of the Maxwell and Reynolds stresses lays below ~ 1 for all filters and at all times. For the highest magnetic field simulation (KH-H3) the norm is slightly above 1 for the Maxwell stress, but still around 1 for the Reynolds stress. This result implies that the model is able to give an order-of-magnitude estimate of the evolution of the Reynolds and Maxwell stresses. However, the norm for the Faraday tensor is higher, around 10, for the same reason it also was in the MRI case. The discrepancy is higher for the Faraday tensor simply because the time and spatial averages of the proportionality coefficients render difficult to capture the variability and the change of sign of this tensor components. All in all, the comparison of this a-priori test with our previous results for the MRI are consistent and promising. In our former work, the values we obtained for the L_2 norm of the Maxwell and Reynolds stresses were also ~ 1 for both the MInIT model and the gradient sub-grid model, and around 10 for the Faraday tensor at late times.

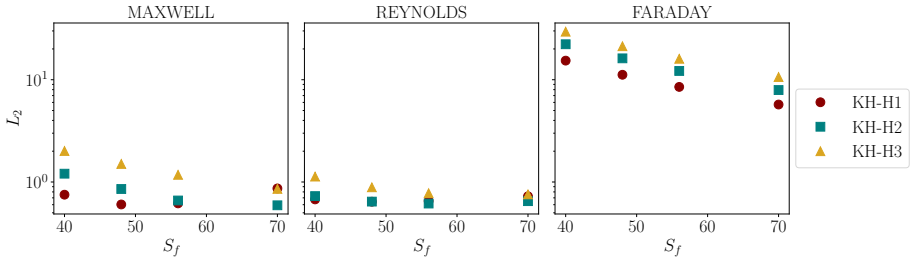

Figure 3.13 L_2-norm of the Maxwell (left), Reynolds (middle) and Faraday (right) stress tensors of the MInIT model for different filter sizes, computed over space and time-averaged. Again, the norm represents the difference between our model and the output of the simulations, as shown in Eq. (3.18). Colours correspond to simulations with different initial magnetic field, as indicated in the legend.

Finally, we depict in Figure 3.13 the dependence of the model performance on the filter size, by computing the root mean square of the L_2-norm over time. As we found for the MRI, the norm is almost independent of the size of the filter. Moreover, it attains slightly lower values for larger filter sizes. We added here a larger filter size, $S_f = 70$, that corresponds to the inertial range of scales for the simulations with the highest resolution (KH-H1, KH-H2 and KH-H3).

3.4 Discussion and conclusions

There are many examples of astrophysical systems for which the proper numerical modelling of their dynamics is severely hampered by insufficient computational resolution. A particularly good example is that of fluids at high Reynolds number where the available resolution of grid-based codes for direct numerical simulations is usually inadequate to capture the physics at all scales. Relativistic astrophysical systems such as BNS mergers or CCSNe may therefore be affected by a deficient modelling when attempting to numerically resolve the amplification of magnetic fields or the transition to fully fledged turbulence from the growth of dynamical instabilities at small scales. However, being able to resolve the KHI and the MRI is essential for a faithful representation of the postmerger evolution of the remnant in BNS mergers.

Notwithstanding the significant progress achieved through DNS, it is still not possible to capture all the (extreme) physics characteristic of those astrophysical systems. An alternative to performing costly high-resolution simulations are subgrid models that attempt to express the effects of the turbulent scales in terms of resolved quantities. Several of those models have been recently implemented in numerical simulations of BNS mergers, such as the α-viscosity and the gradient

models [Giacomazzo et al. 2015, Shibata, Kiuchi, and Sekiguchi 2017, Shibata, Fujibayashi, and Sekiguchi 2021, Viganò, Aguilera-Miret, and Palenzuela 2019, Carrasco, Viganò, and Palenzuela 2020, Viganò et al. 2020, Palenzuela et al. 2022, Aguilera-Miret, Viganò, and Palenzuela 2022].

In this Chapter we have presented an extension of our new sub-grid model MInIT, an MHD-instability-induced-turbulence mean-field model we first proposed in Chapter 2. In our previous investigation we assessed MInIT in the context of the modelling of turbulence generated by the MRI. In the present work we have focused on evaluating MInIT for resolving KHI-induced turbulence. The main appeal of our model is that it is physically motivated, being based on the estimation of the turbulent stress tensors through the modelling of the temporal evolution of a turbulent energy density of the instability. The model consists in evolution equations for the turbulent energy densities plus a closure relation that allows computing all turbulent stresses as proportional to those energy densities. Moreover, it takes into account the fastest growing mode of the instability and the dissipation of the energy at the end of the Kolmogorov cascade. While in our previous work on the MRI MInIT required two evolution equations, one for the MRI and a second one for the turbulence itself (the PIs), for the modelling of the KHI only one evolution equation has been needed.

The MInIT model depends on several coefficients and constants that must be calibrated. This has been done using numerical box simulations of the KHI in which part of the turbulent cascade is resolved and convergence is achieved, at least in the main global features. We have observed that the calibration of the constants does not depend strongly on the numerical resolution used in the simulations or on the initial value of the seed magnetic field, as long as it is weak. For high magnetic fields, however, some deviations have been found.

We have assessed the performance of the MInIT model for the KHI in the same way we previously did for the MRI in Chapter 2, i.e., via an a-priori test. We have used data from DNS and applied a box filter to see the difference between the quantities given by the model and the filtered ones. To do so, the L_2 relative error norm was used to quantitatively compare with the numerical data. We have found that the values of the L_2 norm lay below ~ 1 for the Maxwell and Reynolds stresses. Therefore, we are able to obtain order-of-magnitude accurate estimates of these stresses with our model. In comparison with the MRI version, the MInIT model for the KHI performs slightly better, since the data from the simulation and the modelled stresses have been found to differ less. More precisely, the discrepancy is less than an order of magnitude, which is an achievement worth mentioning given the simplicity of the model.

For the Faraday stress tensor the results are worse; the typical values of the L_2 relative error are around 10 at most. This could be explained by the fact that the model coefficients we found for the Faraday tensor components are actually compatible with zero (a similar result was obtained in Chapter 2 for the MRI). This means that our model is compatible with setting the Faraday stress to zero. However, in reality the Faraday tensor components should probably have some small (but non-zero) value. Its magnitude is actually relevant since it impacts the ability of the model to develop large-scale turbulent dynamos that may operate in BNS mergers and magnetar formation.

In order to obtain more accurate measurements of the Faraday stress one should build more statistics. Increasing the computational time of the simulations might help to some extent. However, since our simulations are effectively ones of decaying turbulence, their time extension is limited by nature. Alternatively, one could explore the case of driven turbulence which shares some similarities with the box simulations displayed in this work. In this case, the sustained nature of the turbulence would allow for longer simulations and build more statistics.

Furthermore, we have also found that our sub-grid model shows no strong dependence on the filter size S_f. This is something to keep in mind, since an ideal sub-grid model should work properly in the limit $S_f \to \infty$. Simulations with different initial magnetic field amplitudes (always in the regime of weak amplitude) yield similar values of the L_2-norm, which is reassuring.

Together with the version of MInIT developed for the MRI in Chapter 2, the sub-grid model presented in this work could eventually be applied to different astrophysical systems, in particular in the study of the dynamics of the merger and postmerger phases in BNS coalescences. The early phase of the merger, when both NSs make contact, is characterised by the excitation of the KHI, which can lead to a substantial amplification of the magnetic field of the system, provided turbulence is properly captured. This is something we plan to investigate with the model put forward in this Chapter. However, before doing that some extra work should be carried out in the present version of the model. In particular, we plan to relax some implicit assumptions of the model, such as considering weak magnetic field seeds or large Reynolds numbers. Our future goals are the generalisation of MInIT to account for a wider range of physical conditions and its implementation in numerical simulations using a GR framework. The generalisation to curved spacetimes will require the inclusion of metric-dependent terms in the right-hand side of equations for the unresolved turbulent energy densities as well as for the large-scale fluid and magnetic field. The additional terms do not change the basic character of the hyperbolic system and can be

treated using standard techniques for dealing with local source terms in GRMHD. The details of such an implementation will be addressed in future work.

CHAPTER 4

Effective angular momentum transport in differentially rotating neutron stars

4.1 Introduction

As previously discussed in the Introduction (Section 1.3), the MRI is the responsible mechanism for angular momentum transport in differentially rotating NSs and accretion discs. In Section 1.2 (and references therein) we have seen that differential rotation in HMNS remnants provides the centrifugal support needed against gravity to delay the collapse to a BH. However, weak magnetic fields, together with a negative gradient of the angular frequency, trigger the MRI. Channel modes develop in the vertical direction and grow exponentially, generating turbulence and changing the dynamics of the bulk flow. One important consequence is the effective angular momentum transport in the remnant star. The damping of the differential rotation reduces the support against gravity and triggers the collapse of the star. Therefore, the lifetime and stability of HMNS remnants strongly depend on the development of MHD instabilities such as the MRI, which lead to viscous turbulent dissipation. It is also worth mentioning that the stability of PNSs, which also exhibit rapid differential rotation at birth, can be also influenced by the development of the MRI.

In spite of the enormous efforts made by the NR community to produce accurate simulations of astrophysical scenarios such as BNS mergers and CCSNe, the big amount of physics involved makes it very challenging. One key issue is capturing small-scale turbulence, as mentioned in Section 1.3 (and references

therein). The prohibitive spatial resolution required to resolve all the scales involved prevents simulations from properly describing the turbulence triggered by MHD instabilities. As an alternative, LES are starting to be used in simulations of BNS and NSBH mergers (see Section 1.2). This approach aims to model, with the application of a sub-grid closure, the small-scale turbulence in terms of resolved quantities. More precisely, this approach aims to provide a closure for the turbulent stress tensors, which appear in the nonlinear mean-field MHD equations.

In Chapters 2 and 3, I have presented a new sub-grid model for MHD turbulence triggered by the MRI (Chapter 2) and the KHI (Chapter 3), which are the dominant MHD instabilities in BNS mergers. The model, named MInIT, is based on evolution equations for the turbulent kinetic energy densities. These equations are built using phenomenological arguments that are physically motivated. The turbulent densities are connected to the stress tensors through certain calibrated coefficients. After performing an a-priori test of the model, numerical simulations of differentially rotating NSs prone to the MRI are carried out in this Chapter. As we will show below, by including the corresponding stresses in the momentum equation and inserting the evolution equations for the MRI and PI energies in the numerical code, effective angular momentum transport arises in simulations which lack enough resolution to solve the MRI.

This Chapter is organised as follows: in Section 4.2, I present the mean-field MHD equations with the inclusion of the turbulent stresses. The numerical methodology is discussed in Section 4.3 and the results are showcased in Section 4.4. Finally, conclusions are drawn in Section 4.5. Unless otherwise stated, cgs units are employed. Latin indices run from 1 to 3.

4.2 Mean-field MHD equations

In Section 2.2 the foundations of mean-field MHD have been already discussed. By taking the Newtonian ideal MHD equations and applying a filtering operation, the equations can be written in terms of mean quantities (resolved scales in numerical simulations) and also of the average of combinations of the fluctuations (unresolved scales). The mean of combinations of two fluctuating variables can be represented by

$$\overline{M}_{ij} = \overline{b'_i b'_j}, \tag{4.1}$$

$$\overline{R}_{ij} = \overline{v'_i v'_j}, \tag{4.2}$$

$$\overline{F}_{ij} = \overline{v'_i b'_j} - \overline{v'_j b'_i}\,, \tag{4.3}$$

which are, respectively, the Maxwell, Reynolds and Faraday turbulent stress tensors, respectively. A sub-grid model provides a closure relation between these quantities and the resolved ones that allows to write the system of equations as a closed system amenable to be solved numerically. The system of equations to be solved is

$$\begin{aligned}
\partial_t \rho + \nabla_j \left[\rho v^j\right] &= 0, && (4.4)\\
\partial_t p^i + \nabla_j \left[p^i v^j + P_\star \delta^{ij} - b^i b^j\right] &= f^i, && (4.5)\\
\partial_t e_\star + \nabla_j \left[(e_\star + P_\star) v^j - b^i v_i b^j\right] &= f^j v_j, && (4.6)\\
\partial_t \vec{b} &= -c\vec{\nabla} \times \vec{E}, && (4.7)\\
\nabla_j b^j &= 0\,, && (4.8)
\end{aligned}$$

where $p^i = \rho v^i$, $P_\star = P_{\rm gas} + b^2/2$, $e_\star = e_{\rm int} + \rho v^2/2 + b^2/2$ and f^i is an external force density. Since the aim of this work is to solely study the angular momentum transport, we focus on the mean-field form of the momentum equation:

$$\partial_t \bar{p}^i + \nabla_j \left[\bar{\rho}\bar{v}^i\bar{v}^j + \bar{P}_\star \delta^{ij} - \bar{b}^i\bar{b}^j + \bar{\rho}\bar{R}^{ij} + {\rm Tr}\{\bar{\boldsymbol{M}}\}\delta^{ij} - \bar{M}^{ij}\right] = \bar{f}^i\,. \qquad (4.9)$$

The Maxwell and Reynold stresses that appear in Eq. (4.9) are modelled with the turbulent kinetic energy densities of the MRI and PI, with evolution equations

$$\begin{aligned}
\partial_t e_{\rm MRI} + \nabla_j(\bar{v}_i e_{\rm MRI}) &= 2\,\gamma_{\rm MRI}\, e_{\rm MRI} - 2\,\gamma_{\rm PI}\, e_{\rm PI} && (4.10)\\
\partial_t e_{\rm PI} + \nabla_j(\bar{v}_i e_{\rm PI}) &= 2\,\gamma_{\rm PI}\, e_{\rm PI} - S_{\rm TD}\,. && (4.11)
\end{aligned}$$

The explicit form of the MRI, $\gamma_{\rm MRI}$, and parasitic, $\gamma_{\rm PI}$, growth rates and the Kolmogorov term, $S_{\rm TD}$, can be found in Eqs. (2.36), (2.56) and (2.74), respectively. The coefficients that link the MRI and parasitic turbulent energies with the stress tensors are presented in Eqs. (2.49)-(2.53) and in Table 2.2, respectively. By applying the closure relation from Eq. (2.63), one can obtain the time evolution of the turbulent stresses.

4.3 Numerical methods

4.3.1 Initial models

The differentially rotating equilibrium models are computed using the Newtonian version of the code described in Dimmelmeier, Font, and Muller 2002, based on Hachisu's self-consistent field method [Komatsu, Eriguchi, and Hachisu 1989].

The rotation law of the equilibrium model is the following:

$$\Omega(\varpi) = \Omega_c \frac{1}{1 + \frac{\varpi^2}{A^2}}\,, \tag{4.12}$$

where $\varpi = r \sin\theta$ is the distance to the rotation axis, A is a positive constant [Komatsu, Eriguchi, and Hachisu 1989] and Ω_c is the value of Ω, the angular frequency, at the coordinate centre. In the limit case where $A \to \infty$, the star becomes a rigid rotator. The initial values of the turbulent energy densities of the MRI and the PI will be a fraction of the total kinetic energy density. Since these energies grow rapidly in time, we set them to be 10^{-12} and 10^{-13} times smaller, respectively. This choice is quite arbitrary, since the saturation amplitude of the MRI is quite insensitive to the amplitude of the seed perturbations, as discussed in Chapter 5.

Regarding the EOS, a polytropic relation between the pressure P and the rest-mass density ρ is employed:

$$P = K\rho^\gamma\,, \tag{4.13}$$

with $\gamma = 2$ and $K = 145529.19$ (in cgs units).

A dipolar magnetic field is implemented as in Suwa et al. 2007, with the following effective vector potential:

$$A_r = A_\theta = 0\,, \tag{4.14}$$

$$A_\phi = \frac{B_0}{2}\frac{r_0^3}{r^3 + r_0^3}\varpi,\,, \tag{4.15}$$

where A_r, A_θ and A_ϕ are the components of the vector potential (in a spherical coordinate system), r is the radial coordinate, and r_0 and B_0, which is the value of the magnetic field at the centre of the star, are model constants.

4.3.2 **Numerical implementation**

The initial conditions are evolved using the Aenus code [Obergaulinger 2008] which solves the ideal MHD equations in its conservative form using finite-volume methods. The simulations are performed using the HLL flux formula [Harten, Lax, and Leer 1983], a Piecewise Parabolic Method (PPM) reconstruction for cell interfaces [Colella and Woodward 1984] and a 3$^{\text{rd}}$ order Runge-Kutta time integrator [Shu and Osher 1988]. For the spatial grid, the code employs spherical polar coordinates (r, θ, ϕ) and axial symmetry with respect to the rotation axis is assumed. The number of grid cells is $(N_r, N_\theta, N_\phi) = (396, 128, 1)$. Since the MInIT coefficients are computed in cylindrical coordinates, a change of basis

from cylindrical to spherical coordinates is required. Furthermore, the angular frequency, Ω, and the shear, q, are computed from the angular velocity, v_ϕ. For the radial direction, boundary conditions that deal with the geometric singularity of the origin, and a constant extrapolation at the outer edge of the grid were employed. Regarding the polar direction, conditions adapted to the polar axis were used, and for the azimuthal direction, periodic boundary conditions were applied.

In order to solve Equations (4.10) and (4.11), the code employs high-resolution shock capturing schemes for the transport of the energies, as done for the other MHD quantities. For the sources, which can have stiff source terms and therefore result in numerical difficulties, an implicit integration with an splitting operator of the hyperbolic terms is employed, similarly to what Just, Obergaulinger, and Janka 2015 did to deal with neutrinos.

4.4 Results

We now discuss the results from the evolution of the differentially rotating NS with and without the implementation of the MInIT model. The initial configuration possesses a central angular frequency with a value $\Omega_c = 2887.9\ \mathrm{s}^{-1}$ and $A = 5$ km. The central rest-mass density is $\rho_c = 7.9 \times 10^{14}\ \mathrm{g/cm^3}$. The NS has a gravitational mass $M_{\mathrm{grav}} = 2.6\ M_\odot$ and an equatorial radius $R_{\mathrm{eq}} = 18.5$ km, corresponding to a HMNS for this choice of EOS. The magnetic dipole is characterised by $B_0 = 7.0 \times 10^{13}$ G and $r_0 = 12$ km. In order to avoid spurious dynamics near the surface of the star, the evolution of the turbulent energy densities is limited to regions with densities above $\rho_{\mathrm{thresh}} = 2.5 \times 10^{14}\ \mathrm{g/cm^3}$, which corresponds to an equatorial radius of about ≈ 14 km. Moreover, the evolutions are performed up to $t = 75$ ms, a plausible timescale for this kind of scenario.

Figure 4.1 depicts the time evolution of the turbulent energy densities averaged over surfaces of different radii. The total kinetic energy density is also added for the sake of comparison, and it is more than 3 orders of magnitude larger than the turbulent energies. In the left panel the average is performed over the whole domain of evolution of the energies (given by ρ_{thresh}), whereas in the right panel the average is carried out over a surface of radius $r = 3.5$ km. Both cases show the same exponential growth of e_{MRI} and the super-exponential increase of e_{PI}, as one would expect from Fig. 2.9. However, turbulence is not self-sustained and decays when considering distances close to the center, where angular momentum transport is more effective. Moreover, the large-scale kinetic

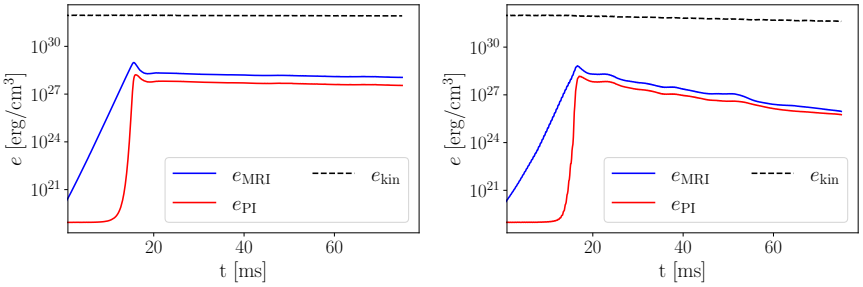

Figure 4.1 Left panel: time evolution of the turbulent energy densities, e_{MRI} (in blue) and e_{PI} (in red), together with the total kinetic energy density (dashed black line), averaged over the surface given by ρ_{thresh}. Right panel: same as the other panel, but the average is carried out over a radius of $r = 3.5$ km, where turbulence eventually starts decaying.

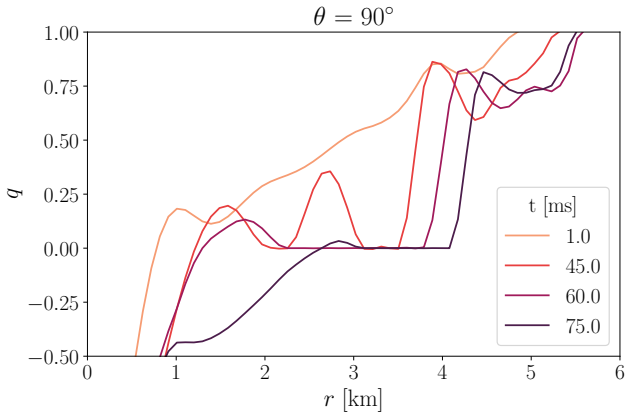

Figure 4.2 Radial profiles of the shear factor at the equator for different times ($t = \{1, 45, 60, 75\}$ ms). Due to angular momentum transport, the degree of differential rotation lessens, leading to $q \to 0$ in this region.

energy density slightly decays as well, since the angular momentum is being transferred to larger distances. This is corroborated with Figure 4.2, where radial profiles of the shear factor q are depicted at different times. The shear factor q reduces to 0, and the positive source term of the evolution equation for the MRI energy density (Eq. (4.10)) vanishes. This results in a gradual decrease of the turbulent energy densities, since the only non-vanishing term in the right-hand side of Eq. (4.10) is negative. This makes that the parasitic energy density decreases as well.

Figure 4.3 shows the radial profiles of the angular frequency Ω at two different angles $\theta = 45°, 90°$ and different times. The dashed curves correspond to a simulation that includes the MInIT model, whereas the solid curves correspond

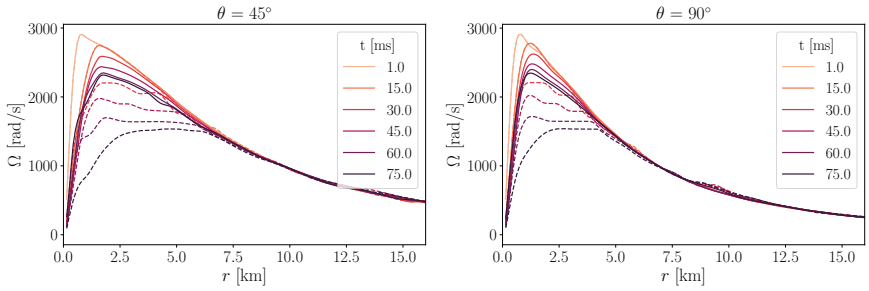

Figure 4.3 Radial profiles of the angular frequency Ω at $\theta = 45°$ (left panel) and $\theta = 90°$ (right panel) for different times ($t = \{1, 15, 30, 45, 60, 75\}$ ms). The solid lines represent the results of the simulation without the MInIT model, whereas the dashed lines depict the simulation that employs it. When the sub-grid model is applied, effective angular momentum transport is triggered, reducing the central angular frequency more than a factor 2.

to the same simulation without the model. During the first ~ 15 ms, the profiles for both cases look the same. Since the turbulent energy densities are still growing (see Figure 4.1), no effects are visible in the bulk flow. At later times, the MRI has already reached saturation and its effects start being evident. The profile flattens, reducing the degree of differential rotation (see Figure 4.2) and its angular velocity, as one would expect. Even though the solid curves also decrease in amplitude, this is due to numerical dissipation, and its effect is not as big as the angular momentum transport triggered by the MRI. Figure 4.4 compares two identical simulations without the sub-grid model that only differ on the number of radial cells ($N_r = 396$ and $N_r = 198$). The rotational profile flattens more rapidly in the simulation with lower radial resolution (dashed curves), due to the increased numerical dissipation. This issue should be further explored with additional simulations with different spatial resolutions.

Figure 4.5 displays the radial profiles of the MRI (upper panel) and PI (lower panel) energy densities. Initially, the energies attain very small values, but they increase very rapidly up to a uniform saturation amplitude. This value is almost constant through the whole domain because the MRI growth rate, $\gamma_{\mathrm{MRI}} = 0.5q\Omega$ and wavelength, λ_{MRI}, are also mostly constant, as well as the magnetic field inside the star (no effective dynamo is inserted and therefore the magnetic field is not amplified by the MRI). As time goes by, the amplitude of the energy densities decreases gradually, as the degree of differential rotation is reduced due to the transport of angular momentum.

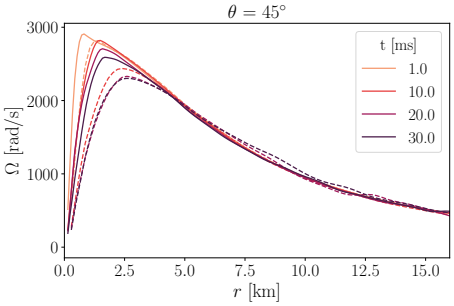

Figure 4.4 Radial profiles of the angular frequency Ω at $\theta = 45°$ for different times ($t = \{1, 10, 20, 30\}$ ms). The solid curves represent the results of the simulation without the MInIT model and $N_r = 396$ cells, whereas the dashed curves depict the same simulation with $N_r = 198$ cells. The increased numerical dissipation in the simulation with less radial resolution (dashed curves) results in a more pronounced flattening of the rotational profile.

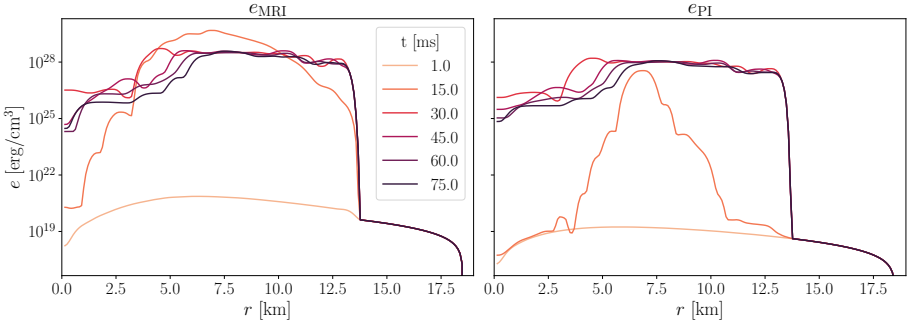

Figure 4.5 Radial profiles of the turbulent energy density of the MRI (upper panel) and the PI (lower panel) at $\theta = 45°$ and $t = \{1, 15, 30, 45, 60, 75\}$ ms. The MRI seems to reach saturation at $t \gtrsim 15$ ms. At later times, both energy densities present a similar amplitude. In the central regions, where angular momentum transport takes place, the amplitude decays in time.

4.5 Discussion and conclusions

In this Chapter, I have assessed the performance of the MInIT model (presented in Chapter 2) in a numerical simulation of a differentially rotating NS prone to the MRI. The lack of spatial resolution in current numerical simulations prevents the development of the MRI in the BNS postmerger phase, where a rapidly rotating magnetised HMNS with a high degree of differential rotation is formed. The angular momentum transport triggered by the growth of the MRI channels can have a substantial impact on the stability and lifetime of the remnant star. If the rotational profile flattens, leading to uniform rotation, the centrifugal support against gravity might be insufficient and the star would collapse to a BH. In addition, the large-scale magnetic field can be amplified due to the effective dynamo triggered by the instability, having an important impact in the formation of GRB jets.

So far, the numerical simulations of BNS mergers with the highest resolution have grid with side-length $\mathcal{O}(10)$ m [Kiuchi et al. 2015, Kiuchi et al. 2024]. However, the molecular dissipation scale in the NS is $\mathcal{O}(1)$ cm [Radice and Hawke 2024]. This means that, at least, the computational resources from the highest resolution simulations should increase by a factor $\sim 10^9$ to fully capture the inertial range of scales. An alternative to the unaffordable DNS is the use of LES. The aim of the work reported in this Chapter was to prove that the MInIT model is able to mimic the transport of angular momentum in a NS unstable to the MRI. In this Chapter, I have applied for the first time the MInIT sub-grid model in Newtonian axisymmetric LES of an isolated NS. After inserting the evolution equations for the turbulent energy densities in the Aenus code [Obergaulinger 2008], and the resulting Maxwell and Reynolds stress tensors in the mean-field MHD equations, an effective angular momentum transport can be observed during the evolution of the NS.

During the first stages of the evolution ($t \lesssim 15$ ms), the amplitude of the MRI channel modes grows exponentially from considerably low values, as well as the PIs, which undergo a super-exponential growth. In this lapse of time, the bulk flow remains in equilibrium, since the MRI growth has not terminated yet. When saturation occurs, i.e., the amplitude of the parasitic energy density is comparable to that of the MRI, the turbulent stresses reach a large enough amplitude to leave an imprint in the bulk flow. This delay is not observed in simulations that employ an α-viscosity parameter [Shibata, Kiuchi, and Sekiguchi 2017], since that approach assumes a constant value of the α parameter, corresponding to the saturated state already. From $t \approx 15$ ms, the rotational profile of the star

flattens, reducing its central rotational frequency an important fraction. The central angular frequency at the equator reduces to half its initial value (from $\Omega_c \approx 3$ kHz to $\Omega_c \approx 1.5$ kHz) at $t \approx 50$ ms, which means that the timescale in which angular momentum is transported is $\mathcal{O}(100)$ ms. The values of the rotation velocity and the magnetic field, which are physically plausible, provide a MRI wavelength difficult to resolve by numerical simulations ($\lambda_{\rm MRI} \sim 10$ m). As shown by Rembiasz et al. 2016b, at least 10 points per MRI channel size are needed to fully solve the instability. Employing a typical radial resolution of ($\Delta_r \sim 100$ m), I also performed a simulation without the MInIT model. As expected, no angular momentum transport arises during the evolution of this MRI-unresolved simulation.

The results presented in this Chapter, albeit promising, are still preliminary. Further simulations with different rotational profiles and magnetic field strengths will be needed to explore a wider parameter space. In addition, the use of higher resolution (or different numerical schema) might reduce the numerical dissipation responsible for the decrease of the angular frequency in the simulations without a sub-grid implementation. The most immediate step is the implementation of the Faraday stress tensor in the induction equation for the magnetic field, which might induce an effective dynamo. To do so, the modelling of this stress tensor needs to be improved to account for the characteristic periodicity of the dynamo. A further action would be the implementation of the model into GRMHD simulations. This requires that our sub-grid approach preserves covariance, and a specific scheme with a Lagrangian filter must be applied to do so. In Chapter 6 I discuss these issues in more detail.

For the EOS employed in this work, the maximum mass for an object with rigid rotation is 1.89 $M_\odot$, lower than the mass of the NS simulated here. This means that, in a GRMHD simulation, when rigid rotation is reached due to the angular momentum transport, the HMNS should collapse to a BH. The timescale of the transport of angular momentum is found to be $\mathcal{O}(100)$ ms, but this would also depend on the rotation of the HMNS and the EOS considered. With this timescale, the BNS remnant is expected to collapse to a BH at $t \approx 100$ ms after merger. This has important implications in the EM and kilonova emission that triggers the r-process nucleosynthesis. The HMNS needs to collapse in order to launch the GRB, which means that a faithful simulation that properly describes the lifetime of the BNS remnant might help understand the gamma-ray detections from BNS mergers. BNS merger simulations that do not capture this turbulent effect might result in very long-lived remnants that are not powerful enough to power a GRB.

However, in addition to differential rotation, the HMNS is supported against gravity through thermal pressure. Realistic EOSs together with a proper neutrino transport scheme are also required to perform faithful numerical studies of this scenario.

CHAPTER 5

Revisiting the saturation of the magnetorotational instability by parasitic modes

5.1 Introduction

The discussion reported in Section 1.3 has shown that the mechanism responsible for the saturation of the MRI and thus the factor by which the seed perturbations are amplified are not yet fully understood. Several authors [Brandenburg et al. 1995, Fleming, Stone, and Hawley 2000, Sano and Inutsuka 2001, Sano et al. 2004, Gardiner and Stone 2005, Lesur and Longaretti 2007, Murphy and Pessah 2015, Rembiasz et al. 2016a, Hirai et al. 2018, Gogichaishvili et al. 2018] have provided further insight into the saturation of the MRI and the resulting nonlinear turbulent regime by performing numerical box simulations and also (semi-)global simulations of accretion discs [Sorathia, Reynolds, and Armitage 2010, Hawley, Guan, and Krolik 2011, Sorathia et al. 2012], fast-rotating PNSs [Obergaulinger et al. 2009, Mösta et al. 2015, Reboul-Salze et al. 2022] and BNS merger remnants [Kiuchi et al. 2018, Shibata, Fujibayashi, and Sekiguchi 2021].

The model for PIs, presented by Goodman and Xu 1994, provides a physical mechanism that explains the termination of the MRI and the subsequent nonlinear regime. The laminar channel flows can be unstable against PIs that can be of KH or tearing-mode (TM) type, depending on the value of the kine-

matic viscosity and resistivity, i.e. non-ideal effects. Pessah and Goodman 2009 and Pessah 2010 performed an analytical study in resistive-viscous MHD of the evolution of the PIs by solving an eigenvalue problem with linear equations for these secondary instabilities. They exhaustively covered a huge parameter space to identify the fastest growing parasitic modes for different values of the kinematic viscosity and the resistivity. The authors (and also Latter, Lesaffre, and Balbus 2009) made several assumptions to make the problem more tractable. The most notable simplifications are the consideration of the primary MRI mode as a time-independent background, and the assumption that the wavevectors of the parasitic modes are also time-independent (by neglecting the background shear from the MHD equations).

In this Chapter, we relax some simplifications made in previous studies to obtain a more accurate description of the evolution of PIs and better estimate for the saturation of the MRI. Building on the approach in Pessah 2010, we derive a set of equations for the parasitic perturbations feeding of the fastest-growing MRI mode for a fixed vertical magnetic field. However, we here account for the exponential growth of the MRI modes and the linear shear of the parasitic wavevector induced by differential rotation of the background flow. By covering a dense parameter space, we identify the fastest secondary modes that lead to the saturation of the MRI. Using different values for the seed perturbations, we obtain amplification factors of the MRI that are similar to the ones obtained in the numerical simulations presented in Rembiasz et al. 2016a.

This Chapter is organised as follows: in Section 5.2 we present and solve the linearised equations for the PIs. We showcase in Section 5.3 the time evolution of several parasitic modes and study the saturation amplitude of the MRI. Summary and conclusions are given in Section 5.4. In Appendix 5.A, we depict the physical structure of the PIs.

5.2 Evolution equations for the parasitic perturbations

To carry out a linear analysis of the parasitic modes feeding off the MRI channels, we need to treat those channels as part of the background fields, as in Goodman and Xu 1994, Pessah and Goodman 2009, Pessah 2010. This is a sensible approach during the MRI growth, since the amplitude of the channel modes is much larger than the parasitic ones. This implies that the primary (the MRI) instability will not be significantly affected by the secondary (parasitic modes) until they reach a similar amplitude. This approximation is bound to break down when the amplitudes involved are comparable. Nevertheless, here we will

consider that the primary MRI modes grow exponentially unimpeded. The novelty compared to previous studies is that we do consider that the parasites, with shearing time-dependent wavevectors, are feeding from a time-dependent MRI mode.

The system of incompressible MHD equations that leads to the equations of the parasitic modes is:

$$\partial_t \boldsymbol{V} + (\boldsymbol{V}\cdot\nabla)\boldsymbol{V} = -2\boldsymbol{\Omega_0}\times\boldsymbol{V} + q\Omega_0^2\nabla(x^2) - \frac{1}{\rho}\nabla\Big(P+\frac{B^2}{8\pi}\Big) + \frac{(\boldsymbol{B}\cdot\nabla)\boldsymbol{B}}{4\pi\rho} + \nu\nabla^2\boldsymbol{V}, \tag{5.1}$$

$$\partial_t \boldsymbol{B} + (\boldsymbol{V}\cdot\nabla)\boldsymbol{B} = (\boldsymbol{B}\cdot\nabla)\boldsymbol{V} + \eta\nabla^2\boldsymbol{B}, \tag{5.2}$$

$$\nabla\cdot\boldsymbol{V} = 0, \tag{5.3}$$

$$\nabla\cdot\boldsymbol{B} = 0\,. \tag{5.4}$$

We seek for solutions for the total velocity and magnetic fields of the form [Goodman and Xu 1994]:

$$\mathbf{U} = \begin{bmatrix} V_x \\ V_y \\ V_z \\ B_x \\ B_y \\ B_z \end{bmatrix} = \begin{bmatrix} 0 \\ -q\Omega x \\ 0 \\ 0 \\ 0 \\ \bar{B}_z \end{bmatrix} + \begin{bmatrix} V_x^{\rm MRI} \\ V_y^{\rm MRI} \\ 0 \\ B_x^{\rm MRI} \\ B_y^{\rm MRI} \\ 0 \end{bmatrix} + \begin{bmatrix} v_x \\ v_y \\ v_z \\ b_x \\ b_y \\ b_z \end{bmatrix}, \tag{5.5}$$

where we include, from left to right, the contribution of the background vertical magnetic field $\bar{B}_z$ and the velocity shear, the MRI fields (that will also constitute the background dynamics of our problem), and the parasitic fields. Note that the vertical magnetic field $\bar{B}_z$ remains unchanged and the MRI grows exponentially unaffected by the parasitic perturbations. The former assumption holds in the incompressible limit because the MRI itself does not produce a feedback into $\bar{B}_z$ [Pessah, Chan, and Psaltis 2006a]. This approximation is expected to break down when the vertical magnetic field generated by PIs is no longer negligible.

In the ideal, i.e., for sufficiently small values of the viscosity ν and the resistivity η, incompressible MHD regime, the MRI evolves as an exact, nonlinear solution with a mode structure given by [Goodman and Xu 1994, Pessah, Chan, and Psaltis 2006b, Pessah and Chan 2008]

$$\boldsymbol{V}^{\rm MRI} = V_0 e^{\gamma_{\rm MRI} t}\sin(Kz)[\cos(\theta_V)\check{\mathbf{x}} + \sin(\theta_V)\check{\mathbf{y}}], \tag{5.6}$$

$$\boldsymbol{B}^{\rm MRI} = B_0 e^{\gamma_{\rm MRI} t}\cos(Kz)[\cos(\theta_B)\check{\mathbf{x}} + \sin(\theta_B)\check{\mathbf{y}}]\,, \tag{5.7}$$

where V_0 and B_0 are the initial MRI velocity and magnetic field amplitudes, respectively, $\check{\mathbf{x}}$ is the unit vector in the radial direction, $\check{\mathbf{y}}$ is the unit vector in the azimuthal direction, $\theta_{\rm V}$ and $\theta_{\rm B}$ are the directions of the channels with respect to the radial direction, $\check{\mathbf{x}}$, and K is the MRI wavenumber that indicates the periodicity in the vertical direction. The maximum MRI growth rate is

$$\gamma_{\rm MRI} = \frac{q}{2}\Omega\,, \tag{5.8}$$

where Ω is rotation frequency and the shear parameter q is given by

$$q \equiv -\frac{d\ln\Omega}{d\ln r}\bigg|_{r_0}\,, \tag{5.9}$$

which is evaluated at some fiducial radius r_0. The wavenumber of the fastest growing MRI mode in the ideal MHD limit is [Pessah and Chan 2008]

$$K = \sqrt{1-\frac{\kappa^4}{16}}\,, \tag{5.10}$$

where $\kappa \equiv \sqrt{2(2-q)}\Omega$ is the epicyclic frequency.

In addition, the ratio between the MRI amplitudes, $V_0/(B_0/\sqrt{4\pi\rho})$, was found in Pessah and Chan 2008 to be, in the ideal MHD limit:

$$\frac{V_0}{B_0/\sqrt{4\pi\rho}} = \sqrt{\frac{4-\kappa^2}{4+\kappa^2}}\,. \tag{5.11}$$

As in Pessah 2010, we will employ dimensionless variables defined in terms of the characteristic length and time-scale set by the background magnetic field and the local angular frequency: $L_0 \equiv \bar{v}_{{\rm A}z}^2/\Omega_0 = \bar{B}_z^2/(4\pi\rho\Omega_0)$ and $T_0 \equiv 1/\Omega_0$. With this, $\bar{B}_z$ sets the scale for all magnetic and velocity fields. From now on, we employ $\boldsymbol{V}$ and $\boldsymbol{B}$ to refer to the MRI velocity and magnetic fields, respectively.

The secondary, parasitic velocity and magnetic fields can be expressed as

$$\boldsymbol{v} = e^{i\boldsymbol{k}_{\boldsymbol{h}}\cdot\boldsymbol{x}}\boldsymbol{u}(t,z)\,, \tag{5.12}$$

$$\boldsymbol{b} = e^{i\boldsymbol{k}_{\boldsymbol{h}}\cdot\boldsymbol{x}}\boldsymbol{w}(t,z)\,. \tag{5.13}$$

where the explicit temporal dependence of the horizontal wavevector is given by

$$\boldsymbol{k}_{\mathbf{h}} = (k_x(0) + q\Omega_0 k_y t)\check{\mathbf{x}} + k_y\check{\mathbf{y}}\,. \tag{5.14}$$

This simply reflects the fact that wave crests are swept by the (linear) shear background flow, thereby increasing their wavenumber and rotating towards the radial direction, $\check{\mathbf{x}}$ [Latter, Fromang, and Gressel 2010, Mamatsashvili et al. 2013].

We can exploit the incompressible nature of the flow and focus on the dynamics in the plane $(\check{\boldsymbol{k}}_{\mathbf{h}}, \check{\boldsymbol{z}})$ (see Pessah 2010). In fact, this condition restricts

our problem to one single direction, since $i\boldsymbol{k}_\mathbf{h}\cdot\boldsymbol{v}_\mathbf{h} = -\partial_z v_z$. We can furthermore eliminate the pressure by using the divergenceless condition for the velocity (Equation (5.3)). Then, the evolution equation for the vertical parasitic velocity will be

$$\begin{aligned}(-\Delta\partial_t - i\boldsymbol{k}_\mathbf{h}\cdot\boldsymbol{V} + \nu\Delta)\Delta u_z - iK^2\boldsymbol{k}_\mathbf{h}\cdot\boldsymbol{V}u_z \\ +q\sin 2\theta\partial_z^2 u_z + i\boldsymbol{k}_\mathbf{h}\cdot\boldsymbol{B}\Delta w_z + iK^2\boldsymbol{k}_\mathbf{h}\cdot\boldsymbol{B}w_z + \Delta\partial_z w_z = 0\,,\end{aligned} \tag{5.15}$$

where $\Delta \equiv \partial_z^2 - k_\mathrm{h}^2$.

The equation for the vertical component of the parasitic magnetic field is

$$(\partial_t + i\boldsymbol{k}_\mathbf{h}\cdot\boldsymbol{V} - \eta\Delta)w_z - i\boldsymbol{k}_\mathbf{h}\cdot\boldsymbol{B}u_z - \partial_z u_z = 0\,. \tag{5.16}$$

After applying all the previous assumptions, i.e., treating the MRI fields as background and adding the time-dependent wavevector, we end up with Equations (5.15) and (5.16), which are linear equations for the parasitic perturbations in the incompressible regime. Now we can express the previous equations in Fourier space. The fields can be expressed solely in terms of their vertical components thanks to the divergenceless nature of the perturbed fields:

$$\begin{aligned}\boldsymbol{u} &= \frac{\partial_z u_z}{ik_\mathrm{h}}\check{\boldsymbol{k}}_\mathbf{h} + u_z\check{\boldsymbol{z}} \\ \boldsymbol{w} &= \frac{\partial_z w_z}{ik_\mathrm{h}}\check{\boldsymbol{k}}_\mathbf{h} + w_z\check{\boldsymbol{z}}\,.\end{aligned}$$

The vertical components in terms of Fourier series are

$$u_z = B_0\sum_{n=-\infty}^{\infty}\alpha_n(t)e^{i(nK+k_z)z} \tag{5.17}$$

$$w_z = B_0\sum_{n=-\infty}^{\infty}\beta_n(t)e^{i(nK+k_z)z}\,, \tag{5.18}$$

where k_z is a parameter with $0 \le k_z/K \le 1/2$ [Pessah 2010]. Moreover, the Fourier coefficients are expressed in terms of the initial amplitude of the MRI channel, B_0, and the wavenumbers $\boldsymbol{k}_\mathbf{h}$ and k_z can be rewritten in terms of the MRI one, K ($\boldsymbol{k}_\mathbf{h} \to \boldsymbol{k}_\mathbf{h}/K$, $k_z \to k_z/K$), as done in Pessah 2010. If one takes into account the Euler formula:

$$\begin{aligned}\sin(Kz) &= \frac{1}{2i}(e^{iKz} - e^{-iKz}) \\ \cos(Kz) &= \frac{1}{2}(e^{iKz} + e^{-iKz})\,,\end{aligned}$$

the resulting differential equations for the temporal evolution of the Fourier coefficients are

$$\begin{aligned}\partial_t\alpha_n(t) =& -i(n+k_z)K\beta_n(t) + \frac{q}{2\Delta_n}\sin 2\theta\frac{(n+k_z)^2}{\Delta_n}\alpha_n(t) \\ &- KV_0\frac{\boldsymbol{k}_\mathbf{h}\cdot\check{\boldsymbol{V}}(t)}{2\Delta_n}\big[\alpha_{n-1}(t)(\Delta_{n-1}-1)-\alpha_{n+1}(t)(\Delta_{n+1}-1)\big] \\ &+ iKB_0\frac{\boldsymbol{k}_\mathbf{h}\cdot\check{\boldsymbol{B}}(t)}{2\Delta_n}\big[\beta_{n-1}(t)(\Delta_{n-1}-1)+\beta_{n+1}(t)(\Delta_{n+1}-1)\big] \\ &- \nu K^2\Delta_n\alpha_n(t)\,,\end{aligned} \tag{5.19}$$

$$\begin{aligned}\partial_t\beta_n(t) =& -KV_0\frac{\boldsymbol{k}_\mathbf{h}\cdot\check{\boldsymbol{V}}(t)}{2}\big[\beta_{n-1}(t)-\beta_{n+1}(t)\big] \\ &+ iKB_0\frac{\boldsymbol{k}_\mathbf{h}\cdot\check{\boldsymbol{B}}(t)}{2}\big[\alpha_{n+1}(t)+\alpha_{n-1}(t)\big] - i(n+k_z)K\alpha_n(t) \\ &- \eta K^2\Delta_n\beta_n(t)\,,\end{aligned} \tag{5.20}$$

where $\Delta_n \equiv k_h^2 + (n+k_z)^2$ and θ is the angle between the parasitic wavevector, $\boldsymbol{k}_\mathbf{h}$, and the radial direction in the anticlockwise sense.

5.2.1 The initial value problem

In every evolution problem, one needs to give an initial value to the evolving quantities. The initial Fourier amplitudes of the PIs, i.e., the coefficients $\alpha_n(0)$ and $\beta_n(0)$, can be obtained using the equations from Pessah 2010, which consist in an eigenvalue problem where the eigenvalues correspond to the growth rate of the PIs and the eigenvectors' components are the values of α_n, β_n. These equations are:

$$\begin{aligned}\frac{s}{KB_0}\alpha_n(0) =& -\frac{i}{B_0}(n+k_z)\beta_n(0) \\ &+ i\frac{\boldsymbol{k}_\mathbf{h}\cdot\check{\boldsymbol{B}}_0}{2\Delta_n}\big[\beta_{n-1}(0)(\Delta_{n-1}-1)+\beta_{n+1}(0)(\Delta_{n+1}-1)\big] \\ &- \frac{\boldsymbol{k}_\mathbf{h}\cdot\check{\boldsymbol{V}}_0}{2\Delta_n}\frac{V_0}{B_0}\big[\alpha_{n-1}(0)(\Delta_{n-1}-1)-\alpha_{n+1}(0)(\Delta_{n+1}-1)\big] \\ &- \frac{\nu K^2}{KB_0}\Delta_n\alpha_n(0)\,,\end{aligned} \tag{5.21}$$

$$\begin{aligned}\frac{s}{KB_0}\beta_n(0) = &-\frac{\boldsymbol{k}_\mathbf{h}\cdot\check{\boldsymbol{V}}_0}{2}\frac{V_0}{B_0}(\beta_{n-1}(0)-\beta_{n+1}(0)) \\ &+ i\frac{\boldsymbol{k}_\mathbf{h}\cdot\check{\boldsymbol{B}}_0}{2}(\alpha_{n-1}(0)+\alpha_{n+1}(0)) - i\frac{1}{B_0}(n+k_z)\alpha_n(0) \\ &-\frac{\eta K^2}{KB_0}\Delta_n\beta_n(0)\,,\end{aligned} \tag{5.22}$$

where s is the growth rate of the parasitic modes. In the ideal MHD limit, the last term in the right-hand side of both equations vanishes. As a note of caution, the problem presented in Pessah 2010 assumes that the MRI background and $\boldsymbol{k}_\mathbf{h}$ do not evolve with time. However, this can be useful to obtain an approximate initial distribution of the parasitic modes.

By taking the eigenvector corresponding to the eigenvalue with the largest real contribution (fastest PI mode), we get a set of α_n and β_n values that will be our initial values for the equations (5.19) and (5.20). Since the eigenvector is normalised, we have the freedom to set an initial amplitude for the PI modes, v_0. Therefore, we re-scale the norm so that the velocity of the PI mode is a fraction of the Alfvén velocity. Consequently, the value of b_0 is determined by the PI eigenvalue problem.

The above equations show that the Fourier components of the parasitic modes exclusively depend on the parasitic wavevector, $(\boldsymbol{k}_\mathbf{h}, k_z)$, the MRI wavenumber, K, and the MRI amplitudes, $(\boldsymbol{B}, \boldsymbol{V})$.

5.2.2 **Solution for the parasitic instabilities**

Now that we got the initial values of the Fourier amplitudes of the velocity and magnetic fields of the PIs, we can evolve the system of equations (5.19) and (5.20). Since it is a system of coupled linear differential equations of the form

$$\partial_t\boldsymbol{x}(t) = \boldsymbol{A}(t)\boldsymbol{x}(t)\,, \tag{5.23}$$

where $\boldsymbol{A}(t)$ is the matrix of coefficients, we can decouple it in the following way. Let the matrix $\boldsymbol{A}(t)$ be expressed in terms of a diagonal matrix, $\boldsymbol{\Lambda}(t)$:

$$\boldsymbol{\Lambda} = \boldsymbol{S}^{-1}\boldsymbol{A}\boldsymbol{S}\,, \tag{5.24}$$

where $\boldsymbol{S}$ is a matrix built with the eigenvectors of $\boldsymbol{A}(t)$ as columns and $\boldsymbol{\Lambda}$ is a diagonal matrix with the eigenvalues of $\boldsymbol{A}$ as elements. We can decouple this system by introducing the variables:

$$\boldsymbol{\eta} = \boldsymbol{S}^{-1}\boldsymbol{x}\,. \tag{5.25}$$

Substituting the expression in Eq. (5.24) in Eq. (5.23), and using the new variable from the above equation, we obtain:

$$\partial_t \boldsymbol{\eta}(t) = \boldsymbol{\Lambda}\boldsymbol{\eta}(t)\,, \tag{5.26}$$

which is a system of decoupled equations. This is valid only when $\boldsymbol{S} \neq \boldsymbol{S}(t)$, and we assume this is the case in a small enough time interval Δt. We can therefore solve for each component, and every equation will be as:

$$\dot{\eta}_i = \lambda_i \eta_i\,, \tag{5.27}$$

and this results in

$$\eta_i(t) = \exp\left[\int_{t-\Delta t}^{t} \lambda_i(\tau) d\tau\right] \eta_i(t-\Delta t)\,. \tag{5.28}$$

We can define the matrix made with the right-hand-side elements from the above equation, and assume that λ_i are constant for small enough time intervals, Δt, i.e., $\boldsymbol{S} \neq \boldsymbol{S}(t)$, ending up with:

$$E_{ij} \equiv \delta_{ij} \exp\left[\int_{t-\Delta t}^{t} \lambda_i(\tau) d\tau\right] \approx \delta_{ij} e^{\Delta t \lambda_i}\,. \tag{5.29}$$

In terms of our variables $\boldsymbol{x}$, the solution has the following form:

$$\boldsymbol{x}(t) = \boldsymbol{S}\boldsymbol{E}\boldsymbol{S}^{-1}\boldsymbol{x}(t-\Delta t)\,. \tag{5.30}$$

The vectors $\boldsymbol{x}(t)$ consist of the Fourier amplitudes $\alpha_n(t)$ and $\beta_n(t)$. Once we solve these coupled differential equations, we can build the physical velocities and magnetic fields:

$$v_z(t;\boldsymbol{x}) = B_0 \sum_{n=-\infty}^{\infty} \alpha_n(t) e^{i(n+k_z)z} e^{i\boldsymbol{k_h}\cdot\boldsymbol{x}} \tag{5.31}$$

$$b_z(t;\boldsymbol{x}) = B_0 \sum_{n=-\infty}^{\infty} \beta_n(t) e^{i(n+k_z)z} e^{i\boldsymbol{k_h}\cdot\boldsymbol{x}}\,. \tag{5.32}$$

Since the horizontal component in the direction of $\boldsymbol{k_h}$ is proportional to the vertical component thanks to the divergence-free condition, the velocity and magnetic fields parallel to the plane defined by $(\check{\boldsymbol{k}}_h, \check{\boldsymbol{z}})$ are given by

$$\begin{aligned}\boldsymbol{v}(t;\boldsymbol{x}) = &-\frac{B_0}{k_h} \sum_{n=-\infty}^{\infty} (n+k_z)\alpha_n(t) e^{i(n+k_z)z} e^{i\boldsymbol{k_h}\cdot\boldsymbol{x}} \check{\boldsymbol{k}}_{\mathbf{h}} \\ &+ B_0 \sum_{n=-\infty}^{\infty} \alpha_n(t) e^{i(n+k_z)z} e^{i\boldsymbol{k_h}\cdot\boldsymbol{x}} \check{\boldsymbol{z}}\,,\end{aligned} \tag{5.33}$$

$$\boldsymbol{b}(t;\boldsymbol{x}) = -\frac{B_0}{k_h}\sum_{n=-\infty}^{\infty}(n+k_z)\beta_n(t)e^{i(n+k_z)z}e^{i\boldsymbol{k_h}\cdot\boldsymbol{x}}\check{\boldsymbol{k}}_{\mathbf{h}} + B_0\sum_{n=-\infty}^{\infty}\beta_n(t)e^{i(n+k_z)z}e^{i\boldsymbol{k_h}\cdot\boldsymbol{x}}\check{\boldsymbol{z}}\,. \tag{5.34}$$

5.2.3 **Growth rate of the parasitic modes**

The volume-averaged value of the velocity of the PI modes can be computed from the Fourier amplitudes $\alpha_n(t)$:

$$v(t) \equiv |\bar{\boldsymbol{v}}(t)| = B_0\sqrt{\sum_{n=-\infty}^{\infty}\left[1+\frac{(n+k_z)^2}{k_{\mathrm{h}}^2}\right]|\alpha_n(t)|^2}\,. \tag{5.35}$$

Then, the growth rate of the velocity of parasitic mode is approximately

$$\gamma_{\mathrm{PI}}(t) = \frac{1}{\Delta t}\frac{v(t)-v(t-\Delta t)}{v(t-\Delta t)} \tag{5.36}$$

and the volume-averaged velocity of the MRI channel mode is given by

$$V(t) \equiv |\bar{\boldsymbol{V}}(t)| = \frac{V_0}{\sqrt{2}}e^{\gamma_{\mathrm{MRI}}t}\,. \tag{5.37}$$

5.2.4 **Saturation**

We assume that the MRI mode saturates when the parasitic velocity reaches a certain fraction of the channel velocity [Latter, Fromang, and Gressel 2010, Rembiasz et al. 2016b]:

$$v(t_{\mathrm{sat}}) = \epsilon V(t_{\mathrm{sat}})\,. \tag{5.38}$$

The parasitic mode that reaches this value first will be the fastest parasitic mode and will set a saturation amplitude for the MRI mode. We can define the amplification factor as the ratio between the volume-averaged Maxwell stress tensor and the initial vertical magnetic field [Rembiasz et al. 2016a]:

$$\mathcal{A} \equiv \sqrt{\mathcal{M}_{xy}^{\mathrm{sat}}} = \frac{B_0}{\sqrt{2}}\sqrt{|\cos\theta_{\mathrm{B}}\sin\theta_{\mathrm{B}}|}e^{\gamma_{\mathrm{MRI}}t_{\mathrm{sat}}}\,, \tag{5.39}$$

which in the ideal MHD limit reads as

$$\mathcal{A} = \frac{B_0}{2}e^{\frac{q}{2}t_{\mathrm{sat}}}\,. \tag{5.40}$$

5.3 Results

The PIs are expected to experience a phase of rapid growth when $\boldsymbol{k_h}$ is aligned with either the velocity or the magnetic field of the primary modes $(\boldsymbol{V}, \boldsymbol{B})$ [Goodman and Xu 1994, Pessah and Goodman 2009, Pessah 2010, Latter, Lesaffre, and Balbus 2009]. The ones aligned with the MRI velocity are identified as KH (or kink) modes, whereas the latter are related to tearing (or pinch) modes. In the context of ideal MHD ($\nu \ll 1, \mu \ll 1$), the parasitic modes of KH type dominate. Since we want to focus on the ideal case, which is more common in numerical simulations involving NSs, we should expect to obtain at saturation modes aligned with the velocity of the MRIs, with $\theta \approx \theta_V$. We therefore set the viscosity to $\nu = 10^{-3}$ and the resistivity to $\eta = 10^{-2}$. The fastest MRI mode (for $q = 1.5$) is characterised by a wavevector with modulus $K \approx 0.96$ and angles $\theta_V = 44.5° \approx 45°$ and $\theta_B = 134.7° \approx 135°$, as shown in Pessah 2010. In addition, the ratio between the MRI amplitudes is $V_0/B_0 \approx 0.77$. We also consider parasitic modes with $k_z = 0$, i.e., with the same vertical periodicity than the MRI modes, since these ones are expected to grow faster [Goodman and Xu 1994, Pessah 2010, Rembiasz et al. 2016b, Hirai et al. 2018]. Moreover, we fix ϵ from Equation (5.38) to 1.

5.3.1 Time evolution of the parasitic modes

In order to solve the equations given by (5.26), we employ the approach shown in Eq. (5.29), using an adaptive time step Δt that decreases as γ_{PI} increases, as shown in Table 5.1. The initial time step is set to $\Delta t_0 = 0.1$.

Table 5.1 Values of the time step as a function of the growth rate of the parasitic mode.

γ_{PI}/γ_{MRI}	$\Delta t/\Delta t_0$
< 0.1	1
≥ 0.1	10^{-1}
≥ 1	10^{-2}
≥ 25	10^{-3}

We consider different initial wavevectors for the PIs, characterising several modes, and evolve them independently, as done in Pessah and Goodman 2009, Pessah 2010. Since we expect to reach a wavevector with modulus $k_h = 0.59$, as shown in Pessah 2010 and Rembiasz et al. 2016a, we should start with a vector with large enough modulus and negative x-component. k_h^x. Therefore, the initial

values of the wavevector components that we consider are

$$k_{\rm h}^x = \{-1, -1.125, -1.25, ..., -15\}, \tag{5.41}$$
$$k_{\rm h}^y = \{0.1, 0.1125, 0.125, ..., 0.7\}\,. \tag{5.42}$$

We explore the time evolution of these modes with different initial amplitudes of the MRI channels, B_0, and different initial amplitudes for the parasitic velocities, v_0. We summarise in Table 5.2 the initial amplitudes we tested, together with the fastest parasitic modes for each initial condition, their value at saturation, the saturation time and the amplification factor. The initial amplitudes of the MRI magnetic field and the initial parasitic amplitudes are

$$B_0 = \{1, 5, 10, 50, 100\} \times 10^{-4}, \tag{5.43}$$
$$v_0 = \{0.1, 0.5, 1, 5, 10\} \times 10^{-4}\,, \tag{5.44}$$

respectively, as depicted in Table 5.2. Even though the initial PIs are larger than the channel modes in some cases, the results seem to be valid as well, since the early growth of the PIs is much slower than that of the MRI. The runs are labelled as follows: the symbols `vl, l, m, h, vh` after `b0` and `dv` stand for "very low", "low", "mid", "high" and "very high", respectively. Thus, the run, e.g., `b0vl-dvh` is characterised by a "low" B_0 and a "very high" v_0. The fastest growing modes possess initial horizontal wavevectors $\sim 3-5$ times larger than K, with $k_{\rm h}^x(0) \gg k_{\rm h}^y$, and values at saturation at around $0.6-0.7$, with $\theta^{\rm sat} \lesssim 20^\circ$. We depict in Figure 5.1 the initial and final wavevectors of the fastest PI modes for all the runs shown in Table 5.2. The amplification factors take values within the range $\sim 35-55$, depending on the initial parasitic amplitude. Although not shown here, there are numerous parasitic modes that grow almost as fast as the rapid ones, and provide amplification factors with similar values as the ones in Table 5.2.

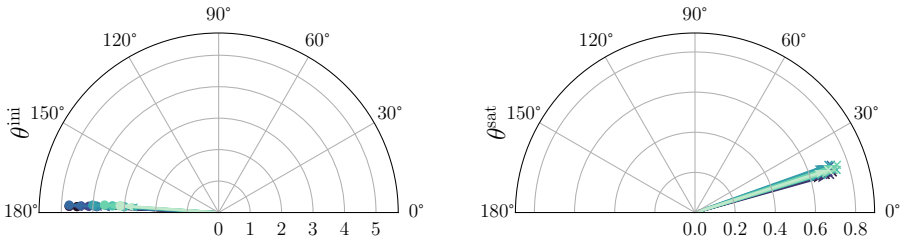

Figure 5.1 Representation of the parasitic wavevectors k_{h} at $t = 0$ and at saturation, $t = t_{\mathrm{sat}}$, for all the runs in Table 5.2. The initial modulus $k_{\mathrm{h}}^{\mathrm{ini}}$ ranges between 3 and 5, but the initial angle θ^{ini} is very close to 180° in all cases. The wavevectors at saturation have almost the same angle θ^{sat} at around 18°, and the modulus $k_{\mathrm{h}}^{\mathrm{sat}}$ lies around 0.7.

Table 5.2 Evolutions of the PIs for different initial amplitudes of the MRI channels and the parasitic velocities. We show the initial wavevector $k_{\rm h}(0)$ that leads to saturation, its modules and angle at saturation, and the amplification factor.

NAME	$B_0[10^{-4}]$	$v_0[10^{-4}]$	q	$k_{\rm h}^{\rm ini}$	$\theta^{\rm ini}$ [°]	$k_{\rm h}^{\rm sat}$	$\theta^{\rm sat}$ [°]	$t_{\rm sat}$ [Orbits]	$\mathcal{A}$
b0vl-dvl	1	0.1	1.5	4.25	177.64	0.65	15.70	2.954	55.63
b0vl-dl	1	0.5	1.5	4.50	177.61	0.70	15.57	2.927	48.93
b0vl-dm	1	1	1.5	4.50	177.61	0.68	16.07	2.915	46.15
b0vl-dh	1	5	1.5	4.75	177.59	0.72	16.25	2.884	39.93
b0vl-dvh	1	10	1.5	4.75	177.59	0.69	16.90	2.869	37.24
b0l-dvl	5	0.1	1.5	4.88	177.36	0.70	18.69	2.613	55.54
b0l-dl	5	0.5	1.5	3.88	177.23	0.72	15.06	2.587	49.26
b0l-dm	5	1	1.5	3.88	177.23	0.70	15.57	2.574	46.22
b0l-dh	5	5	1.5	4.13	177.22	0.70	16.74	2.541	39.69
b0l-dvh	5	10	1.5	4.38	177.22	0.72	17.22	2.527	37.10
b0m-dvl	10	0.1	1.5	4.51	177.14	0.75	17.43	2.460	54.15
b0m-dl	10	0.5	1.5	4.76	177.14	0.74	18.73	2.435	48.14
b0m-dm	10	1	1.5	4.76	177.14	0.72	19.35	2.424	45.74
b0m-dh	10	5	1.5	3.88	177.05	0.67	17.35	2.395	39.91
b0m-dvh	10	10	1.5	3.88	177.05	0.65	18.00	2.382	37.56
b0h-dvl	50	0.1	1.5	4.01	176.60	0.78	17.69	2.120	54.44
b0h-dl	50	0.5	1.5	4.01	176.60	0.73	19.05	2.094	48.32
b0h-dm	50	1	1.5	4.01	176.60	0.71	19.66	2.084	46.02
b0h-dh	50	5	1.5	3.01	176.42	0.66	16.59	2.054	39.94
b0h-dvh	50	10	1.5	3.38	176.40	0.74	16.77	2.037	36.91
b0vh-dvl	100	0.1	1.5	3.51	176.32	0.71	18.36	1.970	53.83
b0vh-dl	100	0.5	1.5	3.63	176.25	0.77	17.94	1.947	48.32
b0vh-dm	100	1	1.5	3.63	176.25	0.75	18.58	1.935	45.65
b0vh-dh	100	5	1.5	3.13	176.11	0.72	17.06	1.906	39.79
b0vh-dvh	100	10	1.5	3.13	176.11	0.70	17.75	1.892	37.22

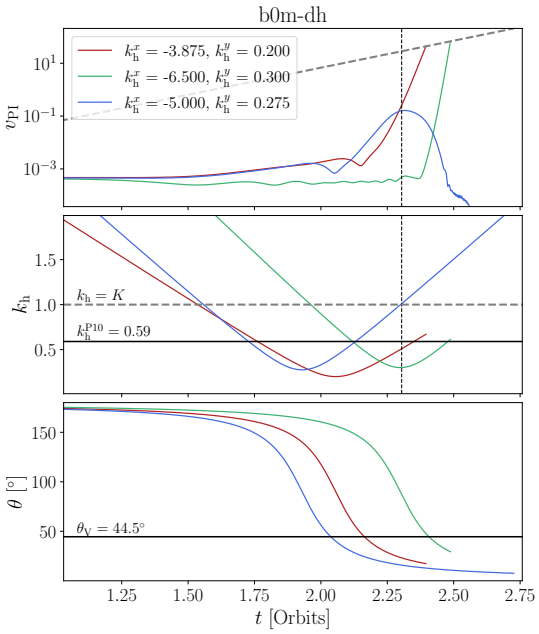

Figure 5.2 Top panel: time evolution of the averaged velocity of three parasitic modes from the run `b0m-dh`: the fastest (in red), another that saturates at later times (in green) and one mode that does not saturate (in blue). Middle panel: time evolution of the parasitic wavevector modulus $k_{\rm h}$ (following Equation (5.14)). Bottom panel: time evolution of the angle θ between the wavevector $\boldsymbol{k_{\rm h}}$ and the radial direction, x. One can see that the modes start growing faster when $k_{\rm h}$ and θ get close to the values appointed by Pessah 2010, $k_{\rm h}^{\rm P10}$ and $\theta^{\rm P10}$, respectively.

The top panel of Figure 5.2 depicts the time evolution of the velocity computed from Eq. (5.35) of some parasitic modes from the `b0m-dh` run. The red colored line represents the fastest parasitic mode, i.e., the mode that reaches the fraction ϵ of the MRI velocity in a shorter time. The green line corresponds to a mode that saturates at later times, and the blue line is a mode that does not reach saturation. The velocity of the mode that does not saturate starts decreasing at a certain point. This could be due to the fact that the angle θ becomes too small (see bottom panel), resulting in a negative growth rate [Pessah 2010]. Alternatively, this can result from $k_{\rm h}$ becoming larger than unity, i.e., larger than K (see middle panel). The values of $k_{\rm h}$ and θ at the right time are key to understand why certain modes grow faster than others. For the fastest growing mode (in red), θ starts decreasing before the slower mode (in green). This means that the fastest mode starts increasing before the mode in green, when the MRI velocity is $\sim 10^3 - 10^4$ times larger than the parasitic velocity, reaching values of $\theta \approx \theta_{\rm V}$ and $k_{\rm h} \approx k_{\rm h}^{\rm P10}$ at earlier times. The non-saturating mode (in blue) starts increasing even before the fastest mode, because θ decreases earlier. However,

k_h goes beyond 1 at some point (highlighted with the vertical dashed line) and therefore it does not saturate.

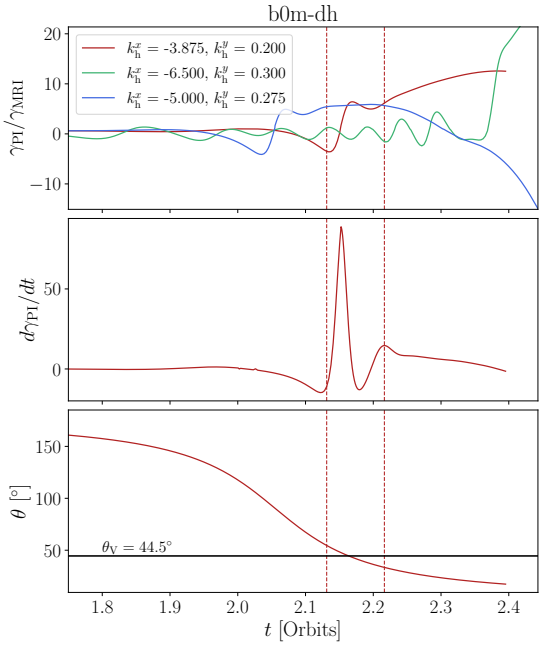

Figure 5.3 Top panel: time evolution of the normalised growth rate for the same modes as in Fig. 5.2. The growth rate stays considerably low up to a certain point, where it starts increasing to become more than ten times larger than the growth rate of the MRI (for the cases that reach saturation). Middle panel: evolution of the time derivative of γ_PI from the fastest mode. We draw vertical lines were the derivative takes positive values and at its last local maximum before saturation. In the bottom panel we show the evolution of θ with the same vertical lines.

We showcase in Figure 5.3 the time evolution of the growth rate of these PI modes (computed with Eq. (5.36)), normalised by the growth rate of the MRI from Eq. (5.8). The growth rate of the fastest mode starts increasing monotonically before the other mode that also saturates. There are some modes that reach a larger growth rate, but they saturate later because they get excited also later. The growth rate of the fastest growing mode starts increasing fast above 0 at $t \approx 2.15$ and then it continues growing at a slower rate. The middle panel shows the evolution of its time derivative. The region where the derivative takes positive values and increases faster coincides with values of θ (lower panel) around $\theta_\mathrm{V} = 44.5°$. The sudden decrease of the derivative between the fast growths is due to the MRI magnetic field, which is perpendicular to the MRI velocity. If no MRI magnetic fields were included, the parasitic growth rate

would increase monotonically, together with its derivative. This behaviour is also observed in the other cases from Table 5.2, and also for other modes that saturate at later times.

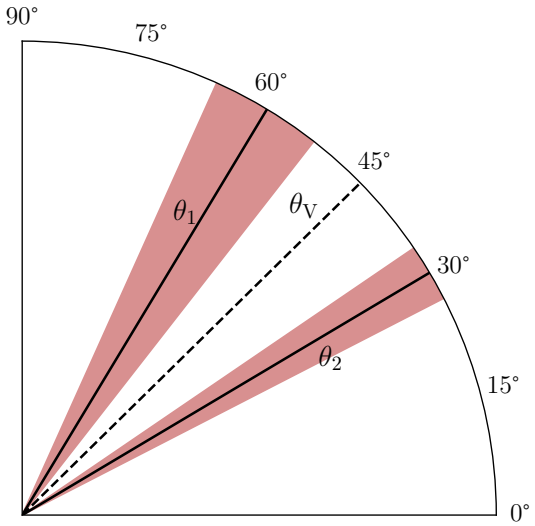

Figure 5.4 Values of the angle θ for which the PIs grow super-exponentially. The rapid increase of the secondary modes occurs between θ_1 and θ_2, depicted with solid black lines. These lines correspond to the mean value of these angles for the runs from Table 5.2. The red shaded regions represent the 1-σ deviation. The black dashed line stands for the direction of the MRI velocity field, $\theta_V = 44.5°$.

Figure 5.4 shows that the rapid increase of the parasitic modes coincides with the time-dependent wavevector $\boldsymbol{k}_\mathbf{h}$ being aligned with the MRI velocity field. When the growth rate starts increasing monotonically (at θ_1), the direction of $\boldsymbol{k}_\mathbf{h}$ is getting close to θ_V. The mode grows faster, and its increase slows down when θ goes below θ_V. The angle θ_2 of Fig. 5.4 corresponds to the last turning point of the growth rate before saturation. The black solid lines for θ_1 and θ_2 correspond to the mean value of these angles from the runs of Table 5.2, and the shaded regions in red depict the 1-σ deviation. After the braking of the parasitic growth, the fastest mode eventually saturates. This result is consistent with the findings made by Pessah 2010, even though the saturation criterion is different. In Pessah 2010, the saturation was estimated at the time when the parasitic growth rate equals the MRI one, while our criterion is the one given in Eq. (5.38). When the parasitic amplitude reaches a similar value than that of the MRI channel, the parasitic growth rate is already several times larger than the MRI growth rate (see Figure 5.3). Furthermore, with the current approach,

it takes more time to the MRI to saturate, leading also to a smaller $\theta^{\rm sat}$ and larger $k_{\rm h}^{\rm sat}$. This is in agreement with the predictions from Latter, Fromang, and Gressel 2010, who stated that it should take more time to saturate due to the inclusion of the background shear in the equations and thus the time dependence of $\boldsymbol{k_{\rm h}}$.

5.3.2 **The amplification factor**

For the sake of comparison, the authors of Rembiasz et al. 2016a computed several estimates of the amplification factor from the theoretical predictions made by Pessah 2010. Using the same saturation criterion as ours (Equation (5.38)), and assuming that the parasitic growth rate is given by

$$\gamma_{\rm PI}^{\rm P10} = \sigma K V \,, \tag{5.45}$$

where $\sigma = 0.27$ [Pessah and Goodman 2009], they obtained the following analytical expression for the parasitic velocity:

$$v(t) = v_0 \exp\left[\frac{\sigma K V_0}{\gamma_{\rm MRI}}(e^{\gamma_{\rm MRI} t} - 1)\right], \tag{5.46}$$

after considering that $\gamma_{\rm PI}^{\rm P10} \equiv \dot{v}(t)/v(t)$. We can obtain an estimate of the amplification factor by equalising $v(t_{\rm sat}) = V(t_{\rm sat})$, using the parasitic velocity from Equation (5.46). Moreover, Rembiasz et al. 2016a obtained an analytical expression for the amplification factor:

$$\mathcal{A} - \frac{1}{2\sigma}\ln\mathcal{A} = \frac{1}{2\sigma}\left[\ln\left(\frac{1}{v_0}\right) + \ln\left(\epsilon\sqrt{\frac{4q}{4-q}}\right)\right] + \sqrt{\frac{4-q}{4q}}V_0 \,. \tag{5.47}$$

Since initially $V_0 \ll 1$, the amplification factor should be almost independent of the initial MRI channel amplitude and depend logarithmically on the initial parasitic amplitude. As previously discussed, further work made by Latter, Fromang, and Gressel 2010 gave an approximate description of the inclusion of the background shear and the subsequent time dependence of the parasitic wavevector. The authors roughly estimated a reduction of $\gamma_{\rm PI}^{\rm P10}$ by a factor ≈ 2 as a result of the shear. Thus, in Rembiasz et al. 2016a, the authors computed an updated expression for the amplification factor, accounting for the shear, but keeping the channel amplitude constant during the rapid growth of the PIs:

$$\mathcal{A} - \frac{0.92}{\sigma}\ln\mathcal{A} = \frac{0.92}{\sigma}\left[\ln\left(\frac{1}{v_0}\right) + \ln\left(\epsilon\sqrt{\frac{4q}{4-q}}\right)\right] + \frac{1}{\sigma} \,, \tag{5.48}$$

which results in a larger amplification factor. For $v_0 = 10^{-3}$, Equation (5.48) yields

$$\mathcal{A} \approx 41\,, \tag{5.49}$$

which is very close to our result (see Tables 5.2 and 5.3).

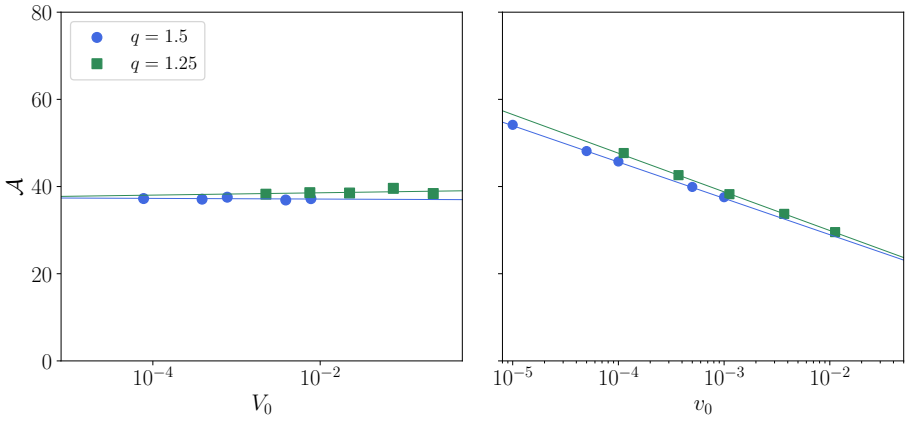

Figure 5.5 Left panel: dependence of the amplification factor (defined in 5.40) on the amplitude of the initial MRI velocity field, V_0, using the runs `b0vl-dvh, b0l-dvh, b0m-dvh, b0h-dvh, b0vh-dvh` (blue circles). We introduce the results from the runs `b0vl-dm-q125, b0l-dm-q125, b0m-dm-q125, b0h-dm-q125,b0vh-dm-q125` (green squares). Right panel: dependence of the amplification factor on the initial amplitude of the parasitic velocity, v_0, using the runs `b0vh-dvl, b0vh-dl, b0vh-dm, b0vh-dh, b0vh-dvh` (blue circles). The green squares represent the results from the runs `b0l-dvl-q125, b0l-dl-q125, b0l-dm-q125, b0l-dh-q125, b0l-dvh-q125`.

In Figure 5.5 we show the amplification factor defined in Eq. (5.40), for different choices of the initial MRI velocities, V_0 (left panel), and initial parasitic velocities, v_0 (right panel). We use runs with $q = 1.5$ from Table 5.2 (Keplerian shear, blue dots) and also $q = 1.25$ from Table 5.3 (green squares). Note that the initial amplitudes from Table 5.3 differ from those from Table 5.2, since we want to use the same initial values as in Rembiasz et al. 2016a. Since $q = 1.25$, the MRI wavenumber is now $K \approx 0.93$ and $V_0/B_0 \approx 0.67$. In the range of initial amplitudes we employed, the amplification factor presents values between 20 and 60. For a fixed initial parasitic amplitude, there is no strong dependence of the amplification factor on the initial MRI field. In contrast, there is a clear dependence on the initial parasitic amplitude. The initial amplitudes we fixed for both panels slightly differ between the runs with $q = 1.5$ (`b0vl-dvh, b0l-dvh, b0m-dvh, b0h-dvh, b0vh-dvh`) and the runs with $q = 1.25$ (`b0vl-dm-q125, b0l-dm-q125, b0m-dm-q125, b0h-dm-q125,b0vh-dm-q125`). However, the results are almost identical for both cases.

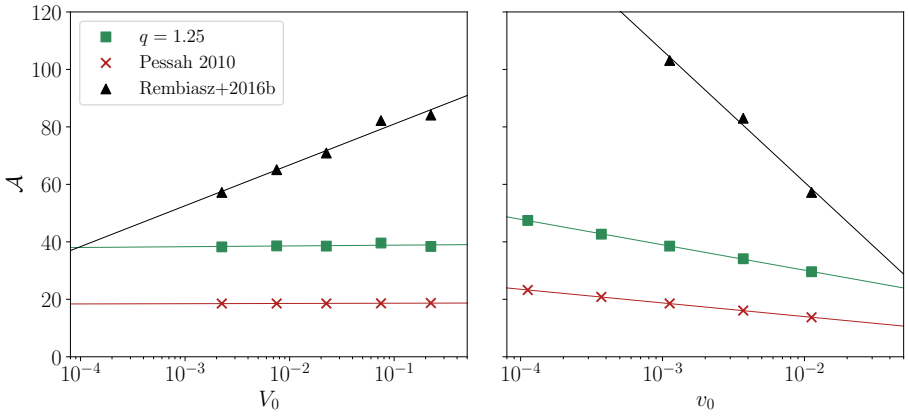

Figure 5.6 Same as Figure 5.5, but in this case we compare the runs with $q = 1.25$ (green squares), the results based on the approach from Eq. (5.46) (red crosses) and the results from the numerical simulations of Rembiasz et al. 2016a (black triangles). In the left panel, we use the runs `b0vl-dm-q125`, `b0l-dm-q125`, `b0m-dm-q125`, `b0h-dm-q125`, `b0vh-dm-q125`, whereas in the right panel, we use `b0m-dvl-q125`, `b0m-dl-q125`, `b0m-dm-q125`, `b0m-dh-q125`, `b0m-dvh-q125`.

Figure 5.6 shows the comparison between our evolutions with $q = 1.25$ and the amplification factors obtained in Rembiasz et al. 2016a with numerical box simulations using the pseudo-spectral code SNOOPY [Lesur and Longaretti 2005, Lesur and Longaretti 2007]. In this case, the differences are more notable. First, the simulations from Rembiasz et al. 2016a exhibit a stronger dependence of the amplification factor on the initial MRI velocity (left panel). Moreover, the slope in the right panel is also considerably larger than the one from our analyses. Having said that, our resulting amplification factors differ at about a factor ≈ 2 with respect to those from Rembiasz et al. 2016a. In addition, we draw the amplification factor obtained using the parasitic velocity from Equation (5.46) (red crosses). In this case, the amplification factors decrease a factor ≈ 2 with respect to ours.

We can obtain the relation between the choice of initial amplitudes of the turbulent fields and the amplification factor, as previously done in Rembiasz et al. 2016a:

$$\mathcal{A}(V_0, v_0) = a \ln V_0 + b \ln v_0 + c\,. \tag{5.50}$$

Using all the runs from Table 5.2, with $q = 1.5$, the values for the coefficients turn out to be $a = -0.14 \pm 0.04$, $b = -3.80 \pm 0.04$ and $c = 10.0 \pm 0.5$. For the runs from Table 5.3, with $q = 1.25$, the coefficients are $a = 0.07 \pm 0.04$, $b = -3.86 \pm 0.04$ and $c = 12.6 \pm 0.3$. The dependencies in both cases are almost

the same, except for the case of the coefficient a, which changes sign. This might be due to the use of different initial amplitudes and the slight change in the shear factor q. However, the magnitude of this coefficient is very small compared to b, which means that the amplification factor barely depends on the initial channel amplitude. With the approach from Equation (5.46), with $q = 1.25$, we obtain $a = 0.036 \pm 0.006$, $b = -2.06 \pm 0.006$ and $c = 4.675 \pm 0.046$. In Rembiasz et al. 2016a, the factors that multiply the logarithms of the initial amplitudes are $a = 5.4 \pm 0.55$ and $b = -20.2 \pm 1.2$, being larger than those obtained with our approach.

The discrepancy between our results and the ones given in Rembiasz et al. 2016a can be partly explained by the difference in the initial conditions. In our case, the initial MRI fields are given by Eq. (5.6), corresponding to the fastest growing MRI mode. In addition, the parasitic mode is the one that reaches the saturation threshold first. Alternatively, Rembiasz et al. 2016a only excited the fastest growing velocity MRI field (letting the magnetic MRI field grow later), and they excited a large set of parasitic velocities applying random factors to their initial amplitudes. Our approach focused directly on the dynamics of the fastest modes involved. In addition, nonlinearities that may arise at termination are not captured by our approach. In the nonlinear regime of the KHI, a growth rate reduction is expected when saturation approaches, meaning that our predictions might underestimate the amplification factor.

It is worth mentioning that Rembiasz et al. 2016a performed simulations with another numerical code, Aenus [Obergaulinger 2008], with different boundary conditions, physical assumptions and numerical schemes. The resulting amplification factor differed in some cases by a factor 5 from that obtained with the SNOOPY code. Moreover, they found that employing a different form of the initial perturbations also changed the amplification factor, obtaining $\mathcal{A} \approx 90$ instead of $\mathcal{A} \approx 60$. Thus, differences in the simulation setup and the use of different numerical codes can have an impact on the amplification factor.

Table 5.3 Same as Table 5.2, but using now a shear factor $q = 1.25$ and different initial amplitudes to make a better comparison with the results from Rembiasz et al. 2016a.

NAME	$B_0[10^{-3}]$	$v_0[10^{-3}]$	q	$k_{\rm h}^{\rm ini}$	$\theta^{\rm ini}$ [°]	$k_{\rm h}^{\rm sat}$	θsat [°]	$t_{\rm sat}$ [Orbits]	$\mathcal{A}$
b0vl-dvl-q125	3.33	0.112	1.25	3.76	176.76	0.65	19.16	2.613	47.69
b0vl-dl-q125	3.33	0.370	1.25	4.13	176.70	0.74	18.84	2.584	42.61
b0vl-dm-q125	3.33	1.12	1.25	4.13	176.70	0.69	20.22	2.557	38.24
b0vl-dh-q125	3.33	3.70	1.25	4.51	176.66	0.75	20.40	2.525	33.73
b0vl-dvh-q125	3.33	11.2	1.25	3.51	176.53	0.69	17.90	2.491	29.54
b0l-dvl-q125	11.1	0.112	1.25	3.88	176.31	0.69	21.15	2.303	47.16
b0l-dl-q125	11.1	0.370	1.25	3.38	176.19	0.69	19.16	2.276	42.54
b0l-dm-q125	11.1	1.12	1.25	3.38	176.19	0.64	20.44	2.252	38.59
b0l-dh-q125	11.1	3.70	1.25	3.88	176.13	0.74	20.72	2.216	33.57
b0l-dvh-q125	11.1	11.2	1.25	3.01	175.95	0.68	18.28	2.183	29.48
b0m-dvl-q125	33.3	0.112	1.25	2.76	175.58	0.67	18.62	2.026	47.45
b0m-dl-q125	33.3	0.370	1.25	2.88	175.53	0.69	18.91	1.999	42.67
b0m-dm-q125	33.3	1.12	1.25	3.01	175.47	0.72	19.27	1.973	38.51
b0m-dh-q125	33.3	3.70	1.25	3.14	175.43	0.73	19.98	1.941	34.11
b0m-dvh-q125	33.3	112	1.25	2.38	175.19	0.65	17.93	1.906	29.60
b0h-dvl-q125	111	0.112	1.25	2.26	174.61	0.66	18.89	1.720	47.66
b0h-dl-q125	111	0.370	1.25	2.39	174.59	0.66	19.93	1.695	43.21
b0h-dm-q125	111	1.12	1.25	2.39	174.59	0.62	21.16	1.673	39.59
b0h-dh-q125	111	3.70	1.25	2.64	174.29	0.80	19.19	1.639	34.65
b0h-dvh-q125	111	112	1.25	2.01	173.94	0.70	17.60	1.600	29.72
b0vh-dvl-q125	333	0.112	1.25	2.27	173.35	0.76	20.15	1.438	47.25
b0vh-dl-q125	333	0.370	1.25	2.27	173.35	0.71	21.59	1.413	42.81
b0vh-dm-q125	333	1.12	1.25	2.02	172.88	0.76	19.14	1.385	38.40
b0vh-dh-q125	333	3.70	1.25	2.02	172.88	0.70	20.88	1.352	33.71
b0vh-dvh-q125	333	11.2	1.25	2.14	172.63	0.78	20.71	1.321	29.77

5.3.3 **Effective growth rate**

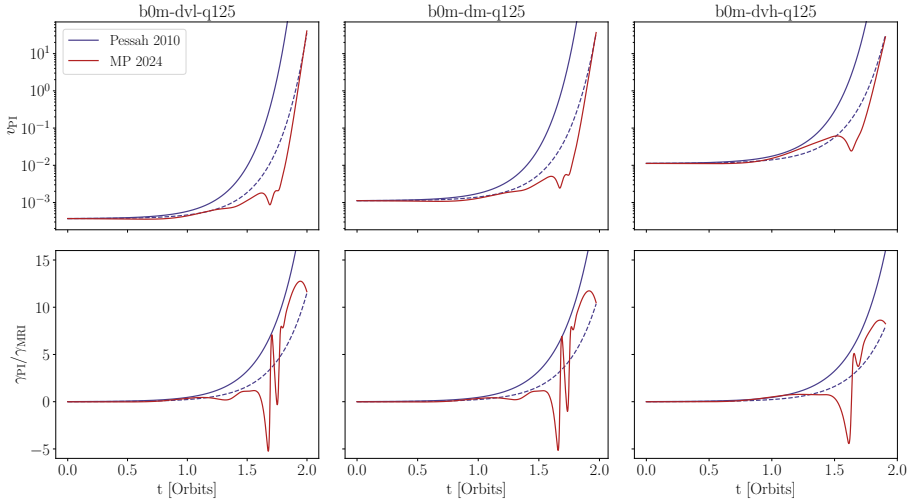

Figure 5.7 Upper panels: time evolution of the parasitic velocity for different initial amplitudes of the PIs (from left to right, $v_0 = \{0.112, 1.12, 11.2\} \times 10^{-3}$) and a fixed initial MRI field, $B_0 = 3.33 \times 10^{-2}$. The solid blue lines refer to the evolution of the parasitic velocity given in Eq. (5.46), whereas the red lines correspond to our approach. The dashed blue lines refer to the same velocity from Eq. (5.46), but adding the correcting factor f to the parasitic growth rate from Eq. (5.45). Lower panels: time evolution of the normalised parasitic growth rate. By adding the correcting factor f to the expression from Eq. (5.45) (dashed blue lines), the parasitic growth rate is more similar to the one we obtain in our study (solid red lines).

In the previous subsection, we have seen that the inclusion of the background shear results in an effective reduction of the parasitic growth rate presented in Equation (5.45). To quantify the difference between the results from Pessah 2010 and our approach, we compute the factor, f, that needs to be applied to the parasitic growth rate from Eq. (5.45) to end up with the amplification factors obtained with our approach, which are closer to those from numerical simulations. Employing the runs from Table 5.3, we get that, on average, the factor needed is

$$f = 0.498 \pm 0.006\,, \tag{5.51}$$

which is in agreement with the prediction made by Latter, Fromang, and Gressel 2010, who estimated a reduction by a factor ≈ 2. Moreover, we observe that this fraction f is independent of the initial parasitic and MRI amplitudes.

The upper panels from Figure 5.7 depict the evolution of the parasitic velocity using Equation (5.46) (solid blue line), using the same equation but introducing the factor f in Eq. (5.45) (dashed blue line), and our approach (solid red line). As

expected, the solid blue curve grows faster than the red one, since Equation (5.46) assumes that the wavevector $\boldsymbol{k}_{\mathbf{h}}$ is constant and aligned with the MRI velocity. In the lower panels we show the evolution of the normalised parasitic growth rate. By introducing the factor f from Equation (5.51) in the analytical expression for the parasitic growth rate from Pessah 2010, we are able to reach the same amplitude as if we consider the effect of the background shear, resulting in a time-dependent wavevector.

5.4 Discussion and conclusions

The role of the PIs in the saturation of the MRI has been studied thoroughly during the last decade [Obergaulinger et al. 2009, Sorathia et al. 2012, Rembiasz et al. 2016b, Hirai et al. 2018, Gogichaishvili et al. 2018]. First proposed by Goodman and Xu 1994, these instabilities feed off the MRI and disrupt the channel modes, terminating the growth of the primary instability leading to a turbulent regime. The correct understanding of this mechanism is key to properly model the angular momentum transport and magnetic field amplification in accretion discs, PNSs and BNS merger remnants. If well treated, these phenomena can have important implications in the evolution and stability of these astrophysical systems.

Several analytical studies have been performed to provide further insight into the linear growth of the MRI [Pessah, Chan, and Psaltis 2006b, Pessah and Chan 2008, Lesaffre, Balbus, and Latter 2009], and also to study the excitation of the parasitic modes and the subsequent saturation of the primary instability [Latter, Lesaffre, and Balbus 2009, Latter, Fromang, and Gressel 2010, Pessah and Goodman 2009, Pessah 2010]. In this work, we relax some assumptions made in past studies and provide a more accurate analysis of the time evolution of the spectrum of parasitic modes in the context of ideal MHD. We perform a local linear approach similar to Pessah 2010, assuming that the MRI mode evolves unimpeded, i.e., treated as a background field. In contrast to Latter, Lesaffre, and Balbus 2009, Pessah 2010, we keep the background shear velocity and vertical magnetic fields in the linearised MHD equations. Furthermore, we take into account the time dependence of the parasitic horizontal wavevector that arises from the background shear. Using a dense grid of initial wavevectors, we explore the spectrum of parasitic modes and look for the fastest one that saturates the MRI.

The resolution of the system of coupled differential equations for the Fourier amplitudes of the parasitic modes allows us to follow their growth. As observed

in numerical simulations [Rembiasz et al. 2016b, Rembiasz et al. 2016a], these secondary instabilities start growing super-exponentially once the MRI mode has reached a certain amplitude. When the parasitic modes achieve a similar amplitude than the primary instability, we stop the amplification of the magnetic and velocity fields from both the MRI and the PI modes.

During the evolution, the x-component of the parasitic wavevector increases linearly and proportionally to its y-component. Therefore, the inclination angle with respect to the x-axis decreases until it asymptotically reaches 0°. We found that the fastest parasitic modes start their rapid growth when their wavevector is almost aligned with the direction of the MRI velocity, at $\theta_{\rm V} \approx 45°$, as stated in Pessah 2010 and in agreement with several numerical studies [Rembiasz et al. 2016b, Hirai et al. 2018]. Indeed, their increase slows down after the parasitic wavevector passes through $\theta_{\rm V}$. Moreover, the value of the wavenumber at saturation is similar to the one found in Pessah 2010. The parasitic wavenumbers, $k_{\rm h}$, at saturation found in numerical simulations [Rembiasz et al. 2016b, Hirai et al. 2018] are somewhat larger than those obtained here. This can be explained by the existence of other MRI modes (that grow more slowly), which results in a shear flow that is not purely sinusoidal [Hirai et al. 2018]. Moreover, the interaction of the PIs with the channels can cause the layered structure to become narrower, which induces a smaller parasitic mode just before saturation [Hirai et al. 2018]. Unfortunately, these nonlinear effects cannot be captured by our approach.

The analysis performed in this Chapter has allowed us to compute the amplification factor of the MRI with different initial amplitudes of both the primary and secondary modes, and different values of the shear factor. We observed that the choice of the seed fields can have an impact on the amplification factor, as opposed to the choice of the shear. For larger initial parasitic amplitudes, the modes saturate before because their amplitude is initially closer to that of the primary field. This behaviour has also been observed in numerical box simulations [Rembiasz et al. 2016a], but in that case the amplification factor is more dependent on the initial conditions. We have also seen that, with our approach, the amplification factor barely depends on the initial channel amplitude, as expected from the analytical predictions of Pessah 2010. This contrasts with the results from numerical simulations, which show an increase of the amplification factor with the MRI amplitude.

The inclusion of the background shear in the analysis of the evolution of the PIs results in a slower growth with respect to previous analyses where the parasitic wavevector was assumed to be aligned with the MRI velocity [Pessah

2010]. Thus, in order to include the effect of the misalignment of the time-dependent wavevector, we have introduced a correcting factor in the analytical expression of the parasitic growth rate obtained by [Pessah 2010]. This factor f, which is independent of the initial amplitudes of the instabilities, reduces the growth rate by half, as expected from the analytical estimations by Latter, Fromang, and Gressel 2010.

There is some discrepancy between our analytical findings and the results from numerical simulations of the MRI. The amplification factors obtained in our study are somewhat smaller to the ones obtained by Rembiasz et al. 2016a. The nonlinearities that arise when the PI amplitude is comparable to the MRI are expected to reduce the growth rate of the PI, which results in a larger amplification factor. Moreover, these differences can be partly due to the way the initial perturbations are excited in the simulations. In fact, [Rembiasz et al. 2016a] observed that the form of the seed perturbations had an impact on the amplification factor. Furthermore, the use of different numerical codes with different boundary conditions and numerical schemes can also lead to discrepancies. An important result from our work is that the amplification factor seems to be less dependent on the initial perturbations than expected from previous numerical simulations. Another implication of our results is that numerical simulations would need a high resolution in the horizontal plane to solve the fastest parasitic modes, since they are found to be initially $\sim 3-5$ times smaller than the MRI channels.

Despite the several differences found between numerical works and our findings, which are mostly due to nonlinearities and the setup of the simulations, the predicted amplification factors are in good agreement, as well as the value of the fastest parasitic wavevector at saturation. In addition, both approaches identify the parasitic modes as KH instabilities that disrupt the MRI channels when they are aligned.

Appendix

5.A Physical structure of the parasitic modes

To study the structure of the parasitic modes and the disruption of the MRI channels, we calculate the components of the vorticity and current density perpendicular to the plane $(\check{\boldsymbol{k}}_{\mathbf{h}}, \check{\boldsymbol{z}})$:

$$\delta\omega_{\perp}(t;\boldsymbol{x}) = (\boldsymbol{\nabla}\times\boldsymbol{v})\cdot\check{\boldsymbol{k}}_{p} \tag{5.52}$$

$$\delta j_{\perp}(t;\boldsymbol{x}) = (\boldsymbol{\nabla}\times\boldsymbol{b})\cdot\check{\boldsymbol{k}}_{p}\,, \tag{5.53}$$

where $\check{\boldsymbol{k}}_{\mathbf{p}}$ is the direction perpendicular to $(\check{\boldsymbol{k}}_{\mathbf{h}}, \check{\boldsymbol{z}})$: $\check{\boldsymbol{k}}_{\mathbf{p}} \equiv \check{\boldsymbol{z}}\wedge\check{\boldsymbol{k}}_{\mathbf{h}}$. Using Eqs. (5.33) and (5.34), we obtain

$$\delta\omega_{\perp}(t;\boldsymbol{x}) = -\frac{i}{k_{\mathrm{h}}}\sum_{n=-\infty}^{\infty}[k_{\mathrm{h}}^2+(n+k_z)^2]\alpha_n(t)e^{i(n+k_z)z}e^{ik_{\mathrm{h}}h} \tag{5.54}$$

$$\delta j_{\perp}(t;\boldsymbol{x}) = -\frac{i}{k_{\mathrm{h}}}\sum_{n=-\infty}^{\infty}[k_{\mathrm{h}}^2+(n+k_z)^2]\beta_n(t)e^{i(n+k_z)z}e^{ik_{\mathrm{h}}h}\,, \tag{5.55}$$

where $k_{\mathrm{h}}h = \boldsymbol{k_h}\cdot\boldsymbol{x}$. The total vorticity and current can be obtained by adding the contribution from the MRI fields projected onto the direction $\check{\boldsymbol{k}}_h$:

$$\omega_{\perp}(t;\boldsymbol{x}) = V_0 e^{\gamma_{\mathrm{MRI}}t}\cos(Kz)\cos(\theta-\theta_{\mathrm{V}}) + \delta\omega_{\perp}(t;\boldsymbol{x}) \tag{5.56}$$

$$j_{\perp}(t;\boldsymbol{x}) = -B_0 e^{\gamma_{\mathrm{MRI}}t}\sin(Kz)\cos(\theta-\theta_{\mathrm{B}}) + \delta j_{\perp}(t;\boldsymbol{x})\,. \tag{5.57}$$

In Figure 5.A.1 we depict the total vorticity field $\omega_{\perp}$ projected onto the plane $(\check{\boldsymbol{k}}_h, \check{\boldsymbol{z}})$, where the arrows represent the total velocity $\boldsymbol{V}+\boldsymbol{v}$ (upper panels) and the vorticity of the parasitic mode $\delta\omega_{\perp}$ with the velocity field $\boldsymbol{v}$ (lower panels), for different times. At early times (first panel) the MRI channels remain steady since the fastest parasitic mode has not reached enough amplitude yet. When saturation approaches (last three panels) the channels are disrupted by the parasitic mode, showing the familiar wave-like structure expected from KHI modes in a periodic background. The lower panels representing the vorticity

and velocity fields of the parasitic mode show a periodic structure of equidistant vortex sheets, similar to those in Figure 8 from Pessah 2010, but transitioning in time to more elongated structures.

Alternatively, Figure 5.A.2 shows the current density and magnetic fields instead of the vorticity and the velocity fields. The magnetic parasitic field forms again periodic vortex sheets that become horizontally elongated as saturation approaches. The MRI channels get disrupted and adopt the same structure as shown in Figure 10 from [Pessah 2010].

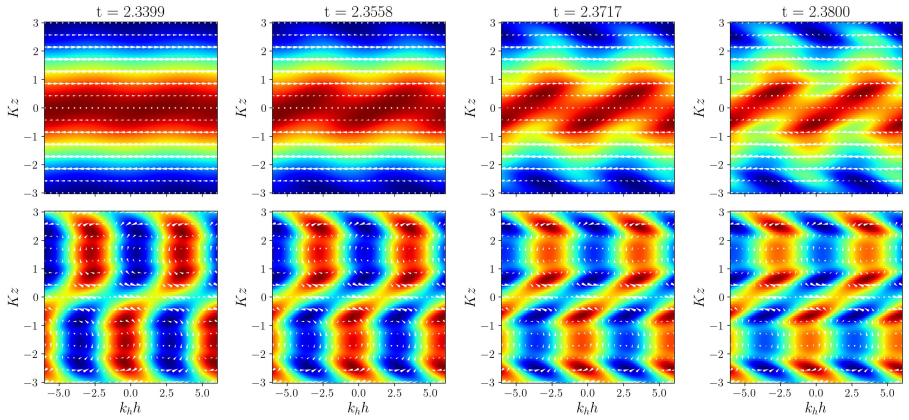

Figure 5.A.1 Physical structure of the fastest parasitic modes, including the velocity field of the primary MRI mode, for different times (increasing from left to right). The arrows in the upper and lower panels correspond, respectively, to the projections of the total velocity, $\boldsymbol{V}(z) + \boldsymbol{v}(h, z)$, and the parasitic velocity, $\boldsymbol{v}(h, z)$, onto the time-dependent plane $(\check{\boldsymbol{k}}_{\mathbf{h}}, \check{z})$. The coloured contours correspond to the associated total vorticity $\omega_\perp$ and the parasitic vorticity $\delta\omega_\perp$ projected onto the direction perpendicular to $\check{\boldsymbol{k}}_{\mathbf{h}}$.

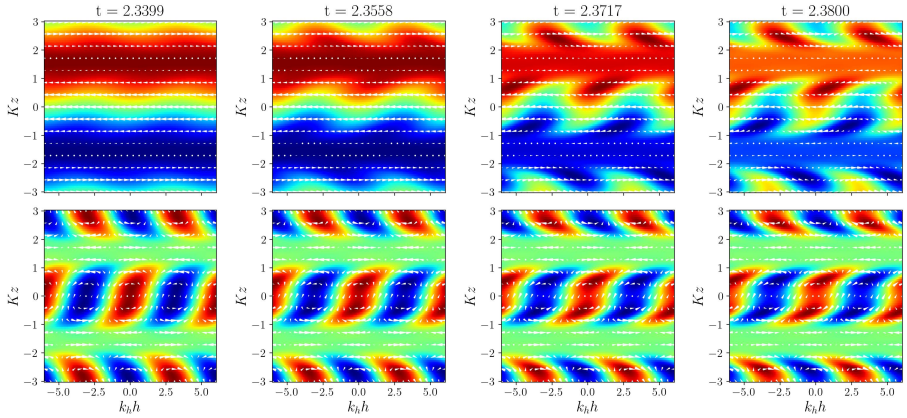

Figure 5.A.2 Same as Figure 5.A.1, but including the magnetic and the current density fields instead of the velocity and the vorticity, respectively.

CHAPTER 6

Summary of part I and future work

In this first part of the thesis, I presented my work focused on the understanding and modelling of MHD turbulence in the context of NSs and their mergers.

6.1 The MInIT model

In **Chapters 2 and 3**, I developed a new sub-grid model for MHD turbulence triggered by the MRI (Chapter 2) and the KHI (Chapter 3): the MInIT mean-field model. Both versions of the model are based on the temporal evolution of the turbulent kinetic energy densities and their connection with the turbulent stress tensors that arise in the mean-field MHD equations. The turbulent stresses represent the effect of the small-scale dynamics in the nonlinear equations.

The work developed in **Chapter 2** focuses on the modelling of turbulence that arises from the MRI. This instability plays an important role in the transport of angular momentum and amplification of weak magnetic fields in accretion discs, newly born PNSs and HMNS merger remnants, which are rapidly differentially rotating objects. After discussing two existing sub-grid approaches, the α,β-dynamo and the gradient models, I turned to describe specific features of the MInIT model, namely the introduction of two partial-differential equations for the energy densities, accounting for the MRI itself and the PI. The model is able to capture the exponential growth of the primary instability and the eventual saturation due to the rapid evolution of the secondary instability, which dissipates at the end of the Kolmogorov cascade. Once the evolution equations for the turbulent energy densities are solved, the turbulent stress tensors are

obtained via the application of constant coefficients to the turbulent energy densities. On the one hand, the coefficients for the MRI energy density are known from previous analytical studies. On the other hand, the PI coefficients have been obtained from control numerical simulations with different resolutions and initial vertical magnetic fields.

In **Chapter 3**, I presented the MInIT model version for the KHI. Since the PI modelled in the previous Chapter is of KH type, the partial-differential evolution equation of the turbulent energy density in this case is similar to the one for the parasitic energy density. For this instability, the growth rate is given by the velocity jump generated by the shear. The dissipation term is the same as the one suggested for the MRI version. By making a comparison with three-dimensional box simulations of the KHI with different resolutions and initial magnetic fields, I obtained the proportionality coefficients that link the turbulent kinetic energy density with the turbulent stresses, as done in Chapter 2.

To assess both versions of the MInIT model, I performed an a-priori test. Using data from control numerical simulations, a box filter was applied to see the difference between the quantities given by the model and the filtered ones from the simulations. For a quantitative comparison, I computed the L_2 relative-error norm. In both versions of the model, the norm takes values around ~ 1 for the Maxwell and Reynolds stresses, being slightly smaller for the KHI version. Also, no dependence on the filter size was observed in the assessment of the sub-grid model. Thus, this means that it is possible to obtain order-of-magnitude accurate estimates of these quantities when applying the model. Furthermore, in its comparison with the gradient model, it was found in Chapter 2 that the MInIT model performs with a similar accuracy. Unfortunately, the Faraday stress tensor gives less accurate results. Since, in both cases, the evolution of this tensor components oscillate around zero, the resulting coefficients are compatible with a zero value. Given the role of this tensor in the generation of large-scale dynamos, future studies and extensions of the model should focus on a better treatment of this quantity. It is however worth highlighting that the similar findings in the assessment of the model for different MHD instabilities demonstrates its universality.

In the following, I summarise ongoing and future applications of the MInIT model in the context of BNS merger simulations:

6.1.1 **Application to numerical simulations**

The theoretical framework developed in Chapters 2 and 3 can be applied to numerical simulations of several astrophysical scenarios. Magnetised discs at different scales, such as discs around compact objects, protostellar and protoplanetary discs, or differentially rotating PNSs can be prone to the MRI. However, the physical conditions in some of such scenarios can go beyond ideal MHD, with smaller values of the Reynolds number and magnetic fields with different strengths. In those cases, the coefficients for the turbulent stresses may be different. Therefore, a more general formulation of the model that also accounts for non-ideal effects would be necessary. Unfortunately, performing three-dimensional non-ideal MHD simulations is not an easy task, and an a-priori test of the re-formulated model would be fairly challenging.

In **Chapter 4**, I have presented the first application of the MInIT model to a global simulation of a differentially rotating NS that is prone to the MRI. By performing axisymmetric MHD simulations with low resolution (or at least not high enough to resolve the MRI) including the sub-grid-scale terms, angular momentum transport is triggered in the star. The rotational profile flattens, driving the star to a more uniform rotation in its central regions. It was also observed that, in those regions, the turbulent energy densities eventually decrease, since MRI turbulence decays due to the absence of differential rotation. The temporal evolution of the turbulent energies is the same as shown in Chapter 2. However, in this preliminary work only the momentum equation was modified by including the Maxwell and Reynolds stresses. For a more complete study of the model, the inclusion of the Faraday tensor is key. When better modelled, additional LES involving the Faraday stress as well would provide a more accurate picture of the large-scale effects of turbulence, and might also show an efficient magnetic-field amplification.

In order to improve the modelling of the Faraday stress tensor in the context of the MRI, it would be useful to include the characteristic dynamo oscillations in the proportionality coefficients for the tensor. To do so, a mixture between the α, β-dynamo model and the MInIT model could help. Adding the time variability of quantities such as the large-scale magnetic field in the model could result in non-zero coefficients that would allow for an efficient large-scale dynamo. For the KHI version, longer simulations would be needed to obtain more statistics to better model the Faraday stress components. Moreover, simulations with sustained turbulence might be helpful to reach this goal.

BNS mergers are not the only scenario that is planned to be studied. Turbulence (and more concretely, the MRI) arises in other astrophysical systems, such as PNSs and accretion discs around massive BHs, as mentioned earlier. If the PNS is formed in a magnetorotational explosion, characterised by a rapid rotation and intense magnetic fields, the MRI can play a role in the early evolution of the newly born PNS. Thus, the MInIT model could also be applied in this scenario to study the angular momentum transport and magnetic-field amplification, and even the Newtonian version might be valid here, since the majority of CCSNe simulations are performed within this frame. Regarding accretion discs around (super)massive BHs, MRI turbulence can also arise from the differential rotation of the disc and the weak magnetic fields present there. However, as already mentioned, the magnetic field strengths and dissipative effects can be considerably different from those from the BNS scenario. If further studies with the MInIT model are performed employing the characteristic values of the physical quantities involved, it might be possible to properly study the development of turbulence in this scenario, and link the numerical results with the recent observations of M87 and Sagittarius A* from the Event Horizon Telescope (EHT) [Event Horizon Telescope Collaboration et al. 2019, Event Horizon Telescope Collaboration et al. 2024].

6.1.2 General-relativistic approach

Another prospect is the generalisation to curved spacetimes. Realistic simulations of BNS mergers are performed within GR. Additional metric-dependent terms would be required in the equations for the turbulent energy densities, and also in the mean-field MHD equations. Moreover, covariance should be preserved in the equations, and not every sub-grid approach does so. Some works [Celora et al. 2021, Celora et al. 2024] have already proposed a covariant scheme applied to relativistic LES using a Lagrangian filter. This technique consists in the application of the filtering scheme with respect to a co-moving observer that moves along the fluid. The application of the filter arises sub-grid-scale residuals that can be regarded as non-ideal contributions.

The covariant formulation I am currently developing is based on the following. The starting point is to devise a procedure to face the issue that, in general, it is not possible to define the average of a tensor in a covariant way. The problem is that, although it is possible to express the volume integral of a scalar as a scalar, this is not possible for tensors of higher rank. Therefore, the averaging procedure is defined at each point in a special frame, dubbed the *mean rest fluid frame (MRFF)*, such that the computation of those quantities would be

the same irrespectively of the observer. The procedure is similar to what is implicitly assumed when one describes the thermodynamics of a fluid in the rest frame. A loose definition of the MRFF, $\{x^{\bar{\mu}}\}$, of a point P, would be:

- It is a local inertial frame.
- The "mean velocity" of the fluid in a small neighbourhood of P, computed in this frame, is zero.
- The spatial axes are oriented in a certain way with the shear of the fluid.

In this frame, the metric is thus Minkowski at P. One can perform a boost and a spatial rotation, i.e., a transformation within the Lorentz group. This boost can result in a mean zero 4-velocity at P, $\bar{u}^{\bar{\mu}}|_P = (1, 0, 0, 0)$. Moreover, since the aim of this work is to provide a framework to study turbulence generated by rotating and sheared fluids, it is natural to choose an axis orientation aligned with the shear of the fluid. That would ease the formulation of closure models based on local simulations that can be used as sub-grid models for global simulations.

Currently, I am working on the application of this covariant scheme within the MInIT model to perform GRMHD simulations of weakly magnetised differentially rotating HMNS remnants including the MInIT model.

6.2 Revisiting the saturation of the magnetorotational instability

In **Chapter 5**, I discussed a local analytical study of the saturation of the MRI by secondary PIs. This analysis includes the background shear velocity and the net vertical large-scale magnetic field in the equations for the parasitic perturbations, in addition to the velocity and magnetic MRI fields which are treated as background as well. The shear introduces a time dependence to the parasitic wavevector that can result in a different saturation amplitude of the MRI magnetic field. These secondary instabilities are initially very small compared to the MRI channel modes, but they grow super-exponentially until they eventually disrupt the channels and saturate the exponential amplification of the MRI fields. In the context of ideal MHD, i.e., for low values of kinetic viscosity and resistivity, the parasitic modes grow faster when their wavevector is aligned with the MRI velocity field. This means that the parasitic modes are of KH type, as one would expect. Also, the wavenumber needs to be smaller than the MRI's for the instability to grow. Due to its time dependence, the wavevector will only be aligned with the primary velocity field during a small

period of time. For this reason, the PIs do not grow as fast as it is expected when their wavevector is treated as static. Besides these differences, the analysis provides consistent results, similar to the ones obtained in previous analytical and numerical studies. With this approach, I have been able to study in more detail the time evolution of several parasitic modes (not only the fastest ones) and the way they feed from the primary instability, something difficult to observe in numerical simulations. In contrast to other analytical works, this study allows to follow the evolution of the parasitic growth rate and to test different initial amplitudes of the primary and secondary instabilities.

By making a comparison with results from three-dimensional box simulations, it was found that the amplification factor of the MRI magnetic field is closer to the numerical one than other previous linear analyses. Furthermore, the dependence of this amplification on the initial amplitude of the parasitic and primary fields is also similar. However, this dependence is not as strong as numerical simulations suggest, where one would always find an amplification factor between $\sim 20 - 80$ regardless the amplitude of the initial perturbations and the value of the shear factor. Nevertheless, it is difficult to compare between results from local linear analyses and those from numerical simulations. The numerical perturbations that may arise in simulations can alter the dynamics of the flow and also limit the control that one has on the initial conditions of the system. Moreover, the way perturbations are excited in simulations differs completely from the initial configuration of the instabilities in linear analyses. It was also observed in numerical studies that the use of different numerical codes with different boundary conditions and numerical schemes can also lead to discrepancies between different simulations. In addition, when the amplitudes of the PIs and the MRI are compatible, the nonlinear effects are expected to decrease the parasitic growth rate and therefore yield a higher amplification factor, which would also explain its larger values obtained in numerical simulations.

The inclusion of the background shear in the analysis of the evolution of the PIs results in a slower growth with respect to previous analyses where the parasitic wavevector was assumed to be aligned with the MRI velocity. A correcting factor f, which accounts for this effect, can be added to the analytical expression of the parasitic growth rate from Chapter 2. This growth rate is used in the evolution equation for the turbulent energy density of the PI, and therefore it would slightly increase the saturation amplitude of the turbulent energy density of the MRI. The reduced growth rate might change the value of the C parameter of the MInIT model, and further tests might be required.

6.2.1 **Future studies and numerical simulations**

Even though the results presented in this Chapter are in agreement with several local box simulations of the MRI, there is still room for improvement in the treatment of PIs. This Chapter focused on the ideal MHD case, which is a good approximation to study NS interiors. Nevertheless, the MRI can also play a role in other astrophysical systems such as accretion discs, where viscosity and resistivity may exhibit non-negligible values. Thus, it would be of interest to perform a similar analysis for larger values of viscosity and resistivity to study the growth of the fastest parasitic mode in this context. Moreover, the inclusion of neutrinos in numerical simulations can be performed via an effective viscosity. Thus, going beyond the ideal MHD limit also means studying the effect of neutrinos in the growth and saturation of the MRI.

Moreover, the fastest parasitic modes found in this analysis have larger initial wavenumbers than the primary MRI ones. This means that, in order to capture the growth of these rapidly growing modes, sufficiently high resolution in the horizontal plane is required. More concretely, these modes seem to possess wavelengths approximately up to four times smaller than the primary channel sizes. Numerical simulations with insufficient resolution might miss the evolution of the fastest secondary instabilities, which would result in a larger amplification factor. Moreover, the way initial perturbations are excited in numerical simulations may have an impact in the consequent dynamics of the system. Applying random perturbations of small amplitude to excite both the MRI and parasitic fields may delay the growth of the instabilities. Alternatively, exciting the fastest primary and secondary modes by choosing the proper wavevectors could result in a prompt saturation.

Part II

Gravitational-wave data analysis

CHAPTER 7

Prospects for the inference of inertial modes from hypermassive neutron stars with future gravitational-wave detectors

This Chapter was originally published in: **Miquel Miravet-Tenés**, Florencia L. Castillo, Roberto De Pietri, Pablo Cerdá-Durán and José A. Font. *Prospects for the inference of inertial modes from hypermassive neutron stars with future gravitational-wave detectors. Phys. Rev. D*, Volume 107, Issue 10, pp. 103053, May 2023. DOI: 10.1103/PhysRevD.107.103053. *Reproduced with permission.*

7.1 Introduction

As discussed in the Introduction (Section 1.4), during the first few milliseconds after its formation, the HMNS exhibits strong nonaxisymmetric deformations and nonlinear oscillations, namely combinations of oscillation modes and spiral deformations [Stergioulas et al. 2011, Hotokezaka et al. 2013, Bauswein and Stergioulas 2015, Takami, Rezzolla, and Baiotti 2015, Bauswein, Stergioulas, and Janka 2016, Bauswein and Stergioulas 2019]. This is accompanied by the emission of GWs in a range of frequencies around a few kHz [Shibata and Uryū 2000, Oechslin, Rosswog, and Thielemann 2002, Baiotti, Giacomazzo, and Rezzolla 2008, Stergioulas et al. 2011, Bauswein and Janka 2012, Lehner et al. 2016, Rezzolla and Takami 2016, De Pietri et al. 2016, Dietrich et al. 2017]. The

GW spectrum of the HMNS is characterised by the presence of many distinct peaks (see e.g. Bauswein and Stergioulas 2019 for a review). The detection and interpretation of postmerger GW signals relies on a proper understanding of the physical mechanisms generating those features in the spectrum. Through their analysis, inference on NS properties might be possible. In particular, information on the EOS of the remnant star can be obtained through the study of the frequency of the $m = 2$ f-mode (quadrupolar mode) [Shibata 2005, Kastaun, Willburger, and Kokkotas 2010, Kastaun and Galeazzi 2015, Clark et al. 2016, Kastaun, Ciolfi, and Giacomazzo 2016, Kastaun et al. 2017, Lioutas, Bauswein, and Stergioulas 2021, Soultanis, Bauswein, and Stergioulas 2022, Iosif and Stergioulas 2022, Wijngaarden et al. 2022]. There exists a significant amount of work to build empirical relations to infer the NS radius from the frequency peak ($f_{\rm peak}$) of this dominant mode [Bauswein et al. 2012, Chatziioannou et al. 2017, Bose et al. 2018, Bauswein and Stergioulas 2019]. The frequency peaks of the postmerger spectra can also be related to other NS properties, such as the tidal coupling constant [Bernuzzi, Dietrich, and Nagar 2015] or the average density [Takami, Rezzolla, and Baiotti 2015]. The empirical relations that link the GW spectrum and physical quantities of the HMNS can directly constrain the EOS (see Takami, Rezzolla, and Baiotti 2015, Bauswein and Stergioulas 2019 and references therein).

On timescales longer than about 50 ms after merger the simulations of De Pietri et al. 2018, De Pietri et al. 2020 (see also Ciolfi et al. 2019) have shown the appearance and growth of convective instabilities in the remnant. The simulations, based on a piecewise polytropic approximation for the EOS treatment supplemented by a thermal component [Read et al. 2009], showed that at $40-50$ ms after merger (depending on the EOS), the amplitude of the $m = 2$ f-mode, which is the dominant mode in the early and intermediate postmerger phases, has noticeably decreased. By that time, convective instabilities set in and trigger inertial modes. The GW emission associated with those modes is found to dominate over the initial $m = 2$ f-mode at late postmerger times, producing new distinctive peaks in the HMNS GW spectrum. The postmerger timescales discussed in De Pietri et al. 2018, De Pietri et al. 2020 at which the HMNS is affected by convective instabilities are compatible with those found by Camelio et al. 2019 who analysed convectively unstable rotating NSs with non-barotropic thermal profiles (as in the case of BNS remnants). Since inertial modes depend on the rotation rate of the star and they are triggered by convection, their detection in GWs would provide a unique opportunity to probe the rotational and thermal state of the merger remnant. As an example to conduct such

inference, an empirical relation between the frequency of the inertial modes and the angular velocity and the rotation rate of the star was proposed by Kastaun 2008.

The results of De Pietri et al. 2018, De Pietri et al. 2020 indicate that the GW emission of inertial modes in the late postmerger phase is potentially detectable by the planned third-generation GW detectors. In this chapter we further investigate this issue by reconstructing the GW signals of De Pietri et al. 2020 using BayesWave[1] Cornish and Littenberg 2015, Littenberg and Cornish 2015, a Bayesian data-analysis algorithm that recovers the postmerger signal through a morphology-independent approach using series of sine-Gaussian wavelets. To assess the detectability of inertial modes we perform injections into the noise of different detectors from sources at different distances: the current Hanford-Livingston-Virgo (HLV) detector network [Harry and LIGO Scientific Collaboration 2010, LIGO Scientific Collaboration 2018, Acernese et al. 2015] and the future Einstein Telescope (ET) [Punturo et al. 2010, Hild et al. 2011]. We also check the dependence of our results on the NS EOS by using two different EOSs, `APR4` and `SLy` [Read et al. 2009]. The reconstructed waveform distributions that we obtain for each injection allows us to infer posteriors of the peak inertial-mode frequency, $f_{\rm inertial}$. Our analysis shows that inertial modes can be potentially detected by third-generation GW detectors up to distances of about 10 Mpc.

The Chapter is organised as follows: in Section 7.2 we briefly present the BayesWave algorithm and introduce the quantities we use to assess the waveform reconstructions. Our main results are presented in Sec. 7.3 where we briefly describe the NR simulations used to generate the waveforms employed for the injections and we discuss the waveform reconstruction performance. Finally, our conclusions are presented in Section 7.4.

7.2 Waveform reconstruction

7.2.1 The BayesWave algorithm

The goal of this work is to analyse the reconstruction of the GW signal produced after the merger of two NSs, particularly in the late postmerger phase. To do so we employ BayesWave, a Bayesian signal reconstruction algorithm that uses Morlet-Gabor (or sine-Gaussian) wavelets [Cornish and Littenberg 2015, Littenberg and Cornish 2015] to model morphologically unknown non-Gaussian

[1] https://git.ligo.org/lscsoft/bayeswave

features with minimal assumptions [Bécsy et al. 2017]. In the time domain, the two GW polarisations of the wavelets are given by

$$h_+(t) = Ae^{-(t-t_0)^2/\tau^2} \cos\left[2\pi f_0(t-t_0) + \phi_0\right], \tag{7.1}$$

$$h_\times(t) = \epsilon h_+(t) e^{i\pi/2}, \tag{7.2}$$

where A is the amplitude of the wavelet, f_0 is the central frequency, t_0 is the central time, ϕ_0 is the offset phase, ϵ is the ellipticity, and $\tau = Q/(2\pi f_0)$, where Q is the quality factor [Cornish and Littenberg 2015]. The factor $e^{i\pi/2}$ in Eq. (7.2) indicates there is a $\pi/2$ difference in the phase of both polarisations.

BayesWave employs a transdimensional reversible jump Markov chain Monte Carlo (RJMCMC) to sample the joint posterior of the parameters of the wavelets, the number N_W of wavelets and ellipticity. These are used to derive the posterior distribution of the reconstructed waveform and, using the waveform samples, it is straightforward to obtain posteriors of quantities that can be derived from the signal. This sampler ensures that the algorithm does not overfit the data, since the addition of wavelets to the reconstruction increases the dimensionality of the model, which provokes a reduction of the posterior probability. There has to be a balance between the improvement of the fit and the addition of wavelets in order to overcome the Occam penalty [Smith and Spiegelhalter 1980].

7.2.2 Overlap and Peak Frequency

A way to check how well a signal that is injected into detector noise is recovered is the use of the *overlap* function between the injected signal, h_i, and the recovered model from BayesWave, h_r:

$$\mathcal{O} = \frac{\langle h_i, h_r \rangle}{\sqrt{\langle h_i, h_i \rangle}\sqrt{\langle h_r, h_r \rangle}}, \tag{7.3}$$

where the inner product of two complex quantities a and b, $\langle a, b \rangle$, is defined as

$$\langle a, b \rangle \equiv 2 \int_0^\infty \frac{a(f)b^*(f) + a^*(f)b(f)}{S_h(f)} df, \tag{7.4}$$

where $S_h(f)$ refers to the one-sided noise power spectral density (PSD) of the detector and the asterisk denotes complex conjugation. The value of the overlap function ranges from -1 to 1, being $\mathcal{O} = 1$ a perfect match between the injected and the reconstructed signal, $\mathcal{O} = -1$ a perfect anticorrelation, and $\mathcal{O} = 0$ means no match between the signals. One can also compute the weighted overlap from

a network of N detectors:

$$\mathcal{O}_{\rm network} = \frac{\sum_{k=1}^{N}\langle h_i^{(k)}, h_r^{(k)}\rangle}{\sqrt{\sum_{k=1}^{N}\langle h_i^{(k)}, h_i^{(k)}\rangle}\sqrt{\sum_{k=1}^{N}\langle h_r^{(k)}, h_r^{(k)}\rangle}}\,, \tag{7.5}$$

where the index k stands for the k-th detector. With the resulting overlap between the injected and reconstructed signals from BayesWave we assess the reconstructions for different distances to the GW source (i.e. different SNRs).

We also compute the peak frequency, defined as the one corresponding to the maximum value of the fast Fourier transform (FFT) [Cooley and Tukey 1965] of the time-domain signal, $|\tilde{h}(f)|$, using a time window over the part of the signal we are interested in. The segments of data have been previously Hann-windowed. We expect the peak frequencies, $f_{\rm peak}$ and $f_{\rm inertial}$, to be located in the range $f \in [1500, 4000]$ Hz [Chatziioannou et al. 2017, De Pietri et al. 2020], and we will use this range to set the low-frequency and high-frequency cutoffs for the computation of the overlap and the frequency peaks.

7.3 Results

7.3.1 Summary of the numerical-relativity simulations

The waveforms we employ for our study were obtained in the NR simulations of BNS mergers performed by De Pietri et al. 2020. The initial data are generated using the Lorene code [Gourgoulhon et al. 2001, Gourgoulhon et al. 2016] and the initial separation of the two stars is ≈ 44.3 km, which corresponds to about four full orbits before merger. The main properties of the initial simulation setup are reported in Table 7.3.1. The evolution of the initial data is performed using the Einstein Toolkit [Löffler et al. 2012], an open source code based on the Cactus framework [Goodale et al. 2003]. The simulation setup employed in the study of De Pietri et al. 2020 is the same as in Maione et al. 2017, De Pietri et al. 2016, De Pietri et al. 2019, to which the reader is addressed for further details, except for the fact that π-symmetry was used to reduce the computational cost by a factor 2. The Einstein Toolkit solves Einstein's field equations in the Baumgarte-Shapiro-Shibata-Nakamura (BSSN) formalism [Shibata and Nakamura 1995, Baumgarte and Shapiro 1998] and the GR hydrodynamics equations in the Valencia formulation Banyuls et al. 1997, Font 2008. The latter are integrated numerically with a finite-volume algorithm based on the Harten, Lax, Van Leer, Einfeldt (HLLE) Riemann solver [Harten, Lax, and Leer 1983, Einfeldt 1988], the weighted essentially non-oscillatory (WENO) reconstruction

EOS	M_0	M	C	$J_{\rm ADM}$	Ω_0 (krad/s)
`APR4`	1.4	1.2755	0.166	6.577	1.767
`SLy`	1.4	1.2810	0.161	6.623	1.770

Table 7.3.1 Main properties of our two BNS simulations. The columns report the EOS, the baryonic mass, M_0, the gravitational mass (at infinite distance), M, and the compactness, $C \coloneqq M/R$, of the individual stars, and the total angular momentum,$J_{\rm ADM}$, and the total angular velocity, Ω_0, of the binary system. Geometrised units are used ($c = G = M_\odot = 1$).

method [Liu, Osher, and Chan 1994, Jiang and Shu 1996], and the Method of Lines with a $4^{\rm th}$ order, conservative Runge-Kutta scheme [Shu and Osher 1988].

The inertial modes identified in the simulations of De Pietri et al. 2018, De Pietri et al. 2020 are triggered by a convective instability appearing in the nonisentropic HMNS which was identified by monitoring the value of the Schwarzschild discriminant. The modes have frequencies slightly smaller than twice the maximum angular frequency of the differentially rotating remnant star $\Omega_{\rm max}$.

7.3.2 **Waveform reconstruction performance**

In order to obtain a distribution of frequency peaks we perform injections in BayesWave of the waveforms computed by [De Pietri et al. 2020]. We use several sensitivity curves (for Advanced LIGO (aLIGO) we use the PSD model `aLIGOZeroDetHighPower` for the two detectors from LIGO Scientific Collaboration 2018, for Advanced Virgo we use the design sensitivity from Acernese et al. 2015 and we take the ET-D configuration from Hild et al. 2011) to see the differences between current and future GW detectors. The reconstructions are compared using the design sensitivities of the HLV detector network and of the ET, formed by a three detector network on the same site. No sources of noise and/or glitches are added; we only consider Gaussian noise [Blackburn et al. 2008, Abbott et al. 2009, Aasi et al. 2012] coloured by the PSD of the detector. We set the source of the injected signals at different distances (giving different SNRs) and assume that the source is also optimally oriented with respect to one of the detectors (Hanford, H1, for HLV and E3 for ET[2]). We set a maximum number of wavelets of $N_W^{\rm max} = 100$ for HLV and $N_W^{\rm max} = 200$ for ET, a maximum quality factor of $Q^{\rm max} = 200$, $n = 2 \times 10^6$ iterations, and a sampling rate of 8192 Hz. The maximum number of wavelets is different for HLV and ET because

[2]The design of the Einstein Telescope consists of three arms forming an equilateral triangle, with three pairs of interferometers acting as a three-detector network, E1, E2 and E3.

selecting $N_W^{\max} = 100$ for ET is not large enough for the algorithm to reconstruct the signal accurately, due to the high sensitivity of third-generation detectors.

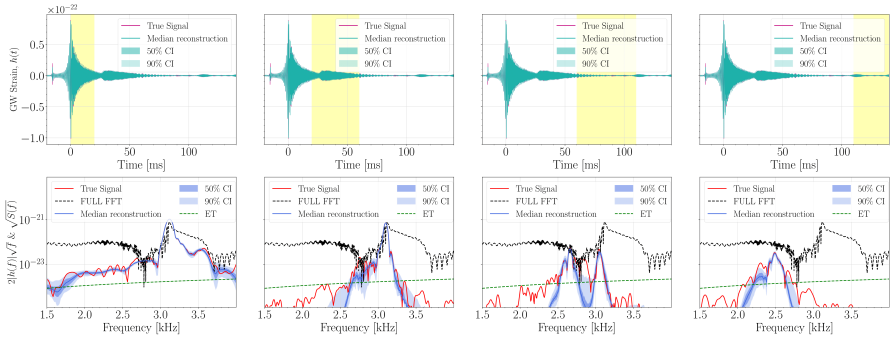

Figure 7.3.1 Injected (red) and recovered (blue) time-domain waveforms (top panels) and ASD (bottom panels) for BNS merger simulations with the `APR4` EOS. Each ASD is computed using the corresponding time window depicted in yellow in the top panels. The source is assumed to be located at $d = 3$ Mpc. The signals are injected into the E3 configuration of the third-generation ET observatory, whose sensitivity curve is shown by the dashed green curve. The width of the time windows is chosen to show how the frequency peak is displaced to lower frequencies depending on the different evolutionary stage of the postmerger remnant.

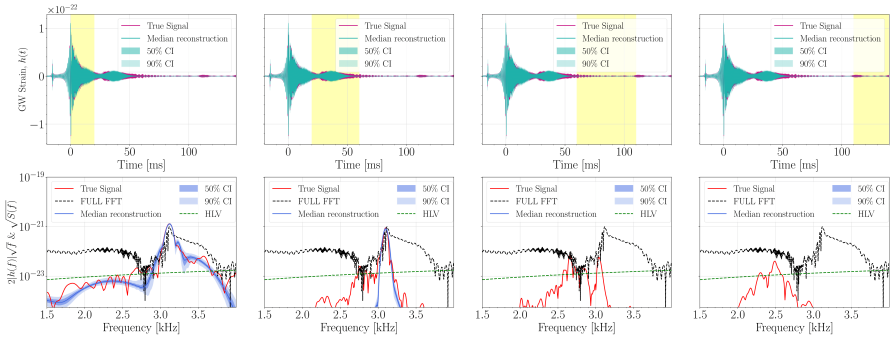

Figure 7.3.2 Same as Fig. 7.3.1, but for the H1 detector.

The complete GW strains and the corresponding amplitude spectral density (ASD) of both injected (red) and recovered (blue) coloured time-domain signals for the `APR4` EOS model of Table 7.3.1 are depicted in Figs. 7.3.1 and 7.3.2, using the PSD of ET and H1, respectively, and for a source at a distance of 3 Mpc. The blue-shaded regions show the 50% and 90% credible intervals (CIs) of the posterior distribution of the reconstructed signal. The limits of these intervals correspond to the values of the 25th/75th and 5th/95th percentiles, respectively. Time windows with different widths located at different stages of the postmerger phase are applied to the time series. Those are indicated by the areas depicted

in yellow in the top panels of both figures. By moving those windows over time we can follow potential changes in the ASD during the evolution of the GW signal, and observe the emergence of different modes in the HMNS. The black dashed line in the bottom row of the two figures corresponds to the ASD of the injected entire signal, from $t_i = -20$ ms (where $t = 0$ ms corresponds to the time of merger) to $t_f = 140$ ms. Correspondingly, the red lines in the ASD plots show the corresponding spectrum for the selected time-window intervals. One can clearly see that the peak frequency changes depending on the time window applied to obtain the ASD, shifting to lower frequencies for increasingly later times. We do not include the corresponding plots for the `SLy` EOS model because a similar behaviour is observed in this case.

By comparing the two figures the differences between the reconstructions of the injections into H1 and E3 are evident. The early postmerger signal corresponding to the f-mode is well recovered for both types of detectors. We note that this is in agreement with the previous findings of Chatziioannou et al. 2017 who used BNS merger waveforms from the NR simulations of Bauswein, Stergioulas, and Janka 2014, Bauswein, Stergioulas, and Janka 2016 (extending only up to ~ 15 ms after merger) to recover with BayesWave the peak frequency of the f-mode. However, when it comes to the late postmerger signal during which the inertial modes are excited, only a third-generation detector such as ET is able to reasonably reconstruct the waveform. We also performed a similar study with Cosmic Explorer (CE) [Evans et al. 2021] finding comparable results.

The waveform posterior distribution can be used to derive some physical parameters of the HMNS. In this case, the reconstructed signals can be used to obtain the posterior for the dominant postmerger frequency $f_{\rm peak}$ [Bauswein et al. 2012, Chatziioannou et al. 2017, Bose et al. 2018]. For both the overlap and the reconstructed peak frequency we study both the entire postmerger signal, which is dominated by the f-mode excited at early times, and the late signal, during which the inertial modes are excited. For completeness, the Appendix discusses a test case using injections that only contain the late postmerger phase.

7.3.2.1 *Study of the full GW signal*

We compute the overlap between the injected and the recovered waveforms to test the performance of BayesWave. In Fig. 7.3.3 we show the overlap as a function of distance for both `APR4` and `SLy` EOSs, computed for the HLV detector network (left panel) and for ET (right panel). The overlap clearly decreases with the distance to the source, as the GW signal becomes more difficult to reconstruct. The behaviour is the same for both EOS, but the reconstruction is slightly

better for the APR4 EOS at larger distances. Note also the difference between the detector networks: the HLV network has $\mathcal{O}_{\rm network} \sim 0.7$ at 15 Mpc and the ET gives a similar overlap at roughly 150 Mpc. For the sake of comparison, in Chatziioannou et al. 2017 an overlap of ~ 0.9 is reported for a postmerger SNR of 5. In our case, $\mathcal{O}_{\rm network} = 0.9$ is achieved for a distance of ~ 12 Mpc, which translates to a postmerger SNR of ~ 5 for both EOS.

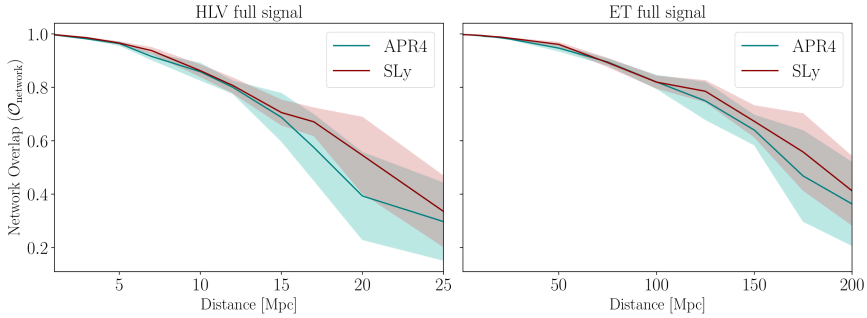

Figure 7.3.3 Detector network overlap between the full injected and recovered signals as a function of the distance to the GW source. The left panel shows the results for the HLV network and the right one for the ET detector. The lines indicate the mean value over the waveform posterior distribution and the shaded areas are the standard deviations.

We show the dependence of the recovered value of $f_{\rm peak}$ with the distance to the source in Fig. 7.3.4, again considering the full waveform, $t \in [-20, 140]$ ms, injected in a window of 1 s of detector data, which corresponds to coloured Gaussian noise. This value, plotted with solid curves, is the mean value obtained from the posterior distributions of the recovered signals. We also depict the standard deviations for both EOSs, which become larger as the distance to the source increases. These results are consistent with the overlap values shown in Fig. 7.3.3, since a low overlap value gives a poorly recovered $f_{\rm peak}$. In the case of H1 (left panel), the dispersion starts increasing at $d \sim 13$ Mpc for APR4 and $d \sim 17$ Mpc for SLy, right where $\mathcal{O}_{\rm network}$ drops below 0.6. Concerning ET (right panel), the uncertainty becomes larger at $d \sim 125$ Mpc, also when $\mathcal{O}_{\rm network} \sim 0.6$. Notice that for high SNRs the distance to the source and the SNR are inversely proportional, and a less accurate value of $f_{\rm peak}$ would be obtained by decreasing the SNR.

In Chatziioannou et al. 2017 an almost flat posterior distribution for a postmerger SNR of 3 was obtained. In our case, at 25 Mpc the recovery of the frequency peak already has a large uncertainty, and corresponds to a postmerger SNR of ~ 3 for both EOS, which is consistent with the results of Chatziioannou et al. 2017.

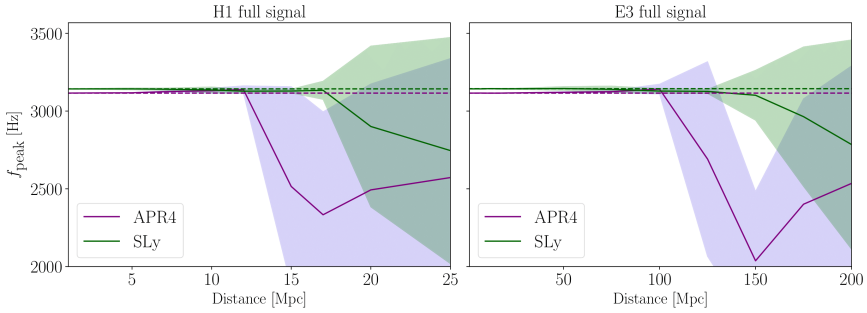

Figure 7.3.4 Dependence of the recovered $f-$mode frequency peak with distance for the H1 detector (left panel) and for the E3 detector (right panel). The solid curves are the mean values and the shaded areas represent the standard deviations of the distributions. The mean of the recovered peak is close to the injected signal (dashed lines) for distances up to 10 Mpc for H1 and 100 Mpc for E3.

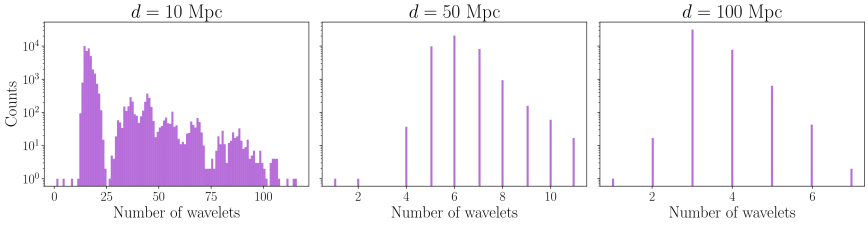

Figure 7.3.5 Histograms of the number of wavelets used by BayesWave for the reconstructions of signals injected in ET coming from sources at $d = \{10, 50, 100\}$ Mpc. The $y-$axis indicates the number of iterations of the RJMCMC algorithm that use a certain number of wavelets. At each iteration, the algorithm might add wavelets to the series, but only when the fit is improved considerably so as to overcome the Occam penalty.

In Fig. 7.3.5 we depict histograms of the numbers of wavelets used for the reconstructions at different distances, $d = \{10, 50, 100\}$ Mpc. The closer the source the larger the number of wavelets employed, resulting in more accurate reconstructions.

7.3.2.2 *Study of the late postmerger phase*

We turn next to analyse the reconstruction of the late postmerger signal ($t \geq 40$ ms for `SLy` EOS and $t \geq 80$ ms for `APR4` EOS [De Pietri et al. 2020]). Once the maximum amplitude of the fundamental quadrupolar f-mode has significantly decreased, a signal with lower frequency and amplitude appears, associated with the manifestation of inertial modes in the remnant. The two rightmost panels of Fig. 7.3.1 clearly show the appearance of this new peak for a source observed at a distance of 3 Mpc. This peak is just above the sensitivity curve of ET at a

frequency of ~ 2.5 kHz (see rightmost panel of Fig. 7.3.2). However, it is out of reach for current detectors, at least for $d = 3$ Mpc (cf. Fig. 7.3.2).

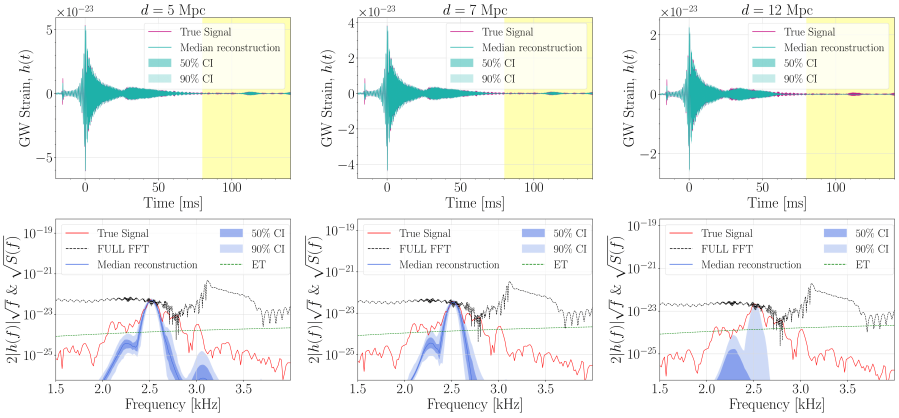

Figure 7.3.6 Injected (red) and recovered (blue) time-domain waveforms (top panels) and ASD (bottom panels) for sources located at $d = \{5, 7, 12\}$ Mpc. Signals are injected in ET (E3). The time window used to compute the ASD only considers the last part of the signal (yellow region). The recovery of the frequency peak degrades with the distance to the source.

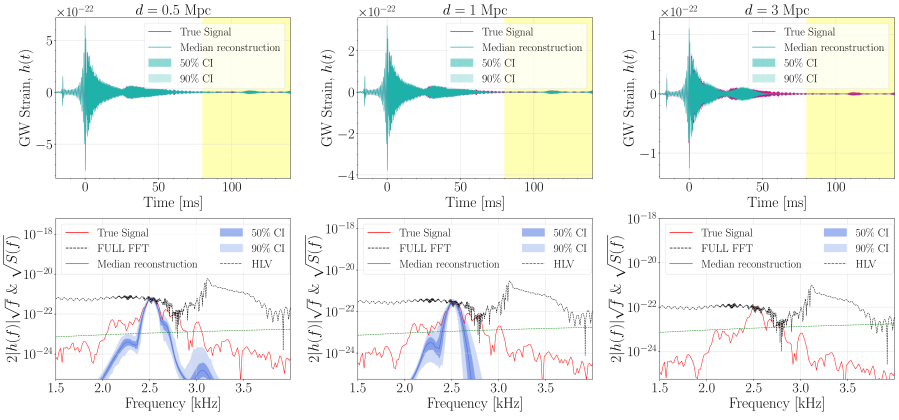

Figure 7.3.7 As Fig. 7.3.6, but for H1 and closer source distances, $d = \{0.5, 1, 3\}$ Mpc

.

To illustrate how the BayesWave reconstruction changes with distance, we show in Fig. 7.3.6 the injected and reconstructed time-domain waveforms and the respective ASD reconstructions for three representative distances, namely 5, 7, and 12 Mpc, and for BNS merger simulations with the `APR4` EOS. As before, the regions in yellow in the top panels show the time window we use to compute the ASD displayed in the bottom panels. The median of the reconstructed

ASD is shown with a blue solid line and the 50% and 90% CIs are indicated by the dark and light blue-shaded areas, respectively. The Hann function (as other window functions) cuts the tails of the time-domain signal, and thus might affect the resulting frequency spectra. However, the inertial modes with largest amplitude are located in the middle of the time window, and are not affected by the cut. We find that the region around the frequency peak at $f \approx 2.5$ kHz is well recovered when the source is at 5 Mpc. On the other hand, as the distance increases the reconstruction worsens, as expected, and for a source at 12 Mpc there is no frequency peak in the reconstructed signal. The corresponding result for current detectors is shown in Fig. 7.3.7 which depicts the dependence of the peak-frequency recovery with distance (for $d = \{0.5, 1, 3\}$ Mpc) with the design sensitivity of H1. In this case, BayesWave is not able to recover the peak-frequency of inertial modes even when the GW source is at 3 Mpc.

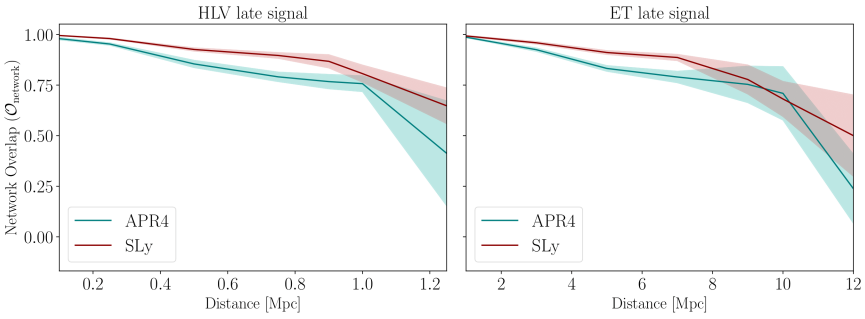

Figure 7.3.8 Detector overlap of the late postmerger GW signals for the HLV network (left panel) and ET (right panel). Solid lines represent the mean values from the posterior distributions and shaded regions are the standard deviations. For both EOS the overlaps drop below ≈ 0.75 for a source distance of about 1 Mpc for HLV and 10 Mpc for ET.

In Fig. 7.3.8 we show the network overlap function of the late postmerger signal, for both HLV and ET. The same initial time windows as in Figs. 7.3.6 and 7.3.7 are used to compute these overlaps. We note, however, that the final time of the window is different for both EOSs, namely 140 ms for the `APR4` EOS and 123 ms for the `SLy` EOS, respectively. For the latter the final time is shorter since a BH forms at $t \approx 123.6$ ms [De Pietri et al. 2020]. Moreover, the initial time of the window is also different, as pointed out before, since the emergence of the inertial modes occurs at different times ($t \sim 40$ ms for `SLy` and $t \sim 80$ ms for `APR4`). For the case of ET (right panel), at $d \approx 8$ Mpc the overlap is around 0.7 for both EOSs, but it rapidly decreases to about 0.5 at ≈ 12.5 Mpc. The `SLy` EOS gives a higher overlap and a more accurate $f_{\rm inertial}$ but both EOSs yield $\mathcal{O}_{\rm network} = 0$ at 15 Mpc. On the other hand, for the HLV detector network the

network overlap for both EOSs falls rapidly to practically 0 from a distance of 1.75 Mpc.

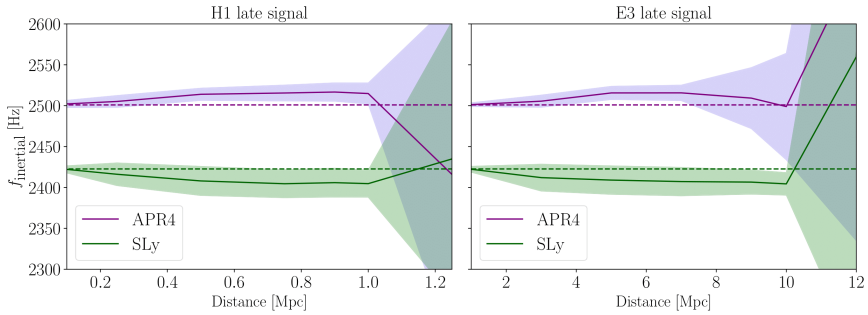

Figure 7.3.9 Dependence with distance of the peak frequency during the late postmerger phase, for signals injected in H1 (left panel) and E3 (right panel). Solid lines and shaded areas are the mean values and the standard deviations of the distributions, respectively. For ET, the peak frequency is well identified up to 10 Mpc for both `APR4` and `SLy` EOSs while for H1 a satisfactory recovery is only possible for sources up to 1 Mpc for both EOSs.

We now focus on the recovery of the frequency peak of these lower-frequency inertial modes, $f_{\rm inertial}$. Fig. 7.3.9 depicts the dependence of the recovered $f_{\rm inertial}$ with distance for H1 and E3. The maximum distance shown in the plots for each detector is selected by the value at which the reconstructions start to significantly fail. These results are in good agreement with the overlap shown in Fig. 7.3.8. We note that there is a slight dependence on the EOS as we obtain a peak frequency that is about 75 Hz higher in the `APR4` case. For the specific case of ET, at $d = 12$ Mpc the recovery of the peak frequency fails for both EOSs. Up to 8 Mpc, the recovered $f_{\rm inertial}$ is close to the injected one with an uncertainty of $\Delta f_{\rm inertial} \lesssim 25$ Hz. For the case of H1, this value of the uncertainty of the method is obtained for much shorter distances ($d \approx 1.0$ Mpc).

7.4 Discussion and conclusions

The existence of convectively unstable regions in long-lived remnants of BNS mergers [De Pietri et al. 2018, De Pietri et al. 2020] triggers the excitation of inertial modes, which depend on the rotational and thermal properties of the remnant. Their presence in the late postmerger GW signal might thus provide further insight in our understanding of NS properties. In this Chapter, we have studied the possibility of reconstructing the late BNS postmerger GW signal with current and future interferometers. To this aim, we have employed the waveforms produced in NR simulations of equal-mass BNS mergers that last

up to $t \approx 140$ ms after merger, performed by De Pietri et al. 2018, De Pietri et al. 2020. These long-lasting simulations showed the excitation of oscillation modes in the postmerger remnant with a smaller frequency and amplitude than those of the quadrupolar f-mode which dominates the GW spectra of the early postmerger phase. These so-called inertial modes are triggered by a convective instability developing in the HMNS, for which the Coriolis force acts as the dominant restoring force [Stergioulas, Apostolatos, and Font 2004, Kastaun 2008, Stergioulas et al. 2011]. The late-time appearance of these modes has also been observed in the BNS simulations of Ciolfi et al. 2019 accounting for the effects of magnetic fields in the dynamics.

Due to their small amplitude, with a strain $h(f)$ more than 1 order of magnitude smaller than that of the f-mode, the detectability of such inertial modes can be challenging. In order to assess their possible detection, we have employed the BayesWave algorithm [Cornish and Littenberg 2015, Littenberg and Cornish 2015] to reconstruct our time-domain waveforms injected into Gaussian noise. The signals were injected at different distances from the source to check the range of detection of those modes. In all cases the source was assumed to be optimally oriented with respect to (one of) the detectors.

Our study reveals that current GW interferometers (i.e., the HLV network) are able to recover the peak frequency of inertial modes only if the BNS merger occurs at distances of about 1 Mpc or less. However, for future detectors such as ET, the range of detection increases by a factor of 10, consistent with their increased sensitivity compared to current detectors. An important point to stress is that the difference between the frequency peaks of the inertial modes for different EOSs (`APR4` and `SLy`) is bigger than the difference between the peaks of the fundamental mode in the early part of the signal. This means that a future detection of those late postmerger modes could give us more insight into the internal matter and structure of a NS, as a result of the broken EOS degeneracy and the relationship of those modes with the rotational properties of differentially rotating stars. In general the frequency $f_{\rm inertial}$ changes with the EOS and the total binary mass, and it also correlates with the tidal deformability. For the simulations discussed in this work, $f_{\rm inertial}$ appears to be very close for all models because of the properties of the initial systems, in particular the total mass. Employing different initial data with a wider spread in the total mass might be something worth trying in a future investigation. Furthermore, the value of the peak frequency can be used to infer different physical parameters of the star [Kastaun 2008], extending what has already been done for the f-mode to infer the radius, the tidal coupling constant or the average density of the

NS [Bauswein and Janka 2012, Takami, Rezzolla, and Baiotti 2015, Bernuzzi, Dietrich, and Nagar 2015, Chatziioannou et al. 2017]. However, as mentioned in De Pietri et al. 2018, one would need to employ perturbative studies to identify the particular inertial modes that are excited. Such a challenging project is outside the scope of this work, which has purely focused on the prospects of detectability of inertial modes.

Appendix

7.A Reconstruction of late postmerger injections

In this Appendix we consider injections that only contain the late postmerger phase when inertial modes are active. This test case allows us to assess the capability of BayesWave of recovering only the part of the GW signal containing the inertial-mode emission and to find out whether there is an improvement with respect to the case of full-signal injections discussed in the main text. For `APR4` we inject the signal from 80 ms to 140 ms after merger while for `SLy` the respective range goes from 45 ms to 140 ms after merger. For this test, we only consider the ET detector.

In Figs. 7.A.1 and 7.A.2 we depict the time-domain reconstructions and their ASD for `APR4` and `SLy`, respectively. The ASD of the signal of the `APR4` EOS shows also a noticeable secondary peak at a lower frequency (≈ 2250 Hz). This peak, while being present, is not so clearly prominent in the injections and reconstructions of the full merger and postmerger signal (see fourth column in Fig. 7.3.1). Both peaks are properly captured by BayesWave up to a distance similar to the one obtained when injecting the full signal. The variability of the highlighted peaks is a sign that different frequencies are present, at different times, on the postmerger signal. The number of wavelets used for the reconstructions is displayed in Fig. 7.A.3, in which the histograms show, as in Fig. 7.3.5, the number of iterations that use a certain number of wavelets. Since in this case BayesWave only reconstructs the part of the signal corresponding to the inertial-mode emission, the number of wavelets employed for a distance of 10 Mpc is low.

Fig. 7.A.4 shows the frequency peaks from the ASD of the recovered signals. The larger uncertainty in the case of the `APR4` EOS is due to the secondary peak that arises in those injections. The peak from the `SLy` EOS signal is very well recovered with small uncertainty up to some distance. Even in the case of

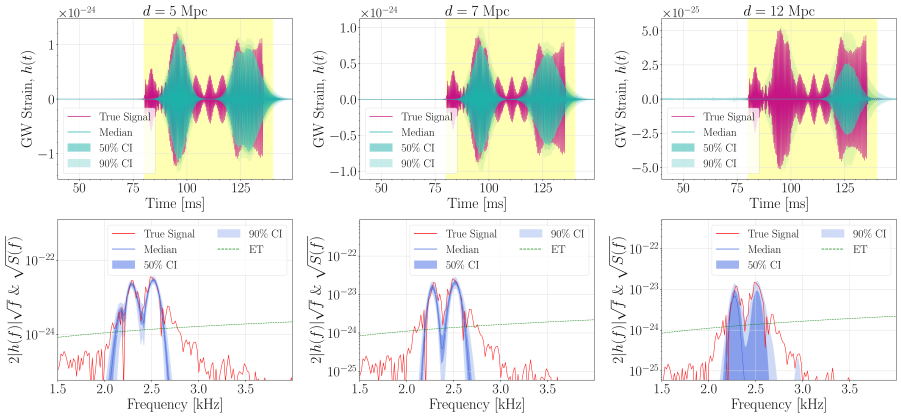

Figure 7.A.1 Injected (red) and recovered (blue) time-domain waveforms (top panels) and ASD (bottom panels) for sources located at $d = \{5, 7, 12\}$ Mpc and for `APR4` EOS. In this case the injected signal only contains the intertial-mode emission.

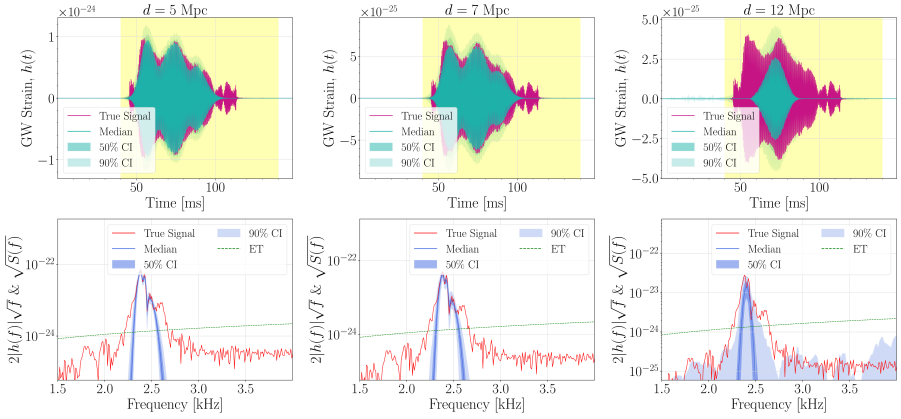

Figure 7.A.2 As Fig. 7.A.1 but for the `SLy` EOS.

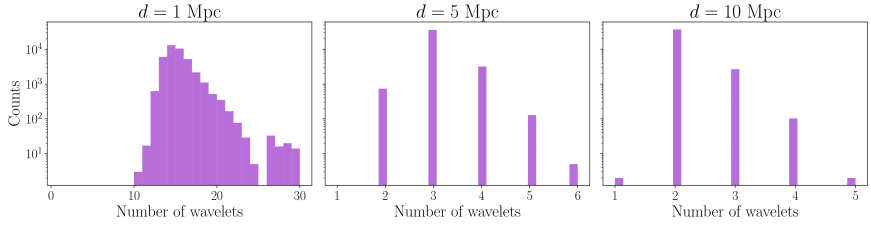

Figure 7.A.3 Histograms of the number of wavelets used by BayesWave for the reconstructions of injected signals containing only the inertial-mode emission and located at distances $d = \{1, 5, 10\}$ Mpc. The $y-$axis indicates the number of iterations that BayesWave uses to build the waveforms by model selection.

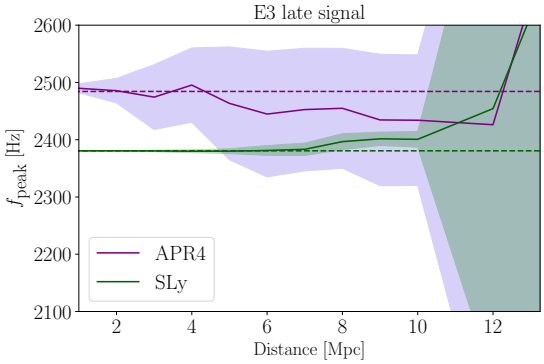

Figure 7.A.4 Dependence of the recovered frequency peak of the inertial modes with distance for both EOSs, when injecting only the part of the postmerger signal corresponding to the inertial modes. Solid lines represent the mean values from the posterior distributions and shaded areas are the standard deviations.

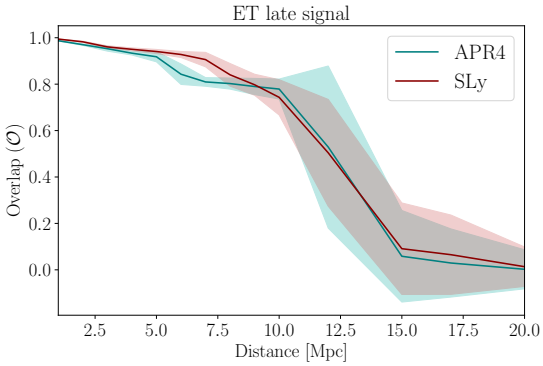

Figure 7.A.5 Evolution of the overlap between the injected and recovered GW signals with distance for the two EOSs. Solid lines represent the mean values from the posterior distributions and shaded areas are the standard deviations.

injecting the part of the signal corresponding to the inertial-mode emission we obtain similar results to the case in which we injected the full postmerger signal. No improvements are obtained, and the peak frequency is well recovered up to a distance of ≈ 12 Mpc. The overlap between the injected and reconstructed waveforms is depicted in Fig. 7.A.5. As expected, there is a good agreement with the recovery of the frequency peaks. The overlap drops below 0.5 at $d \approx 12$ Mpc, the largest distance at which the peak is recovered with ET.

From these results we conclude that BayesWave yields no difference between reconstructing the full waveform with an early stage in which the signal is much

larger or reconstructing only the fraction of the postmerger signal associated with the emission of the inertial modes.

CHAPTER 8

Identifying thermal effects in neutron star merger remnants with model-agnostic waveform reconstructions and third-generation detectors

The content of this Chapter is originally from: **Miquel Miravet-Tenés**, Davide Guerra, Milton Ruiz, Pablo Cerdá-Durán and José A. Font. **Identifying thermal effects in neutron star merger remnants with model-agnostic waveform reconstructions and third-generation detectors**. January 2024. Submitted to *Phys. Rev. D.* arXiv:2401.02493.

8.1 Introduction

GW searches of BNS mergers and inference of source parameters rely on accurate waveform models for the inspiral signal. Those are based on analytical relativity (computing waveform approximants using PN expansions or the EOB approach [Lackey et al. 2017, Narikawa and Uchikata 2022]) and NR, the full-fledged numerical solution of Einstein's field equations coupled to the equations describing NS matter and radiation processes (see, e.g., Sun et al. 2022, Foucart et al. 2023, Foucart et al. 2020, Gieg et al. 2022, Hayashi et al. 2022, Radice et al. 2022). In numerical simulations of BNS mergers thermal effects are incorporated using two alternative approaches. The first one is a "hybrid

approach" which assumes that the pressure and the internal energy have two contributions, namely a cold, zero temperature part described by a polytropic EOS (or a family of piecewise polytropes) and a thermal part described by an ideal-gas-like EOS [Janka, Zwerger, and Moenchmeyer 1993, Dimmelmeier, Font, and Muller 2002, Shibata, Taniguchi, and Uryū 2005]. The latter is given by $P_{\rm th} = \rho_0\,\epsilon_{\rm th}(\Gamma_{\rm th}-1)$, with ρ_0 the rest-mass density, and $P_{\rm th}$ and $\epsilon_{\rm th}$ the thermal pressure and thermal energy density, respectively, and $\Gamma_{\rm th}$ the adiabatic index, a constant that lays in the range $1 \lesssim \Gamma_{\rm th} \lesssim 2$ for causality constraints, but that in typical BNS merger simulations is set between 1.6 and 2 (see e.g. [Constantinou et al. 2015, Takami, Rezzolla, and Baiotti 2015]). The second approach employs tabulated representations of microphysical finite-temperature EOSs, providing a self-consistent method to probe the impact of thermal effects in the merger dynamics. Although the hybrid approach is computationally preferred, it has some limitations. In particular, it has been shown that the value of the thermal adiabatic index $\Gamma_{\rm th}$ above half saturation density strongly depends on the nucleon effective mass [Lim and Holt 2019]. Therefore, it is likely that this approach overestimates the thermal pressure by a few orders of magnitude [Raithel, Paschalidis, and Özel 2021], which may induce significant changes in the GW frequencies [Bauswein, Janka, and Oechslin 2010, Figura et al. 2021]. As the tabulated approach incorporates the temperature self-consistently the above issue is not present. BNS merger simulations based on tabulated EOSs, while computationally more challenging than those based on the hybrid approach, are becoming increasingly more common [Oechslin, Janka, and Marek 2007, Bauswein, Janka, and Oechslin 2010, Sekiguchi et al. 2011, Fields et al. 2023, Espino, Bozzola, and Paschalidis 2022, Werneck et al. 2023, Guerra et al. 2024]. These two alternative ways of including thermal effects in the numerical simulations results in measurable differences in the GW signal, especially in the postmerger part, significantly affecting the frequency spectra (see e.g. Bauswein, Janka, and Oechslin 2010, Guerra et al. 2024).

During the first $\sim 5\,$ms after merger, nonaxisymmetric deformations of the remnant are accompanied by the emission of high-frequency GWs. The frequency spectra are characterised by the presence of distinctive peaks associated with oscillation modes due to nonlinear interactions between the quadrupole and quasi-radial modes, and the rotation of the nonaxisymmetric binary remnant. These peaks are typically denoted as $f_{2\pm0}$, $f_{\rm spiral}$, and f_2 (or $f_{\rm peak}$) [Stergioulas et al. 2011, Hotokezaka et al. 2013, Bauswein and Stergioulas 2015, Takami, Rezzolla, and Baiotti 2015, Bauswein, Stergioulas, and Janka 2016, Bauswein and Stergioulas 2019]. As pointed out in Rezzolla and Takami 2016 the frequency

of the f_2 mode changes by around $\sim 5\%$ in time. These (initial) frequency values are denoted as $f_{2,i}$ to distinguish them from the value of f_2 reached during the quasi-stationary evolution of the GW signal. Through the analysis of these peaks, inference on NS properties may be possible. In particular, it has been shown that their frequencies are related quasi-universally with the tidal deformability of the stars, and the maximum-mass of non-rotating configurations [Read et al. 2013, Bauswein and Stergioulas 2015, Takami, Rezzolla, and Baiotti 2015, Rezzolla and Takami 2016, Guerra et al. 2024, Topolski, Tootle, and Rezzolla 2024].

Long-term simulations of the postmerger remnant extending beyond ~ 50 ms have also revealed the appearance of inertial modes [De Pietri et al. 2018, De Pietri et al. 2020]. Their GWs dominate over those associated with the initial f_2 mode at late postmerger times, but have lower frequencies and amplitudes. As inertial modes depend on the rotation rate of the star and on its thermal stratification, their detection in GWs would provide a unique opportunity to probe the rotational and thermal states of the merger remnant (see, e.g., Kastaun 2008).

Recently, long-term simulations of BNS mergers exploring the influence of the treatment of the thermal part of the EOS by comparing models using hybrid and tabulated approaches have been reported in Guerra et al. 2024. The differences found in the dynamics and GW emission can be used to gauge the importance of the numerical treatment of thermal effects in the EOS, which has observational implications. In this work, we investigate the identification of such differences in BNS merger remnants by reconstructing the GW signals of Guerra et al. 2024 using BayesWave[1] [Cornish and Littenberg 2015, Littenberg and Cornish 2015], a Bayesian data-analysis algorithm that recovers the postmerger signal through a morphology-independent approach using series of sine-Gaussian wavelets. We stress that our simulations focus on the possible identification of a single difference in the postmerger remnant – the implementation of thermal effects in the EOS – and thus assume that potential effects from neglected ingredients in the modelling (e.g. magnetic fields, viscosity, neutrinos or the knowledge of the underlying nuclear interaction) would be identical in both setups. Notice that magnetic viscosity and/or cooling processes, such as neutrino emissions, can modify the characteristic GW frequencies of the binary remnant. In particular, the GRMHD simulations of BNS mergers reported in Ruiz, Tsokaros, and Shapiro 2021 found that magnetic viscosity tends to shift the f_2 mode frequency to lower frequencies by around $\sim 30 - 150\,\mathrm{Hz}$ depending on the stiffness of the EOS as well as on the

[1] https://git.ligo.org/lscsoft/bayeswave

numerical resolution. Neutrino processes, on the other hand, tend to slightly increase its frequency (see e.g. Sun et al. 2022, Foucart et al. 2016).

This investigation is a follow-up of Chapter 7, where we first employed BayesWave to analyse the detectability prospects of the inertial modes computed in the simulations of De Pietri et al. 2018, De Pietri et al. 2020 employing only hybrid BNS models. Moreover, we further extend the analysis of Chapter 7 by studying the identification of differences in the treatment of thermal effects across the *entire* postmerger signal, i.e., both in the early part where the f_2 mode dominates and in the late part where inertial modes are excited. As done in Chapter 7, we perform waveform injections corresponding to a set of EOSs, each with a hybrid and a tabulated version, into the noise of the third-generation GW detector ET [Punturo et al. 2010, Hild et al. 2011, Maggiore et al. 2020, Branchesi et al. 2023] from BNS sources at different distances. The posterior distributions of the recovered waveforms give us distributions of the peak frequencies, which can be related to physical properties of the merger remnant via empirical relations.

Our analysis is complementary to the recent work reported in Villa-Ortega et al. 2023 where Bayesian model selection was used to explore differences between the hybrid and the tabulated approaches with the same set of GW signals from Guerra et al. 2024. This is a completely different approach to our model-agnostic reconstructions. The findings reported in Villa-Ortega et al. 2023, where differences between tabulated and hybrid treatments of thermal effects were found to lead to differences in the postmerger GW observable by third-generation detectors at source distances ≤ 50 Mpc, are consistent with what is reported here. We find that differences in the distribution of the main frequency peaks in the postmerger GW spectra in hybrid and tabulated models can be resolved in third-generation detectors up to distances similar to those reported in Villa-Ortega et al. 2023. Recently, the studies in Raithel and Paschalidis 2023 showed that finite-temperature effects included through the hybrid approach can be measurable with future detectors if the cold EOS is well constrained.

The Chapter is organised as follows: we summarise the setup of the BNS merger simulations of Guerra et al. 2024 in Section 8.2. Our main results are discussed in Section 8.3. We divide this section in two parts: the first one is focused on the early postmerger signal, where we also discuss different EOS-insensitive fits that relate the $f_{2,i}$ and f_2 modes with the tidal deformability of NSs. Then, in the second part we consider the late postmerger phase and study the differences in the frequencies of the inertial modes for our set of EOSs. The conclusions of our work are presented in Section 8.4. Finally, Appendix 8.A

contains a brief summary of our findings for source inclinations and sky locations different than those considered in the main body of the paper where optimal orientation and sky location is assumed.

8.2 Summary of the binary neutron star mergers setup

The gravitational waveforms employed in our analysis were computed in the NR simulations of BNS mergers recently conducted by Guerra et al. 2024. The initial data for those simulations consist of two equal-mass, irrotational NSs modelled by finite-temperature (tabulated) microphysical EOSs, namely `DD2` [Typel et al. 2010], `HShen` [Shen et al. 2011], `LS220` [James M. Lattimer 1991], and `SLy4` [Chabanat et al. 1998]. These initial data were built using Lorene Gourgoulhon et al. 2001, Taniguchi and Gourgoulhon 2002, n.d.[b]. The EOS tables are obtained following the work of Schneider, Roberts, and Ott 2017 and are freely available at n.d.[c]. The initial temperature is fixed to $T = 0.01\,\mathrm{MeV}$, the lowest value on the tables. These EOSs span a reasonable range of central densities, radii, and maximum gravitational masses for irrotational neutron stars. The initial separation of the two stars is 44.3 km and the rest-mass of each star is $M_0 = 1.4\,M_\odot$. Their properties are summarised in Table 8.2.1. For comparison purposes we also consider waveforms obtained in simulations of BNS mergers based on hybrid EOSs, consisting of a cold and a thermal part. The cold component of each EOS is made of piecewise polytropic representations of the above EOSs using a piecewise regression as in Pilgrim 2021 with seven pieces [Read et al. 2009]. Correspondingly, the thermal component is based on a Γ-law EOS with a constant adiabatic index $\Gamma_{\rm th} = 1.8$.

The two types of BNS models we use – hybrid and tabulated – are built as similar as possible, to minimise the effects of differences that the initial data may have in our study. However, there are intrinsic differences in the way the models are built (e.g. the lowest value of the temperature in the tables is $T = 0.01$ MeV, which affects the density distribution at low densities) that make not possible to build the exact same stars. The gravitational mass vs circumferential radius for the two types of configurations and for the four EOSs used in this Chapter are displayed in Fig. 8.2.1 with solid red circles. The unavoidable small discrepancy visible in this plot leads to a difference of $\lesssim 10\%$ between the values of the tidal deformability Λ of the tabulated and the hybrid EOSs listed in Table 8.2.1. We refer the reader to Guerra et al. 2024 for further details.

Table 8.2.1 Summary of the initial properties of the BNS configurations. We list the EOSs, the temperature T[MeV], the gravitational mass $M[M_\odot]$, and the compactness $\mathcal{C} \equiv M/R_{\rm eq}$ and the tidal deformability $\Lambda = (2/3)\kappa_2 \mathcal{C}^{-5}$ for each individual star. Here $R_{\rm eq}$ is the equatorial coordinate radius toward the companion of each star, and κ_2 is the second Love number. The ADM mass $M_{\rm ADM}[M_\odot]$, the ADM angular momentum $J_{\rm ADM}[M_\odot^2]$ and the angular velocity Ω[krad/s], for an initial binary coordinate separation of ~ 44.3 km. In all cases the NS has a rest-mass $M_0 = 1.4 M_\odot$. The first (last) four rows correspond to the BNS modelled through a fully-tabulated (piecewise polytropic) EOS. Dash symbol denotes "not applicable".

EOS	T	M	$\mathcal{C}$	Λ	$M_{\rm ADM}$	$J_{\rm ADM}$	Ω
SLy4	0.01	1.28	0.16	536.00	2.54	6.63	1.77
DD2	0.01	1.29	0.14	1098.68	2.56	6.73	1.78
HShen	0.01	1.30	0.13	1804.67	2.58	6.82	1.78
LS220	0.01	1.29	0.15	851.72	2.55	6.68	1.77
SLy4	-	1.28	0.16	511.70	2.54	6.62	1.77
DD2	-	1.29	0.14	1113.92	2.56	6.73	1.78
HShen	-	1.30	0.13	1633.24	2.58	6.82	1.78
LS220	-	1.29	0.15	899.05	2.55	6.69	1.77

The initial data were evolved in Guerra et al. 2024 using the `IllinoisGRMHD` code [Werneck et al. 2023, Etienne et al. 2015] embedded in the `Einstein Toolkit` infrastructure [Löffler et al. 2012]. Much of the numerical infrastructure has been extensively discussed in Werneck et al. 2023, Etienne et al. 2015, Noble et al. 2006, Guerra et al. 2024 to which the interested reader is addressed for details. As a summary we only mention that the code evolves the BSSN equations [Baumgarte and Shapiro 1998, Shibata and Nakamura 1995] coupled to the puncture gauge conditions using fourth-order spatial differentiation. In all cases the damping coefficient appearing in the shift condition was set to $1/M$, where M is the Arnowitt–Deser–Misner (ADM) mass of the system. Moreover, the `IllinoisGRMHD` adopts the Valencia formalism for the GR hydrodynamics equations [Banyuls et al. 1997, Font 2008] which are integrated with a state-of-the-art finite-volume algorithm. Time integration is performed using the method of lines with a fourth-order Runge-Kutta integration scheme with a Courant-Friedrichs-Lewy (CFL) factor of 0.5.

Some of the evolutions reported in Guerra et al. 2024 extend for over $t - t_0 \sim 150$ ms after merger. This permits to identify the imprint of thermal effects on the postmerger GW signals and in the frequency spectra. In particular, such long-term simulations allow us to study the potential dependence on the treatment of thermal effects for both, the frequencies associated with the fundamental quadrupolar mode, excited about some 5 ms after merger, along with those of

inertial models, typically appearing at significantly longer postmerger times [De Pietri et al. 2018, De Pietri et al. 2020, Guerra et al. 2024].

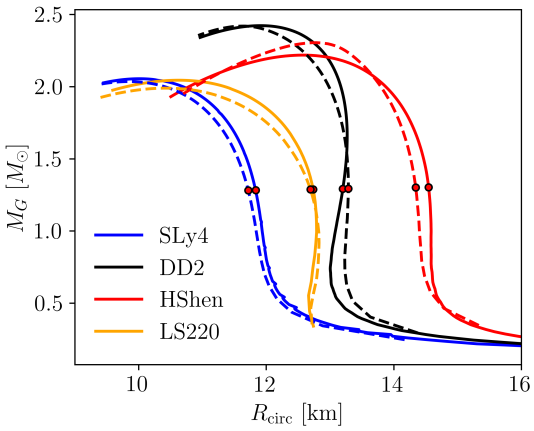

Figure 8.2.1 Gravitational mass vs circumferential radius for the tabulated (solid lines) and the hybrid (dotted lines) EOSs used in this work. The selected NS configurations are depicted with red dots.

8.3 Results

For all of our injections, we use the ET-D configuration from Hild et al. 2011 as the sensitivity curve of the ET, which is formed by a three-detector network on the same site. Our conclusions should also broadly hold for CE [Evans et al. 2021], as its detection capabilities are similar to those of ET. For simplicity and as we did in Chapter 7, we consider Gaussian noise [Blackburn et al. 2008, Abbott et al. 2009, Aasi et al. 2012] (coloured by the PSD of the detector) and no sources of noise/glitches are added. The waveforms are injected at different distances, which result in different SNRs. We also assume that the source is optimally oriented with respect to the detector. For completeness, in Appendix 8.A we discuss the differences in the overlap function for non-optimal orientation and sky location.

We set a maximum number of wavelets of $N_W^{\rm max} = 200$, a maximum quality factor of $Q^{\rm max} = 200$, $n = 2 \times 10^6$ iterations, and a sampling rate of 8192 Hz, resulting in the same setup used in Chapter 7.

8.3.1 Early postmerger phase

We begin by focusing on the first milliseconds after merger. During this early phase, strong nonaxisymmetric deformations and nonlinear oscillations are present, namely combinations of oscillation modes and spiral deformations, leading to the emission of GW signals with frequencies around a few kHz. Since the amplitude of these signals is considerably larger than in the late postmerger phase, we also consider correspondingly larger distances, from 1 Mpc up to 200 Mpc.

8.3.1.1 *Waveform reconstructions*

Figures 8.3.1 and 8.3.2 show the coloured, time-domain signal (top panels) and the ASD (bottom panels) of the injected (red) and reconstructed (blue) GW signals (with the detector ASD), at a fixed distance of 20 Mpc. Fig. 8.3.1 corresponds to the `HShen` EOS and Fig. 8.3.2 to the `SLy4` EOS, respectively. Panels (a) and (b) in both figures differ by the time window used to compute the ASD, highlighted in yellow in the time-domain waveform plots. We adapt the time windows to each particular model and phase of the waveform. The time windows employed for each EOS and phase of the simulation (characterised by a dominant oscillation mode) are summarised in Table 8.3.1. The blue-shaded regions in the ASD plots in both figures show the 50% and 90% CIs of the distribution of the recovered waveforms. These intervals are given by values of the percentiles 25th/75th and 5th/95th, respectively.

The windows used in panel (a) of Figures 8.3.1 and 8.3.2 correspond to the time interval $t \in [-10, 4]$ ms and $t \in [-10, 6]$ ms, respectively, being $t = 0$ the time of merger. During this phase, the $f_{2,i}$ modes are excited, and they exhibit the frequency peaks shown in the bottom rows. The left column of the panels in both figures show the reconstructions of the hybrid version of the EOS, whereas the right column depicts the tabulated version. For the case of `HShen`, in panel (a) of Fig. 8.3.1, the $f_{2,i}$ peaks are located around 2200 Hz. The ASD of the hybrid and tabulated version of the EOS are similar, but the tabulated one produces $f_{2,i}$ modes with a slightly lower frequency. Regarding `SLy4`, in panel (a) of Fig. 8.3.2, the peaks are located around 3250 Hz, and the tabulated version of the EOS also has the peaks at slightly lower frequencies than the hybrid version. The differences between the hybrid and tabulated versions of the EOSs are almost negligible, with a difference between the frequency peaks of $\approx 4\%$. For the `DD2` and `LS220` EOSs the mismatch is even smaller.

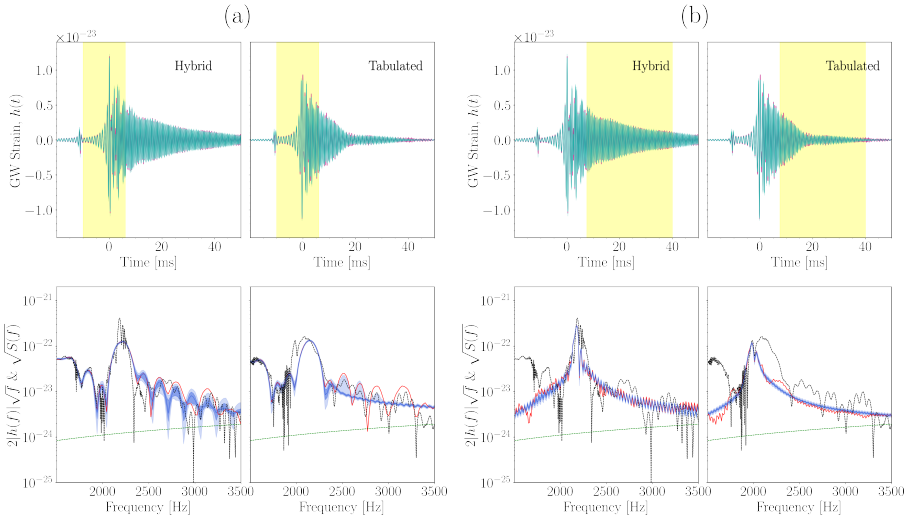

Figure 8.3.1 Top row: injected (red) and reconstructed (blue) time-domain waveforms from BNS mergers with the `HShen` EOS. Bottom row: corresponding ASD, computed either using the complete waveforms (dotted line) or at the time windows depicted in yellow in the strain plots in panels (a) and (b) (see Table 8.3.1). The left (right) column of each of the two panels corresponds to the hybrid (tabulated) version of the EOS. The source is located at $D = 20$ Mpc. The signals are injected into the ET-D configuration of the ET detector, whose sensitivity curve is shown by the dashed green curve within the frequency range depicted.

In panels (b) of Figs. 8.3.1 and 8.3.2 we depict again the time-domain and the spectra of the injected and recovered signals for the same two EOSs, but the time window is applied now for the intervals $t \in [7.5, 40]$ ms (`HShen`) and $t \in [20, 30]$ ms (`SLy4`). Therefore, the ASD of the bottom panels show the appearance of the f_2 modes. For the `SLy4` EOS the amplitude of the f_2 modes is lower than that of the $f_{2,i}$ modes. For the `HShen` EOS there are more noticeable differences in the position of the peaks between the hybrid and tabulated models than for the `SLy4` EOS. For both cases, the peaks of the f_2 modes appear at lower frequencies than for the $f_{2,i}$ modes.

Table 8.3.1 Time windows employed to capture the different oscillation modes appearing during postmerger. Times are expressed in milliseconds and $t = 0$ ms is the merger time.

EOS	Mode		
	$f_{2,i}$	f_2	Inertial
`SLy4`	[-10, 4]	[20, 30]	[75, 140]
`DD2`	[-10, 4]	[7, 17]	[70, 140]
`HShen`	[-10, 6]	[7.5, 40]	[105, 140]
`LS220`	[-10, 6]	[8, 15]	[80, 140]

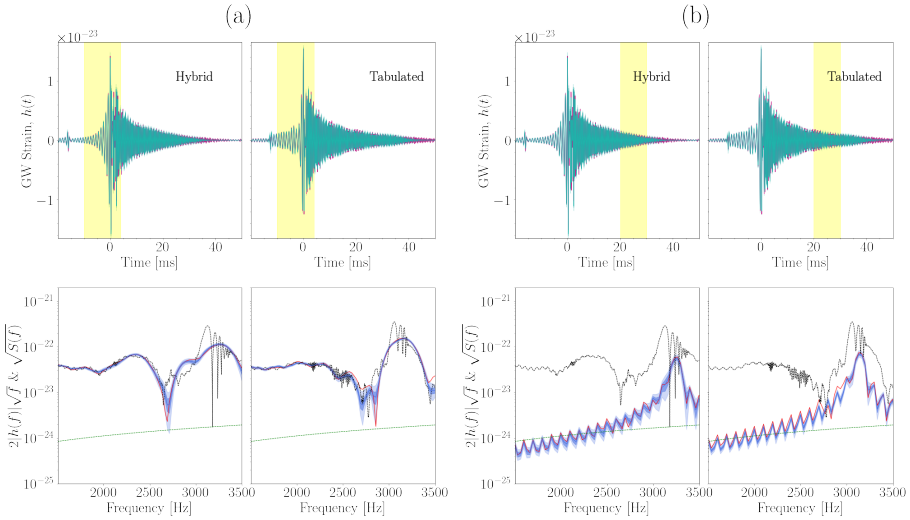

Figure 8.3.2 Same as in Figure 8.3.1 but for the `SLy4` EOS.

Spectrograms of the median of the reconstructed signals are shown in Figure 8.3.3 for the case of `HShen` (left) and `LS220` (right). In both panels, the plots in the upper row refer to the hybrid version of the EOS and the lower row to the tabulated version. This figure shows the spectrograms for two difference source distances, 10 Mpc and 50 Mpc. For a distance of 10 Mpc all the stages of the postmerger signal are visible in the spectrogram of the `HShen` EOS: there is an initial part where the signal is louder followed by a decrease in frequency and amplitude, visible up to more than 100 ms after merger. This trend occurs for both hybrid and tabulated versions of the `HShen` EOS. As the distance increases, however, the last part of the signal cannot be reconstructed. Beyond 50 Mpc, the signal is only visible up to $t \sim 50$ ms. Note that, for the hybrid version of the `HShen` EOS, the signal is detectable for longer times.

The four plots in the right panel of Figure 8.3.3 depict two completely different behaviours between the hybrid and tabulated versions of the `LS220` EOS. In the first case (upper row), the frequency of the signal increases with time up to $t \sim 40$ ms for sources located at short distances (10 Mpc). At that point, the signal disappears because the remnant collapses to a BH (at $t = 66.2$ ms after merger) [Guerra et al. 2024]. However, the tabulated version of the `LS220` EOS (lower row) shows that a stable remnant evolves for more than 100 ms after merger. In this case, the GW signal decreases in amplitude, reaching

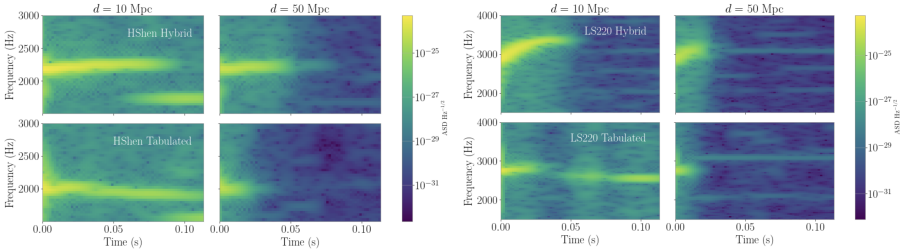

Figure 8.3.3 Spectrograms of the reconstructed GW signals at two source distances, $D = 10$ Mpc and 50 Mpc. The left (right) panels correspond to the `HShen` (`LS220`) EOS. Plots in the upper row depict the hybrid version of the EOS and those in the lower row the tabulated model. As the distance to the source increases, it becomes more difficult to capture the time evolution of the frequency of the signal at late times.

frequencies of about 2 kHz. At larger source distances (50 Mpc) BayesWave only recovers the inspiral phase and the very early stages after merger, not capturing the collapse of the remnant for the hybrid version of the EOS.

8.3.1.2 *Frequency peaks of the $f_{2,i}$ and f_2 modes*

From the posterior distributions of the GW signals that BayesWave provides, one can compute the ASD via the FFT of the time-domain signal using a certain time window. This yields posterior distributions of the frequency peaks of the spectra. We start considering time windows spanning from $t \approx 10$ ms before merger to a few tens of milliseconds after merger (depending on the EOS; see Table 8.3.1). The size and position of the time windows are chosen to distinguish the frequency peaks related to the $f_{2,i}$ and f_2 modes.

The top and middle panels of Figure 8.3.4 show the posterior distributions of the frequency peaks for the $f_{2,i}$ and the f_2 modes, respectively. (The bottom panel in this figure will be discussed below.) The posterior distributions are constructed using a Gaussian kernel density estimator and setting the bandwidth equal to the frequency resolution given by the FFT (which will be different depending on the time window considered). Each column corresponds to a certain EOS, from left to right `SLy4`, `HShen`, `DD2` and `LS220`. The upper row shows the hybrid version of each EOS, and the lower one the tabulated version. The different colors refer to several distances to the source, that range from $D = 25$ Mpc to $D = 200$ Mpc. For the $f_{2,i}$ mode, shown in the top panel of Figure 8.3.4, differences between the treatment of thermal effects in the EOS are only detectable for `SLy4` (first column) and `HShen` (second column). These two EOSs show the largest deviation in the frequency peaks as a result of the distinct consideration of thermal effects. The frequency peak of `SLy4` is not

well recovered for $D \geq 50$ Mpc, with a p-value[2] of 0.05 and 0.13 for the hybrid and tabulated cases, respectively, at $D = 200$ Mpc. This results in detectable differences between both versions of the EOS only for close enough sources. In the case of `DD2` and `LS220`, the curves of the posterior distributions overlap for all distances, and no differences between the tabulated and hybrid EOS might be seen. The range of detectability is almost the same for all EOS but `SLy4` (first column). For the other cases, the peaks are detectable up to $D \gtrsim 200$ Mpc, with p-values over 0.15 for all distances.

The middle panel of Figure 8.3.4 depicts the frequency peaks corresponding to the f_2 mode. These peaks are more difficult to recover than those of the $f_{2,i}$ mode, even though the differences between the hybrid and tabulated versions of the EOSs are more prominent. For `SLy4`, the recovery is inaccurate for distances $D \gtrsim 50$ Mpc, as the peaks of the posterior distributions are located at significantly lower frequencies than the injected value, for both versions of the EOS. The corresponding p-values are 0.03 and 0.025 for the hybrid and tabulated versions, respectively, at $D = 100$ Mpc. On the other hand, `HShen` is the EOS for which the peaks of the f_2 mode are best recovered, especially for the hybrid model, even at the largest distances considered. (This also holds for the case of the $f_{2,i}$ mode shown in the top panel). For this EOS there is a shift in the peak frequency of almost 200 Hz between the hybrid and tabulated treatments of thermal effects, which corresponds to a difference of about 10%. This difference might be detectable up to $D \lesssim 200$ Mpc. As the distance to the source increases, the peaks for the tabulated version of the `HShen` EOS are reconstructed at increasingly higher frequencies, to reach values that eventually overlap with the ones inferred for the hybrid case. The `DD2` EOS also gives f_2 peaks at almost the same frequency for both versions of the EOS (only with a difference of $\approx 1.45\%$), as in the case of the $f_{2,i}$ mode shown in the top panel of Figure 8.3.4. However, the peaks of the f_2 mode are well recovered up to $D \approx 100$ Mpc, larger than for the $f_{2,i}$ mode. Beyond this distance, the mean of the distribution starts differing more than 100 Hz from the injected value. For the tabulated version of the `LS220` EOS, the f_2-mode frequency peak only decreases about 100 Hz compared to the $f_{2,i}$ mode. However, the hybrid version of this EOS displays a peak at a higher frequency. This can also be seen in the right panels of Fig. 8.3.3. This is due to the fact that the remnant collapses to a BH only when the `LS220` EOS implements a hybrid treatment of thermal effects. Both peaks of the f_2 mode might be detectable for `LS220` up to 200 Mpc.

[2]We set a threshold of $p > 0.05$ (corresponding to 2-σ) to consider as null-hypothesis that the mean of the distribution is equal to the frequency peak of the injected signal.

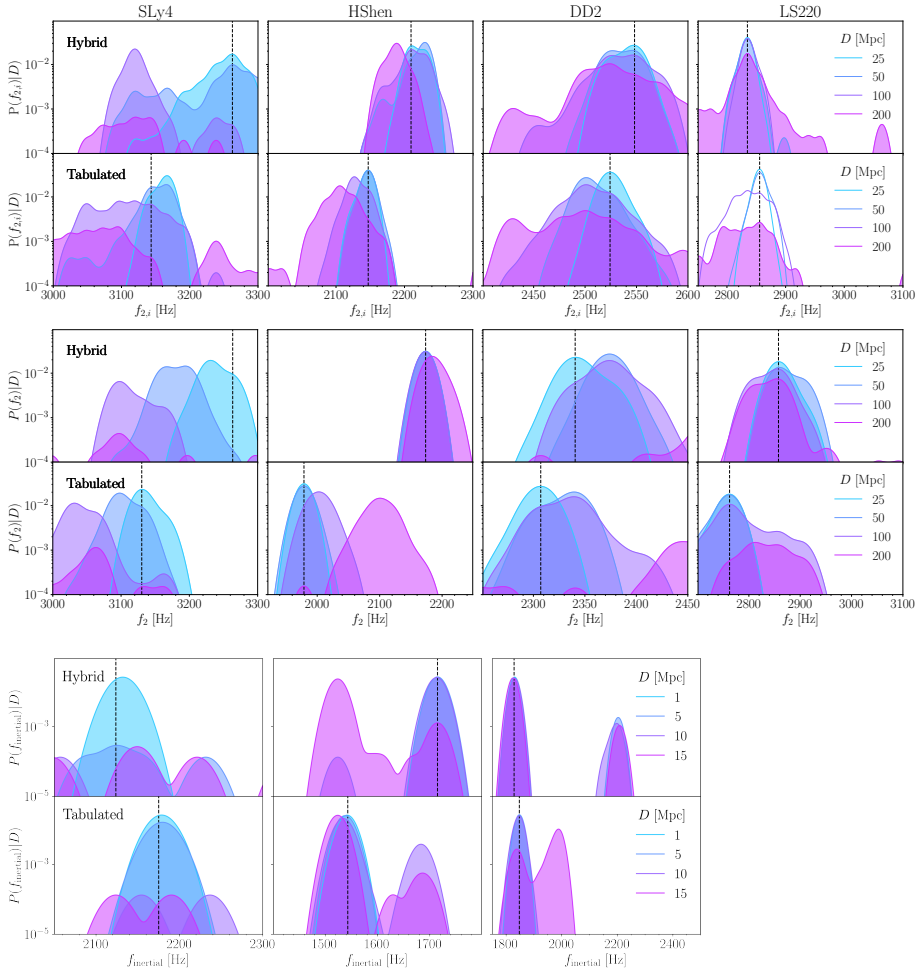

Figure 8.3.4 Posterior distributions of the frequency peaks for the f_{2i} modes (top), f_2 modes (middle), and $f_{\rm inertial}$ modes (bottom). Each column corresponds to a different EOS (`SLy4`, `HShen`, `DD2` and `LS220`, from left to right). The upper (lower) rows are the hybrid (tabulated) versions of the corresponding EOS. Each color in the posterior distributions corresponds to a different distance to the source, indicated in the legends. The vertical black dashed lines are the frequency peaks of the injected signals. As expected, the shorter the distance the narrower the distributions and the closer they are to the injected values. We do not show the peaks for `LS220` in the bottom row because the hybrid version collapses to a BH and there is no late postmerger signal.

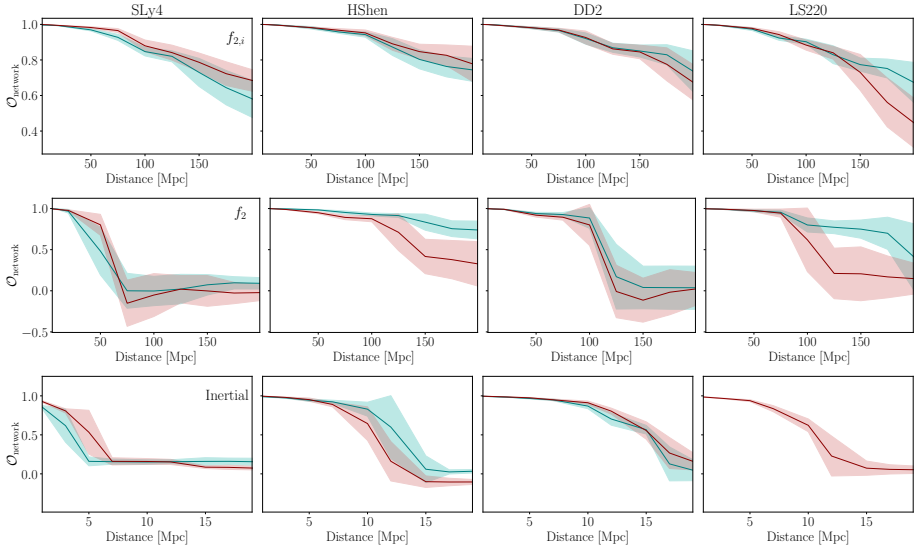

Figure 8.3.5 Detector network overlap between the injected and reconstructed signals as a function of the distance to the source. Top, middle and bottom rows correspond to the $f_{2,i}$ modes, the f_2 modes and the $f_{\rm inertial}$ modes, respectively. Each column corresponds to one EOS. Solid lines indicate the mean value over the waveform posterior distribution and shaded areas are the standard deviations. The blue color corresponds to the hybrid version of the EOS and the red color to the tabulated version. Notice that the blue curve and shaded area are not shown for the `LS220` EOS in the bottom-right plot as the remnant for the hybrid version of this EOS collapses to a BH.

In general, the hybrid and tabulated posterior distributions of the f_2 mode frequency peaks do not overlap as much as in the case of the $f_{2,i}$ mode. This fact favours the prospects of detecting thermal effects in the postmerger signal using the f_2 mode. For example, the frequency shift in the f_2 mode for the `HShen` EOS is detectable up to almost 200 Mpc. For `SLy4`, the shift in the f_2 mode frequency is still large to be detectable, but only for small distances to the source, since the signal amplitude is lower for this EOS. The difference in the frequency peaks for the f_2 mode is also detectable for `LS220`, as the peak of the posterior distribution for the tabulated version is over the left tail of the distribution of the hybrid version of this EOS. Finally, both posterior distributions for the `DD2` EOS still overlap even at $D = 25$ Mpc, which makes it very difficult to distinguish the treatment of thermal effects for this EOS in the GW signal.

8.3.1.3 *Overlap of the early postmerger phase*

The detector network overlap between the injected and reconstructed GW signals as a function of the distance to the source is displayed in Figure 8.3.5 for our four

EOSs. The top and middle rows in this figure correspond to the early postmerger phase (i.e., to the times reported in the first two columns in Table 8.3.1). The plots in the bottom row correspond to the late phase and will be discussed below.

We start considering the network overlap for the $f_{2,i}$ mode, shown in the top row of Figure 8.3.5. The blue coloured line corresponds to the average value of the overlap for the hybrid version of the EOSs and the red line to the tabulated version. The shaded regions are the standard deviations from the overlap posterior distributions. Each column corresponds to a different EOS. As expected, for lower distances the overlap is closer to one (perfect match). For all cases but the tabulated version of the `LS220` EOS, the average value of the posterior distribution of the network overlap is over 0.5 up to distances of about 200 Mpc. The higher values of the overlap are obtained for the `HShen` and for the `DD2` EOSs. No common trend for higher or lower values of the overlap depending on the treatment of thermal effects is observed across our EOS sample.

The middle row of Figure 8.3.5 depicts the corresponding network overlap for later postmerger times, in which the f_2 mode is dominant. In this case, the overlap at a given distance is lower than that achieved for the $f_{2,i}$ mode, for all EOS. For the case of `SLy4`, the average values of the posterior distributions fall abruptly below 0.5 for $D \gtrsim 50$ Mpc. As happens for the $f_{2,i}$ mode, `HShen` also reaches the highest overlap for the f_2 mode, particularly for the hybrid version of this EOS, significantly larger than the value for the tabulated version. The latter reaches an overlap of about 0.5 at 150 Mpc. Regarding the `DD2` EOS, values of the overlap higher than 0.75 are attained up to 100 Mpc. However, those values abruptly fall to no overlap for larger distances. A similar trend is also observed for `LS220` even though the hybrid version of this EOS yields higher overlap values for the f_2 mode than the tabulated version for significantly larger distances.

8.3.1.4 *Tidal deformability*

As previously seen in Section 1.4 from the Introduction, the frequency peaks of the early postmerger phase of the remnant can be used to infer properties ofNSs by exploiting correlations with physical parameters through EOS-insensitive, quasi-universal relations (see e.g. Read et al. 2013, Bernuzzi et al. 2014, Bauswein and Stergioulas 2015, Takami, Rezzolla, and Baiotti 2015, Rezzolla and Takami 2016, Bauswein and Stergioulas 2019, Bauswein et al. 2019, Soultanis, Bauswein, and Stergioulas 2022, Topolski, Tootle, and Rezzolla 2024). In particular, a number of empirical fits between the frequencies of various modes (e.g. the peak frequency at merger, the $f_{2,i}$ mode, and the f_2 mode) and the tidal deformability

parameter Λ characterising the quadrupole deformability of an isolated NS, have been proposed (see Soultanis, Bauswein, and Stergioulas 2022, Topolski, Tootle, and Rezzolla 2024 and references therein for up-to-date revisions of existing literature). In Guerra et al. 2024 we present new fits of the frequencies of the $f_{2,i}$ and f_2 modes to the tidal deformability parameter using our set of EOSs. We note that those quasi-universal relations are built using hybrid EOSs only since the number of simulations with tabulated EOSs is not large enough to yield a meaningful fit. However, their validity when applied to simulations with tabulated EOSs can be tested, using the standard deviation of the correlation for the hybrid EOSs as a reference metric. For the $f_{2,i}$ and f_2 modes, the standard deviation is 67.54 Hz and 97.56 Hz, respectively [Guerra et al. 2024]. Using those fits we discuss here the posterior probability distributions of the tidal deformability parameter obtained from both, the frequencies of the $f_{2,i}$ and f_2 modes, and for the two different treatments of thermal effects.

In the top row of Figure 8.3.6 we show the results for the $f_{2,i}$ mode, for different distances and all four EOSs. The distributions displayed are built using the empirical relations from Guerra et al. 2024. The upper panels correspond to the hybrid version of the EOSs and the lower panels to the tabulated version. Since Λ_i is directly calculated from $f_{2,i}$, the behaviour of the posterior distributions of the two quantities with the distance is the same (cf. uppermost row of Fig. 8.3.4). Our results indicate that Λ_i could be reconstructed up to $D \approx 200$ Mpc for all EOSs except for `SLy4` for which the reconstruction is acceptable only up to $D \lesssim 100$ Mpc. For the `SLy4` EOS (first column), the distributions of Λ_i are closer to the injected value (red vertical dashed line) for the tabulated version. On the other hand, `HShen` and `DD2` both yield a good recovery of Λ_i for all the distances shown. Their p-values at 200 Mpc are above 0.175 for both versions of the EOSs.

The tidal deformability parameter can also be computed using the frequency of the f_2 mode. To do so we use the fits for this mode presented in Guerra et al. 2024. The `LS220` EOS is discarded in this analysis because at the postmerger times considered the evolution of the remnant when using the hybrid version of this EOS already shows the formation of a BH. The differences on the distributions of Λ between the hybrid and tabulated versions of the EOSs for the f_2 mode are displayed in the bottom row of Fig. 8.3.6. As expected, the posterior distributions are similar to those obtained with the f_2 mode (middle row of Fig. 8.3.4). The most striking difference is that for the tabulated version of the `HShen` EOS, Λ is inaccurately inferred at $D = 200$ Mpc.

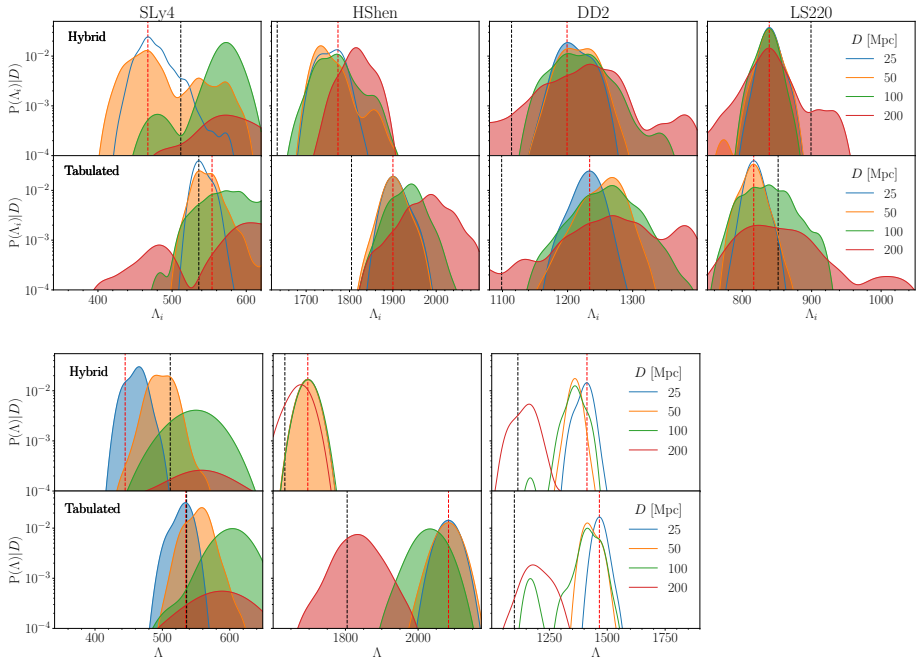

Figure 8.3.6 Posterior distributions of the tidal deformability parameter computed from the frequency peaks of the $f_{2,i}$ mode, Λ_i (top row) and of the f_2 mode, Λ (bottom row). Each column corresponds to a different EOS and different colors correspond to different distances to the source. The vertical red dashed line is the injected value of the parameter (obtained with the fit from Guerra et al. 2024) and the vertical black dashed line is the true value shown in Table 8.2.1. We do not show the distributions for `LS220` in the bottom row because the hybrid version collapses to a BH after the early postmerger phase. See main text for details.

As stated in Section 8.2 using tabulated or hybrid EOSs leads to slightly different initial NS configurations and, thus, to different values of the tidal deformability. This is why the vertical black lines displayed in Fig. 8.3.6, corresponding to the values of Λ reported in Table 8.2.1, are not the same for the two approaches for the EOS. This figure shows that the empirical fits of Guerra et al. 2024 can be also applied to simulations with tabulated EOSs in most cases, as the variations in frequency are within one standard deviation of the mean of the correlation. In general, we find that the fit for the $f_{2,i}$ mode (red vertical lines) is closest to the "true" value from the simulation. We observe that the tidal deformability might be detected up to several tens of Mpc for all EOSs (when computed from empirical fits built for hybrid models only).

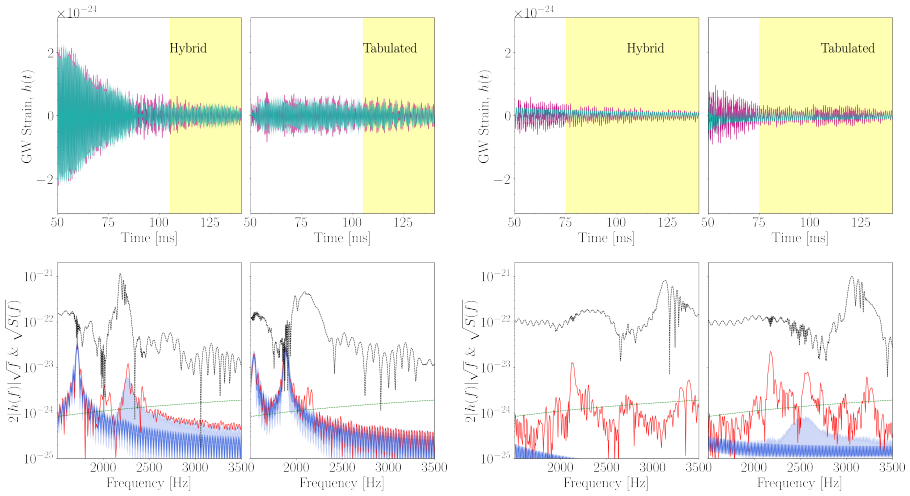

Figure 8.3.7 Waveforms (top row) and ASD (bottom row) of the injected (red) and reconstructed (blue) late postmerger GW signals for a source located at $D = 7$ Mpc. The left panel corresponds to the `HShen` EOS and the right panel to the `SLy4` EOS. Within each panel, the left (right) column displays the hybrid (tabulated) version of the respective EOS. The black and green dotted lines in the bottom-row plots are the ASD computed from the complete waveforms and the sensitivity curve of the ET detector, respectively.

8.3.2 **Late postmerger phase: inertial modes**

At later postmerger times than those considered in the preceding section ($t \gtrsim 50$ ms) the amplitude of the f_2 mode decreases and convective instabilities in the interior of the remnant set in (see De Pietri et al. 2018, De Pietri et al. 2020, Guerra et al. 2024). Those trigger the excitation of inertial modes, whose dynamics leave an imprint in the late postmerger signal. Inertial modes attain smaller amplitudes than the modes from the early postmerger phase and their frequency peaks in the spectra are also lower than those of the $f_{2,i}$ and f_2 modes.

8.3.2.1 *Waveform reconstructions*

Figure 8.3.7 shows the coloured, time-domain signal (top row) and the ASD (bottom row) of the injected (red) and reconstructed (blue) late postmerger GW signals (with the detector ASD), for a source located at a distance of 7 Mpc. The left panel shows the waveforms and ASD for the `HShen` EOS while the right panel displays the corresponding quantities for the case of the `SLy4` EOS. Within each panel, the left (right) column corresponds to the hybrid (tabulated) version of the respective EOS. As before, the ASD shown in the bottom row have been computed by Fourier-transforming the waveforms in the time windows

highlighted in yellow in the plots in the top row (see also Table 8.3.1). Likewise, the blue-shaded regions in the ASD plots in both figures show the 50% and 90% CIs of the distribution of the reconstructed waveforms.

At the distance considered and regardless of the treatment of thermal effects, the reconstructions of the late-time signals BayesWave produces are only accurate for the `HShen` EOS. This is due to the small amplitude of the late postmerger signal in the case of `SLy4`. The frequency peak of the dominant inertial mode for this EOS is located around 2.2 kHz (see the ASD of the injected signal, coloured in red). Despite the peak amplitude is above the sensitivity curve of the ET detector, BayesWave cannot correctly capture it, as apparent from the CI of the reconstructed distributions. Regarding the `HShen` EOS, the dominant frequency peak of the inertial modes is located below 2 kHz for both versions of the EOS. In the case of the tabulated version, two peaks are visible around 1.5 kHz and 2 kHz, while for the hybrid version of this EOS those two peaks appear at frequencies around 1.75 kHz and 2.5 kHz. Notice that the peak located at around 2 kHz for the tabulated EOS is actually the f_2 mode. This mode is not yet completely damped at this late postmerger time. Therefore, we do not consider it when computing the posterior probability for the frequency peaks in the last row of Fig. 8.3.4. The same explanation holds for the peak at around 2.5 kHz in the hybrid case (see Guerra et al. 2024 for more details).

8.3.2.2 *Frequency peaks of the inertial modes*

The posterior distributions of the frequency peaks of the inertial modes are displayed in the bottom row of Fig. 8.3.4 for all EOSs except `LS220` (as the simulation with the hybrid version of this EOS collapses to a BH at early postmerger times). The upper (lower) rows in this figure represent the hybrid (tabulated) versions of the corresponding EOSs. The injections, whose frequencies are depicted by the dashed vertical lines, are now performed at much shorter distances than we did for the $f_{2,i}$ and f_2 modes, due to the smaller amplitude of inertial modes. The largest distance considered is now $D = 15$ Mpc.

The characteristic peak frequencies of inertial modes, $f_{\rm inertial}$, are lower than the ones from the fundamental modes, $f_{2,i}$ and f_2, as can be seen by direct comparison in Fig. 8.3.4. As for the quadrupolar modes, inertial modes also display a shift in frequencies depending on the particular treatment of thermal effects in the EOS. This shift appears to be only detectable for the case of the `HShen` EOS (middle panel) as the posterior distributions of the hybrid and the tabulated versions of the EOS do not overlap up to $D \approx 10$ Mpc. On the other hand, the small amplitude of the late postmerger signal for the `SLy4` EOS is

too low to yield a good reconstruction unless the source is located at a distance of less than 5 Mpc. Only for such short distances the frequency shift in the posterior distributions might be distinguished.

8.3.2.3 *Overlap of the inertial modes*

As we did before for the $f_{2,i}$ and f_2 modes, we also use the network overlap function to assess the reconstruction of the waveforms for the case of inertial modes. Those overlaps are shown in the bottom row of Figure 8.3.5. For the `SLy4` EOS (first column) the overlap is above 0.5 for a distance to the source of less than 5 Mpc, with the tabulated version of the EOS attaining a higher value of the overlap for slightly larger distances. For both implementations of the thermal effects, the average overlap falls below 0.25 for distances above ≈ 7 Mpc, which means that the injected and reconstructed waveforms differ considerably. Correspondingly, the waveform signals for `HShen` and `DD2` (second and third columns, respectively) are still reconstructed with a network overlap over 0.5 up to a distance of about 12 Mpc. The tabulaled version of the `HShen` EOS is more poorly recovered than its hybrid counterpart, with a smaller overlap at about 10 Mpc. Finally, in the case of the `LS220` EOS (fourth column), the network overlap is above 0.5 for distances up to 15 Mpc. Notice that only the overlap of the tabulated version of `LS220` is plotted in Fig. 8.3.5 as the simulation with a hybrid EOS collapses to a BH before inertial modes have been excited.

8.4 Conclusions

Numerical simulations of BNS mergers incorporate thermal effects in the EOS using two alternative approaches. The first one is a *hybrid* approach which assumes that the pressure and the internal energy are composed of two constituents, a cold, zero temperature part described by a family of piecewise polytropes and a thermal part described by an ideal-gas-like EOS. The second approach employs *tabulated* representations of microphysical finite-temperature EOSs, providing a self-consistent method to probe the impact of thermal effects in the merger dynamics. These two ways of incorporating thermal effects in the numerical modelling lead to measurable differences in the GW signal, especially in the postmerger emission, well visible in the frequency spectra (see e.g. Bauswein, Janka, and Oechslin 2010, Guerra et al. 2024). In this Chapter we have investigated the prospects for identifying such differences by reconstructing the GW signals of Guerra et al. 2024 using BayesWave [Cornish and Littenberg 2015, Littenberg and Cornish 2015], building on our previous work in Chap-

ter 7 where we focused on inertial modes only, excited in the very late part of the postmerger signal. Here, we have considered the entire postmerger signal, i.e. both its early part where the fundamental quadrupolar f_2 mode dominates the GW spectrum and its late part where inertial modes are excited. The time-domain waveforms of Guerra et al. 2024, obtained through BNS merger simulations with four different EOSs, accounting for both descriptions of thermal effects, have been injected into Gaussian noise given by the sensitivity of the third-generation detector ET [Punturo et al. 2010, Hild et al. 2011], selecting optimal sky location and inclination. (Results for non-optimal configurations are discussed in Appendix 8.A.) The capability of BayesWave to reconstruct the injected signals has been assessed by computing the overlap function of the detector network. As the postmerger remnant evolves, the amplitude of the GW signal significantly decreases, resulting in a corresponding reduction of the overlap between injected and reconstructed waveforms. The same occurs as the distance to the source increases, irrespective of the portion of the postmerger signal being analysed.

The two representations of thermal effects in the EOS result in frequency shifts of the dominant peaks in the GW spectra. In some cases, those differences are large enough to be told apart, especially in the early postmerger phase, when the signal amplitude is the loudest, and at sufficiently small distances. The detectability prospects have been found to strongly depend on the EOS. Both, the `SLy4` EOS (at small enough distances) and the `HShen` EOS (at significantly bigger distances) present large frequency shifts of the dominant $f_{2,i}$ and f_2 modes. These shifts may allow distinguishing the differences in the implementation of thermal effects between hybrid and tabulated versions of these two EOSs with third-generation detectors. On the other hand, for the `DD2` and `LS220` EOS, no large enough frequency shifts between the hybrid and tabulated cases have been found to unambiguously differentiate with BayesWave the treatment of thermal effects in the EOS.

Differences in the dominant peaks of the GW spectra are still present during the late postmerger phase, where the inertial modes dominate [Kastaun 2008, De Pietri et al. 2018, De Pietri et al. 2020, Guerra et al. 2024]. These modes are associated with a part of the GW signal with a much lower amplitude than that of the $f_{2,i}$ and f_2 modes. Therefore, they are more difficult to detect (see Chapter 7). Our results indicate that third-generation detectors such as ET may be able to observe inertial modes up to a distance of about 10 Mpc, depending of the EOS. For this late-time part of the signal, the shift in the peak frequency due to the different treatment of thermal effects can be above 200 Hz at most,

for the case of the `HShen` EOS. On the other hand, for the `LS220` EOS, the difference is more obvious: the hybrid version of this EOS leads to the collapse of the remnant to a BH, as opposed to its tabulated version [Guerra et al. 2024].

Finally, we have also computed the tidal deformability from the frequency peaks of both the $f_{2,i}$ and f_2 modes and through the empirical fits presented in Guerra et al. 2024. The differences in thermal effects between the hybrid and the tabulated versions of the EOS inferred through the analysis of the tidal deformability parameter are also more apparent for the f_2 mode, since the shift in the frequency peaks is more pronounced.

The results of the work reported here are consistent with those recently presented by Villa-Ortega et al. 2023, who employed Bayesian model selection to explore differences between the hybrid and the tabulated approaches for the same set of GW signals. The differences in the posterior distributions of the main frequency peaks in the early postmerger GW spectra in hybrid and tabulated models reported here might be resolved in third-generation detectors up to distances of about tens of Mpc, compatible with the values found by Villa-Ortega et al. 2023.

Appendix

8.A Reconstruction of injections with non-optimal sky location and orientation

The injections discussed in the main text of this Chapter were performed considering an optimal source inclination with respect to the ET detector ($\iota = 0$) and an optimal sky location, with a right ascension of 2.9109 rad and a declination of 0.7627 rad. Therefore, the results represent the best-case scenario for a given source distance. However, in reality the source can be anywhere in the sky and have an arbitrary declination. Hence, the effective distance to the source can be actually larger. This possibility is briefly discussed in this Appendix.

Table 8.A.1 Overlap functions for different inclinations and sky localisations for a distance $D = 150$ Mpc to the source. The first (second) row corresponds to the mode $f_{2,i}$ (f_2). In parentheses we show the percentage value with respect to the overlap for the optimal case.

Mode	Optimal ι Optimal sky loc	Non-optimal ι Optimal sky loc	Optimal ι Non-optimal sky loc	Non-optimal ι Non-optimal sky loc
$f_{2,i}$	0.803	0.650 (81.0 %)	0.656 (81.7 %)	0.630 (78.5 %)
f_2	0.835	0.791 (94.7 %)	0.793 (95.0 %)	0.728 (87.2 %)

In Table 8.A.1 we report the value of the overlap function for the fundamental quadrupolar frequency peaks for a source at a distance $D = 150$ Mpc and for different combinations of sky locations and inclinations. We only consider the hybrid version of the `HShen` EOS as this is the one yielding the best detectability prospects in the optimal case. The non-optimal inclination is set to $\iota = 0.5585$ rad and the right ascension and declination in the sky for a representative non-optimal case are chosen to be 3.4462 rad and 0.45 rad, respectively. As expected,

the overlap function decreases with respect to the optimal case. The lowest values found are 78.5% (with respect to the optimal case) and 87.2% for the $f_{2,i}$ and f_2 modes, respectively. Therefore, for signals coming from a non-optimal sky location and/or from a source with a non-optimal inclination, the effective distance will not be much larger than the optimal case. Furthermore, we note that the effect of the actual sky position of the source will become less of a concern if a network of detectors built in different locations is used.

CHAPTER 9

Bayesian real-time classification of multi-messenger electromagnetic and gravitational-wave observations

This Chapter was originally published in: Marina Berbel, **Miquel Miravet-Tenés**[1], Sushant Sharma Chaudhary, Simone Albanesi, Marco Cavaglià, Lorena Magaña Zertuche, Dimitra Tseneklidou, Yanyan Zheng, Michael W. Coughlin and Andrew Toivonen. *Bayesian real-time classification of multi-messenger electromagnetic and gravitational-wave observations. Class. Quantum Grav.*, Volume 41, Issue 8, pp. 085012, April 2024. DOI: 10.1088/1361-6382/ad3279. *Reproduced with permission.*

9.1 Introduction

The first detection of a GW signal from a pair of coalescing BHs in 2015 and the first observation of a coalescing BNS system two years later have established multi-messenger astronomy (MMA) as a powerful tool for the exploration of the cosmos [Abbott et al. 2016b, Abbott et al. 2017d, Abbott et al. 2018a]. The third LVK catalog of transient GW signals (GWTC-3) [Abbott et al. 2021d] has shown that GW astronomy has entered its mature phase, becoming a true observational branch of astronomy. MMA allows scientists to explore in depth

[1]Corresponding author

the origin and structure of NSs [Ruiz, Shapiro, and Tsokaros 2021, Baiotti and Rezzolla 2017, Lasky 2015], GRBs [Murase and Bartos 2019, Ciolfi 2018], and BHs through the observation of their progenitors [Schmidt 2020, Nitz et al. 2023, Barack et al. 2019], test GR [Abbott et al. 2021e, Berti, Yagi, and Yunes 2018, Berti et al. 2018, Isi et al. 2019], probe the fundamental nature of gravity [Seoane et al. 2023, Barausse et al. 2020, Piórkowska-Kurpas and Biesiada 2022], and measure the evolution of the Universe [Abbott et al. 2023b, Abbott et al. 2021b].

A wealth of new detections is being amassed to achieve these science goals [Aasi et al. 2015, Acernese et al. 2015]. The rate of detections in LVK's O4 is close to one per day and is expected to further increase in the fifth observing run (O5) [Abbott et al. 2018b]. Over the course of O4 and the next observing runs, the LVK collaborations are expected to analyse hundreds of BBH candidate detections, as well as dozens of BNS and NSBH merger events that could potentially be MMA sources. Among the challenges that this new phase of GW astronomy brings is the necessity to coordinate the activities of EM and GW observatories in real time.

One of the most interesting areas of study in MMA is the physics of gravity-matter interaction in GW sources. Tidally disrupted matter in systems with a NS may form a high-temperature accretion disc around the BH and trigger the creation of a prompt EM emission in the form of a short GRB (see Introduction, Section 1.2). If the system ejecta are unbound, r-process nucleosynthesis may lead to a kilonova [Lattimer and Schramm 1974, Li and Paczynski 1998, Korobkin et al. 2012, Barnes and Kasen 2013, Tanaka and Hotokezaka 2013, Kasen, Fernandez, and Metzger 2015]. These phenomena could also arise in BNS postmergers through the expulsion of neutron-rich material even when tidal forces are weak [Abbott et al. 2017e, Arcavi et al. 2017, Coulter et al. 2017, Kasliwal et al. 2017, Lipunov et al. 2017, Soares-Santos et al. 2017, Tanvir et al. 2017]. The presence of a postmerger matter remnant, which results in an EM signature or a prompt collapse, is a common factor in all of these scenarios. Determining the potential of a GW source to become an EM emitter and enabling coincident observations of these systems by EM and GW observatories in low latency are crucial for the success of MMA.

The LVK employs different matched-filtering pipelines for low-latency GW searches [Sachdev et al. 2019, Messick et al. 2017, Sachdev et al. 2020, Nitz et al. 2018, Adams et al. 2016, Chu et al. 2022, Klimenko et al. 2016]. These searches are based on discrete template banks of CBC waveforms that provide, among other parameters, the component masses and the dimensionless (anti-)aligned spins of the objects along the orbital angular momentum. These parameters can

be used to determine the EM properties of GW candidates in real time through empirical fits of NR simulations [Foucart 2012, Foucart, Hinderer, and Nissanke 2018]. Alerts of candidate GW events that included two EM-property metrics identifying whether the CBC system contains a NS, `HasNS`, and a postmerger matter remnant, `HasRemnant`, were issued in the third observing run (O3) with a median latency of the order of a few minutes after detection. Alerts with similar content continue to be issued in O4 with even lower latency. Additionally, LVK's O4 alerts include a measure of the `HasMassGap` property, i.e., the likelihood that one of the source compact objects has a mass in the lower-mass gap region between NSs and BHs [Farah et al. 2022] (see the LVK online user guide[2]).

Classification of GW candidate events in low latency poses several challenges as the need for accuracy contrasts with the urgency to issue the information as quickly as possible. The approach taken by the LVK so far has been to use a specific implementation of a supervised KNeighborClassifier (KNN) ML algorithm [Pedregosa et al. 2011] with input from the detection pipelines and EOS models to generate independent `HasNS` and `HasRemnant` *binary* classification probabilities [Chatterjee et al. 2020]. The KNN model is trained on a broad set of synthetic CBC signals injected in real detector noise from the second observing run (O2). The advantage of this scheme relies on its capability to handle the statistical systematic uncertainties in the parameters recovered by the search pipelines. This approach allowed for a marked improvement in speed compared to the semi-analytic effective Fisher formalism method that was deployed in O2.

In this work, we revisit the problem of the real-time production of `HasNS` and `HasRemnant` probability metrics with the aim of further improving the latency and performance of the current LVK ML-based scheme [Chatterjee et al. 2020]. In the current LVK implementation, the validity of an event's classification outcome is evaluated using elements from the algorithm's confusion matrix and its Receiver Operating Characteristic (ROC) curve, which is typically used to evaluate the performance of an algorithm by plotting the true positive rate (TPR) against the false positive rate (FPR) at various threshold values. *Algorithmic* probabilities for `HasNS` and `HasRemnant` are the fractions of KNN neighbours around an event that, according to the algorithm's training, indicate whether the event has a NS or is EM-bright. In this work, we adopt a new strategy, constructing *Bayesian* probabilities from a complementary data set to the training data set. A second limitation of the current classification implementation is the fact that the `HasNS` and `HasRemnant` labels are treated as independent variables. In reality, the probability of the formation of tidally disrupted matter, i.e., an EM bright event,

[2]https://rtd.igwn.org/projects/userguide/en/v17.1/content.html

is always smaller than the probability of the system hosting a NS. Therefore, the `HasNS` and `HasRemnant` labels cannot be treated as disjoint. Currently, this physical requirement is not implemented mathematically but rather is based on data; the lack of inversions is tested a posteriori using a technique known as *parameter sweep*, which involves assessing the algorithm's performance across the whole parameter space. One of the main purposes of this work is to go beyond the above scheme and calculate true *conditional* probabilities for `HasNS` and `HasRemnant`.

To achieve this, we design a new classification scheme and perform a thorough study and comparison of two ML algorithms. We first implement a definition for conditional `HasNS` and `HasRemnant` metrics that incorporates *ab initio* the physical requirement that a system with a postmerger matter remnant must necessarily contain a NS. Then we calculate Bayesian probabilities for `HasNS` and `HasRemnant`. We also implement a marginalisation procedure over a set of EOS that minimises possible systematics arising from the use of a single EOS. Finally, we test the performance of the scheme and the algorithms on synthetic O3 signals and confident GW detections from the latest GWTC-3 catalog.

The structure of the Chapter is as follows. Section 9.2 introduces the classification algorithms. Bayesian probabilities for `HasNS` and `HasRemnant` and the labelling scheme are defined in Sec. 9.3. The data set is described in Sec. 9.3.2. Results and algorithm comparisons are reported in Sec. 9.4. Conclusions and future developments are presented in Sec. 9.5. The process of cross-validation of our algorithms is covered in depth in Appendix 9.A. A direct comparison of our approach with the current LVK method is provided in Appendix 9.B.

9.2 Classification Algorithms

We consider two alternative algorithms for unsupervised classification: KNN and random forest (RF). These methods were chosen because of their versatility, ease of implementation in low-latency, and comparison with the algorithms currently being used by the LVK (KNN for `HasNS` and `HasRemnant`, RF for `HasMassGap`). In this section, we briefly describe the relevant features of the algorithms and their implementation.

K-Nearest Neighbours

K-Nearest Neighbours is a non-parametric, supervised algorithm [Fix and Hodges 1989, Cover and Hart 1967] that uses the fact that similar points in a data set are "near" each other in their parameter space. When it is applied to

classification problems [Guo et al. 2003], the algorithm is usually renamed KNN. The algorithm captures the idea of similarity between points by computing the distance between each point in a training set and its neighbours according to a pre-determined metric. Next, it sorts the neighbours in ascending order based on their distance to the testing point. By choosing the top K neighbours from the sorted array, KNN assigns the label to the testing point that corresponds to the most frequent neighbour.

In this work, we use the open-source Python KNN implementation of scikit-learn [Pedregosa et al. 2011]. We fix the algorithm hyperparameters by cross-validating over the data set and obtain the highest accuracy. Throughout our analysis we use $K = 8$ neighbours, the Manhattan metric, the BallTree algorithm and the neighbours are weighted by the inverse of their distance to the event. Further details on hyperparameter tuning are given in Appendix 9.A. This configuration differs from the LVK's current implementation, which employs the Mahalanobis metric and $K = 2n + 1 = 11$ neighbours, where n is the number of features. Our configuration is the optimal choice for the new labelling scheme that is presented in Sect. 9.3.3.

Random Forest

RF is a classification method based on an ensemble of decision trees. The trees are hierarchical models that make decisions by recursively splitting the data at the separation nodes into different categories based on the values of features. Each tree in the forest is trained independently. To classify a data point, each tree predicts a category and the algorithm assigns the one that has been chosen the most. RF is known for its parallelisation capabilities, as computations inside each tree are independent of the rest. A RF algorithm is usually trained using bootstrapping, a technique that randomly assigns subsets of the training data set to each tree. This helps prevent overfitting, as each individual classifier is not exposed to the same data, and encourages pattern recognition by studying the same data from different subsets. The model's performance on the given data set can be optimised by tuning the input hyperparameters.

In this work, we use the open-source Python RF implementation of scikit-learn [Pedregosa et al. 2011]. The main tunable hyperparameters are the number of trees, the maximum allowed depth, and the information gain criteria used at splitting. Similar to KNN, we choose the algorithm's optimal hyperparameters by measuring the accuracy in the testing set. We use 50 trees in the forest, with a maximum depth of 15, and the maximum number of features considered in a

node is the square root of the total number of features. Appendix 9.A provides details on the cross-validation method used to determine these hyperparameters.

9.3 Probability and Labelling Scheme

Bayesian probabilities for the `HasNS` and `HasRemnant` metrics can be defined using the results of the KNN and RF algorithms, namely the fraction of KNN's neighbours and RF's trees that predict a given label. In this section, we define the probabilities and explain how to derive them from a data set of simulated signals.

9.3.1 Definition of Bayesian Probabilities

Let us define the probability of a candidate event E being originated by a system with a NS [$E(\texttt{HasNS}) = \texttt{TRUE}$] and EM bright [$E(\texttt{HasRemnant}) = \texttt{TRUE}$] given the classifier's outcome evaluated on the detection pipeline output, $\mathbf{A_X}$, as $P(\texttt{HasNS}|\mathbf{A_X})$ and $P(\texttt{HasRemnant}|\mathbf{A_X})$, respectively. The classifier outcome can be understood as a map $A : \mathbf{X} \to \mathbf{A_X}$, where $\mathbf{X}(E)$ is a vector that identifies the output of the detection pipeline and $\mathbf{A_X}$ is a vector that uniquely identifies the classifier algorithm's output for $\mathbf{X}$.

Since a system can be EM bright only when a NS is present in the system, the condition $P(\texttt{HasRemnant}|\mathbf{A_X}) \leq P(\texttt{HasNS}|\mathbf{A_X})$ must hold. However, if the probabilities are calculated disjointly, this condition may be violated because of statistical and systematic errors in the pipeline's reconstructed signal parameters, as well as bias and limited accuracy of the ML algorithm. The approach discussed below avoids the occurrence of this inconsistency.

The true properties (ground truth) of an observed event are unknown. Therefore, the probabilities $P(\texttt{HasNS}|\mathbf{A_X})$ and $P(\texttt{HasRemnant}|\mathbf{A_X})$ cannot be calculated from observations. However, estimators for $P(\texttt{HasNS}|\mathbf{A_X})$ and $P(\texttt{HasRemnant}|\mathbf{A_X})$ can be calculated from synthetic events under the assumption that these events are a faithful representation of real observations. This can be done as follows.

According to Bayes' theorem, $P(\texttt{HasNS}|\mathbf{A_X})$ can be written as

$$P(\texttt{HasNS}|\mathbf{A_X}) = \frac{P(\mathbf{A_X}|\texttt{HasNS})P(\texttt{HasNS})}{P(\mathbf{A_X})}\,, \tag{9.1}$$

where $P(\mathbf{A_X}|\texttt{HasNS})$ is the likelihood of observing the classifier's outcome given an event with a NS in the system, $P(\texttt{HasNS})$ is the probability that a system includes a NS, and $P(\mathbf{A_X})$ is the probability of observing the classifier outcome

$\mathbf{A}_{\mathbf{X}}$. Now consider a data set of synthetic events E' defined as $D = \{\mathbf{X}(E') \otimes \mathbf{L}(E')\}$, where $\mathbf{L}$ is a map to a vector space that assigns `HasNS` and `HasRemnant` *labels* given the event's *properties*. We assume that the synthetic set is a faithful representation of the space of possible real events, i.e., $E \simeq E'$. The probability $P(\texttt{HasNS}|A_{\mathbf{X}})$ in Eq. (9.1) can be approximated as:

$$\begin{aligned} P(\texttt{HasNS}|\mathbf{A}_{\mathbf{X}}) &\simeq P(\texttt{HasNS}_+|\mathbf{A}_{\mathbf{X}'}) \\ &= \frac{P(\mathbf{A}_{\mathbf{X}'}|\texttt{HasNS}_+)P(\texttt{HasNS}_+)}{P(\mathbf{A}_{\mathbf{X}'})}, \end{aligned} \tag{9.2}$$

where $\texttt{HasNS}_+ = \{E' \,|\, E'(\texttt{HasNS}) = \texttt{TRUE}\}$ identifies the elements in D with positive (+) `HasNS` true property, i.e., the subset of synthetic events that have been simulated to contain a NS, and $\mathbf{A}_{\mathbf{X}'}$ is the outcome of the classifier on $\mathbf{X}' = \mathbf{X}(E')$. The label $\texttt{HasNS}_+$ is determined by the values of the simulated parameters of the events E' before they are injected into the detection pipeline. Therefore, the classification label does not depend on the pipeline's outcome. The probability $P(\texttt{HasRemnant}|\mathbf{A}_{\mathbf{X}})$ can be approximated as:

$$\begin{aligned} &P(\texttt{HasRemnant}|\mathbf{A}_{\mathbf{X}}) \\ &\quad = P(\texttt{HasRemnant}|\texttt{HasNS}, \mathbf{A}_{\mathbf{X}})P(\texttt{HasNS}|\mathbf{A}_{\mathbf{X}}) \\ &\quad \simeq P(\texttt{HasRemnant}_+|\mathbf{A}_{\mathbf{X}''})P(\texttt{HasNS}_+|\mathbf{A}_{\mathbf{X}'}), \end{aligned} \tag{9.3}$$

where $\texttt{HasRemnant}_+ = \{E' \,|\, E'(\texttt{HasRemnant}) = \texttt{TRUE}\}$ identifies the elements in D with positive (+) `HasRemnant` true property, i.e., the subset of synthetic events that have been simulated to be EM-bright, and $\mathbf{A}_{\mathbf{X}''}$ is the algorithm's outcome on the subset of events with property $E'(\texttt{HasNS}) = \texttt{TRUE}$, $\mathbf{X}'' = \mathbf{X}'(\texttt{HasNS}_+)$.

To evaluate Eqs. (9.2) and (9.3) with a ML classifier, the synthetic data set is divided into two subsets, $D = D_R \oplus D_S$, where the $\oplus$ sign indicates complementary subsets. The D_R subset is used for algorithm training and validation. The D_S subset is used to estimate the probabilities. Throughout this Chapter we use a 70% – 30% split for D_R and D_S, respectively [Xu and Goodacre 2018].

The choice of the labelling scheme and the algorithm's outcome depend on the ML algorithm characteristics. Throughout this Chapter we implement a multi-label classification scheme, where each element in D is classified into n mutually exclusive categories that uniquely define the n possible physical states of the system. Given that we want to specify two probabilities for `HasNS` and `HasRemnant`, we select the classifier outcome as a vector in a two-dimensional slice of the vector space $\mathbf{A}_{\mathbf{X}'} \subset \mathbb{R}^n$. This scheme allows the calculation of Eqs. (9.2) and (9.3) with a single training process. In the problem at hand, there

are three possible physical states. A suitable labelling is

$$\begin{aligned}
&\mathbf{L}[E'(\texttt{HasNS}) = \texttt{FALSE}] = 0\\
&\mathbf{L}[E'(\texttt{HasNS}) = \texttt{TRUE}, (\texttt{HasRemnant}) = \texttt{FALSE}] = 1\\
&\mathbf{L}[E'(\texttt{HasNS}) = \texttt{TRUE}, (\texttt{HasRemnant}) = \texttt{TRUE}] = 2\,.
\end{aligned} \tag{9.4}$$

With the above definitions, $\texttt{HasRemnant}_+$ is the set of events labelled "2" and $\texttt{HasNS}_+$ is the union of the sets labelled "1" and "2". Therefore, a natural choice for the algorithm outcome is

$$\mathbf{A}_{\mathbf{X}'} = (f_1 + f_2, f_2) \subset (f_0, f_1, f_2)\,, \tag{9.5}$$

where $f_0(\mathbf{X}') = 1 - f_1(\mathbf{X}') - f_2(\mathbf{X}')$, $f_1(\mathbf{X}')$, and $f_2(\mathbf{X}')$ are the fractions of KNN neighbours or RF trees that predict the event to have labels 0, 1, and 2, respectively.

The factors on the right-hand side of Eqs. (9.2) and (9.3) can be obtained from D_S once the algorithm has been trained on D_R. For example, for the KNN and RF scheme described earlier, the factors in Eq. (9.2) can be estimated as

$$\begin{aligned}
P(\texttt{HasNS}_+) &= \frac{N_{\texttt{HasNS}_+}}{N_s}\,,\\
P(\mathbf{A}_{\mathbf{X}'}|\texttt{HasNS}_+) &= \frac{N^+{}_{\texttt{HasNS}_+}(f_1 + f_2)}{N_{\texttt{HasNS}_+}}\,,\\
P(\mathbf{A}_{\mathbf{X}'}) &= \frac{N^+{}_{\texttt{HasNS}_+}(f_1 + f_2) + N^-{}_{\texttt{HasNS}_+}(f_1 + f_2)}{N_s}\,,
\end{aligned} \tag{9.6}$$

where N_s is the number of events in D_S, $N_{\texttt{HasNS}_+}$ is the number of $\texttt{HasNS}_+$ events in D_S, and $N^+{}_{\texttt{HasNS}_+}(f_1 + f_2)$ and $N^-{}_{\texttt{HasNS}_+}(f_1 + f_2)$ are the number of $\texttt{HasNS}_+$ events in D_S that are correctly and incorrectly classified by the outcome $f_1 + f_2$, respectively. The first factor on the right-hand side of Eq. (9.3) can be evaluated similarly to Eq. (9.2) by replacing HasNS with HasRemnant and restricting D_S to $\texttt{HasNS}_+$ elements.

The probability estimators are generally noisy because they are evaluated on a finite data set. Smooth probability functions can be obtained by mapping them from the $(0, 1)$ space to the real line with a logistic function, smoothing them with a Savitzky-Golay filter, fitting them with Gaussian process regression (GPR), and finally mapping them back to the $(0, 1)$ space.

Both $P(\texttt{HasNS}|\mathbf{A}_\mathbf{X})$ and $P(\texttt{HasRemnant}|\mathbf{A}_\mathbf{X})$ depend on the EOS that is used to label the synthetic events. As the true EOS of matter at NS densities is unknown, in order to minimise the systematics that arise in adopting a specific EOS we consider a set of 23 different EOS and marginalise Eqs. (9.2) and (9.3) over them. The marginalised probabilities $P_M(\texttt{HasNS}|\mathbf{A}_\mathbf{X})$ and $P_M(\texttt{HasRemnant}|\mathbf{A}_\mathbf{X})$

are defined as

$$P_M(I|\mathbf{A_X}) = \frac{\sum_J \beta_J P_J(I|\mathbf{A_X})}{\sum_J \beta_J}\,, \tag{9.7}$$

where $I =$ `HasNS` or `HasRemnant`, $P_J(I|\mathbf{A_X})$ $(J = 1, \ldots 23)$ are the Bayesian probabilities in Eqs. (9.2) and (9.3) calculated from the data set D_S with labels assigned according to the J-th EOS, and β_J are Bayes' factors from Table II (third column) of Ghosh et al. 2021. The probabilities $P_J(I|\mathbf{A_X})$ in Eq. (9.7) can be tabulated and used to compute the marginalised probabilities $P_M(\texttt{HasNS}|\mathbf{A_E})$ and $P_M(\texttt{HasRemnant}|\mathbf{A_E})$ for any new event $\mathbf{E}$ with algorithm outcome $\mathbf{A_E}$. It is important to point out that this method does not depend on the specific value of the Bayes' factors.

9.3.2 Data Set

We use a large data set D of simulated BNS, NSBH, and BBH events that was first used for the space-time volume sensitivity analysis of the LVK GstLAL search [Messick et al. 2017, Sachdev et al. 2019, Sachdev et al. 2020] and later employed in Chatterjee et al. 2020. This allows us to directly compare the performance of the various algorithms and the new labelling scheme to the performance of the KNN algorithm that is deployed in the current LVK observing run.

The simulated signals are coherently injected in two-detector data from the O2 LIGO and Virgo Collaboration (LVC) observing run. The injection population is built with uniform/loguniform distribution of component masses whereas the component spins are aligned and injected according to isotropic distributions. Further details on the waveforms and injection parameters can be found in Chatterjee et al. 2020. The data set D includes approximately 200000 injected signals that are recovered by the GstLAL pipeline with a false alarm rate (FAR) ≤ 1/month. The RF and KNN algorithms are trained and tested on the injected and recovered intrinsic source properties (primary and secondary masses and spins) and on the recovered SNR.

9.3.3 Labelling Scheme

To label the synthetic data set $D = D_R \oplus D_S$, we follow the practice in use in the LVK and identify an event with `HasNS:TRUE` when at least one of the injected component masses is less than the maximum NS mass allowed by the EOS. The value of the maximum NS mass ranges from 1.922 $M_\odot$ to 2.753 $M_\odot$ across the various EOSs. The lowest and largest maximum NS masses

correspond to the `BHF_BBB2` and `MS1_PP` EOSs, respectively. We will highlight these two cases together with the `SLy` EOS, which is the most accepted EOS in the astrophysics community. We set the `HasRemnant` label as `HasRemnant:TRUE` and `HasRemnant:FALSE` for BNS and BBH systems, respectively. The value of the `HasRemnant` label for NSBH events depends on the EOS of the NS. To identify the `HasRemnant` event class for NSBH systems, we follow Chatterjee et al. 2020 and apply Eq. (4) from Foucart, Hinderer, and Nissanke 2018, colloquially known as the *Foucart formula*.

The Foucart formula is an empirical fit that predicts the total mass of the accretion disc, the tidal tail, and the ejected mass from the final BH. The main parameters of the fit are the compactness of the NS, the NSBH binary system's symmetric mass ratio, and the normalised innermost stable circular orbit (ISCO) radius. The tidal disruption of the NS is affected by the mass and spin of the BH. A highly spinning, low-mass BH's small ISCO allows the NS to inspiral closer to the BH and its tidal force to tear the NS apart, resulting in matter ejecta. If the tidal forces are weak or the NS is very compact, the BH will swallow the NS and there will be no remnant mass.

Different EOSs have different thresholds for the mass of the remnant. We label events with inferred masses less than this threshold as `HasRemnant:TRUE`. For events with component masses between ~ 2.5 and $3.5 M_{\odot}$, the stiffness of the EOS is the main factor determining the `HasRemnant` label.

9.4 Results

In this Section, we first discuss the performance of the trained RF and KNN classifiers on the testing data set D_S and use the latter to calculate the Bayesian probabilities $P_M(I|\mathbf{A})$. Then we evaluate $P_M(I|\mathbf{A})$ on two independent data sets. The first set includes a population of simulated CBC events that were injected in the real-time replay of O3 data and was used for the LVK Mock Data Challenge (MDC) [Chaudhary et al. 2024]. The second set contains the confident LVK O3 detections that are reported in LVK's Gravitational-wave Transient Catalog (GWTC) [Abbott et al. 2023a].

9.4.1 Performance on the O2 Testing Set

We assess the performance of the classifiers by measuring the TPR and the FPR of the events in D_S. We present our findings as ROC curves that illustrate how the TPR varies for various score thresholds as a function of the FPR.

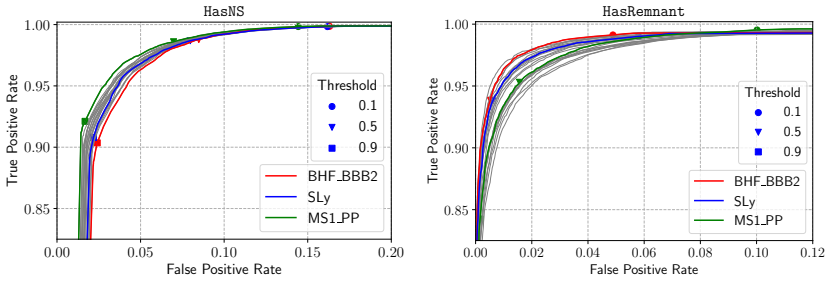

Figure 9.4.1 ROC curves obtained from the O2 testing data set D_S for the KNN classifier (left: `HasNS`, right: `HasRemnant`). The curves for the 23 different EOSs are displayed in gray, with the curves for `BHF_BBB2`, `MS1_PP`, and `SLy` highlighted in red, green, and blue, respectively. The circle, triangle, and square markers denote score thresholds of 0.1, 0.5, and 0.9, respectively.

The `HasNS` and `HasRemnant` ROC curves for the KNN algorithm are displayed in the left and right panels of Fig. 9.4.1, respectively. Figure 9.4.2 displays the analogous curves for the RF classifier. The ROC curves for the 23 EOSs are plotted in gray, with three of them highlighted in colour: `BHF_BBB2`, the EOS with the lowest maximum mass for the NS; `MS1_PP`, the EOS with the largest maximum mass for the NS; and `SLy`, which allows for a maximum mass of $2.05M_\odot$ and is the standard EOS used in LVK low-latency investigations [Ghosh et al. 2021]. The markers denote different thresholds for the algorithm scores.

The two classifiers perform consistently across all EOSs. The TPR for a score threshold of 0.5 is around 0.99 for both `HasNS` and `HasRemnant`. A comparison of the `HasNS` and `HasRemnant` ROC curves for each algorithm shows that the FPR for `HasNS` is generally higher than the FPR for `HasRemnant` at a given threshold. Thus, the algorithms typically do a better job in classifying `HasRemnant` than `HasNS`. Separate comparisons of the KNN and RF ROC curves for `HasNS` and `HasRemnant` reveal that at a given threshold, RF produces slightly higher TPR and lower FPR than KNN.

9.4.2 **Bayesian Probability Computation**

After the algorithms have been trained and tested, we compute the Bayesian probabilities defined in Sec. 9.3.1 in terms of their outcomes. Equations (9.2) and (9.3) must be assessed on a data set independent of the training data set, as stated in Sec. 9.3.1. To do so, we employ D_S.

The KNN and RF probability estimators are shown for each of the 23 EOSs in Figs. 9.4.3 and 9.4.4, respectively. As expected, the `HasNS` and `HasRemnant` probabilities increase with the fractions of KNN neighbours (RF trees). Local

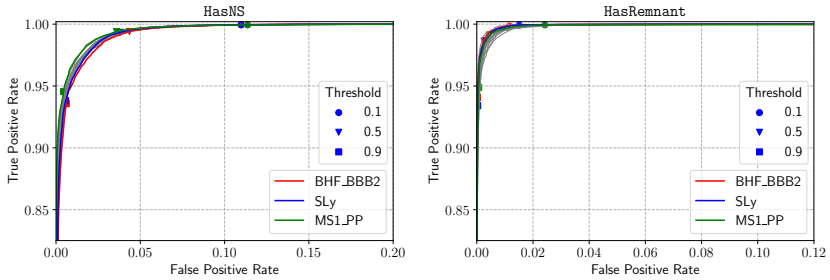

Figure 9.4.2 ROC curves obtained from the O2 testing data set D_S for the RF classifier (left: `HasNS`, right: `HasRemnant`). The curves for the 23 different EOSs are displayed in gray, with the curves for `BHF_BBB2`, `MS1_PP`, and `SLy` highlighted in red, green, and blue, respectively. The circle, triangle, and square markers denote score thresholds of 0.1, 0.5, and 0.9, respectively.

fluctuations in the probabilities are due to noise arising from the finiteness of the data set.

The probabilities in Figs. 9.4.3 and 9.4.4 can be tabulated and used to compute the marginalised probabilities $P_M(\texttt{HasNS}|\mathbf{A_E})$ and $P_M(\texttt{HasRemnant}|\mathbf{A_E})$ as in Eq. (9.7).

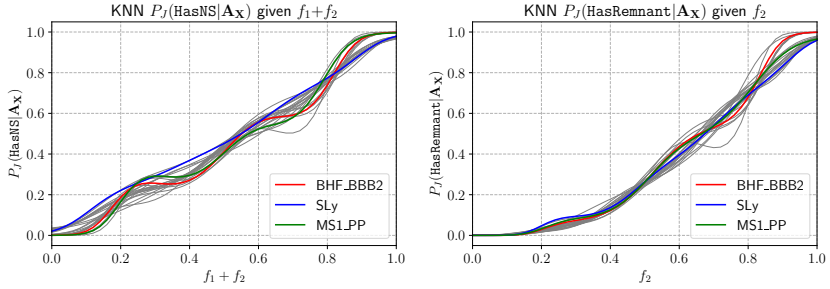

Figure 9.4.3 Left panel: `HasNS` Bayesian probability curves for the 23 EOS as a function of the fraction of KNN neighbours $f_1 + f_2$. Right panel: `HasRemnant` Bayesian probability curves as a function of the fraction of KNN neighbours f_2. Curves for the `BHF_BBB2`, `MS1_PP`, and `SLy` EOSs are highlighted in red, green, and blue, respectively. The probabilities show an increasing trend as the fraction of neighbours increases. Non-monotonic fluctuations are due to the data set's finite size.

9.4.3 **Bayesian Probabilities for the O3 Sets**

To evaluate the method, we classify the events from the MDC data set and compute the ROC curves based on the ground truth using Bayesian probability (rather than score) thresholds. The ROC curves are shown in Figs. 9.4.5 and 9.4.6 for KNN and RF, respectively. In contrast to the O2 data set, the MDC set contains outputs from four matched-filtering pipelines (GstLAL [Messick

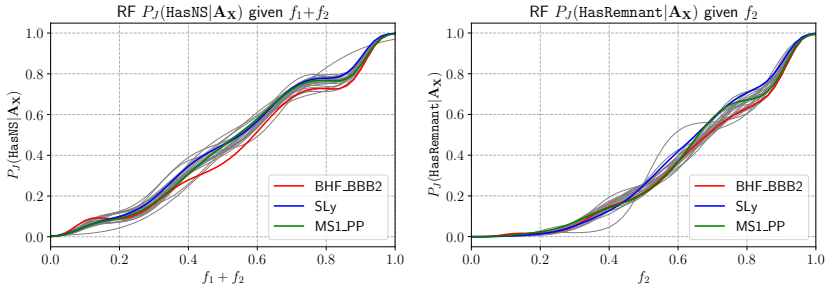

Figure 9.4.4 Left panel: `HasNS` Bayesian probability curves for the 23 EOSs as a function of the fraction of RF trees $f_1 + f_2$. Right panel: `HasRemnant` Bayesian probability curves for `HasRemnant` as a function of the fraction of RF trees f_2. Curves for the `BHF_BBB2`, `MS1_PP`, and `SLy` EOSs are highlighted in red, green, and blue, respectively. The probabilities show an increasing trend as the fraction of trees increases. Non-monotonic fluctuations are due to the data set's finite size.

et al. 2017, Sachdev et al. 2019, Sachdev et al. 2020], PyCBC [Nitz et al. 2018, Dal Canton et al. 2021], SPIIR [Chu et al. 2022], and MBTA [Adams et al. 2016]). Therefore, we present separate ROC curves for these pipelines.

In the case of `HasNS`, KNN yields a TPR between 0.95 and 0.98 and a FPR smaller than 0.20 for a probability threshold of 0.5 across all pipelines, with the exception of SPIIR. Even though the ML algorithms are generally portable across pipelines and data sets, accurate results critically depend on the training set's faithful representation of the observations. The pipelines' suboptimal performance, particularly SPIIR, can be explained by the fact that we only employed GstLAL to train the algorithms. SPIIR's interesting performance can also be seen in current LVK implementation [Chaudhary et al. 2024]. Unfortunately, the inclusion of the other pipelines in the training phase requires the generation of additional injections by the LVK and is deferred to a future publication. Despite the restriction on GstLAL triggers, our approaches perform exceptionally well when applied to other pipelines. We believe that an increased injection set will further improve the performance of all pipelines.

In regard to `HasRemnant`, KNN yields a TPR around 0.975 and an FPR slightly higher than 0.2 for the same threshold across all pipelines, with the exception of GstLAL. RF's results are similar to KNN's results. The RF ROC curves for `HasNS` typically have steeper slopes than for KNN, resulting in a comparable TPR but a lower FPR at a given threshold. In the case of `HasRemnant`, RF performs similarly to KNN for GstLAL but worse for the other pipelines.

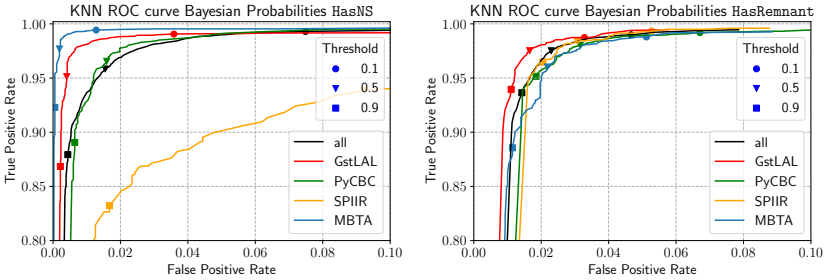

Figure 9.4.5 ROC curves obtained from the O3 MDC data set for the KNN classifier (left: `HasNS`, right: `HasRemnant`). The different LVK matched-filtering pipelines are indicated by different colors (GstLAL: red; PyCBC: green; gold: SPIIR; blue: MBTA). The results for all pipelines are shown in black. The circle, triangle, and square markers denote probability thresholds of 0.1, 0.5, and 0.9, respectively.

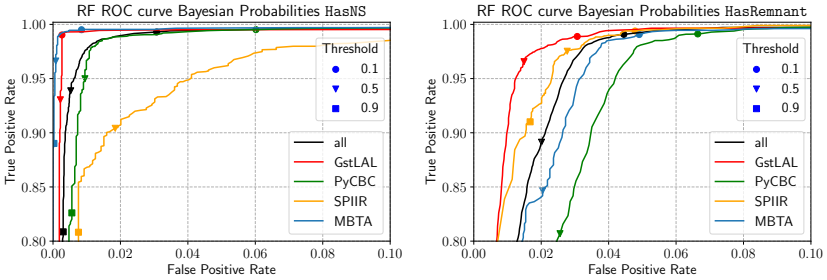

Figure 9.4.6 ROC curves obtained from the O3 MDC data set for the RF classifier (left: `HasNS`, right: `HasRemnant`). The different LVK matched-filtering pipelines are indicated by different colors (GstLAL: red; PyCBC: green; gold: SPIIR; blue: MBTA). The results for all pipelines are shown in black. The circle, triangle, and square markers denote probability thresholds of 0.1, 0.5, and 0.9, respectively.

A few interesting results are worth mentioning. On the MDC set, both algorithms perform better for `HasNS` than `HasRemnant`, whereas on the O2 set, the reverse is true (see Figs. 9.4.1 and 9.4.2). KNN performs better than RF on `HasRemnant`, but does worse on `HasNS`. However, on events recovered by GstLAL, the pipeline on which the algorithms have been trained, both algorithms exhibit comparable (high) performance. This seems to indicate that when used with other pipelines, RF is less flexible than KNN. The conclusions provide more details about this and a possible explanation for this effect.

Finally, we apply the method to derive Bayesian probabilities for the events in the LVK GWTC [Abbott et al. 2021a, Abbott et al. 2023a]. In Table 9.4.1 we report the results for some of the most significant GWTC events, labeled with their event ID, and with their `HasNS` and `HasRemnant` probabilities given

in their General Coordinates Network (GCN) Circulars[3]. The $P_M(\texttt{HasNS}|\mathbf{A_E})$ and $P_M(\texttt{HasRemnant}|\mathbf{A_E})$ probabilities for GW170817 and GW190425, the two confirmed BNS detections are ~ 1 as expected. The probabilities for GW190426 and GW200115 (NSBH mergers) are $P_M(\texttt{HasNS}|\mathbf{A_E}) \sim 1$ and $P_M(\texttt{HasRemnant}|\mathbf{A_E}) < 10^{-3}$. The two remaining significant events with non-zero probabilities are GW190814 and GW190924. These events were reported as high mass-ratio BBH mergers.

The fact that the system's component masses differ greatly from one another can be used to explain why $P_M(\texttt{HasNS}|\mathbf{A_E})$ for these events is not zero. In particular, the discrepancy between RF and KNN for GW190814 can be understood from the different ways the two algorithms operate. RF applies hard cuts on decision trees to evaluate its outcome. KNN looks at the fractions of neighbours surrounding the event. The detection pipeline returned a secondary mass compatible with a NS for three of the 23 EOSs. However, since the region of the parameter space close to the mass gap, i.e., the region between high NS masses and low BH masses, is not well covered in the O2 training data set, KNN overestimates the effect of the three EOS predicting a secondary mass in the NS region.

[3]https://gcn.nasa.gov

Table 9.4.1 Bayesian probabilities of a few significant GW events from the GWTC catalog. GW170817 and GW190425, GW190426 and GW200115, and GW190814 and GW190924 were determined in LVK's follow-up investigations to be BNS, NSBH, and BBH mergers, respectively. Probabilities for GW170817 are not reported as the event was observed by EM observatories and its true nature is confirmed. The probability values in the table are rounded to two decimal figures.

	GCN Circular		$P_M(\texttt{HasNS}\vert\mathbf{A_E})$		$P_M(\texttt{HasRemnant}\vert\mathbf{A_E})$	
event ID	$P(\texttt{HasNS})$	$P(\texttt{HasRemnant})$	RF	KNN	RF	KNN
GW170817	–	–	> 0.99	0.99	> 0.99	0.99
GW190425	> 0.99	> 0.99	> 0.99	0.99	> 0.99	0.99
GW190426	> 0.99	> 0.99	> 0.99	0.99	< 0.01	< 0.01
GW190814	< 0.01	< 0.01	0.04	0.57	< 0.01	< 0.01
GW190924	0.30	< 0.01	0.01	0.05	< 0.01	< 0.01
GW200115	> 0.99	0.09	> 0.99	0.99	< 0.01	< 0.01

Figures 9.4.7 and 9.4.8 show parameter sweeps in the space of the binary component masses for the KNN and RF Bayesian probabilities, respectively. Different rows correspond to different values of the component spins. Both algorithms perform similarly for $P_M(\texttt{HasNS}|\mathbf{A_E})$. However, the parameter sweeps for $P_M(\texttt{HasNS}|\mathbf{A_E})$ for KNN are noisier than RF for large primary masses. As was noted above, the KNN algorithm operates by looking at the closest neighbours. If neighbours with different labels are present in the region of interest, the outcome is bound to be noisy. The RF algorithm applies hard selection cuts to primary masses. This results in a more uniform probability. Changes in spin seem to not significantly affect the outcome. Similar behaviours for KNN and RF can also be observed in the case of $P_M(\texttt{HasRemnant}|\mathbf{A_E})$. As expected from the Foucart formula, $P_M(\texttt{HasRemnant}|\mathbf{A_E})$ increases with the primary mass for large primary spins, and the region with $P_M(\texttt{HasRemnant}|\mathbf{A_E}) \sim 1$ is included in the region where $P_M(\texttt{HasNS}|\mathbf{A_E}) \sim 1$.

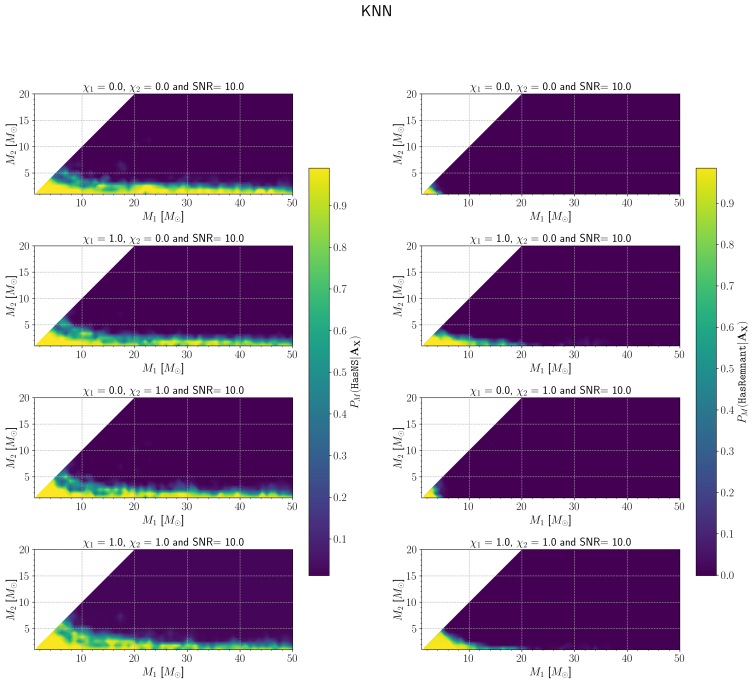

Figure 9.4.7 Parameter sweeps for $P_M(\texttt{HasNS}|\mathbf{A_E})$ (left panels) and $P_M(\texttt{HasRemnant}|\mathbf{A_E})$ (right panels) for the KNN algorithm. M_1 and M_2 are the primary and secondary component masses of the binary. χ_1 and χ_2 are their effective spins. The SNR is fixed to 10.

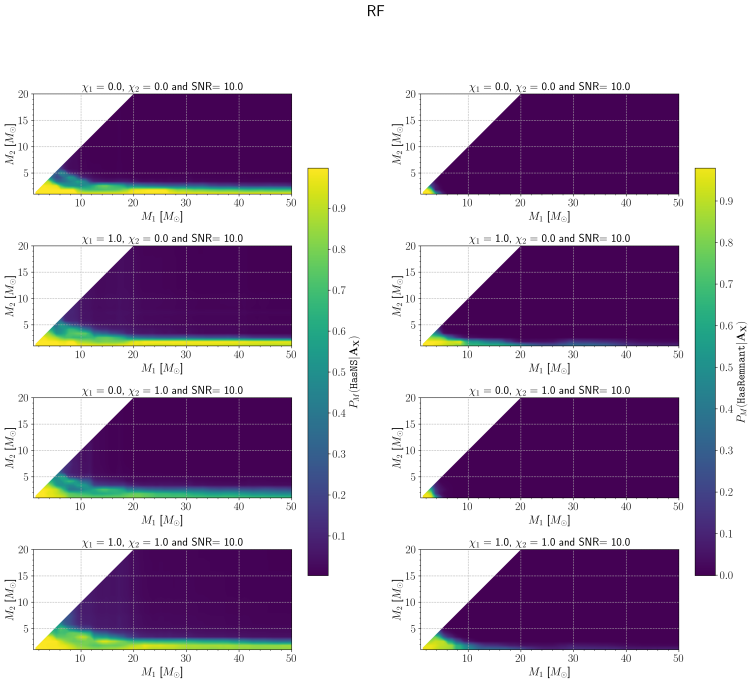

Figure 9.4.8 Parameter sweeps for $P_M(\texttt{HasNS}|\mathbf{A_E})$ (left panels) and $P_M(\texttt{HasRemnant}|\mathbf{A_E})$ (right panels) for the RF algorithm. M_1 and M_2 are the primary and secondary component masses of the binary. χ_1 and χ_2 are their effective spins. The SNR is fixed to 10.

9.5 Discussion and conclusions

In this Chapter, we have presented a new scheme for real-time classification of GW CBC signals detected by the LVK detectors. The method uses the output of the LVK low-latency pipelines to identify whether the GW source progenitor contains a NS (`HasNS`) and a postmerger matter remnant is produced in the merger (`HasRemnant`). Estimates of these metrics are included in public alerts for candidate GW events issued by the LVK. Determining these metrics in low latency is crucial to enabling coincident MMA observations of GW and EM signatures.

We have assessed the viability and measured the performance of two classifiers, KNN and RF, on two sets of real detector data augmented with synthetic GW injections of GW signals that were generated for space-time volume sensitivity analyses of O2 LVK GW searches [Chatterjee et al. 2020] and an MDC real-time replay of O3 data [Chaudhary et al. 2024].

One important novel ingredient of the proposed scheme is the computation of Bayesian probabilities for `HasNS` and `HasRemnant`. Until now, the information that has been passed to astronomers in public alerts has been in the form of binary classification scores for these metrics. Here, we provide a method to compute `HasNS` and `HasRemnant` as actual probabilities that the GW source includes a NS and postmerger matter remnant. Therefore, our scheme provides more direct and easily interpretable information to aid the community of astronomers in deciding whether to follow up on GW candidate events with EM observatories.

To construct the Bayesian probabilities for `HasNS` and `HasRemnant`, we train and test the classifiers on the O2 data set following the customary 70% – 30% split between training and testing data. After evaluating the performance of the classifiers with standard ROC curves, we use the testing set to generate numerical Bayesian probability expressions for the models. This minimises potential biases that may result from the use of data sets with different properties while ensuring that the Bayesian fits are built with data that is independent of the data used for training the classifiers. The effectiveness of the Bayesian fits is then evaluated on fully independent data sets using the O3 set and real detections.

As shown in Appendix 9.B, our RF implementation outperforms the specific KNN algorithm implementation currently utilised in the LVK low-latency infrastructure, while our KNN method performs similarly. When tested on the O3 set, both algorithms improve on `HasNS` while underperforming on `HasRemnant`. In this case, KNN outperforms RF, which exhibits more variation across different pipelines. If only the injections recovered by GstLAL are considered in O3, the

O3 results of both RF and KNN are consistent with O2. RF's performance on O3 events recovered by other pipelines, on the other hand, is noticeably lower. This appears to imply that RF is less portable than KNN across different data sets and pipelines. The different ways RF and KNN operate, as well as the different characteristics of the sets, may explain their behavior.

The RF classifier is a decision tree-based classifier that sets decision rules by implementing specific cuts (conditions) on input features. The KNN algorithm implements decision rules by computing the nearest neighbours of input features in the parameter space for the data point of interest. RF is designed to construct hard boundaries based on input parameters, whereas the KNN algorithm is designed to produce an outcome based on differences between features. As a result, the RF algorithm's nature may make it more suitable for classifying events with `HasNS`, which is based on a well-defined, hard boundary between positive and negative outcomes, such as the secondary mass value. To distinguish between systems with zero and nonzero post-remnant matter in `HasRemnant`, the algorithms must learn Foucart's fit from the recovered parameters. Foucart's formula is dependent on the EOS under consideration, as well as the pipeline that recovers the injection. Because RF and KNN are trained on injections that are only recovered by GstLAL, RF is more affected than KNN. However, a comprehensive evaluation, involving datasets from new observing runs and diverse pipelines, would be needed to definitely compare the performance of the two algorithms.

This work provides an improved scheme to implement Bayesian probabilities for `HasNS` and `HasRemnant` classification of candidate events that would be straightforward to deploy in the existing LVK infrastructure. Our method can also be easily extended to other properties of GW signals that are being or may be released in low latency, such as `HasMassGap` among other data products. Other future extensions of this work include improving algorithm training and Bayesian fit estimation with updated data sets of simulated injections in LVK O4 data generated with different pipelines and with better coverage of the mass gap region than the O2 data set. It would also be worthwhile to investigate the use of additional ML classifiers that could further improve the process's accuracy, reduce the need for computational resources, and decrease latency. Finally, a similar infrastructure could be designed and deployed to aid in the rapid parameter estimation of pipeline outputs, but with a focus on feature regression rather than classification. This latter line of investigation will be presented in a future publication.

Appendix

9.A Cross validation of the ML algorithms

To obtain the optimal hyperparameters of our ML algorithms, we perform cross-validation across different values of the algorithm parameters. We apply the algorithms to the O2 data set for different choices of parameters, and we select the combination that gives the highest accuracy.

9.A.1 K-Nearest Neighbours

We utilise the k-fold cross validation implemented in scikit-learn [Pedregosa et al. 2011] with $k = 10$ folds, which is a common choice in applied ML. As consistency checks, we use different numbers of folds ($k = 4$ and $k = 5$) and achieve consistent results in all cases, with an accuracy ranging between 0.9449 and 0.9517. The dataset used for cross-validation is $D = D_R \oplus D_S$.

Table 9.A.1 Values of the accuracy for different combinations of the hyperparameters. The accuracy in all cases is larger than 0.935.

Neighbours	Metric	Weights	Algorithm	Accuracy
2	Manhattan	Distance	BallTree	0.9399
2	Euclidean	Distance	KDTree	0.9392
2	Manhattan	Uniform	Auto	0.9359
8	Manhattan	Distance	BallTree	0.9485
8	Euclidean	Distance	KDTree	0.9477
8	Manhattan	Uniform	Auto	0.9468
20	Manhattan	Distance	BallTree	0.9469
20	Euclidean	Distance	KDTree	0.9459
20	Manhattan	Uniform	Auto	0.9437

The KNN algorithm's hyperparameters include the number of neighbours (K), distance metric, nearest neighbour method, and prediction weight function.

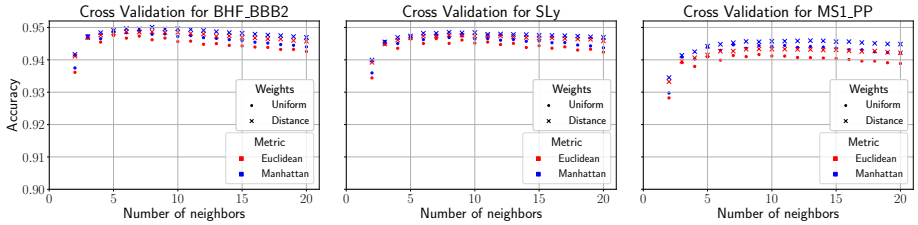

Figure 9.A.1 Accuracy of the KNN algorithm as a function of the number of neighbours. The color red (blue) denotes the Euclidean (Manhattan) metric, and the dots (crosses) denote uniform (distance) weights. The BallTree algorithm is used to find the nearest neighbours. The accuracy does not significantly change when more than 5 neighbours are considered.

Table 9.A.1 displays many combinations of these parameters and the resulting accuracy following cross-validation. It is worth noting that the choice of hyperparameters has little to no impact on accuracy.

Figure 9.A.1 illustrates the accuracy dependence on different hyperparameter options while keeping the algorithm used to compute nearest neighbours, the BallTree, constant.

The ideal hyperparameters are the same for all EOSs, with the exception of the number of neighbours, which varies between 6 and 12. We use the Bayes' factors described in Ghosh et al. 2021 to marginalise over all EOSs. The marginalised optimal number of neighbours is 8. However, as illustrated in Fig. 9.A.1, there is no significant change in accuracy when a higher number of neighbours is used. Table 9.A.2 shows the fixed hyperparameters used in our KNN implementation.

Table 9.A.2 Optimal hyperparameters for the KNN algorithm. These are the values we use to train and test the algorithm, as well as to calculate Bayesian probabilities.

Nº of neighbours	Metric	Weights	Algorithm
8	Manhattan	Distance	BallTree

9.A.2 **Random Forest**

To apply cross-validation to the RF algorithm, we use the training (D_R) and testing (D_S) data sets presented in Section 9.3. We choose possible values for the various hyperparameters and compare the accuracy of the generated forests. Unlike KNN, RF does not apply the k-fold cross-validation procedure. This is because the implementation of RF we employ admits the bootstrap technique in the training. Each tree in the forest accesses a random subset of the training data, thus achieving the same effect.

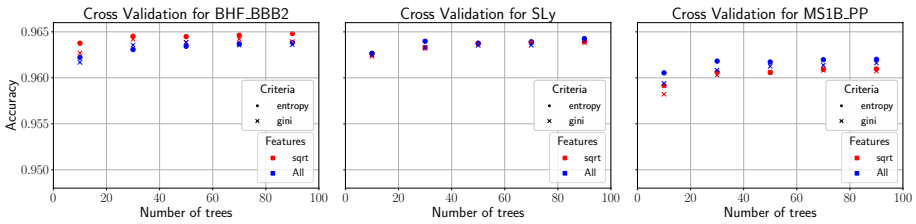

Figure 9.A.2 Accuracy of the RF algorithm as a function of the number of trees. The color red (blue) denotes "sqrt" ("all") features, while the dots (crosses) denote "entropy" ("gini") criteria. The depth of the trees is set at 15. All cases have an accuracy range of 0.960 to 0.965.

We investigate the effect on accuracy by varying the number of trees in the forest, the method used to compute the information gain after each node split (gini or entropy), the maximum number of features considered in each node (the square root of the total number of features, or all of them), and the maximum depth that the trees can reach. For tree depth, we explore two options: None, which consists of allowing the trees to grow until data points are isolated at the leaves, and 15. We chose this figure since it is half the average depth obtained with the None option.

We use the Bayes' factors to marginalise on the configurations that lead to the highest score for each EOS. We conclude that for all EOSs, we should employ 81.017 trees, the "entropy" criterion, the square root of the number of features at split, and a depth equal to 15.

Table 9.A.3 Optimal hyperparameters for the RF algorithm.

Trees	81.02
Criteria (0-gini, 1-entropy)	0.9577
Features (0-sqrt, 1-All)	0.3902
Depth (0-15 depth, 1-None)	0.0000

Table 9.A.3 displays the results of hyperparameter marginalisation over the EOSs. For any EOS, regardless of other hyperparameters, a depth of 15 yields higher accuracy. The "entropy" criterion is adopted for practically every EOS, whereas the number of features to consider is more tightly restricted.

Figure 9.A.2 displays the accuracies obtained during cross-validation, with the depth fixed to 15. It is worth noting that using more trees results in higher scores. Nonetheless, the goal of making this method run in low latency favours smaller files (with less tree information) that can be loaded rapidly. Therefore, given the difference in accuracy and size of the trained models, we limit ourselves to 50 trees.

9.B Comparison between our algorithms and the current LVK implementation

To compare the existing LVK implementation of KNN Chatterjee et al. 2020 with our multi-label KNN and RF schemes, we show the ROC curves for the three methods in Fig. 9.B.1. To provide a fair comparison, we trained the LVK's KNN classifier for two cases (`HasNS`and `HasRemnant`) separately, resulting in a binary label method. In this instance, we use the hyperparameters that are currently configured in the low-latency implementation: $K = 2n + 1 = 11$ neighbours (where n is the number of features), and neighbor weighting by the inverse of distance. Both classifiers were trained using the same 70% of the O2 dataset (the D_R subset)[4]. The ROC curve below was generated using the remaining 30% of the dataset (the D_S subset). The multi-label RF method achieves a high TPR across the entire range of FPR for both `HasNS` and `HasRemnant`. Both multi-label and binary-label KNN methods perform similarly. These ROC curve comparisons were done in the same way as in Figures 9.4.1 and 9.4.2 before defining Bayesian probabilities, as they were generated from the testing set.

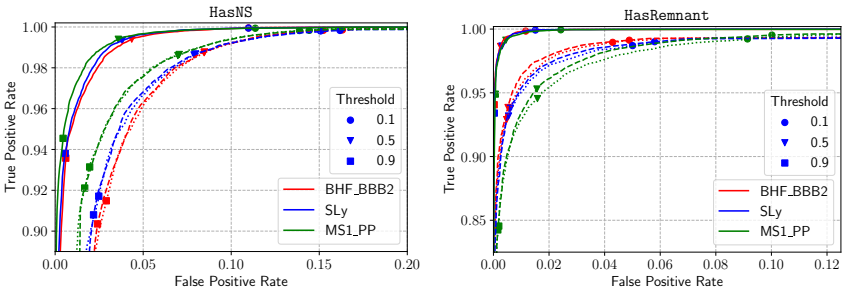

Figure 9.B.1 ROC curves derived from the O2 testing data set D_S for the RF classifier (solid lines), the KNN implementation presented in this paper (dashed lines), and the KNN approach currently used by the LVK Collaborations (dotted lines). The curves for `BHF_BBB2`, `MS1_PP`, and `SLy` are colored red, green, and blue, respectively. The circle, triangle, and square marks represent score thresholds of 0.1, 0.5, and 0.9, respectively.

[4]The current LVK implementation trains the KNN algorithm on the entire dataset D. This leaves no events to test. Therefore, to ensure a fair comparison, we use a 70%-30% split.

CHAPTER 10

Summary of part II and future work

The second part of the thesis has focused on the analysis of GW signals from BNS mergers and their remnants, along with other classes of CBC sources.

10.1 Unmodelled reconstructions of binary neutron star postmerger signals

During **Chapters 7 and 8**, I have studied the detectability prospects of several modes that are excited during the BNS postmerger phase. As previously discussed, this phase is characterised by the highly dynamical formation of a HMNS that will eventually collapse to a BH. The remnant star undergoes several oscillations, emitting gravitational radiation with characteristic frequencies in the range of kHz, considerably above those from the inspiral phase. These oscillations are connected to the excitation of several quasi-normal modes, being the quadrupolar ($l = m = 2$) f-mode the dominant one during the early postmerger phase. However, once these oscillations damp out, further modes may become dominant at later times. It is the case of the inertial modes, triggered by convective instabilities. These modes are characterised by smaller frequencies and amplitudes than those of the quadrupolar mode, making them more challenging to detect. The work in **Chapter 7** focused on the detectability of these modes by current and future GW interferometers.

To assess their possible detection, the BayesWave algorithm was employed to perform unmodelled reconstructions of the GW signals. Due to the lack of

NR simulations that would be needed to apply matched-filtering techniques, the best alternative to analyse these signals is the application of unmodelled searches. To this aim, BayesWave reconstructed long postmerger signals injected into Gaussian noise, for networks of current and future GW detectors, and with an optimal inclination and sky localisation. The study reveals that current detectors do not possess enough sensitivity to observe the GW emission from the inertial modes, unless the source is located at about ~ 1 Mpc or less. In contrast, future detectors with improved sensitivity, such as the ET, increase the detection range by a factor ~ 10. Furthermore, I also employed waveforms obtained with different EOSs. The frequency of the modes changes with the choice of the EOS, similarly to the frequencies of the f-modes. Thus, the identification of inertial modes in the late postmerger phase might provide additional constraints to the EOS, in addition to a deeper insight into the internal structure of HMNS remnants.

Further simulations are needed to explore possible quasi-universal relations between the characteristic frequency of the inertial modes and physical parameters of the star. Numerical studies with different initial configurations (e.g., total binary mass) and EOSs would be required to fulfil this aim, but the long timescales needed by the inertial modes to arise limit the realisation of such simulations. Moreover, to properly characterise the inertial modes, perturbative studies should be applied.

In addition to this work, I assessed in **Chapter 8** the identification of thermal effects in BNS merger remnants with model-agnostic waveform reconstructions. When the HMNS is formed, temperature cannot be neglected and needs to be accounted for in numerical simulations. The way to introduce non-zero temperature effects in BNS simulations is with the EOS. Two approaches are currently used: the *hybrid* approach, which is computationally less expensive but less realistic, and the *tabulated* approach, more computationally demanding, but it incorporates thermal effects in a more realistic way. In this Chapter, injections into Gaussian noise of the ET were performed for different EOSs described by both *hybrid* and *tabulated* approaches. The recovered frequencies from the dominant quadrupolar f-mode are different between both approaches, and these differences could be detectable by future interferometers for distances up to few hundred Mpc in some cases. Moreover, the differences increase as the mode frequencies evolve in time, but the amplitude of the signals simultaneously decreases, thus making them difficult to detect. The treatment of thermal effects also impacts the frequency of the inertial modes, but those are found to be detectable for up to 15 Mpc, as expected from Chapter 7.

Differences in the treatment of thermal effects can be large enough to be identified in future detections of BNS GW postmerger signals. However, these differences strongly depend on the EOS considered, yielding different frequency shifts and different amplitudes that determine their detection range. Thus, a larger set of simulations with different EOSs would be required to extract more solid conclusions. Furthermore, it would be interesting to study the impact of a different number of pieces when building the piecewise polytropic EOS employed for the hybrid approach.

10.1.1 Further applications of unmodelled gravitational-wave searches

It has been proven that the BayesWave algorithm is a good replacement of matched filtering techniques when the modelling of the GW signal is challenging. Thus, in addition to BNS postmerger waveforms, CCSN signals are the ideal candidates to be searched by BayesWave (or other pipelines such as cWB). Their stochastic nature makes it impossible to model them, so model-agnostic searches are the best alternative, together with the application of ML techniques. The frequency of the core-bounce part of the GW signal (with a frequency at around $\sim$ 800 Hz) can be related to rotational properties of the stellar core. The GW emission from CCSNe is also produced from the excitation of different oscillation modes in the newly born PNS and its surroundings, including the accretion shock. Moreover, asteroseismology studies have revealed that there is a relationship between the post-bounce oscillation spectrum of the combined PNS and shock system, and the peak frequencies of the emitted GW signal, which can be as low as 100 Hz. Thus, it is possible to infer physical properties of the PNS with the identification of the mode frequencies in the GW signal, without the use of matched-filtering techniques that require a large amount of computationally expensive simulations.

Other plausible purposes of unmodelled reconstructions could be the analysis of the detectability of the impact that bosonic fields could provoke when interacting gravitationally with the fermionic matter from NSs. It is shown in Appendix A that the interaction between a cloud of ultralight bosonic particles and a NS prone to the bar-mode instability can alter the stability and dynamics of the system, leading to changes in the GW signal amplitude and its characteristic frequency. Moreover, the presence of dark matter particles in the merger of a BNS system might also have an impact on the postmerger GW emission.

It has already been shown in Chapter 8 that differences in the EOS modelling lead to changes in the characteristic frequencies of the postmerger GW signal. Apart from the treatment of thermal effects, the inclusion of PTs to quark

matter in the EOS also alters the postmerger GW spectrum, as well as the use of non-convex EOSs (see Section 1.4 from the Introduction), which can have a detectable impact on the emitted GWs. Unmodelled reconstructions might be able to detect those frequency shifts in the signal without the need of large waveform templates.

10.2 Real-time classification of CBC sources with a Bayesian approach

Finally, in **Chapter 9** I presented a novel scheme for real-time classification of GW signals detected by the current LVK detectors. This new method makes use of the output from LVK low-latency pipelines, i.e., inferred component masses and spins of the objects along the orbital angular momentum, to provide probabilities for the GW source to have a NS component (`HasNS`) and to have postmerger matter remnant (`HasRemnant`). These metrics are provided by supervised ML algorithms, RF and KNN, that have been trained over large injection data sets and a big variety of EOSs.

The novelty presented in this work is the use of a Bayesian approach to compute more realistic probabilities from the output of the ML classifiers. In contrast to the current LVK implementation, which uses the binary classification scores for `HasNS` and `HasRemnant`, this method provides actual probabilities for these metrics. To build the Bayesian probabilities, the ML algorithms are trained and optimised with real detector data augmented with synthetic GW injections. The testing set is used to generate fits for the Bayesian probabilities, which are evaluated on independent data sets and real detections. Moreover, the classification algorithms employed in this work seem to slightly outperform the current LVK implementation. Although being exclusively trained with triggers from a single pipeline, GstLAL, the approach works surprisingly well when applied to other low-latency pipelines such as MBTA and PyCBC.

Therefore, this scheme offers more direct and easily interpretable information that would be useful to the astronomy community, helping in the rapid response to follow-up observations of EM signatures from CBC that contain (at least) a NS.

Nevertheless, the performance of the method seems to not be optimal when applied to triggers from the SPIIR pipeline. A possible solution to this issue that could be explored in a future work is the use of triggers from several low-latency pipelines to train the ML classifiers. An increased injection set would further improve the performance on all pipelines. Moreover, the use of

synthetic injections from the current (and future) observing run together with simulated triggers computed from additional EOSs will improve the Bayesian fit estimation.

10.2.1 **Extension to other gravitational-wave signal properties**

This method can be easily extended to other properties of the GW signals detected by the LVK observatories. For example, it could also provide the probability that one of the binary components is located in the NS mass gap. Since the maximum mass of a NS is expected to be around 2.5 solar masses, and BHs with less than 5 solar masses have rarely been observed, there exists a *mass gap* between the most massive NS and the least massive BH ever detected. Finding objects inside this critical region would give us very important information. If a NS is found, this observation would put strong constraints on the EOS of dense matter. Alternatively, if a BH is detected within this gap, it could impact the understanding of CCSN explosions, which are the formation mechanism of stellar BHs, and also make us consider other formation channels, such as CBC.

Part III

Appendices

APPENDIX A

Publications as a co-author

Here, I summarise the projects I have been involved in as a co-author. I also state my own contribution to their development.

A.1 Impact of ultralight bosonic dark matter on the dynamical bar-mode instability of rotating neutron stars

This work was originally published in *Impact of ultralight bosonic dark matter on the dynamical bar-mode instability of rotating neutron stars*. Fabrizio Di Giovanni, Nicolás Sanchis-Gual, Davide Guerra, **Miquel Miravet-Tenés**, Pablo Cerdá-Durán and José A. Font.*Phys. Rev. D*, Volume 106, Issue 4, pp. 044008, August 2022. DOI: 10.1103/PhysRevD.106.044008.

Context: Rapidly differentially rotating NSs are expected to be subject to various nonaxisymmetric instabilities. If the ratio between the rotational kinetic energy and the gravitational potential energy is sufficiently high, they can undergo the dynamical bar-mode instability. The nonlinear growth of the $l = m = 2$ (l, m are the spherical harmonic indices) oscillation mode will deform the star into a bar shape (see Section 1.1 from the Introduction). However, not only fermionic stars can be subject to these nonaxisymmetric instabilities. In fact, it has been shown through numerical simulations that rotating boson stars can also be affected by the same kind of instabilities. These objects are self-gravitating compact objects that can be constructed by minimally coupling a complex, massive bosonic field to Einstein's gravity. These exotic compact

objects are dark matter candidates that could help explain a wide set of observational results, such as the measurements of galaxy rotation curves, gravitational lensing, and the CMB. The constituent particles of the bosonic stars lack EM interactions with baryonic matter, thus being invisible through EM observations. The only way to observe and study these objects is through their GW emission and their gravitational interaction with fermionic matter. Having observed that both fermionic and bosonic objects can suffer from the bar-mode instability, it is natural to ask what would happen if a bosonic field is added to a rapidly spinning NS that is prone to develop the bar-mode deformation.

Goals: To investigate the gravitational interaction between ultralight bosonic field dark matter and the fermions that constitute the NS. This interaction might provoke changes on the dynamics of unstable differentially rotating NSs prone to the bar-mode instability, and also on the associated GW emission.

Methods: We perform NR simulations of differentially rotating NSs that accrete an initial spherically symmetric bosonic field cloud. These simulations solve the coupled Einstein-Klein-Gordon-Euler system for scalar bosonic fields, and the Einstein-Proca-Euler system for vector (Proca) fields. We choose different NS configurations and also several masses for the bosonic cloud and the bosonic particle. Moreover, we compute the Newman-Penrose scalar to study the GW spectrum of the simulations.

Results: We find that the presence of a bosonic field can critically modify the development of the bar-mode instability of NSs, depending on the total mass of the bosonic field and on the boson particle mass. Purely NS models undergo a bar-like deformation, and we observe the excitation of the $l = m = 2$ mode, as expected. The inclusion of a bosonic field leads, in some cases, to a different mode excitation, being the $l = 2$, $m = 1$ mode the dominant one, instead of the $l = m = 2$ mode of the bar-deformation. Indeed, in some cases we observe a quenching of the dominant mode of the bar-deformation, retaining part of the angular momentum from the NS. For the cases that lead to the formation of a mixed bar, it has been observed that the timescale of the instability is also affected by the presence of dark matter, being delayed as the amount of bosonic field increases. Moreover, the resulting GW spectra indicate that this dark-matter accretion could change the frequency of the gravitational radiation emitted by the bar-mode instability.

Conclusions: Our work explicitly shows that the gravitational coupling between ultralight bosonic particles and fermionic NS matter can have important effects in the dynamics and stability of the NS. The increase of the dominant frequency of the emitted GWs can be potentially observed by future GW detectors within several tens of Mpc, making these results useful for ongoing and future searches of continuous GW signals from NSs.

My contribution: In this work, I built some initial NS configurations with differential rotation, and I also performed and monitored several numerical evolutions. Moreover, I performed some post-processing tasks, such as making the snapshots of the rest-mass density contours. I also contributed to the writing of the manuscript and I participated in all the discussions about the project.

A.2 Fermion-axion stars: Static solutions and dynamical stability

This work was originally published in *Fermion-axion stars: Static solutions and dynamical stability*. Fabrizio Di Giovanni, Davide Guerra, Simone Albanesi, **Miquel Miravet-Tenés**, Dimitra Tseneklidou. *Phys. Rev. D*, Volume 106, Issue 8, pp. 084013, October 2022. DOI: 10.1103/PhysRevD.106.084013.

Context: One of the most compelling particle dark-matter candidates is the axion, a pseudo-scalar particle that could play a key role in cosmology and was introduced to solve the CP problem. The axion particles can clump together and resemble Bose-Einstein condensates, i.e., bosonic stars. The scalar axion field has a characteristic periodic potential, inspired by quantum chromodynamics (QCD) theory, which depends on the mass of the axion and the decay constant. Studies of axion boson stars show that new stability branches emerge at high densities. Therefore, if such axion-like particles exist and can form compact objects, there could also exist objects made by a mixture of fermions and axions. Purely fermionic NSs posses a single stable branch, but the addition of an axion-like particle could significantly change their stability.

Goals: To study the stability of solutions of the coupled Einstein-Klein-Gordon-Euler system. The system involves bosonic dark matter with a periodic potential, characteristic of axion-like models, and fermionic matter modelled by a perfect fluid that resembles a NS.

Methods: We construct spherically symmetric equilibrium configurations for different values of the decay constant of the axion potential. Then, we build an existence diagram in the parameter space given by the central rest-mass density of the star and the central axion-field amplitude, and identify the stable and unstable regions. Finally, we perform a nonlinear evolution to assess the stability of several cases.

Results: The solutions for the mixed fermion-axion stars show the presence of multiple *islands of stability* that depend on the choice of the decay constant of the axion potential. This is opposed to the case of a purely fermionic star, which only possesses one stable branch. The nonlinear evolution of some initial configurations confirms the observations from the linear analysis. Models from the linearly unstable region face different fates when weakly perturbed: some cases migrate to the stable region, others collapse to a BH, and there are some models in which the scalar field is dispersed away, leaving behind a purely fermionic star.

Conclusions: Equilibrium models of fermion-axion stars allow for stable regions in the parameter space that do not exist when considering a purely fermionic NS. The characteristic periodic potential of the axion dark-matter particle leads to the appearance of several islands of stability in the existence domain. The nonlinear evolution of the linearly unstable models can result in the dispersion of the bosonic field and the dilution of the fermionic matter, which is something that has never been observed in previous works.

My contribution: For this project, I computed equilibrium solutions of the fermion-axion stars for certain values of the axion decay constant that appears in the potential. I also helped prepare some figures and build the algorithm to compute equal-mass curves in the parameter space. Moreover, I contributed to the writing of the manuscript and I participated in all the discussions about the project.

A.3 Gravitational Wave Memory Imprints on the CMB from Populations of Massive Black Hole Mergers

This work is originally from *Gravitational Wave Memory Imprints on the CMB from Populations of Massive Black Hole Mergers*. Lorenz Zwick, David O'Neill, Kai Hendriks, Philip Kirkeberg and **Miquel Miravet-Tenés**. April 2024. Sub-

mitted to *Astron. Astrophys.*. arXiv:2404.06927

Context: The GWM is a GR effect that occurs when the passing of a GW leaves a persistent change in the relative position of pairs of masses. There exist two kinds of GWM effects: the linear and the nonlinear. Their detection would be a convincing evidence of the validity of the theory of GR. In addition, the observational consequences would be copious, from an improvement in the parameter estimation of GW sources to implications in cosmology. The CMB radiation constitutes an important keystone of the understanding of the early Universe. The effect of the GWM could alter the paths of the CMB photons, but also provoke temperature fluctuations.

Goals: Explore and characterise the temperature fluctuations that are imprinted on the CMB by GWM effects from mergers of massive BHs binaries.

Methods: By computing the strain tensor for linear GWM using a PN expansion, we assume that the memory effect acts as a step function and propagates from the merger event outwards in a shell. We calculate the variation of the wavelength of the CMB photons that intersect the GWM shell, which results in a corresponding change in the bulk blackbody temperature. We study these fluctuations for both individual binary mergers and populations of binaries that are distributed in local cosmological boxes at a given redshift.

Results: For a single merger event, the resulting maximum temperature fluctuations, observed by a local observer, scale with the total mass of the binary and are inversely proportional to the elapsed time after the merger. When considering populations of mergers, the temperature fluctuations are basically composed of the superpositions of the individual merger contributions. The maximum and the standard deviation of the fluctuations follow a random-walk process and scale with the number of events considered, that can be given by a certain merger rate. It is found that fluctuations of order $\sim 10^{-10}$ K can be reached across scales of $\sim 1'$ to $\sim 1^\circ$ for volumetric merger rates of 10^{-3} Mpc^{-3} Gyr^{-1}, characteristic of galaxies located at redshift $z = 1$. Moreover, the accumulation of temperature fluctuations gives rise to a power spectrum the amplitude of which also increases with the merger density and scales as $P(k) \propto k^{-2.7}$.

Conclusions: Every single BH merger has its imprint on the CMB radiation by producing temperature fluctuations due to its GWM emission. The resulting fluctuations from populations of mergers accumulate following a random-walk process and provide a universal power law with a specific scaling. The detection of such fluctuations is exceedingly challenging. Their very small amplitude and the existence of noise sources such as lensing and path deflections makes them extremely difficult to observe by current observatories.

My contribution: In this project, I took part in the early discussions and contributed to the computation of the GWM strain produced by a single BBH merger. In addition, I participated in the writing process and review of the manuscript.

Bibliography

[1] http://www.lorene.obspm.fr/.

[2] https://stellarcollapse.org/SROEOS.

[3] J. Aasi et al. "The characterization of Virgo data and its impact on gravitational-wave searches." In: *Class. Quantum Grav.* 29.15, 155002 (Aug. 2012), p. 155002. DOI: 10.1088/0264-9381/29/15/155002. arXiv: 1203.5613 [gr-qc].

[4] J. Aasi et al. "Advanced LIGO." In: *Class. Quant. Grav.* 32 (2015), p. 074001. DOI: 10.1088/0264-9381/32/7/074001. arXiv: 1411.4547 [gr-qc].

[5] B. P. Abbott et al. "LIGO: the Laser Interferometer Gravitational-Wave Observatory." In: *Reports on Progress in Physics* 72.7, 076901 (July 2009), p. 076901. DOI: 10.1088/0034-4885/72/7/076901. arXiv: 0711.3041 [gr-qc].

[6] B. P. Abbott et al. "GW150914: First results from the search for binary black hole coalescence with Advanced LIGO." In: *Phys. Rev. D* 93.12, 122003 (June 2016), p. 122003. DOI: 10.1103/PhysRevD.93.122003. arXiv: 1602.03839 [gr-qc].

[7] B. P. Abbott et al. "Observation of Gravitational Waves from a Binary Black Hole Merger." In: *Phys. Rev. Lett.* 116.6 (2016), p. 061102. DOI: 10.1103/PhysRevLett.116.061102. arXiv: 1602.03837 [gr-qc].

[8] B. P. Abbott et al. "A gravitational-wave standard siren measurement of the Hubble constant." In: *Nature* 551.7678 (Nov. 2017), pp. 85–88. DOI: 10.1038/nature24471. arXiv: 1710.05835 [astro-ph.CO].

[9] B. P. Abbott et al. "Estimating the Contribution of Dynamical Ejecta in the Kilonova Associated with GW170817." In: *Astrophys. J. Lett.* 850.2, L39 (Dec. 2017), p. L39. DOI: 10.3847/2041-8213/aa9478. arXiv: 1710.05836 [astro-ph.HE].

[10] B. P. Abbott et al. "Gravitational Waves and Gamma-rays from a Binary Neutron Star Merger: GW170817 and GRB 170817A." In: *Astrophys. J. Lett.* 848.2 (2017), p. L13. DOI: 10.3847/2041-8213/aa920c. arXiv: 1710.05834 [astro-ph.HE].

[11] B. P. Abbott et al. "GW170817: Observation of Gravitational Waves from a Binary Neutron Star Inspiral." In: *Phys. Rev. Lett.* 119.16, 161101 (Oct. 2017), p. 161101. DOI: 10.1103/PhysRevLett.119.161101. arXiv: 1710.05832 [gr-qc].

[12] B. P. Abbott et al. "Multi-messenger Observations of a Binary Neutron Star Merger." In: *Astrophys. J. Lett.* 848.2, L12 (Oct. 2017), p. L12. DOI: 10.3847/2041-8213/aa91c9. arXiv: 1710.05833 [astro-ph.HE].

[13] B. P. Abbott et al. "Search for Post-merger Gravitational Waves from the Remnant of the Binary Neutron Star Merger GW170817." In: *Astrophys. J. Lett.* 851.1, L16 (Dec. 2017), p. L16. DOI: 10.3847/2041-8213/aa9a35. arXiv: 1710.09320 [astro-ph.HE].

[14] B. P. Abbott et al. "GW170817: Measurements of Neutron Star Radii and Equation of State." In: *Phys. Rev. Lett.* 121.16, 161101 (Oct. 2018), p. 161101. DOI: 10.1103/PhysRevLett.121.161101. arXiv: 1805.11581 [gr-qc].

[15] B. P. Abbott et al. "Prospects for observing and localizing gravitational-wave transients with Advanced LIGO, Advanced Virgo and KAGRA." In: *Living Rev. Rel.* 21.1 (2018), p. 3. DOI: 10.1007/s41114-020-00026-9. arXiv: 1304.0670 [gr-qc].

[16] B. P. Abbott et al. "GWTC-1: A Gravitational-Wave Transient Catalog of Compact Binary Mergers Observed by LIGO and Virgo during the First and Second Observing Runs." In: *Phys. Rev. X* 9.3, 031040 (July 2019), p. 031040. DOI: 10.1103/PhysRevX.9.031040. arXiv: 1811.12907 [astro-ph.HE].

[17] B. P. Abbott et al. "Properties of the Binary Neutron Star Merger GW170817." In: *Physical Review X* 9.1, 011001 (Jan. 2019), p. 011001. DOI: 10.1103/PhysRevX.9.011001. arXiv: 1805.11579 [gr-qc].

[18] B. P. Abbott et al. "A guide to LIGO-Virgo detector noise and extraction of transient gravitational-wave signals." In: *Class. Quantum Grav.* 37.5, 055002 (Mar. 2020), p. 055002. DOI: 10.1088/1361-6382/ab685e. arXiv: 1908.11170 [gr-qc].

[19] B. P. Abbott et al. "GW190425: Observation of a Compact Binary Coalescence with Total Mass $\sim 3.4\ M_\odot$." In: *Astrophys. J. Lett.* 892.1, L3 (Mar. 2020), p. L3. DOI: 10.3847/2041-8213/ab75f5. arXiv: 2001.01761 [astro-ph.HE].

[20] B. P. Abbott et al. "Open data from the first and second observing runs of Advanced LIGO and Advanced Virgo." In: *SoftwareX* 13, 100658 (Jan. 2021), p. 100658. DOI: 10.1016/j.softx.2021.100658. arXiv: 1912.11716 [gr-qc].

[21] B. P. Abbott et al. "Open Data from the Third Observing Run of LIGO, Virgo, KAGRA, and GEO." In: *ApJS* 267.2, 29 (Aug. 2023), p. 29. DOI: 10.3847/1538-4365/acdc9f. arXiv: 2302.03676 [gr-qc].

[22] R. Abbott et al. "Constraints on the cosmic expansion history from GWTC-3." In: (Nov. 2021). arXiv: 2111.03604 [astro-ph.CO].

[23] R. Abbott et al. "GWTC-2: Compact Binary Coalescences Observed by LIGO and Virgo during the First Half of the Third Observing Run." In: *Phys. Rev. X* 11.2, 021053 (Apr. 2021), p. 021053. DOI: 10.1103/PhysRevX.11.021053. arXiv: 2010.14527 [gr-qc].

[24] R. Abbott et al. "GWTC-3: Compact Binary Coalescences Observed by LIGO and Virgo During the Second Part of the Third Observing Run." In: (Nov. 2021). arXiv: 2111.03606 [gr-qc].

[25] R. Abbott et al. "Tests of General Relativity with GWTC-3." In: (Dec. 2021). arXiv: 2112.06861 [gr-qc].

[26] R. Abbott et al. "Population of Merging Compact Binaries Inferred Using Gravitational Waves through GWTC-3." In: *Phys. Rev. X* 13.1, 011048 (Jan. 2023), p. 011048. DOI: 10.1103/PhysRevX.13.011048. arXiv: 2111.03634 [astro-ph.HE].

[27] R. Abbott et al. "GWTC-2.1: Deep extended catalog of compact binary coalescences observed by LIGO and Virgo during the first half of the third observing run." In: *Phys. Rev. D* 109.2, 022001 (Jan. 2024), p. 022001. DOI: 10.1103/PhysRevD.109.022001. arXiv: 2108.01045 [gr-qc].

[28] F. Acernese et al. "Advanced Virgo: a second-generation interferometric gravitational wave detector." In: *Class. Quantum Grav.* 32.2, 024001 (Jan. 2015), p. 024001. DOI: 10.1088/0264-9381/32/2/024001. arXiv: 1408.3978 [gr-qc].

[29] T. Adams et al. "Low-latency analysis pipeline for compact binary coalescences in the advanced gravitational wave detector era." In: *Class. Quant. Grav.* 33.17 (2016), p. 175012. DOI: 10.1088/0264-9381/33/17/175012. arXiv: 1512.02864 [gr-qc].

[30] G. Agazie et al. "The NANOGrav 15 yr Data Set: Evidence for a Gravitational-wave Background." In: *Astrophys. J. Lett.* 951.1, L8 (July 2023), p. L8. DOI: 10.3847/2041-8213/acdac6. arXiv: 2306.16213 [astro-ph.HE].

[31] R. Aguilera-Miret, D. Viganò, and C. Palenzuela. "Universality of the Turbulent Magnetic Field in Hypermassive Neutron Stars Produced by Binary Mergers." In: *Astrophys. J. Lett.* 926.2, L31 (Feb. 2022), p. L31. DOI: 10.3847/2041-8213/ac50a7. arXiv: 2112.08406 [gr-qc].

[32] R. Aguilera-Miret et al. "Turbulent magnetic-field amplification in the first 10 milliseconds after a binary neutron star merger: Comparing high-resolution and large-eddy simulations." In: *Phys. Rev. D* 102.10, 103006 (Nov. 2020), p. 103006. DOI: 10.1103/PhysRevD.102.103006. arXiv: 2009.06669 [gr-qc].

[33] R. Aguilera-Miret et al. "The role of turbulence and winding in the development of large-scale, strong magnetic fields in long-lived remnants of binary neutron star mergers." In: *arXiv e-prints*, arXiv:2307.04837 (July 2023), arXiv:2307.04837. DOI: 10.48550/arXiv.2307.04837. arXiv: 2307.04837 [astro-ph.HE].

[34] P. Ajith et al. "A phenomenological template family for black-hole coalescence waveforms." In: *Class. Quantum Grav.* 24.19 (Oct. 2007), S689–S699. DOI: 10.1088/0264-9381/24/19/S31. arXiv: 0704.3764 [gr-qc].

[35] S. Akiyama et al. "The Magnetorotational Instability in Core-Collapse Supernova Explosions." In: *Astrophys. J.* 584.2 (Feb. 2003), pp. 954–970. DOI: 10.1086/344135. arXiv: astro-ph/0208128 [astro-ph].

[36] M. Alford. "Color-Superconducting Quark Matter." In: *Annual Review of Nuclear and Particle Science* 51 (Jan. 2001), pp. 131–160. DOI: 10.1146/annurev.nucl.51.101701.132449. arXiv: hep-ph/0102047 [hep-ph].

[37] J. D. Álvares et al. "Exploring gravitational-wave detection and parameter inference using deep learning methods." In: *Class. Quantum Grav.* 38.15, 155010 (Aug. 2021), p. 155010. DOI: 10.1088/1361-6382/ac0455. arXiv: 2011.10425 [gr-qc].

[38] M. Anderson et al. "Magnetized Neutron-Star Mergers and Gravitational-Wave Signals." In: *Phys. Rev. Lett.* 100.19, 191101 (May 2008), p. 191101. DOI: 10.1103/PhysRevLett.100.191101. arXiv: 0801.4387 [gr-qc].

[39] N. Andersson. "Resistive relativistic magnetohydrodynamics from a charged multifluids perspective." In: *Phys. Rev. D* 86.4, 043002 (Aug. 2012), p. 043002. DOI: 10.1103/PhysRevD.86.043002. arXiv: 1204.2695 [astro-ph.SR].

[40] N. Andersson et al. "The physics of non-ideal general relativistic magnetohydrodynamics." In: *MNRAS* 509.3 (Jan. 2022), pp. 3737–3750. DOI: 10.1093/mnras/stab3257. arXiv: 2108.08732 [astro-ph.HE].

[41] N. Andersson. "A New Class of Unstable Modes of Rotating Relativistic Stars." In: *Astrophys. J.* 502.2 (Aug. 1998), pp. 708–713. DOI: 10.1086/305919. arXiv: gr-qc/9706075 [gr-qc].

[42] N. Andersson and K. D. Kokkotas. "Towards gravitational wave asteroseismology." In: *MNRAS* 299.4 (Oct. 1998), pp. 1059–1068. DOI: 10.1046/j.1365-8711.1998.01840.x. arXiv: gr-qc/9711088 [gr-qc].

[43] N. Andersson and K. D. Kokkotas. "The R-Mode Instability in Rotating Neutron Stars." In: *International Journal of Modern Physics D* 10.4 (Jan. 2001), pp. 381–441. DOI: 10.1142/S0218271801001062. arXiv: gr-qc/0010102 [gr-qc].

[44] N. Andersson, K. D. Kokkotas, and N. Stergioulas. "On the Relevance of the R-Mode Instability for Accreting Neutron Stars and White Dwarfs." In: *Astrophys. J.* 516.1 (May 1999), pp. 307–314. DOI: 10.1086/307082. arXiv: astro-ph/9806089 [astro-ph].

[45] J. Antoniadis et al. "A Massive Pulsar in a Compact Relativistic Binary." In: *Science* 340.6131 (Apr. 2013), p. 448. DOI: 10.1126/science.1233232. arXiv: 1304.6875 [astro-ph.HE].

[46] I. Arcavi et al. "Optical emission from a kilonova following a gravitational-wave-detected neutron-star merger." In: *Nature* 551 (2017), p. 64. DOI: 10.1038/nature24291. arXiv: 1710.05843 [astro-ph.HE].

[47] S. Ascenzi et al. "Electromagnetic counterparts of compact binary mergers." In: *Journal of Plasma Physics* 87.1 (Feb. 2021), p. 845870102. DOI: 10.1017/S0022377820001646. arXiv: 2011.04001 [astro-ph.HE].

[48] S. Babak, A. Taracchini, and A. Buonanno. "Validating the effective-one-body model of spinning, precessing binary black holes against numerical relativity." In: *Phys. Rev. D* 95.2, 024010 (Jan. 2017), p. 024010. DOI: 10.1103/PhysRevD.95.024010. arXiv: 1607.05661 [gr-qc].

[49] L. Baiotti, B. Giacomazzo, and L. Rezzolla. "Accurate evolutions of inspiralling neutron-star binaries: Prompt and delayed collapse to a black hole." In: *Phys. Rev. D* 78.8, 084033 (Oct. 2008), p. 084033. DOI: 10.1103/PhysRevD.78.084033. arXiv: 0804.0594 [gr-qc].

[50] L. Baiotti and L. Rezzolla. "Binary neutron star mergers: a review of Einstein's richest laboratory." In: *Reports on Progress in Physics* 80.9, 096901 (Sept. 2017), p. 096901. DOI: 10.1088/1361-6633/aa67bb. arXiv: 1607.03540 [gr-qc].

[51] L. Baiotti et al. "Accurate simulations of the dynamical bar-mode instability in full general relativity." In: *Phys. Rev. D* 75.4, 044023 (Feb. 2007), p. 044023. DOI: 10.1103/PhysRevD.75.044023. arXiv: astro-ph/0609473 [astro-ph].

[52] L. Baiotti et al. "Analytic Modeling of Tidal Effects in the Relativistic Inspiral of Binary Neutron Stars." In: *Phys. Rev. Lett.* 105.26, 261101 (Dec. 2010), p. 261101. DOI: 10.1103/PhysRevLett.105.261101. arXiv: 1009.0521 [gr-qc].

[53] A. Balasubramanian et al. "GW170817 4.5 Yr After Merger: Dynamical Ejecta Afterglow Constraints." In: *Astrophys. J.* 938.1, 12 (Oct. 2022), p. 12. DOI: 10.3847/1538-4357/ac9133. arXiv: 2205.14788 [astro-ph.HE].

[54] S. A. Balbus. "General Local Stability Criteria for Stratified, Weakly Magnetized Rotating Systems." In: *Astrophys. J.* 453 (Nov. 1995), p. 380. DOI: 10.1086/176397.

[55] S. A. Balbus and J. F. Hawley. "A Powerful Local Shear Instability in Weakly Magnetized Disks. I. Linear Analysis." In: *Astrophys. J.* 376 (July 1991), p. 214. DOI: 10.1086/170270.

[56] S. A. Balbus and J. F. Hawley. "A Powerful Local Shear Instability in Weakly Magnetized Disks. IV. Nonaxisymmetric Perturbations." In: *Astrophys. J.* 400 (Dec. 1992), pp. 610–621. DOI: 10.1086/172022.

[57] S. A. Balbus and J. F. Hawley. "Instability, turbulence, and enhanced transport in accretion disks." In: *Reviews of Modern Physics* 70.1 (Jan. 1998), pp. 1–53. DOI: 10.1103/RevModPhys.70.1.

[58] M. Baldo and G. F. Burgio. "Properties of the nuclear medium." In: *Reports on Progress in Physics* 75.2, 026301 (Feb. 2012), p. 026301. DOI: 10.1088/0034-4885/75/2/026301. arXiv: 1102.1364 [nucl-th].

[59] J. Bamber et al. "Jet-like structures in low-mass binary neutron star merger remnants." In: *arXiv e-prints*, arXiv:2405.03705 (May 2024), arXiv:2405.03705. DOI: 10.48550/arXiv.2405.03705. arXiv: 2405.03705 [astro-ph.HE].

[60] F. Banyuls et al. "Numerical $\{3 + 1\}$ General Relativistic Hydrodynamics: A Local Characteristic Approach." In: *Astrophys. J.* 476.1 (Feb. 1997), pp. 221–231. DOI: 10.1086/303604.

[61] L. Barack et al. "Black holes, gravitational waves and fundamental physics: a roadmap." In: *Class. Quant. Grav.* 36.14 (2019), p. 143001. DOI: 10.1088/1361-6382/ab0587. arXiv: 1806.05195 [gr-qc].

[62] E. Barausse and A. Buonanno. "Extending the effective-one-body Hamiltonian of black-hole binaries to include next-to-next-to-leading spin-orbit couplings." In: *Phys. Rev. D* 84.10, 104027 (Nov. 2011), p. 104027. DOI: 10.1103/PhysRevD.84.104027. arXiv: 1107.2904 [gr-qc].

[63] E. Barausse et al. "Prospects for Fundamental Physics with LISA." In: *Gen. Rel. Grav.* 52.8 (2020), p. 81. DOI: 10.1007/s10714-020-02691-1. arXiv: 2001.09793 [gr-qc].

[64] J. Barnes and D. Kasen. "Effect of a High Opacity on the Light Curves of Radioactively Powered Transients from Compact Object Mergers." In: *Astrophys. J.* 775 (2013), p. 18. DOI: 10.1088/0004-637X/775/1/18. arXiv: 1303.5787 [astro-ph.HE].

[65] P. Barrère et al. "A new scenario for magnetar formation: Tayler-Spruit dynamo in a proto-neutron star spun up by fallback." In: *Astron. Astrophys.* 668, A79 (Dec. 2022), A79. DOI: 10.1051/0004-6361/202244172. arXiv: 2206.01269 [astro-ph.HE].

[66] T. W. Baumgarte and S. L. Shapiro. "Numerical integration of Einstein's field equations." In: *Phys. Rev. D* 59.2, 024007 (Dec. 1998), p. 024007. DOI: 10.1103/PhysRevD.59.024007. arXiv: gr-qc/9810065 [gr-qc].

[67] T. W. Baumgarte, S. L. Shapiro, and M. Shibata. "On the Maximum Mass of Differentially Rotating Neutron Stars." In: *Astrophys. J. Lett.* 528.1 (Jan. 2000), pp. L29–L32. DOI: 10.1086/312425. arXiv: astro-ph/9910565 [astro-ph].

[68] A. Bauswein, T. W. Baumgarte, and H. T. Janka. "Prompt Merger Collapse and the Maximum Mass of Neutron Stars." In: *Phys. Rev. Lett.* 111.13, 131101 (Sept. 2013), p. 131101. DOI: 10.1103/PhysRevLett.111.131101. arXiv: 1307.5191 [astro-ph.SR].

[69] A. Bauswein, S. Goriely, and H. T. Janka. "Systematics of Dynamical Mass Ejection, Nucleosynthesis, and Radioactively Powered Electromagnetic Signals from Neutron-star Mergers." In: *Astrophys. J.* 773.1, 78 (Aug. 2013), p. 78. DOI: 10.1088/0004-637X/773/1/78. arXiv: 1302.6530 [astro-ph.SR].

[70] A. Bauswein and H. T. Janka. "Measuring Neutron-Star Properties via Gravitational Waves from Neutron-Star Mergers." In: *Phys. Rev. Lett.* 108.1, 011101 (Jan. 2012), p. 011101. DOI: 10.1103/PhysRevLett.108.011101. arXiv: 1106.1616 [astro-ph.SR].

[71] A. Bauswein, H. T. Janka, and R. Oechslin. "Testing Approximations of Thermal Effects in Neutron Star Merger Simulations." In: *Phys. Rev. D* 82 (2010), p. 084043. DOI: 10.1103/PhysRevD.82.084043. arXiv: 1006.3315 [astro-ph.SR].

[72] A. Bauswein and N. Stergioulas. "Unified picture of the post-merger dynamics and gravitational wave emission in neutron star mergers." In: *Phys. Rev. D* 91.12, 124056 (June 2015), p. 124056. DOI: 10.1103/PhysRevD.91.124056. arXiv: 1502.03176 [astro-ph.SR].

[73] A. Bauswein and N. Stergioulas. "Spectral classification of gravitational-wave emission and equation of state constraints in binary neutron star mergers." In: *Journal of Physics G Nuclear Physics* 46.11, 113002 (Nov. 2019), p. 113002. DOI: 10.1088/1361-6471/ab2b90. arXiv: 1901.06969 [gr-qc].

[74] A. Bauswein, N. Stergioulas, and H. T. Janka. "Revealing the high-density equation of state through binary neutron star mergers." In: *Phys. Rev. D* 90.2, 023002 (July 2014), p. 023002. DOI: 10.1103/PhysRevD.90.023002. arXiv: 1403.5301 [astro-ph.SR].

[75] A. Bauswein et al. "Equation-of-state dependence of the gravitational-wave signal from the ring-down phase of neutron-star mergers." In: *Phys. Rev. D* 86.6, 063001 (Sept. 2012), p. 063001. DOI: 10.1103/PhysRevD.86.063001. arXiv: 1204.1888 [astro-ph.SR].

[76] A. Bauswein, N. Stergioulas, and H.-T. Janka. "Exploring properties of high-density matter through remnants of neutron-star mergers." In: *European Physical Journal A* 52, 56 (Mar. 2016), p. 56. DOI: 10.1140/epja/i2016-16056-7. arXiv: 1508.05493 [astro-ph.HE].

[77] A. Bauswein et al. "Neutron-star Radius Constraints from GW170817 and Future Detections." In: *Astrophys. J. Lett.* 850.2, L34 (Dec. 2017), p. L34. DOI: 10.3847/2041-8213/aa9994. arXiv: 1710.06843 [astro-ph.HE].

[78] A. Bauswein et al. "Identifying a First-Order Phase Transition in Neutron-Star Mergers through Gravitational Waves." In: *Phys. Rev. Lett.* 122.6, 061102 (Feb. 2019), p. 061102. DOI: 10.1103/PhysRevLett.122.061102. arXiv: 1809.01116 [astro-ph.HE].

[79] B. Bécsy et al. "Parameter Estimation for Gravitational-wave Bursts with the BayesWave Pipeline." In: *Astrophys. J.* 839.1, 15 (Apr. 2017), p. 15. DOI: 10.3847/1538-4357/aa63ef. arXiv: 1612.02003 [astro-ph.HE].

[80] M. Bender, P.-H. Heenen, and P.-G. Reinhard. "Self-consistent mean-field models for nuclear structure." In: *Reviews of Modern Physics* 75.1 (Jan. 2003), pp. 121–180. DOI: 10.1103/RevModPhys.75.121.

[81] L. Bernard et al. "Dimensional regularization of the IR divergences in the Fokker action of point-particle binaries at the fourth post-Newtonian order." In: *Phys. Rev. D* 96.10, 104043 (Nov. 2017), p. 104043. DOI: 10.1103/PhysRevD.96.104043. arXiv: 1706.08480 [gr-qc].

[82] L. Bernard et al. "Center-of-mass equations of motion and conserved integrals of compact binary systems at the fourth post-Newtonian order." In: *Phys. Rev. D* 97.4, 044037 (Feb. 2018), p. 044037. DOI: 10.1103/PhysRevD.97.044037. arXiv: 1711.00283 [gr-qc].

[83] S. Bernuzzi. "Neutron star merger remnants." In: *General Relativity and Gravitation* 52.11, 108 (Nov. 2020), p. 108. DOI: 10.1007/s10714-020-02752-5. arXiv: 2004.06419 [astro-ph.HE].

[84] S. Bernuzzi, T. Dietrich, and A. Nagar. "Modeling the Complete Gravitational Wave Spectrum of Neutron Star Mergers." In: *Phys. Rev. Lett.* 115.9, 091101 (Aug. 2015), p. 091101. DOI: 10.1103/PhysRevLett.115.091101. arXiv: 1504.01764 [gr-qc].

[85] S. Bernuzzi et al. "Tidal effects in binary neutron star coalescence." In: *Phys. Rev. D* 86.4, 044030 (Aug. 2012), p. 044030. DOI: 10.1103/PhysRevD.86.044030. arXiv: 1205.3403 [gr-qc].

[86] S. Bernuzzi et al. "Quasiuniversal Properties of Neutron Star Mergers." In: *Phys. Rev. Lett.* 112.20, 201101 (May 2014), p. 201101. DOI: 10.1103/PhysRevLett.112.201101. arXiv: 1402.6244 [gr-qc].

[87] E. Berti, K. Yagi, and N. Yunes. "Extreme Gravity Tests with Gravitational Waves from Compact Binary Coalescences: (I) Inspiral-Merger." In: *Gen. Rel. Grav.* 50.4 (2018), p. 46. DOI: 10.1007/s10714-018-2362-8. arXiv: 1801.03208 [gr-qc].

[88] E. Berti et al. "Extreme Gravity Tests with Gravitational Waves from Compact Binary Coalescences: (II) Ringdown." In: *Gen. Rel. Grav.* 50.5 (2018), p. 49. DOI: 10.1007/s10714-018-2372-6. arXiv: 1801.03587 [gr-qc].

[89] H. A. Bethe and J. R. Wilson. "Revival of a stalled supernova shock by neutrino heating." In: *Astrophys. J.* 295 (Aug. 1985), pp. 14–23. DOI: 10.1086/163343.

[90] D. Bhattacharya and E. P. J. van den Heuvel. "Formation and evolution of binary and millisecond radio pulsars." In: *Phys. Rep.* 203.1-2 (Jan. 1991), pp. 1–124. DOI: 10.1016/0370-1573(91)90064-S.

[91] L. Blackburn et al. "The LSC glitch group: monitoring noise transients during the fifth LIGO science run." In: *Class. Quantum Grav.* 25.18, 184004 (Sept. 2008), p. 184004. DOI: 10.1088/0264-9381/25/18/184004. arXiv: 0804.0800 [gr-qc].

[92] L. Blanchet. "Gravitational Radiation from Post-Newtonian Sources and Inspiralling Compact Binaries." In: *Living Reviews in Relativity* 9.1, 4 (Dec. 2006), p. 4. DOI: 10.12942/lrr-2006-4.

[93] L. Blanchet. "Gravitational Radiation from Post-Newtonian Sources and Inspiralling Compact Binaries." In: *Living Reviews in Relativity* 17.1, 2 (Dec. 2014), p. 2. DOI: 10.12942/lrr-2014-2. arXiv: 1310.1528 [gr-qc].

[94] R. D. Blandford and R. L. Znajek. "Electromagnetic extraction of energy from Kerr black holes." In: *MNRAS* 179 (May 1977), pp. 433–456. DOI: 10.1093/mnras/179.3.433.

[95] M. Bocquet et al. "Rotating neutron star models with a magnetic field." In: *Astron. Astrophys.* 301 (Sept. 1995), p. 757. DOI: 10.48550/arXiv.gr-qc/9503044. arXiv: gr-qc/9503044 [gr-qc].

[96] I. Bombaci and B. Datta. "Conversion of Neutron Stars to Strange Stars as the Central Engine of Gamma-Ray Bursts." In: *Astrophys. J. Lett.* 530.2 (Feb. 2000), pp. L69–L72. DOI: 10.1086/312497. arXiv: astro-ph/0001478 [astro-ph].

[97] A. Bonanno, V. Urpin, and G. Belvedere. "Protoneutron star dynamos and pulsar magnetism." In: *Astron. Astrophys.* 440.1 (Sept. 2005), pp. 199–205. DOI: 10.1051/0004-6361:20042098. arXiv: astro-ph/0504328 [astro-ph].

[98] S. Bonazzola, J. Frieben, and E. Gourgoulhon. "Spontaneous symmetry breaking of rapidly rotating stars in general relativity: influence of the 3D-shift vector." In: *Astron. Astrophys.* 331 (Mar. 1998), pp. 280–290. DOI: 10.48550/arXiv.gr-qc/9710121. arXiv: gr-qc/9710121 [gr-qc].

[99] S. Bose et al. "Neutron-Star Radius from a Population of Binary Neutron Star Mergers." In: *Phys. Rev. Lett.* 120.3, 031102 (Jan. 2018), p. 031102. DOI: 10.1103/PhysRevLett.120.031102. arXiv: 1705.10850 [gr-qc].

[100] V. Boudart and M. Fays. "Machine learning algorithm for minute-long burst searches." In: *Phys. Rev. D* 105.8, 083007 (Apr. 2022), p. 083007. DOI: 10.1103/PhysRevD.105.083007. arXiv: 2201.08727 [gr-qc].

[101] J. Braithwaite. "A differential rotation driven dynamo in a stably stratified star." In: *Astron. Astrophys.* 449.2 (Apr. 2006), pp. 451–460. DOI: 10.1051/0004-6361:20054241. arXiv: astro-ph/0509693 [astro-ph].

[102] J. Braithwaite. "The stability of toroidal fields in stars." In: *Astron. Astrophys.* 453.2 (July 2006), pp. 687–698. DOI: 10.1051/0004-6361:20041282. arXiv: astro-ph/0512182 [astro-ph].

[103] J. Braithwaite and H. C. Spruit. "Evolution of the magnetic field in magnetars." In: *Astron. Astrophys.* 450.3 (May 2006), pp. 1097–1106. DOI: 10.1051/0004-6361:20041981. arXiv: astro-ph/0510287 [astro-ph].

[104] M. Branchesi et al. "Science with the Einstein Telescope: a comparison of different designs." In: *JCAP* 2023.7, 068 (July 2023), p. 068. DOI: 10.1088/1475-7516/2023/07/068. arXiv: 2303.15923 [gr-qc].

[105] A. Brandenburg and K. Subramanian. "Astrophysical magnetic fields and nonlinear dynamo theory." In: *Phys. Rep.* 417.1-4 (Oct. 2005), pp. 1–209. DOI: 10.1016/j.physrep.2005.06.005. arXiv: astro-ph/0405052 [astro-ph].

[106] A. Brandenburg et al. "Dynamo-generated Turbulence and Large-Scale Magnetic Fields in a Keplerian Shear Flow." In: *Astrophys. J.* 446 (June 1995), p. 741. DOI: 10.1086/175831.

[107] M. Breschi et al. "Kilohertz gravitational waves from binary neutron star remnants: Time-domain model and constraints on extreme matter." In: *Phys. Rev. D* 100.10, 104029 (Nov. 2019), p. 104029. DOI: 10.1103/PhysRevD.100.104029. arXiv: 1908.11418 [gr-qc].

[108] M. Breschi et al. "Kilohertz Gravitational Waves From Binary Neutron Star Mergers: Numerical-relativity Informed Postmerger Model." In: *arXiv e-prints*, arXiv:2205.09112 (May 2022), arXiv:2205.09112. arXiv: 2205.09112 [gr-qc].

[109] S. W. Bruenn and T. Dineva. "The Role of Doubly Diffusive Instabilities in the Core-Collapse Supernova Mechanism." In: *Astrophys. J. Lett.* 458 (Feb. 1996), p. L71. DOI: 10.1086/309921.

[110] A. Buonanno and T. Damour. "Effective one-body approach to general relativistic two-body dynamics." In: *Phys. Rev. D* 59.8, 084006 (Apr. 1999), p. 084006. DOI: 10.1103/PhysRevD.59.084006. arXiv: gr-qc/9811091 [gr-qc].

[111] A. Buonanno and T. Damour. "Transition from inspiral to plunge in binary black hole coalescences." In: *Phys. Rev. D* 62.6, 064015 (Sept. 2000), p. 064015. DOI: 10.1103/PhysRevD.62.064015. arXiv: gr-qc/0001013 [gr-qc].

[112] E. M. Burbidge et al. "Synthesis of the Elements in Stars." In: *Reviews of Modern Physics* 29.4 (Jan. 1957), pp. 547–650. DOI: 10.1103/RevModPhys.29.547.

[113] A. Burrows and J. M. Lattimer. "The Birth of Neutron Stars." In: *Astrophys. J.* 307 (Aug. 1986), p. 178. DOI: 10.1086/164405.

[114] A. Burrows and D. Vartanyan. "Core-collapse supernova explosion theory." In: *Nature* 589.7840 (Jan. 2021), pp. 29–39. DOI: 10.1038/s41586-020-03059-w. arXiv: 2009.14157 [astro-ph.SR].

[115] A. Burrows and J. M. Lattimer. "Neutrinos from SN 1987A." In: *Astrophys. J. Lett.* 318 (July 1987), p. L63. DOI: 10.1086/184938.

[116] K. D. Camarda et al. "Dynamical Bar-Mode Instability in Differentially Rotating Magnetized Neutron Stars." In: *Astrophys. J.* 707.2 (Dec. 2009), pp. 1610–1622. DOI: 10.1088/0004-637X/707/2/1610. arXiv: 0911.0670 [astro-ph.SR].

[117] G. Camelio et al. "Rotating neutron stars with nonbarotropic thermal profile." In: *Phys. Rev. D* 100.12, 123001 (Dec. 2019), p. 123001. DOI: 10.1103/PhysRevD.100.123001. arXiv: 1908.11258 [gr-qc].

[118] F. Carrasco, C. Palenzuela, and O. Reula. "Pulsar magnetospheres in general relativity." In: *Phys. Rev. D* 98.2, 023010 (July 2018), p. 023010. DOI: 10.1103/PhysRevD.98.023010. arXiv: 1805.04123 [astro-ph.HE].

[119] F. Carrasco, D. Viganò, and C. Palenzuela. "Gradient subgrid-scale model for relativistic MHD large-eddy simulations." In: *Phys. Rev. D* 101.6, 063003 (Mar. 2020), p. 063003. DOI: 10.1103/PhysRevD.101.063003. arXiv: 1908.01419 [astro-ph.HE].

[120] B. Carter. "Black hole equilibrium states." In: *Les Houches Summer School of Theoretical Physics: Black Holes*. Jan. 1973, pp. 57–214.

[121] M. Cassing and L. Rezzolla. "Realistic models of general-relativistic differentially rotating stars." In: *arXiv e-prints*, arXiv:2405.06609 (May 2024), arXiv:2405.06609. DOI: 10.48550/arXiv.2405.06609. arXiv: 2405.06609 [gr-qc].

[122] T. Celora et al. "Covariant approach to relativistic large-eddy simulations: The fibration picture." In: *Phys. Rev. D* 104.8, 084090 (Oct. 2021), p. 084090. DOI: 10.1103/PhysRevD.104.084090. arXiv: 2107.01083 [gr-qc].

[123] T. Celora et al. "Covariant approach to relativistic large-eddy simulations: Lagrangian filtering." In: *arXiv e-prints*, arXiv:2405.13593 (May 2024), arXiv:2405.13593. DOI: 10.48550/arXiv.2405.13593. arXiv: 2405.13593 [astro-ph.HE].

[124] J. M. Centrella et al. "Dynamical Rotational Instability at Low T/W." In: *Astrophys. J. Lett.* 550.2 (Apr. 2001), pp. L193–L196. DOI: 10.1086/319634. arXiv: astro-ph/0010574 [astro-ph].

[125] P. Cerdá-Durán, J. A. Font, and H. Dimmelmeier. "General relativistic simulations of passive-magneto-rotational core collapse with microphysics." In: *Astron. Astrophys.* 474.1 (Oct. 2007), pp. 169–191. DOI: 10.1051/0004-6361:20077432. arXiv: astro-ph/0703597 [astro-ph].

[126] P. Cerdá-Durán et al. "A new general relativistic magnetohydrodynamics code for dynamical spacetimes." In: *Astron. Astrophys.* 492.3 (Dec. 2008), pp. 937–953. DOI: 10.1051/0004-6361:200810086. arXiv: 0804.4572 [astro-ph].

[127] P. Cerdá-Durán, V. Quilis, and J. A. Font. "AMR simulations of the low T/|W| bar-mode instability of neutron stars." In: *Computer Physics Communications* 177.3 (Aug. 2007), pp. 288–297. DOI: 10.1016/j.cpc.2007.04.001. arXiv: 0704.0356 [astro-ph].

[128] E. Chabanat et al. "A Skyrme parametrization from subnuclear to neutron star densities Part II. Nuclei far from stabilities." In: *Nucl. Phys. A* 635 (1998), p. 231. DOI: 10.1016/S0375-9474(98)00180-8.

[129] C. Chan et al. "Black Hole Formation and Fallback during the Supernova Explosion of a 40 $M_\odot$ Star." In: *Astrophys. J. Lett.* 852.1, L19 (Jan. 2018), p. L19. DOI: 10.3847/2041-8213/aaa28c. arXiv: 1710.00838 [astro-ph.SR].

[130] S. Chandrasekhar. "The Stability of Non-Dissipative Couette Flow in Hydromagnetics." In: *Proceedings of the National Academy of Science* 46.2 (Feb. 1960), pp. 253–257. DOI: 10.1073/pnas.46.2.253.

[131] S. Chandrasekhar. "Solutions of Two Problems in the Theory of Gravitational Radiation." In: *Phys. Rev. Lett.* 24.11 (Mar. 1970), pp. 611–615. DOI: 10.1103/PhysRevLett.24.611.

[132] S. Chandrasekhar. *Hydrodynamic and hydromagnetic stability*. International series of monographs on physics. Clarendon Press, 1961.

[133] P. Charbonneau. *Solar and Stellar Dynamos*. Saas-Fee Advanced Course. Jan. 2013. DOI: 10.1007/978-3-642-32093-4.

[134] D. Chatterjee et al. "A Machine Learning Based Source Property Inference for Compact Binary Mergers." In: *Astrophys. J.* 896.1 (2020), p. 54. DOI: 10.3847/1538-4357/ab8dbe. arXiv: 1911.00116 [astro-ph.IM].

[135] K. Chatziioannou, C.-J. Haster, and A. Zimmerman. "Measuring the neutron star tidal deformability with equation-of-state-independent relations and gravitational waves." In: *Phys. Rev. D* 97.10, 104036 (May 2018), p. 104036. DOI: 10.1103/PhysRevD.97.104036. arXiv: 1804.03221 [gr-qc].

[136] K. Chatziioannou et al. "Inferring the post-merger gravitational wave emission from binary neutron star coalescences." In: *Phys. Rev. D* 96 (12 Dec. 2017), p. 124035. DOI: 10.1103/PhysRevD.96.124035.

[137] S. S. Chaudhary et al. "Low-latency gravitational wave alert products and their performance at the time of the fourth LIGO-Virgo-KAGRA observing run." In: *Proceedings of the National Academy of Sciences* 121.18 (2024), e2316474121. DOI: 10.1073/pnas.2316474121. eprint: https://www.pnas.org/doi/pdf/10.1073/pnas.2316474121. URL: https://www.pnas.org/doi/abs/10.1073/pnas.2316474121.

[138] K. S. Cheng and Z. G. Dai. "Conversion of Neutron Stars to Strange Stars as a Possible Origin of γ-Ray Bursts." In: *Phys. Rev. Lett.* 77.7 (Aug. 1996), pp. 1210–1213. DOI: 10.1103/PhysRevLett.77.1210. arXiv: astro-ph/9510073 [astro-ph].

[139] A. Chodos et al. "New extended model of hadrons." In: *Phys. Rev. D* 9.12 (June 1974), pp. 3471–3495. DOI: 10.1103/PhysRevD.9.3471.

[140] Q. Chu et al. "SPIIR online coherent pipeline to search for gravitational waves from compact binary coalescences." In: *Phys. Rev. D* 105.2 (2022), p. 024023. DOI: 10.1103/PhysRevD.105.024023. arXiv: 2011.06787 [gr-qc].

[141] R. Ciolfi. "Short gamma-ray burst central engines." In: *Int. J. Mod. Phys. D* 27.13 (2018), p. 1842004. DOI: 10.1142/S021827181842004X. arXiv: 1804.03684 [astro-ph.HE].

[142] R. Ciolfi. "Collimated outflows from long-lived binary neutron star merger remnants." In: *MNRAS* 495.1 (June 2020), pp. L66–L70. DOI: 10.1093/mnrasl/slaa062. arXiv: 2001.10241 [astro-ph.HE].

[143] R. Ciolfi. "The key role of magnetic fields in binary neutron star mergers." In: *General Relativity and Gravitation* 52.6, 59 (June 2020), p. 59. DOI: 10.1007/s10714-020-02714-x. arXiv: 2003.07572 [astro-ph.HE].

[144] R. Ciolfi et al. "First 100 ms of a long-lived magnetized neutron star formed in a binary neutron star merger." In: *Phys. Rev. D* 100.2, 023005 (July 2019), p. 023005. DOI: 10.1103/PhysRevD.100.023005. arXiv: 1904.10222 [astro-ph.HE].

[145] J. A. Clark et al. "Observing gravitational waves from the post-merger phase of binary neutron star coalescence." In: *Class. Quantum Grav.* 33.8, 085003 (Apr. 2016), p. 085003. DOI: 10.1088/0264-9381/33/8/085003. arXiv: 1509.08522 [astro-ph.HE].

[146] P. Colella and P. R. Woodward. "The Piecewise Parabolic Method (PPM) for Gas-Dynamical Simulations." In: *Journal of Computational Physics* 54 (1984), pp. 174–201.

[147] L. Combi and D. M. Siegel. "Jets from Neutron-Star Merger Remnants and Massive Blue Kilonovae." In: *Phys. Rev. Lett.* 131.23, 231402 (Dec. 2023), p. 231402. DOI: 10.1103/PhysRevLett.131.231402. arXiv: 2303.12284 [astro-ph.HE].

[148] C. Constantinou et al. "Thermal properties of hot and dense matter with finite range interactions." In: *Phys. Rev. C* 92.2 (2015), p. 025801. DOI: 10.1103/PhysRevC.92.025801. arXiv: 1504.03982 [astro-ph.SR].

[149] I. Contopoulos, C. Kalapotharakos, and D. Kazanas. "A New Standard Pulsar Magnetosphere." In: *Astrophys. J.* 781.1, 46 (Jan. 2014), p. 46. DOI: 10.1088/0004-637X/781/1/46. arXiv: 1310.4931 [astro-ph.HE].

[150] I. Contopoulos, D. Kazanas, and C. Fendt. "The Axisymmetric Pulsar Magnetosphere." In: *Astrophys. J.* 511.1 (Jan. 1999), pp. 351–358. DOI: 10.1086/306652. arXiv: astro-ph/9903049 [astro-ph].

[151] J. W. Cooley and J. W. Tukey. "An algorithm for the machine calculation of complex Fourier series." In: *Mathematics of Computation* 19 (1965), pp. 297–301.

[152] N. J. Cornish and T. B. Littenberg. "Bayeswave: Bayesian inference for gravitational wave bursts and instrument glitches." In: *Class. Quantum Grav.* 32.13, 135012 (July 2015), p. 135012. DOI: 10.1088/0264-9381/32/13/135012. arXiv: 1410.3835 [gr-qc].

[153] G. Corvino et al. "On the shear instability in relativistic neutron stars." In: *Class. Quantum Grav.* 27.11, 114104 (June 2010), p. 114104. DOI: 10.1088/0264-9381/27/11/114104. arXiv: 1001.5281 [gr-qc].

[154] D. A. Coulter et al. "Swope Supernova Survey 2017a (SSS17a), the Optical Counterpart to a Gravitational Wave Source." In: *Science* 358 (2017), p. 1556. DOI: 10.1126/science.aap9811. arXiv: 1710.05452 [astro-ph.HE].

[155] T. Cover and P. Hart. "Nearest neighbor pattern classification." In: *IEEE Transactions on Information Theory* 13.1 (1967), pp. 21–27. DOI: 10.1109/TIT.1967.1053964.

[156] P. S. Cowperthwaite et al. "The Electromagnetic Counterpart of the Binary Neutron Star Merger LIGO/Virgo GW170817. II. UV, Optical, and Near-infrared Light Curves and Comparison to Kilonova Models." In: *Astrophys. J. Lett.* 848.2, L17 (Oct. 2017), p. L17. DOI: 10.3847/2041-8213/aa8fc7. arXiv: 1710.05840 [astro-ph.HE].

[157] E. Cuoco et al. "Enhancing gravitational-wave science with machine learning." In: *Machine Learning: Science and Technology* 2.1, 011002 (Jan. 2021), p. 011002. DOI: 10.1088/2632-2153/abb93a. arXiv: 2005.03745 [astro-ph.HE].

[158] S. Curtis et al. "Nucleosynthesis in Outflows from Black Hole-Neutron Star Merger Disks with Full GR(ν)RMHD." In: *Astrophys. J. Lett.* 945.1, L13 (Mar. 2023), p. L13. DOI: 10.3847/2041-8213/acba16. arXiv: 2212.10691 [astro-ph.HE].

[159] T. Dal Canton et al. "Real-time Search for Compact Binary Mergers in Advanced LIGO and Virgo's Third Observing Run Using PyCBC Live." In: *Astrophys. J.* 923.2 (2021), p. 254. DOI: 10.3847/1538-4357/ac2f9a. arXiv: 2008.07494 [astro-ph.HE].

[160] T. Damour. "Coalescence of two spinning black holes: An effective one-body approach." In: *Phys. Rev. D* 64.12 (Dec. 2001), p. 124013. DOI: 10.1103/PhysRevD.64.124013. arXiv: gr-qc/0103018 [gr-qc].

[161] T. Damour, B. R. Iyer, and A. Nagar. "Improved resummation of post-Newtonian multipolar waveforms from circularized compact binaries." In: *Phys. Rev. D* 79.6, 064004 (Mar. 2009), p. 064004. DOI: 10.1103/PhysRevD.79.064004. arXiv: 0811.2069 [gr-qc].

[162] T. Damour, P. Jaranowski, and G. Schäfer. "Nonlocal-in-time action for the fourth post-Newtonian conservative dynamics of two-body systems." In: *Phys. Rev. D* 89.6, 064058 (Mar. 2014), p. 064058. DOI: 10.1103/PhysRevD.89.064058. arXiv: 1401.4548 [gr-qc].

[163] T. Damour and A. Nagar. "Improved analytical description of inspiralling and coalescing black-hole binaries." In: *Phys. Rev. D* 79.8, 081503 (Apr. 2009), p. 081503. DOI: 10.1103/PhysRevD.79.081503. arXiv: 0902.0136 [gr-qc].

[164] T. Damour and A. Nagar. "Effective one body description of tidal effects in inspiralling compact binaries." In: *Phys. Rev. D* 81.8, 084016 (Apr. 2010), p. 084016. DOI: 10.1103/PhysRevD.81.084016. arXiv: 0911.5041 [gr-qc].

[165] T. Damour and A. Nagar. "New effective-one-body description of coalescing nonprecessing spinning black-hole binaries." In: *Phys. Rev. D* 90.4, 044018 (Aug. 2014), p. 044018. DOI: 10.1103/PhysRevD.90.044018. arXiv: 1406.6913 [gr-qc].

[166] T. Damour et al. "Accurate effective-one-body waveforms of inspiralling and coalescing black-hole binaries." In: *Phys. Rev. D* 78.4, 044039 (Aug. 2008), p. 044039. DOI: 10.1103/PhysRevD.78.044039. arXiv: 0803.3162 [gr-qc].

[167] S. De et al. "Tidal Deformabilities and Radii of Neutron Stars from the Observation of GW170817." In: *Phys. Rev. Lett.* 121.9, 091102 (Aug. 2018), p. 091102. DOI: 10.1103/PhysRevLett.121.091102. arXiv: 1804.08583 [astro-ph.HE].

[168] R. De Pietri et al. "Neutron star instabilities in full general relativity using a Γ =2.75 ideal fluid." In: *Phys. Rev. D* 90.2, 024034 (July 2014), p. 024034. DOI: 10.1103/PhysRevD.90.024034. arXiv: 1403.8066 [gr-qc].

[169] R. De Pietri et al. "Modeling equal and unequal mass binary neutron star mergers using public codes." In: *Phys. Rev. D* 93.6, 064047 (Mar. 2016), p. 064047. DOI: 10.1103/PhysRevD.93.064047. arXiv: 1509.08804 [gr-qc].

[170] R. De Pietri et al. "Convective Excitation of Inertial Modes in Binary Neutron Star Mergers." In: *Phys. Rev. Lett.* 120.22, 221101 (June 2018), p. 221101. DOI: 10.1103/PhysRevLett.120.221101. arXiv: 1802.03288 [gr-qc].

[171] R. De Pietri et al. "Merger of Compact Stars in the Two-families Scenario." In: *Astrophys. J.* 881.2, 122 (Aug. 2019), p. 122. DOI: 10.3847/1538-4357/ab2fd0. arXiv: 1904.01545 [astro-ph.HE].

[172] R. De Pietri et al. "Numerical-relativity simulations of long-lived remnants of binary neutron star mergers." In: *Phys. Rev. D* 101.6, 064052 (Mar. 2020), p. 064052. DOI: 10.1103/PhysRevD.101.064052. arXiv: 1910.04036 [gr-qc].

[173] P. B. Demorest et al. "A two-solar-mass neutron star measured using Shapiro delay." In: *Nature* 467.7319 (Oct. 2010), pp. 1081–1083. DOI: 10.1038/nature09466. arXiv: 1010.5788 [astro-ph.HE].

[174] F. Di Giovanni et al. "Can fermion-boson stars reconcile multimessenger observations of compact stars?" In: *Phys. Rev. D* 105.6, 063005 (Mar. 2022), p. 063005. DOI: 10.1103/PhysRevD.105.063005. arXiv: 2110.11997 [gr-qc].

[175] T. Dietrich, S. Bernuzzi, and W. Tichy. "Closed-form tidal approximants for binary neutron star gravitational waveforms constructed from high-resolution numerical relativity simulations." In: *Phys. Rev. D* 96.12, 121501 (Dec. 2017), p. 121501. DOI: 10.1103/PhysRevD.96.121501. arXiv: 1706.02969 [gr-qc].

[176] T. Dietrich, T. Hinderer, and A. Samajdar. "Interpreting binary neutron star mergers: describing the binary neutron star dynamics, modelling gravitational waveforms, and analyzing detections." In: *General Relativity and Gravitation* 53.3, 27 (Mar. 2021), p. 27. DOI: 10.1007/s10714-020-02751-6. arXiv: 2004.02527 [gr-qc].

[177] T. Dietrich et al. "Gravitational waves and mass ejecta from binary neutron star mergers: Effect of the mass ratio." In: *Phys. Rev. D* 95.2, 024029 (Jan. 2017), p. 024029. DOI: 10.1103/PhysRevD.95.024029. arXiv: 1607.06636 [gr-qc].

[178] T. Dietrich et al. "CoRe database of binary neutron star merger waveforms." In: *Class. Quantum Grav.* 35.24, 24LT01 (Dec. 2018), 24LT01. DOI: 10.1088/1361-6382/aaebc0. arXiv: 1806.01625 [gr-qc].

[179] T. Dietrich et al. "Improving the NRTidal model for binary neutron star systems." In: *Phys. Rev. D* 100.4, 044003 (Aug. 2019), p. 044003. DOI: 10.1103/PhysRevD.100.044003. arXiv: 1905.06011 [gr-qc].

[180] T. Dietrich et al. "Multimessenger constraints on the neutron-star equation of state and the Hubble constant." In: *Science* 370.6523 (2020), pp. 1450–1453. DOI: 10.1126/science.abb4317. arXiv: 2002.11355.

[181] H. Dimmelmeier. "General relativistic collapse of rotating stellar cores in axisymmetry." PhD thesis. Munich University of Technology, Germany, Jan. 2001.

[182] H. Dimmelmeier, J. A. Font, and E. Muller. "Relativistic simulations of rotational core collapse. 1. Methods, initial models, and code tests." In: *Astron. Astrophys.* 388 (2002), pp. 917–935. DOI: 10.1051/0004-6361:20020563. arXiv: astro-ph/0204288.

[183] H. Dimmelmeier, N. Stergioulas, and J. A. Font. "Non-linear axisymmetric pulsations of rotating relativistic stars in the conformal flatness approximation." In: *MNRAS* 368.4 (June 2006), pp. 1609–1630. DOI: 10.1111/j.1365-2966.2006.10274.x. arXiv: astro-ph/0511394 [astro-ph].

[184] K. Dionysopoulou, D. Alic, and L. Rezzolla. "General-relativistic resistive-magnetohydrodynamic simulations of binary neutron stars." In: *Phys. Rev. D* 92.8, 084064 (Oct. 2015), p. 084064. DOI: 10.1103/PhysRevD.92.084064. arXiv: 1502.02021 [gr-qc].

[185] K. Dionysopoulou et al. "General-relativistic resistive magnetohydrodynamics in three dimensions: Formulation and tests." In: *Phys. Rev. D* 88.4, 044020 (Aug. 2013), p. 044020. DOI: 10.1103/PhysRevD.88.044020. arXiv: 1208.3487 [gr-qc].

[186] M. D. Duez and Y. Zlochower. "Numerical relativity of compact binaries in the 21st century." In: *Reports on Progress in Physics* 82.1, 016902 (Jan. 2019), p. 016902. DOI: 10.1088/1361-6633/aadb16. arXiv: 1808.06011 [gr-qc].

[187] M. D. Duez et al. "General relativistic hydrodynamics with viscosity: Contraction, catastrophic collapse, and disk formation in hypermassive neutron stars." In: *Phys. Rev. D* 69.10, 104030 (May 2004), p. 104030. DOI: 10.1103/PhysRevD.69.104030. arXiv: astro-ph/0402502 [astro-ph].

[188] M. D. Duez et al. "Comparison of momentum transport models for numerical relativity." In: *Phys. Rev. D* 102.10, 104050 (Nov. 2020), p. 104050. DOI: 10.1103/PhysRevD.102.104050. arXiv: 2008.05019 [gr-qc].

[189] W. E. East and F. Pretorius. "Dynamical Capture Binary Neutron Star Mergers." In: *Astrophys. J. Lett.* 760.1, L4 (Nov. 2012), p. L4. DOI: 10.1088/2041-8205/760/1/L4. arXiv: 1208.5279 [astro-ph.HE].

[190] W. E. East et al. "Relativistic simulations of eccentric binary neutron star mergers: One-arm spiral instability and effects of neutron star spin." In: *Phys. Rev. D* 93.2, 024011 (Jan. 2016), p. 024011. DOI: 10.1103/PhysRevD.93.024011. arXiv: 1511.01093 [astro-ph.HE].

[191] P. J. Easter et al. "Computing fast and reliable gravitational waveforms of binary neutron star merger remnants." In: *Phys. Rev. D* 100.4, 043005 (Aug. 2019), p. 043005. DOI: 10.1103/PhysRevD.100.043005. arXiv: 1811.11183 [gr-qc].

[192] D. Eichler et al. "Nucleosynthesis, neutrino bursts and γ-rays from coalescing neutron stars." In: *Nature* 340.6229 (July 1989), pp. 126–128. DOI: 10.1038/340126a0.

[193] B. Einfeldt. "On Godunov-Type Methods for Gas Dynamics." In: *SIAM Journal on Numerical Analysis* 25.2 (1988), pp. 294–318. DOI: 10.1137/0725021. eprint: https://doi.org/10.1137/0725021. URL: https://doi.org/10.1137/0725021.

[194] P. Ekman et al. "Importance of Sub-Grid Scale Modeling for Accurate Aerodynamic Simulations." In: *Journal of Fluids Engineering* 143 (Sept. 2020). DOI: 10.1115/1.4048351.

[195] Y. Eriguchi and E. Mueller. "A general computational method for obtaining equilibria of self-gravitating and rotating gases." In: *Astron. Astrophys.* 146.2 (May 1985), pp. 260–268.

[196] P. L. Espino and V. Paschalidis. "Revisiting the maximum mass of differentially rotating neutron stars in general relativity with realistic equations of state." In: *Phys. Rev. D* 99.8, 083017 (Apr. 2019), p. 083017. DOI: 10.1103/PhysRevD.99.083017. arXiv: 1901.05479 [astro-ph.HE].

[197] P. L. Espino, G. Bozzola, and V. Paschalidis. "Quantifying uncertainties in general relativistic magnetohydrodynamic codes." In: (Oct. 2022). arXiv: 2210.13481 [gr-qc].

[198] Z. B. Etienne et al. "IllinoisGRMHD: An Open-Source, User-Friendly GRMHD Code for Dynamical Spacetimes." In: *Class. Quant. Grav.* 32 (2015), p. 175009. DOI: 10.1088/0264-9381/32/17/175009. arXiv: 1501.07276 [astro-ph.HE].

[199] M. Evans et al. "A Horizon Study for Cosmic Explorer: Science, Observatories, and Community." In: *arXiv e-prints*, arXiv:2109.09882 (Sept. 2021), arXiv:2109.09882. DOI: 10.48550/arXiv.2109.09882. arXiv: 2109.09882 [astro-ph.IM].

[200] Event Horizon Telescope Collaboration et al. "First M87 Event Horizon Telescope Results. V. Physical Origin of the Asymmetric Ring." In: *Astrophys. J. Lett.* 875.1, L5 (Apr. 2019), p. L5. DOI: 10.3847/2041-8213/ab0f43. arXiv: 1906.11242 [astro-ph.GA].

[201] Event Horizon Telescope Collaboration et al. "First Sagittarius A* Event Horizon Telescope Results. VIII. Physical Interpretation of the Polarized Ring." In: *Astrophys. J. Lett.* 964.2, L26 (Apr. 2024), p. L26. DOI: 10.3847/2041-8213/ad2df1.

[202] J. A. Faber and F. A. Rasio. "Binary Neutron Star Mergers." In: *Living Reviews in Relativity* 15.1, 8 (Dec. 2012), p. 8. DOI: 10.12942/lrr-2012-8. arXiv: 1204.3858 [gr-qc].

[203] M. Falanga et al. "Ephemeris, orbital decay, and masses of ten eclipsing high-mass X-ray binaries." In: *Astron. Astrophys.* 577, A130 (May 2015), A130. DOI: 10.1051/0004-6361/201425191. arXiv: 1502.07126 [astro-ph.HE].

[204] H. Falcke and L. Rezzolla. "Fast radio bursts: the last sign of supramassive neutron stars." In: *Astron. Astrophys.* 562, A137 (Feb. 2014), A137. DOI: 10.1051/0004-6361/201321996. arXiv: 1307.1409 [astro-ph.HE].

[205] A. M. Farah et al. "Bridging the Gap: Categorizing Gravitational-wave Events at the Transition between Neutron Stars and Black Holes." In: *Astrophys. J.* 931.2 (2022), p. 108. DOI: 10.3847/1538-4357/ac5f03. arXiv: 2111.03498 [astro-ph.HE].

[206] R. Fernández, F. Foucart, and J. Lippuner. "The landscape of disc outflows from black hole-neutron star mergers." In: *MNRAS* 497.3 (Sept. 2020), pp. 3221–3233. DOI: 10.1093/mnras/staa2209. arXiv: 2005.14208 [astro-ph.HE].

[207] R. Fernández and B. D. Metzger. "Delayed outflows from black hole accretion tori following neutron star binary coalescence." In: *MNRAS* 435.1 (Oct. 2013), pp. 502–517. DOI: 10.1093/mnras/stt1312. arXiv: 1304.6720 [astro-ph.HE].

[208] R. Fernández and B. D. Metzger. "Electromagnetic Signatures of Neutron Star Mergers in the Advanced LIGO Era." In: *Annual Review of Nuclear and Particle Science* 66.1 (Oct. 2016), pp. 23–45. DOI: 10.1146/annurev-nucl-102115-044819. arXiv: 1512.05435 [astro-ph.HE].

[209] R. Fernández et al. "Long-term GRMHD simulations of neutron star merger accretion discs: implications for electromagnetic counterparts." In: *MNRAS* 482.3 (Jan. 2019), pp. 3373–3393. DOI: 10.1093/mnras/sty2932. arXiv: 1808.00461 [astro-ph.HE].

[210] A. L. Fetter and J. D. Walecka. *Quantum Theory of Many-particle Systems*. Dover Books on Physics. Dover Publications, 2003.

[211] S. E. Field et al. "Fast Prediction and Evaluation of Gravitational Waveforms Using Surrogate Models." In: *Physical Review X* 4.3, 031006 (July 2014), p. 031006. DOI: 10.1103/PhysRevX.4.031006. arXiv: 1308.3565 [gr-qc].

[212] J. Fields et al. "Thermal Effects in Binary Neutron Star Mergers." In: *Astrophys. J. Lett.* 952.2, L36 (Aug. 2023), p. L36. DOI: 10.3847/2041-8213/ace5b2. arXiv: 2302.11359 [astro-ph.HE].

[213] A. Figura et al. "Binary neutron star merger simulations with hot microscopic equations of state." In: *Phys. Rev. D* 103.8 (2021), p. 083012. DOI: 10.1103/PhysRevD.103.083012. arXiv: 2103.02365 [gr-qc].

[214] E. Fix and J. L. Hodges. "Discriminatory Analysis. Nonparametric Discrimination: Consistency Properties." In: *International Statistical Review / Revue Internationale de Statistique* 57.3 (1989), pp. 238–247. ISSN: 03067734, 17515823. URL: http://www.jstor.org/stable/1403797 (visited on 03/01/2023).

[215] T. P. Fleming, J. M. Stone, and J. F. Hawley. "The Effect of Resistivity on the Nonlinear Stage of the Magnetorotational Instability in Accretion Disks." In: *Astrophys. J.* 530.1 (Feb. 2000), pp. 464–477. DOI: 10.1086/308338. arXiv: astro-ph/0001164 [astro-ph].

[216] S. Foffa et al. "Effective field theory approach to the gravitational two-body dynamics at fourth post-Newtonian order and quintic in the Newton constant." In: *Phys. Rev. D* 95.10, 104009 (May 2017), p. 104009. DOI: 10.1103/PhysRevD.95.104009. arXiv: 1612.00482 [gr-qc].

[217] J. A. Font. "Numerical Hydrodynamics and Magnetohydrodynamics in General Relativity." In: *Living Reviews in Relativity* 11.1, 7 (Sept. 2008), p. 7. DOI: 10.12942/lrr-2008-7.

[218] J. A. Font et al. "Axisymmetric modes of rotating relativistic stars in the Cowling approximation." In: *MNRAS* 325.4 (Aug. 2001), pp. 1463–1470. DOI: 10.1046/j.1365-8711.2001.04555.x. arXiv: astro-ph/0012477 [astro-ph].

[219] J. A. Font et al. "Three-dimensional numerical general relativistic hydrodynamics. II. Long-term dynamics of single relativistic stars." In: *Phys. Rev. D* 65.8, 084024 (Apr. 2002), p. 084024. DOI: 10.1103/PhysRevD.65.084024. arXiv: gr-qc/0110047 [gr-qc].

[220] C. J. Fontes et al. "Relativistic opacities for astrophysical applications." In: *High Energy Density Physics* 16 (Sept. 2015), pp. 53–59. DOI: 10.1016/j.hedp.2015.06.002.

[221] M. Fortin et al. "Neutron star radii and crusts: Uncertainties and unified equations of state." In: *Phys. Rev. C* 94.3, 035804 (Sept. 2016), p. 035804. DOI: 10.1103/PhysRevC.94.035804. arXiv: 1604.01944 [astro-ph.SR].

[222] F. Foucart et al. "Dynamical ejecta from precessing neutron star-black hole mergers with a hot, nuclear-theory based equation of state." In: *Class. Quantum Grav.* 34.4, 044002 (Feb. 2017), p. 044002. DOI: 10.1088/1361-6382/aa573b. arXiv: 1611.01159 [astro-ph.HE].

[223] F. Foucart. "Black Hole-Neutron Star Mergers: Disk Mass Predictions." In: *Phys. Rev. D* 86 (2012), p. 124007. DOI: 10.1103/PhysRevD.86.124007. arXiv: 1207.6304 [astro-ph.HE].

[224] F. Foucart, T. Hinderer, and S. Nissanke. "Remnant baryon mass in neutron star-black hole mergers: Predictions for binary neutron star mimickers and rapidly spinning black holes." In: *Phys. Rev. D* 98.8 (2018), p. 081501. DOI: 10.1103/PhysRevD.98.081501. arXiv: 1807.00011 [astro-ph.HE].

[225] F. Foucart et al. "Low mass binary neutron star mergers : gravitational waves and neutrino emission." In: *Phys. Rev. D* 93.4 (2016), p. 044019. DOI: 10.1103/PhysRevD.93.044019. arXiv: 1510.06398 [astro-ph.HE].

[226] F. Foucart et al. "Monte-Carlo neutrino transport in neutron star merger simulations." In: *Astrophys. J. Lett.* 902 (2020), p. L27. DOI: 10.3847/2041-8213/abbb87. arXiv: 2008.08089 [astro-ph.HE].

[227] F. Foucart et al. "General relativistic simulations of collapsing binary neutron star mergers with Monte Carlo neutrino transport." In: *Phys. Rev. D* 107.10 (2023), p. 103055. DOI: 10.1103/PhysRevD.107.103055. arXiv: 2210.05670 [astro-ph.HE].

[228] L. Franci et al. "Dynamical bar-mode instability in rotating and magnetized relativistic stars." In: *Phys. Rev. D* 88.10, 104028 (Nov. 2013), p. 104028. DOI: 10.1103/PhysRevD.88.104028. arXiv: 1308.3989 [gr-qc].

[229] C. Freiburghaus, S. Rosswog, and F. K. Thielemann. "R-Process in Neutron Star Mergers." In: *Astrophys. J. Lett.* 525.2 (Nov. 1999), pp. L121–L124. DOI: 10.1086/312343.

[230] J. Frieben and L. Rezzolla. "Equilibrium models of relativistic stars with a toroidal magnetic field." In: *MNRAS* 427.4 (Dec. 2012), pp. 3406–3426. DOI: 10.1111/j.1365-2966.2012.22027.x. arXiv: 1207.4035 [gr-qc].

[231] J. L. Friedman and B. F. Schutz. "Secular instability of rotating Newtonian stars." In: *Astrophys. J.* 222 (May 1978), pp. 281–296. DOI: 10.1086/156143.

[232] U. Frisch. *Turbulence. The legacy of A.N. Kolmogorov*. Cambridge University Press, 1995. DOI: 10.1017/CBO9781139170666.

[233] W. Fu and D. Lai. "Low-T/|W| instabilities in differentially rotating protoneutron stars with magnetic fields." In: *MNRAS* 413.3 (May 2011), pp. 2207–2217. DOI: 10.1111/j.1365-2966.2011.18296.x. arXiv: 1011.4887 [astro-ph.SR].

[234] S. Fujibayashi et al. "Mass ejection from disks surrounding a low-mass black hole: Viscous neutrino-radiation hydrodynamics simulation in full general relativity." In: *Phys. Rev. D* 101.8, 083029 (Apr. 2020), p. 083029. DOI: 10.1103/PhysRevD.101.083029. arXiv: 2001.04467 [astro-ph.HE].

[235] T. Futamase and Y. Itoh. "The Post-Newtonian Approximation for Relativistic Compact Binaries." In: *Living Reviews in Relativity* 10.1, 2 (Mar. 2007), p. 2. DOI: 10.12942/lrr-2007-2.

[236] H. Gabbard et al. "Matching Matched Filtering with Deep Networks for Gravitational-Wave Astronomy." In: *Phys. Rev. Lett.* 120.14, 141103 (Apr. 2018), p. 141103. DOI: 10.1103/PhysRevLett.120.141103. arXiv: 1712.06041 [astro-ph.IM].

[237] H. Gabbard et al. "Bayesian parameter estimation using conditional variational autoencoders for gravitational-wave astronomy." In: *Nature Physics* 18.1 (Jan. 2022), pp. 112–117. DOI: 10.1038/s41567-021-01425-7. arXiv: 1909.06296 [astro-ph.IM].

[238] E. Gaertig and K. D. Kokkotas. "Gravitational wave asteroseismology with fast rotating neutron stars." In: *Phys. Rev. D* 83.6, 064031 (Mar. 2011), p. 064031. DOI: 10.1103/PhysRevD.83.064031. arXiv: 1005.5228 [astro-ph.SR].

[239] D. K. Galloway and N. Lampe. "On the Consistency of Neutron-star Radius Measurements from Thermonuclear Bursts." In: *Astrophys. J.* 747.1, 75 (Mar. 2012), p. 75. DOI: 10.1088/0004-637X/747/1/75. arXiv: 1201.1680 [astro-ph.HE].

[240] T. A. Gardiner and J. M. Stone. "Energetics in MRI driven Turbulence." In: *Magnetic Fields in the Universe: From Laboratory and Stars to Primordial Structures.* Ed. by E. M. de Gouveia dal Pino, G. Lugones, and A. Lazarian. Vol. 784. American Institute of Physics Conference Series. AIP, Sept. 2005, pp. 475–488. DOI: 10.1063/1.2077209. arXiv: astro-ph/0502519 [astro-ph].

[241] K. C. Gendreau et al. "The Neutron star Interior Composition ExploreR (NICER): an Explorer mission of opportunity for soft x-ray timing spectroscopy." In: *Space Telescopes and Instrumentation 2012: Ultraviolet to Gamma Ray*. Ed. by T. Takahashi, S. S. Murray, and J.-W. A. den Herder. Vol. 8443. Society of Photo-Optical Instrumentation Engineers (SPIE) Conference Series. Sept. 2012, 844313, p. 844313. DOI: 10.1117/12.926396.

[242] K. C. Gendreau et al. "The Neutron star Interior Composition Explorer (NICER): design and development." In: *Space Telescopes and Instrumentation 2016: Ultraviolet to Gamma Ray*. Ed. by J.-W. A. den Herder, T. Takahashi, and M. Bautz. Vol. 9905. Society of Photo-Optical Instrumentation Engineers (SPIE) Conference Series. July 2016, 99051H, 99051H. DOI: 10.1117/12.2231304.

[243] D. George and E. A. Huerta. "Deep Learning for real-time gravitational wave detection and parameter estimation: Results with Advanced LIGO data." In: *Physics Letters B* 778 (Mar. 2018), pp. 64–70. DOI: 10.1016/j.physletb.2017.12.053. arXiv: 1711.03121 [gr-qc].

[244] U. Geppert, M. Küker, and D. Page. "Temperature distribution in magnetized neutron star crusts." In: *Astron. Astrophys.* 426 (Oct. 2004), pp. 267–277. DOI: 10.1051/0004-6361:20040455. arXiv: astro-ph/0403441 [astro-ph].

[245] S. Ghosh et al. "Rapid model comparison of equations of state from gravitational wave observation of binary neutron star coalescences." In: *Phys. Rev. D* 104.8 (2021), p. 083003. DOI: 10.1103/PhysRevD.104.083003. arXiv: 2104.08681 [gr-qc].

[246] B. Giacomazzo, L. Rezzolla, and L. Baiotti. "Can magnetic fields be detected during the inspiral of binary neutron stars?" In: *MNRAS* 399.1 (Oct. 2009), pp. L164–L168. DOI: 10.1111/j.1745-3933.2009.00745.x. arXiv: 0901.2722 [gr-qc].

[247] B. Giacomazzo, L. Rezzolla, and L. Baiotti. "Accurate evolutions of inspiralling and magnetized neutron stars: Equal-mass binaries." In: *Phys. Rev. D* 83.4, 044014 (Feb. 2011), p. 044014. DOI: 10.1103/PhysRevD.83.044014. arXiv: 1009.2468 [gr-qc].

[248] B. Giacomazzo et al. "Producing Magnetar Magnetic Fields in the Merger of Binary Neutron Stars." In: *Astrophys. J.* 809.1, 39 (Aug. 2015), p. 39. DOI: 10.1088/0004-637X/809/1/39. arXiv: 1410.0013 [astro-ph.HE].

[249] H. Gieg et al. "Incorporating a Radiative Hydrodynamics Scheme in the Numerical-Relativity Code BAM." In: *Universe* 8.7 (2022), p. 370. DOI: 10.3390/universe8070370. arXiv: 2206.01337 [gr-qc].

[250] J. Gil, G. I. Melikidze, and U. Geppert. "Drifting subpulses and inner accelerationregions in radio pulsars." In: *Astron. Astrophys.* 407 (Aug. 2003), pp. 315–324. DOI: 10.1051/0004-6361:20030854. arXiv: astro-ph/0305463 [astro-ph].

[251] N. K. Glendenning. "First-order phase transitions with more than one conserved charge: Consequences for neutron stars." In: *Phys. Rev. D* 46.4 (Aug. 1992), pp. 1274–1287. DOI: 10.1103/PhysRevD.46.1274.

[252] N. K. Glendenning. *Compact stars. Nuclear physics, particle physics, and general relativity*. Springer New York, NY, 1997.

[253] D. Gogichaishvili et al. "Active Modes and Dynamical Balances in MRI Turbulence of Keplerian Disks with a Net Vertical Magnetic Field." In: *Astrophys. J.* 866.2, 134 (Oct. 2018), p. 134. DOI: 10.3847/1538-4357/aadbad. arXiv: 1808.06147 [astro-ph.SR].

[254] P. Goldreich and D. Lynden-Bell. "II. Spiral arms as sheared gravitational instabilities." In: *MNRAS* 130 (Jan. 1965), p. 125. DOI: 10.1093/mnras/130.2.125.

[255] A. Goldstein et al. "An Ordinary Short Gamma-Ray Burst with Extraordinary Implications: Fermi-GBM Detection of GRB 170817A." In: *Astrophys. J. Lett.* 848.2, L14 (Oct. 2017), p. L14. DOI: 10.3847/2041-8213/aa8f41. arXiv: 1710.05446 [astro-ph.HE].

[256] D. Gondek-Rosińska et al. "Rapidly rotating compact strange stars." In: *Astron. Astrophys.* 363 (Nov. 2000), pp. 1005–1012. DOI: 10.48550/arXiv.astro-ph/0007004. arXiv: astro-ph/0007004 [astro-ph].

[257] D. Gondek-Rosińska and E. Gourgoulhon. "Jacobi-like bar mode instability of relativistic rotating bodies." In: *Phys. Rev. D* 66.4, 044021 (Aug. 2002), p. 044021. DOI: 10.1103/PhysRevD.66.044021. arXiv: gr-qc/0205102 [gr-qc].

[258] A. Gonzalez et al. "Second release of the CORE database of binary neutron star merger waveforms." In: *Class. Quantum Grav.* 40.8, 085011 (Apr. 2023), p. 085011. DOI: 10.1088/1361-6382/acc231. arXiv: 2210.16366 [gr-qc].

[259] T. Goodale et al. "The cactus framework and toolkit: Design and applications." English (US). In: *Lecture Notes in Computer Science (including subseries Lecture Notes in Artificial Intelligence and Lecture Notes in Bioinformatics)*. Lecture Notes in Computer Science (including subseries Lecture Notes in Artificial Intelligence and Lecture Notes in Bioinformatics). Germany: Springer, 2003, pp. 197–227. ISBN: 3540008527. DOI: 10.1007/3-540-36569-9_13.

[260] J. Goodman and G. Xu. "Parasitic Instabilities in Magnetized, Differentially Rotating Disks." In: *Astrophys. J.* 432 (Sept. 1994), p. 213. DOI: 10.1086/174562.

[261] E. Gourgoulhon et al. "Quasiequilibrium sequences of synchronized and irrotational binary neutron stars in general relativity: Method and tests." In: *Phys. Rev. D* 63.6, 064029 (Mar. 2001), p. 064029. DOI: 10.1103/PhysRevD.63.064029. arXiv: gr-qc/0007028 [gr-qc].

[262] E. Gourgoulhon et al. *LORENE: Spectral methods differential equations solver*. Astrophysics Source Code Library, record ascl:1608.018. Aug. 2016. ascl: 1608.018.

[263] K. N. Gourgouliatos, D. De Grandis, and A. Igoshev. "Magnetic Field Evolution in Neutron Star Crusts: Beyond the Hall Effect." In: *Symmetry* 14.1, 130 (Jan. 2022), p. 130. DOI: 10.3390/sym14010130. arXiv: 2201.08345 [astro-ph.HE].

[264] S. R. Green, C. Simpson, and J. Gair. "Gravitational-wave parameter estimation with autoregressive neural network flows." In: *Phys. Rev. D* 102.10, 104057 (Nov. 2020), p. 104057. DOI: 10.1103/PhysRevD.102.104057. arXiv: 2002.07656 [astro-ph.IM].

[265] R. Guardiola. "Monte Carlo methods in quantum many-body theories." In: *Lecture Notes in Physics, Berlin Springer Verlag*. Ed. by J. Navarro and A. Polls. Vol. 510. 1998, p. 269. DOI: 10.1007/BFb0104529.

[266] D. Guerra et al. “Thermal effects on long-lived remnants of binary neutron star mergers.” In: *in preparation* (2024).

[267] J. Guilet et al. “MRI-driven dynamo at very high magnetic Prandtl numbers.” In: *MNRAS* 516.3 (Nov. 2022), pp. 4346–4353. DOI: 10.1093/mnras/stac2499. arXiv: 2205.08602 [astro-ph.HE].

[268] S. Guillot et al. “Measurement of the Radius of Neutron Stars with High Signal-to-noise Quiescent Low-mass X-Ray Binaries in Globular Clusters.” In: *Astrophys. J.* 772.1, 7 (July 2013), p. 7. DOI: 10.1088/0004-637X/772/1/7. arXiv: 1302.0023 [astro-ph.HE].

[269] G. Guo et al. “KNN Model-Based Approach in Classification.” In: *On The Move to Meaningful Internet Systems 2003: CoopIS, DOA, and ODBASE*. Vol. 2888. Jan. 2003, pp. 986–996. ISBN: 978-3-540-20498-5. DOI: 10.1007/978-3-540-39964-3_62.

[270] P. Haensel, A. Y. Potekhin, and D. G. Yakovlev. *Neutron Stars 1 : Equation of State and Structure*. Vol. 326. 2007.

[271] M. Hanauske et al. “Rotational properties of hypermassive neutron stars from binary mergers.” In: *Phys. Rev. D* 96.4, 043004 (Aug. 2017), p. 043004. DOI: 10.1103/PhysRevD.96.043004. arXiv: 1611.07152 [gr-qc].

[272] B. M. S. Hansen and M. Lyutikov. “Radio and X-ray signatures of merging neutron stars.” In: *MNRAS* 322.4 (Apr. 2001), pp. 695–701. DOI: 10.1046/j.1365-8711.2001.04103.x. arXiv: astro-ph/0003218 [astro-ph].

[273] G. M. Harry and LIGO Scientific Collaboration. “Advanced LIGO: the next generation of gravitational wave detectors.” In: *Class. Quantum Grav.* 27.8, 084006 (Apr. 2010), p. 084006. DOI: 10.1088/0264-9381/27/8/084006.

[274] A. Harten, P. D. Lax, and B. v. Leer. “On Upstream Differencing and Godunov-Type Schemes for Hyperbolic Conservation Laws.” In: *SIAM Review* 25.1 (1983), pp. 35–61. DOI: 10.1137/1025002. eprint: https://doi.org/10.1137/1025002. URL: https://doi.org/10.1137/1025002.

[275] J. W. Hartman et al. “A study of the evolution of radio pulsars through improved population synthesis.” In: *Astron. Astrophys.* 322 (June 1997), pp. 477–488.

[276] J. F. Hawley, X. Guan, and J. H. Krolik. “Assessing Quantitative Results in Accretion Simulations: From Local to Global.” In: *Astrophys. J.* 738.1, 84 (Sept. 2011), p. 84. DOI: 10.1088/0004-637X/738/1/84. arXiv: 1103.5987 [astro-ph.HE].

[277] K. Hayashi et al. “General-relativistic neutrino-radiation magnetohydrodynamic simulation of seconds-long black hole-neutron star mergers.” In: *Phys. Rev. D* 106.2 (2022), p. 023008. DOI: 10.1103/PhysRevD.106.023008. arXiv: 2111.04621 [astro-ph.HE].

[278] H. Heiselberg and M. Hjorth-Jensen. “Phases of dense matter in neutron stars.” In: *Phys. Rep.* 328.5-6 (May 2000), pp. 237–327. DOI: 10.1016/S0370-1573(99)00110-6. arXiv: nucl-th/9902033 [nucl-th].

[279] A. Hewish et al. “Observation of a Rapidly Pulsating Radio Source.” In: *Nature* 217.5130 (Feb. 1968), pp. 709–713. DOI: 10.1038/217709a0.

[280] S. Hild et al. "Sensitivity studies for third-generation gravitational wave observatories." In: *Class. Quantum Grav.* 28.9, 094013 (May 2011), p. 094013. DOI: 10.1088/0264-9381/28/9/094013. arXiv: 1012.0908 [gr-qc].

[281] T. Hinderer et al. "Effects of Neutron-Star Dynamic Tides on Gravitational Waveforms within the Effective-One-Body Approach." In: *Phys. Rev. Lett.* 116.18, 181101 (May 2016), p. 181101. DOI: 10.1103/PhysRevLett.116.181101. arXiv: 1602.00599 [gr-qc].

[282] K. Hirai et al. "Study of the Transition from MRI to Magnetic Turbulence via Parasitic Instability by a High-order MHD Simulation Code." In: *Astrophys. J.* 853.2, 174 (Feb. 2018), p. 174. DOI: 10.3847/1538-4357/aaa5b2.

[283] K. Hirata et al. "Observation of a neutrino burst from the supernova SN1987A." In: *Phys. Rev. Lett.* 58.14 (Apr. 1987), pp. 1490–1493. DOI: 10.1103/PhysRevLett.58.1490.

[284] J. Hjorth et al. "A very energetic supernova associated with the γ-ray burst of 29 March 2003." In: *Nature* 423.6942 (June 2003), pp. 847–850. DOI: 10.1038/nature01750. arXiv: astro-ph/0306347 [astro-ph].

[285] W. C. G. Ho and D. Lai. "Resonant tidal excitations of rotating neutron stars in coalescing binaries." In: *MNRAS* 308.1 (Sept. 1999), pp. 153–166. DOI: 10.1046/j.1365-8711.1999.02703.x. arXiv: astro-ph/9812116 [astro-ph].

[286] G. Hobbs et al. "The International Pulsar Timing Array project: using pulsars as a gravitational wave detector." In: *Class. Quantum Grav.* 27.8, 084013 (Apr. 2010), p. 084013. DOI: 10.1088/0264-9381/27/8/084013. arXiv: 0911.5206 [astro-ph.SR].

[287] K. Hotokezaka et al. "Radio Counterparts of Compact Binary Mergers Detectable in Gravitational Waves: A Simulation for an Optimized Survey." In: *Astrophys. J.* 831.2, 190 (Nov. 2016), p. 190. DOI: 10.3847/0004-637X/831/2/190. arXiv: 1605.09395 [astro-ph.HE].

[288] K. Hotokezaka et al. "Remnant massive neutron stars of binary neutron star mergers: Evolution process and gravitational waveform." In: *Phys. Rev. D* 88.4, 044026 (Aug. 2013), p. 044026. DOI: 10.1103/PhysRevD.88.044026. arXiv: 1307.5888 [astro-ph.HE].

[289] J. L. Houser, J. M. Centrella, and S. C. Smith. "Gravitational radiation from nonaxisymmetric instability in a rotating star." In: *Phys. Rev. Lett.* 72.9 (Jan. 1994), pp. 1314–1317. DOI: 10.1103/PhysRevLett.72.1314. arXiv: gr-qc/9409057 [gr-qc].

[290] E. A. Huerta et al. "Enabling real-time multi-messenger astrophysics discoveries with deep learning." In: *Nature Reviews Physics* 1.10 (Oct. 2019), pp. 600–608. DOI: 10.1038/s42254-019-0097-4. arXiv: 1911.11779 [gr-qc].

[291] J. N. Imamura, J. L. Friedman, and R. H. Durisen. "Secular stability limits for rotating polytropic stars." In: *Astrophys. J.* 294 (July 1985), pp. 474–478. DOI: 10.1086/163313.

[292] P. Iosif and N. Stergioulas. "Models of binary neutron star remnants with tabulated equations of state." In: *Mon. Not. Roy. Astron. Soc.* 510.2 (Feb. 2022), pp. 2948–2967. DOI: 10.1093/mnras/stab3565. arXiv: 2104.13672 [astro-ph.HE].

[293] J. R. Ipser and L. Lindblom. "The Oscillations of Rapidly Rotating Newtonian Stellar Models." In: *Astrophys. J.* 355 (May 1990), p. 226. DOI: 10.1086/168757.

[294] M. Isi et al. "Testing the no-hair theorem with GW150914." In: *Phys. Rev. Lett.* 123.11 (2019), p. 111102. DOI: 10.1103/PhysRevLett.123.111102. arXiv: 1905.00869 [gr-qc].

[295] J. D. Jackson. *Classical electrodynamics*. Wiley, 1975.

[296] R. A. James. "The Structure and Stability of Rotating Gas Masses." In: *Astrophys. J.* 140 (Aug. 1964), p. 552. DOI: 10.1086/147949.

[297] F. D. S. James M. Lattimer. "A generalized equation of state for hot, dense matter." In: *Nucl. Phys. A* 535 (1991), p. 331. DOI: 10.1016/0375-9474(91)90452-C.

[298] H. T. Janka, T. Zwerger, and R. Moenchmeyer. "Does artificial viscosity destroy prompt type-II supernova explosions?" In: *"Astronomy and Astrophysics"* 268.1 (Feb. 1993), pp. 360–368.

[299] G.-S. Jiang and C.-W. Shu. "Efficient Implementation of Weighted ENO Schemes." In: *Journal of Computational Physics* 126.1 (June 1996), pp. 202–228. DOI: 10.1006/jcph.1996.0130.

[300] O. Just, M. Obergaulinger, and H. T. Janka. "A new multidimensional, energy-dependent two-moment transport code for neutrino-hydrodynamics." In: *MNRAS* 453.4 (Nov. 2015), pp. 3386–3413. DOI: 10.1093/mnras/stv1892. arXiv: 1501.02999 [astro-ph.HE].

[301] O. Just et al. "Comprehensive nucleosynthesis analysis for ejecta of compact binary mergers." In: *MNRAS* 448.1 (Mar. 2015), pp. 541–567. DOI: 10.1093/mnras/stv009. arXiv: 1406.2687 [astro-ph.SR].

[302] O. Just et al. "Neutrino absorption and other physics dependencies in neutrino-cooled black hole accretion discs." In: *MNRAS* 509.1 (Jan. 2022), pp. 1377–1412. DOI: 10.1093/mnras/stab2861. arXiv: 2102.08387 [astro-ph.HE].

[303] KAGRA Collaboration et al. "KAGRA: 2.5 generation interferometric gravitational wave detector." In: *Nature Astronomy* 3 (Jan. 2019), pp. 35–40. DOI: 10.1038/s41550-018-0658-y. arXiv: 1811.08079 [gr-qc].

[304] C. Kalapotharakos, I. Contopoulos, and D. Kazanas. "The extended pulsar magnetosphere." In: *MNRAS* 420.4 (Mar. 2012), pp. 2793–2798. DOI: 10.1111/j.1365-2966.2011.19884.x. arXiv: 1109.5122 [astro-ph.HE].

[305] C. Kalapotharakos et al. "Toward a Realistic Pulsar Magnetosphere." In: *Astrophys. J.* 749.1, 2 (Apr. 2012), p. 2. DOI: 10.1088/0004-637X/749/1/2. arXiv: 1108.2138 [astro-ph.SR].

[306] V. Kalogera et al. "The Coalescence Rate of Double Neutron Star Systems." In: *Astrophys. J.* 556.1 (July 2001), pp. 340–356. DOI: 10.1086/321583. arXiv: astro-ph/0012038 [astro-ph].

[307] J. D. Kaplan et al. "The Influence of Thermal Pressure on Equilibrium Models of Hypermassive Neutron Star Merger Remnants." In: *Astrophys. J.* 790.1, 19 (July 2014), p. 19. DOI: 10.1088/0004-637X/790/1/19. arXiv: 1306.4034 [astro-ph.HE].

[308] P. I. Karpov et al. "Physics-informed Machine Learning for Modeling Turbulence in Supernovae." In: *Astrophys. J.* 940.1, 26 (Nov. 2022), p. 26. DOI: 10.3847/1538-4357/ac88cc. arXiv: 2205.08663 [physics.comp-ph].

[309] D. Kasen, N. R. Badnell, and J. Barnes. "Opacities and Spectra of the r-process Ejecta from Neutron Star Mergers." In: *Astrophys. J.* 774.1, 25 (Sept. 2013), p. 25. DOI: 10.1088/0004-637X/774/1/25. arXiv: 1303.5788 [astro-ph.HE].

[310] D. Kasen, R. Fernandez, and B. Metzger. "Kilonova light curves from the disc wind outflows of compact object mergers." In: *Mon. Not. Roy. Astron. Soc.* 450 (2015), pp. 1777–1786. DOI: 10.1093/mnras/stv721. arXiv: 1411.3726 [astro-ph.HE].

[311] M. M. Kasliwal et al. "Illuminating Gravitational Waves: A Concordant Picture of Photons from a Neutron Star Merger." In: *Science* 358 (2017), p. 1559. DOI: 10.1126/science.aap9455. arXiv: 1710.05436 [astro-ph.HE].

[312] V. M. Kaspi. "Grand unification of neutron stars." In: *Proceedings of the National Academy of Science* 107.16 (Apr. 2010), pp. 7147–7152. DOI: 10.1073/pnas.1000812107. arXiv: 1005.0876 [astro-ph.HE].

[313] W. Kastaun, R. Ciolfi, and B. Giacomazzo. "Structure of stable binary neutron star merger remnants: A case study." In: *Phys. Rev. D* 94.4, 044060 (Aug. 2016), p. 044060. DOI: 10.1103/PhysRevD.94.044060. arXiv: 1607.02186 [astro-ph.HE].

[314] W. Kastaun et al. "Structure of stable binary neutron star merger remnants: Role of initial spin." In: *Phys. Rev. D* 96.4, 043019 (Aug. 2017), p. 043019. DOI: 10.1103/PhysRevD.96.043019. arXiv: 1612.03671 [astro-ph.HE].

[315] W. Kastaun. "Inertial modes of rigidly rotating neutron stars in Cowling approximation." In: *Phys. Rev. D* 77.12, 124019 (June 2008), p. 124019. DOI: 10.1103/PhysRevD.77.124019. arXiv: 0804.1151 [astro-ph].

[316] W. Kastaun and F. Galeazzi. "Properties of hypermassive neutron stars formed in mergers of spinning binaries." In: *Phys. Rev. D* 91.6, 064027 (Mar. 2015), p. 064027. DOI: 10.1103/PhysRevD.91.064027. arXiv: 1411.7975 [gr-qc].

[317] W. Kastaun, B. Willburger, and K. D. Kokkotas. "Saturation amplitude of the f-mode instability." In: *Phys. Rev. D* 82.10, 104036 (Nov. 2010), p. 104036. DOI: 10.1103/PhysRevD.82.104036. arXiv: 1006.3885 [gr-qc].

[318] K. Kawaguchi et al. "Frequency-domain gravitational waveform models for inspiraling binary neutron stars." In: *Phys. Rev. D* 97.4, 044044 (Feb. 2018), p. 044044. DOI: 10.1103/PhysRevD.97.044044. arXiv: 1802.06518 [gr-qc].

[319] T. Kawamura et al. "Binary neutron star mergers and short gamma-ray bursts: Effects of magnetic field orientation, equation of state, and mass ratio." In: *Phys. Rev. D* 94.6, 064012 (Sept. 2016), p. 064012. DOI: 10.1103/PhysRevD.94.064012. arXiv: 1607.01791 [astro-ph.HE].

[320] W. Keil and H. T. Janka. "Hadronic phase transitions at supranuclear densities and the delayed collapse of newly formed neutron stars." In: *Astron. Astrophys.* 296 (Apr. 1995), p. 145.

[321] W. Keil, H. T. Janka, and E. Mueller. "Ledoux Convection in Protoneutron Stars—A Clue to Supernova Nucleosynthesis?" In: *Astrophys. J. Lett.* 473 (Dec. 1996), p. L111. DOI: 10.1086/310404. arXiv: astro-ph/9610203 [astro-ph].

[322] K. Kiuchi et al. "High resolution numerical relativity simulations for the merger of binary magnetized neutron stars." In: *Phys. Rev. D* 90.4, 041502 (Aug. 2014), p. 041502. DOI: 10.1103/PhysRevD.90.041502. arXiv: 1407.2660 [astro-ph.HE].

[323] K. Kiuchi et al. "Efficient magnetic-field amplification due to the Kelvin-Helmholtz instability in binary neutron star mergers." In: *Phys. Rev. D* 92.12, 124034 (Dec. 2015), p. 124034. DOI: 10.1103/PhysRevD.92.124034. arXiv: 1509.09205 [astro-ph.HE].

[324] K. Kiuchi et al. "Global simulations of strongly magnetized remnant massive neutron stars formed in binary neutron star mergers." In: *Phys. Rev. D* 97.12, 124039 (June 2018), p. 124039. DOI: 10.1103/PhysRevD.97.124039. arXiv: 1710.01311 [astro-ph.HE].

[325] K. Kiuchi et al. "A large-scale magnetic field produced by a solar-like dynamo in binary neutron star mergers." In: *Nature Astronomy* 8 (Mar. 2024), pp. 298–307. DOI: 10.1038/s41550-024-02194-y. arXiv: 2306.15721 [astro-ph.HE].

[326] T. Klähn et al. "Constraints on the high-density nuclear equation of state from the phenomenology of compact stars and heavy-ion collisions." In: *Phys. Rev. C* 74.3, 035802 (Sept. 2006), p. 035802. DOI: 10.1103/PhysRevC.74.035802. arXiv: nucl-th/0602038 [nucl-th].

[327] S. Klimenko et al. "Method for detection and reconstruction of gravitational wave transients with networks of advanced detectors." In: *Phys. Rev. D* 93.4, 042004 (Feb. 2016), p. 042004. DOI: 10.1103/PhysRevD.93.042004. arXiv: 1511.05999 [gr-qc].

[328] C. S. Kochanek. "Coalescing Binary Neutron Stars." In: *Astrophys. J.* 398 (Oct. 1992), p. 234. DOI: 10.1086/171851.

[329] K. D. Kokkotas and B. G. Schmidt. "Quasi-Normal Modes of Stars and Black Holes." In: *Living Reviews in Relativity* 2.1, 2 (Sept. 1999), p. 2. DOI: 10.12942/lrr-1999-2. arXiv: gr-qc/9909058 [gr-qc].

[330] H. Komatsu, Y. Eriguchi, and I. Hachisu. "Rapidly rotating general relativistic stars. I - Numerical method and its application to uniformly rotating polytropes." In: *MNRAS* 237 (Mar. 1989), pp. 355–379. DOI: 10.1093/mnras/237.2.355.

[331] O. Korobkin et al. "On the astrophysical robustness of neutron star merger r-process." In: *Mon. Not. Roy. Astron. Soc.* 426 (2012), p. 1940. DOI: 10.1111/j.1365-2966.2012.21859.x. arXiv: 1206.2379 [astro-ph.SR].

[332] K. Kotake, K. Sato, and K. Takahashi. "Explosion mechanism, neutrino burst and gravitational wave in core-collapse supernovae." In: *Reports on Progress in Physics* 69.4 (Apr. 2006), pp. 971–1143. DOI: 10.1088/0034-4885/69/4/R03. arXiv: astro-ph/0509456 [astro-ph].

[333] C. Kouveliotou et al. "An X-ray pulsar with a superstrong magnetic field in the soft γ-ray repeater SGR1806 - 20." In: *Nature* 393.6682 (May 1998), pp. 235–237. DOI: 10.1038/30410.

[334] C. Kouveliotou et al. "Identification of Two Classes of Gamma-Ray Bursts." In: *Astrophys. J. Lett.* 413 (Aug. 1993), p. L101. DOI: 10.1086/186969.

[335] F. Krause and K. Rädler. *Mean-field magnetohydrodynamics and dynamo theory*. Pergamon Press, 1980.

[336] C. J. Krüger et al. "Fast Rotating Neutron Stars: Oscillations and Instabilities." In: *Frontiers in Astronomy and Space Sciences* 8, 166 (Sept. 2021), p. 166. DOI: 10.3389/fspas.2021.736918. arXiv: 2110.00393 [gr-qc].

[337] T. Kuroda, T. Takiwaki, and K. Kotake. "Gravitational wave signatures from low-mode spiral instabilities in rapidly rotating supernova cores." In: *Phys. Rev. D* 89.4, 044011 (Feb. 2014), p. 044011. DOI: 10.1103/PhysRevD.89.044011. arXiv: 1304.4372 [astro-ph.HE].

[338] T. Kuroda et al. "Magnetorotational Explosion of a Massive Star Supported by Neutrino Heating in General Relativistic Three-dimensional Simulations." In: *Astrophys. J.* 896.2, 102 (June 2020), p. 102. DOI: 10.3847/1538-4357/ab9308. arXiv: 2003.02004 [astro-ph.HE].

[339] B. D. Lackey et al. "Effective-one-body waveforms for binary neutron stars using surrogate models." In: *Phys. Rev. D* 95.10, 104036 (May 2017), p. 104036. DOI: 10.1103/PhysRevD.95.104036. arXiv: 1610.04742 [gr-qc].

[340] B. D. Lackey et al. "Effective-one-body waveforms for binary neutron stars using surrogate models." In: *Phys. Rev. D* 95.10 (2017), p. 104036. DOI: 10.1103/PhysRevD.95.104036. arXiv: 1610.04742 [gr-qc].

[341] B. D. Lackey et al. "Surrogate model for an aligned-spin effective-one-body waveform model of binary neutron star inspirals using Gaussian process regression." In: *Phys. Rev. D* 100.2, 024002 (July 2019), p. 024002. DOI: 10.1103/PhysRevD.100.024002. arXiv: 1812.08643 [gr-qc].

[342] D. Lai. "DC Circuit Powered by Orbital Motion: Magnetic Interactions in Compact Object Binaries and Exoplanetary Systems." In: *Astrophys. J. Lett.* 757.1, L3 (Sept. 2012), p. L3. DOI: 10.1088/2041-8205/757/1/L3. arXiv: 1206.3723 [astro-ph.HE].

[343] L. D. Landau and E. M. Lifshitz. *Fluid Mechanics*. Pergamon, 1987.

[344] P. Landry and R. Essick. "Nonparametric inference of the neutron star equation of state from gravitational wave observations." In: *Phys. Rev. D* 99.8, 084049 (Apr. 2019), p. 084049. DOI: 10.1103/PhysRevD.99.084049. arXiv: 1811.12529 [gr-qc].

[345] P. D. Lasky. "Gravitational Waves from Neutron Stars: A Review." In: *Publ. Astron. Soc. Austral.* 32 (2015), e034. DOI: 10.1017/pasa.2015.35. arXiv: 1508.06643 [astro-ph.HE].

[346] H. N. Latter, S. Fromang, and O. Gressel. "MRI channel flows in vertically stratified models of accretion discs." In: *MNRAS* 406.2 (Aug. 2010), pp. 848–862. DOI: 10.1111/j.1365-2966.2010.16759.x. arXiv: 1004.0109 [astro-ph.HE].

[347] H. N. Latter, P. Lesaffre, and S. A. Balbus. "MRI channel flows and their parasites." In: *MNRAS* 394.2 (Apr. 2009), pp. 715–729. DOI: 10.1111/j.1365-2966.2009.14395.x. arXiv: 0901.4712 [astro-ph.HE].

[348] J. M. Lattimer and M. Prakash. "The Physics of Neutron Stars." In: *Science* 304.5670 (Apr. 2004), pp. 536–542. DOI: 10.1126/science.1090720. arXiv: astro-ph/0405262 [astro-ph].

[349] J. M. Lattimer and D. N. Schramm. "Black-hole-neutron-star collisions." In: *Astrophys. J. Lett.* 192 (1974), p. L145. DOI: 10.1086/181612.

[350] J. M. Lattimer. "The Nuclear Equation of State and Neutron Star Masses." In: *Annual Review of Nuclear and Particle Science* 62.1 (Nov. 2012), pp. 485–515. DOI: 10.1146/annurev-nucl-102711-095018. arXiv: 1305.3510 [nucl-th].

[351] J. M. Lattimer and M. Prakash. "Neutron star observations: Prognosis for equation of state constraints." In: *Phys. Rep.* 442.1-6 (Apr. 2007), pp. 109–165. DOI: 10.1016/j.physrep.2007.02.003. arXiv: astro-ph/0612440 [astro-ph].

[352] D. Lee. "Lattice simulations for few- and many-body systems." In: *Progress in Particle and Nuclear Physics* 63.1 (July 2009), pp. 117–154. DOI: 10.1016/j.ppnp.2008.12.001. arXiv: 0804.3501 [nucl-th].

[353] L. Lehner et al. "Intense electromagnetic outbursts from collapsing hypermassive neutron stars." In: *Phys. Rev. D* 86.10, 104035 (Nov. 2012), p. 104035. DOI: 10.1103/PhysRevD.86.104035. arXiv: 1112.2622 [astro-ph.HE].

[354] L. Lehner et al. "Unequal mass binary neutron star mergers and multimessenger signals." In: *Class. Quantum Grav.* 33.18, 184002 (Sept. 2016), p. 184002. DOI: 10.1088/0264-9381/33/18/184002. arXiv: 1603.00501 [gr-qc].

[355] A. Leonard. "Energy Cascade in Large-Eddy Simulations of Turbulent Fluid Flows." In: *Advances in Geophysics* 18 (Jan. 1975), pp. 237–248. DOI: 10.1016/S0065-2687(08)60464-1.

[356] P. Lesaffre, S. A. Balbus, and H. Latter. "A comparison of local simulations and reduced models of MRI-induced turbulence." In: *MNRAS* 396.2 (June 2009), pp. 779–787. DOI: 10.1111/j.1365-2966.2009.14798.x. arXiv: 0904.3190 [astro-ph.SR].

[357] G. Lesur and P. Y. Longaretti. "On the relevance of subcritical hydrodynamic turbulence to accretion disk transport." In: *Astron. Astrophys.* 444.1 (Dec. 2005), pp. 25–44. DOI: 10.1051/0004-6361:20053683. arXiv: astro-ph/0509541 [astro-ph].

[358] G. Lesur and P. Y. Longaretti. "Impact of dimensionless numbers on the efficiency of magnetorotational instability induced turbulent transport." In: *MNRAS* 378.4 (July 2007), pp. 1471–1480. DOI: 10.1111/j.1365-2966.2007.11888.x. arXiv: 0704.2943 [astro-ph].

[359] M. Levi. "Effective field theories of post-Newtonian gravity: a comprehensive review." In: *Reports on Progress in Physics* 83.7, 075901 (July 2020), p. 075901. DOI: 10.1088/1361-6633/ab12bc. arXiv: 1807.01699 [hep-th].

[360] L.-X. Li and B. Paczynski. "Transient events from neutron star mergers." In: *Astrophys. J. Lett.* 507 (1998), p. L59. DOI: 10.1086/311680. arXiv: astro-ph/9807272.

[361] LIGO Scientific Collaboration. *LIGO Algorithm Library - LALSuite*. free software (GPL). 2018. DOI: 10.7935/GT1W-FZ16.

[362] Y. Lim and J. W. Holt. "Neutron Star Tidal Deformabilities Constrained by Nuclear Theory and Experiment." In: *Phys. Rev. Lett.* 121.6, 062701 (Aug. 2018), p. 062701. DOI: 10.1103/PhysRevLett.121.062701. arXiv: 1803.02803 [nucl-th].

[363] Y. Lim and J. W. Holt. "Enhanced adiabatic index for hot neutron-rich matter from microscopic nuclear forces." In: (Sept. 2019). arXiv: 1909.09089 [nucl-th].

[364] G. Lioutas, A. Bauswein, and N. Stergioulas. "Frequency deviations in universal relations of isolated neutron stars and postmerger remnants." In: *Phys. Rev. D* 104.4, 043011 (Aug. 2021), p. 043011. DOI: 10.1103/PhysRevD.104.043011. arXiv: 2102.12455 [astro-ph.HE].

[365] V. M. Lipunov et al. "MASTER Optical Detection of the First LIGO/Virgo Neutron Star Binary Merger GW170817." In: *Astrophys. J. Lett.* 850.1 (2017), p. L1. DOI: 10.3847/2041-8213/aa92c0. arXiv: 1710.05461 [astro-ph.HE].

[366] T. B. Littenberg and N. J. Cornish. "Bayesian inference for spectral estimation of gravitational wave detector noise." In: *Phys. Rev. D* 91.8, 084034 (Apr. 2015), p. 084034. DOI: 10.1103/PhysRevD.91.084034. arXiv: 1410.3852 [gr-qc].

[367] X.-D. Liu, S. Osher, and T. Chan. "Weighted Essentially Non-oscillatory Schemes." In: *Journal of Computational Physics* 115.1 (Nov. 1994), pp. 200–212. DOI: 10.1006/jcph.1994.1187.

[368] Y. T. Liu et al. "General relativistic simulations of magnetized binary neutron star mergers." In: *Phys. Rev. D* 78.2, 024012 (July 2008), p. 024012. DOI: 10.1103/PhysRevD.78.024012. arXiv: 0803.4193 [astro-ph].

[369] F. Löffler et al. "The Einstein Toolkit: a community computational infrastructure for relativistic astrophysics." In: *Class. Quantum Grav.* 29.11, 115001 (June 2012), p. 115001. DOI: 10.1088/0264-9381/29/11/115001. arXiv: 1111.3344 [gr-qc].

[370] F. Löffler et al. "Stiffness effects on the dynamics of the bar-mode instability of neutron stars in full general relativity." In: *Phys. Rev. D* 91.6, 064057 (Mar. 2015), p. 064057. DOI: 10.1103/PhysRevD.91.064057. arXiv: 1411.1963 [gr-qc].

[371] P. Y. Longaretti and G. Lesur. "MRI-driven turbulent transport: the role of dissipation, channel modes and their parasites." In: *Astron. Astrophys.* 516, A51 (June 2010), A51. DOI: 10.1051/0004-6361/201014093. arXiv: 1004.1384 [astro-ph.SR].

[372] D. R. Lorimer. "Binary and Millisecond Pulsars." In: *Living Reviews in Relativity* 11.1, 8 (Nov. 2008), p. 8. DOI: 10.12942/lrr-2008-8. arXiv: 0811.0762 [astro-ph].

[373] D. Lynden-Bell and J. E. Pringle. "The evolution of viscous discs and the origin of the nebular variables." In: *MNRAS* 168 (Sept. 1974), pp. 603–637. DOI: 10.1093/mnras/168.3.603.

[374] A. G. Lyne et al. "A Double-Pulsar System: A Rare Laboratory for Relativistic Gravity and Plasma Physics." In: *Science* 303.5661 (Feb. 2004), pp. 1153–1157. DOI: 10.1126/science.1094645. arXiv: astro-ph/0401086 [astro-ph].

[375] A. I. MacFadyen and S. E. Woosley. "Collapsars: Gamma-Ray Bursts and Explosions in "Failed Supernovae"." In: *Astrophys. J.* 524.1 (Oct. 1999), pp. 262–289. DOI: 10.1086/307790. arXiv: astro-ph/9810274 [astro-ph].

[376] M. Maggiore et al. "Science case for the Einstein telescope." In: *JCAP* 2020.3, 050 (Mar. 2020), p. 050. DOI: 10.1088/1475-7516/2020/03/050. arXiv: 1912.02622 [astro-ph.CO].

[377] J. F. Mahlmann and M. A. Aloy. "Diffusivity in force-free simulations of global magnetospheres." In: *MNRAS* 509.1 (Jan. 2022), pp. 1504–1520. DOI: 10.1093/mnras/stab2830. arXiv: 2109.13936 [astro-ph.HE].

[378] F. Maione et al. "Spectral analysis of gravitational waves from binary neutron star merger remnants." In: *Phys. Rev. D* 96.6, 063011 (Sept. 2017), p. 063011. DOI: 10.1103/PhysRevD.96.063011. arXiv: 1707.03368 [gr-qc].

[379] G. R. Mamatsashvili et al. "Revisiting linear dynamics of non-axisymmetric perturbations in weakly magnetized accretion discs." In: *MNRAS* 435.3 (Nov. 2013), pp. 2552–2567. DOI: 10.1093/mnras/stt1470. arXiv: 1308.1058 [astro-ph.EP].

[380] R. A. Managan. "On the secular instability of axisymmetric rotating stars to gravitational radiation reaction." In: *Astrophys. J.* 294 (July 1985), pp. 463–473. DOI: 10.1086/163312.

[381] G. M. Manca et al. "Dynamical non-axisymmetric instabilities in rotating relativistic stars." In: *Class. Quantum Grav.* 24.12 (June 2007), S171–S186. DOI: 10.1088/0264-9381/24/12/S12. arXiv: 0705.1826 [astro-ph].

[382] R. N. Manchester and J. H. Taylor. *Pulsars*. W.H. Freeman and Company, 1977.

[383] B. Margalit et al. "Angular-momentum Transport in Proto-neutron Stars and the Fate of Neutron Star Merger Remnants." In: *Astrophys. J.* 939.1, 51 (Nov. 2022), p. 51. DOI: 10.3847/1538-4357/ac8b01. arXiv: 2206.10645 [astro-ph.HE].

[384] Y. Masada, T. Takiwaki, and K. Kotake. "Convection and Dynamo in Newly Born Neutron Stars." In: *Astrophys. J.* 924.2, 75 (Jan. 2022), p. 75. DOI: 10.3847/1538-4357/ac34f6. arXiv: 2001.08452 [astro-ph.HE].

[385] P. N. McDermott, H. M. van Horn, and C. J. Hansen. "Nonradial Oscillations of Neutron Stars." In: *Astrophys. J.* 325 (Feb. 1988), p. 725. DOI: 10.1086/166044.

[386] C. Messick et al. "Analysis framework for the prompt discovery of compact binary mergers in gravitational-wave data." In: *Phys. Rev. D* 95 (4 Feb. 2017), p. 042001. DOI: 10.1103/PhysRevD.95.042001. URL: https://link.aps.org/doi/10.1103/PhysRevD.95.042001.

[387] B. D. Metzger, A. L. Piro, and E. Quataert. "Neutron-rich freeze-out in viscously spreading accretion discs formed from compact object mergers." In: *MNRAS* 396.1 (June 2009), pp. 304–314. DOI: 10.1111/j.1365-2966.2008.14380.x. arXiv: 0810.2535 [astro-ph].

[388] B. D. Metzger et al. "Electromagnetic counterparts of compact object mergers powered by the radioactive decay of r-process nuclei." In: *MNRAS* 406.4 (Aug. 2010), pp. 2650–2662. DOI: 10.1111/j.1365-2966.2010.16864.x. arXiv: 1001.5029 [astro-ph.HE].

[389] B. D. Metzger et al. "The effects of r-process heating on fallback accretion in compact object mergers." In: *MNRAS* 402.4 (Mar. 2010), pp. 2771–2777. DOI: 10.1111/j.1365-2966.2009.16107.x. arXiv: 0908.0530 [astro-ph.HE].

[390] B. D. Metzger. "Kilonovae." In: *Living Reviews in Relativity* 23.1, 1 (Dec. 2019), p. 1. DOI: 10.1007/s41114-019-0024-0. arXiv: 1910.01617 [astro-ph.HE].

[391] B. D. Metzger and R. Fernández. "Red or blue? A potential kilonova imprint of the delay until black hole formation following a neutron star merger." In: *MNRAS* 441.4 (July 2014), pp. 3444–3453. DOI: 10.1093/mnras/stu802. arXiv: 1402.4803 [astro-ph.HE].

[392] K. O. Mikaelian. "New Mechanism for Slowing Down the Rotation of Dense Stars." In: *Astrophys. J. Lett.* 214 (May 1977), p. L23. DOI: 10.1086/182434.

[393] M. C. Miller et al. "PSR J0030+0451 Mass and Radius from NICER Data and Implications for the Properties of Neutron Star Matter." In: *Astrophys. J. Lett.* 887.1, L24 (Dec. 2019), p. L24. DOI: 10.3847/2041-8213/ab50c5. arXiv: 1912.05705 [astro-ph.HE].

[394] M. C. Miller et al. "The Radius of PSR J0740+6620 from NICER and XMM-Newton Data." In: *Astrophys. J. Lett.* 918.2, L28 (Sept. 2021), p. L28. DOI: 10.3847/2041-8213/ac089b. arXiv: 2105.06979 [astro-ph.HE].

[395] J. A. Miralles, J. A. Pons, and V. A. Urpin. "Convective Instability in Proto-Neutron Stars." In: *Astrophys. J.* 543.2 (Nov. 2000), pp. 1001–1006. DOI: 10.1086/317163. arXiv: astro-ph/0007069 [astro-ph].

[396] A. Miura and P. L. Pritchett. "Nonlocal stability analysis of the MHD Kelvin-Helmholtz instability in a compressible plasma." In: *J. Geophys. Res.* 87.A9 (Sept. 1982), pp. 7431–7444. DOI: 10.1029/JA087iA09p07431.

[397] A. Miura and T. Sato. "Shear instability: Auroral arc deformation and anomalous momentum transport." In: *J. Geophys. Res.* 83.A5 (May 1978), pp. 2109–2117. DOI: 10.1029/JA083iA05p02109.

[398] R. Moenchmeyer et al. "Gravitational waves from the collapse of rotating stellar cores." In: *Astron. Astrophys.* 246 (June 1991), pp. 417–440.

[399] C. Mondal et al. "Detectability of a phase transition in neutron star matter with third-generation gravitational wave interferometers." In: *MNRAS* 524.3 (Sept. 2023), pp. 3464–3473. DOI: 10.1093/mnras/stad2082. arXiv: 2305.05999 [astro-ph.HE].

[400] E. R. Most. "Impact of a mean field dynamo on neutron star mergers leading to magnetar remnants." In: *Phys. Rev. D* 108.12, 123012 (Dec. 2023), p. 123012. DOI: 10.1103/PhysRevD.108.123012. arXiv: 2311.03333 [astro-ph.HE].

[401] P. Mösta et al. "A large-scale dynamo and magnetoturbulence in rapidly rotating core-collapse supernovae." In: *Nature* 528.7582 (Dec. 2015), pp. 376–379. DOI: 10.1038/nature15755. arXiv: 1512.00838 [astro-ph.HE].

[402] C. D. Muhlberger et al. "Magnetic effects on the low-T /|W | instability in differentially rotating neutron stars." In: *Phys. Rev. D* 90.10, 104014 (Nov. 2014), p. 104014. DOI: 10.1103/PhysRevD.90.104014. arXiv: 1405.2144 [astro-ph.HE].

[403] W.-C. Müller and D. Carati. "Dynamic gradient-diffusion subgrid models for incompressible magnetohydrodynamic turbulence." In: *Physics of Plasmas* 9.3 (Mar. 2002), pp. 824–834. DOI: 10.1063/1.1448498.

[404] K. Murase and I. Bartos. "High-Energy Multimessenger Transient Astrophysics." In: *Ann. Rev. Nucl. Part. Sci.* 69 (2019), pp. 477–506. DOI: 10.1146/annurev-nucl-101918-023510. arXiv: 1907.12506 [astro-ph.HE].

[405] A. Murguia-Berthier et al. "The Properties of Short Gamma-Ray Burst Jets Triggered by Neutron Star Mergers." In: *Astrophys. J. Lett.* 835.2, L34 (Feb. 2017), p. L34. DOI: 10.3847/2041-8213/aa5b9e. arXiv: 1609.04828 [astro-ph.HE].

[406] G. C. Murphy and M. E. Pessah. "On the Anisotropic Nature of MRI-driven Turbulence in Astrophysical Disks." In: *Astrophys. J.* 802.2, 139 (Apr. 2015), p. 139. DOI: 10.1088/0004-637X/802/2/139. arXiv: 1410.6196 [astro-ph.SR].

[407] H. Müther and A. Polls. "Two-Body Correlations in Nuclear Systems." In: *Progress in Particle and Nuclear Physics* 45.1 (Jan. 2000), pp. 243–334. DOI: 10.1016/S0146-6410(00)00105-8. arXiv: nucl-th/0001007 [nucl-th].

[408] M. Müller and D. Scherer. "A Grid and Subgrid-Scale Radiation Parameterization of Topographic Effects for Mesoscale Weather Forecast Models." In: *Monthly Weather Review - MON WEATHER REV* 133 (June 2005), pp. 1431–1442. DOI: 10.1175/MWR2927.1.

[409] D. K. Nadezhin. "Some Secondary Indications of Gravitational Collapse." In: *Astrophysics and Space Science* 69.1 (May 1980), pp. 115–125. DOI: 10.1007/BF00638971.

[410] E. Nakar and T. Piran. "Detectable radio flares following gravitational waves from mergers of binary neutron stars." In: *Nature* 478.7367 (Oct. 2011), pp. 82–84. DOI: 10.1038/nature10365. arXiv: 1102.1020.

[411] K. Nakazato, K. Sumiyoshi, and S. Yamada. "Astrophysical implications of equation of state for hadron-quark mixed phase: Compact stars and stellar collapses." In: *Phys. Rev. D* 77.10, 103006 (May 2008), p. 103006. DOI: 10.1103/PhysRevD.77.103006. arXiv: 0804.0661 [astro-ph].

[412] Y. Nambu and G. Jona-Lasinio. "Dynamical Model of Elementary Particles Based on an Analogy with Superconductivity. I." In: *Physical Review* 122.1 (Apr. 1961), pp. 345–358. DOI: 10.1103/PhysRev.122.345.

[413] Y. Nambu and G. Jona-Lasinio. "Dynamical Model of Elementary Particles Based on an Analogy with Superconductivity. II." In: *Physical Review* 124.1 (Oct. 1961), pp. 246–254. DOI: 10.1103/PhysRev.124.246.

[414] R. Narayan, B. Paczynski, and T. Piran. "Gamma-Ray Bursts as the Death Throes of Massive Binary Stars." In: *Astrophys. J. Lett.* 395 (Aug. 1992), p. L83. DOI: 10.1086/186493. arXiv: astro-ph/9204001 [astro-ph].

[415] T. Narikawa and N. Uchikata. "Follow-up analyses of the binary-neutron-star signals GW170817 and GW190425 by using post-Newtonian waveform models." In: *Phys. Rev. D* 106.10 (2022), p. 103006. DOI: 10.1103/PhysRevD.106.103006. arXiv: 2205.06023 [gr-qc].

[416] S. Nissanke et al. "Exploring Short Gamma-ray Bursts as Gravitational-wave Standard Sirens." In: *Astrophys. J.* 725.1 (Dec. 2010), pp. 496–514. DOI: 10.1088/0004-637X/725/1/496. arXiv: 0904.1017 [astro-ph.CO].

[417] A. H. Nitz et al. "Rapid detection of gravitational waves from compact binary mergers with PyCBC Live." In: *Phys. Rev. D* 98.2 (2018), p. 024050. DOI: 10.1103/PhysRevD.98.024050. arXiv: 1805.11174 [gr-qc].

[418] A. H. Nitz et al. "4-OGC: Catalog of Gravitational Waves from Compact Binary Mergers." In: *Astrophys. J.* 946.2 (2023), p. 59. DOI: 10.3847/1538-4357/aca591. arXiv: 2112.06878 [astro-ph.HE].

[419] S. C. Noble et al. "Primitive variable solvers for conservative general relativistic magnetohydrodynamics." In: *Astrophys. J.* 641 (2006), pp. 626–637. DOI: 10.1086/500349. arXiv: astro-ph/0512420.

[420] K. Nomoto. "Accreting white dwarf models for type I supernovae. I - Presupernova evolution and triggering mechanisms." In: *Astrophys. J.* 253 (Feb. 1982), pp. 798–810. DOI: 10.1086/159682.

[421] T. Nozawa et al. "Construction of highly accurate models of rotating neutron stars - comparison of three different numerical schemes." In: *Astron. Astrophys. Suppl.* 132 (Nov. 1998), pp. 431–454. DOI: 10.1051/aas:1998304. arXiv: gr-qc/9804048 [gr-qc].

[422] M. Obergaulinger. "Astrophysical magnetohydrodynamics and radiative transfer: numerical methods and applications." PhD thesis. Max-Planck-Institute for Astrophysics, Garching, Jan. 2008.

[423] M. Obergaulinger and M. A. Aloy. "Magnetorotational core collapse of possible GRB progenitors - III. Three-dimensional models." In: *MNRAS* 503.4 (May 2021), pp. 4942–4963. DOI: 10.1093/mnras/stab295. arXiv: 2008.07205 [astro-ph.HE].

[424] M. Obergaulinger, M. A. Aloy, and E. Müller. "Axisymmetric simulations of magneto-rotational core collapse: dynamics and gravitational wave signal." In: *Astron. Astrophys.* 450.3 (May 2006), pp. 1107–1134. DOI: 10.1051/0004-6361:20054306. arXiv: astro-ph/0510184 [astro-ph].

[425] M. Obergaulinger, M. A. Aloy, and E. Müller. "Local simulations of the magnetized Kelvin-Helmholtz instability in neutron-star mergers." In: *Astron. Astrophys.* 515, A30 (June 2010), A30. DOI: 10.1051/0004-6361/200913386. arXiv: 1003.6031 [astro-ph.SR].

[426] M. Obergaulinger et al. "Axisymmetric simulations of magnetorotational core collapse: approximate inclusion of general relativistic effects." In: *Astron. Astrophys.* 457.1 (Oct. 2006), pp. 209–222. DOI: 10.1051/0004-6361:20064982. arXiv: astro-ph/0602187 [astro-ph].

[427] M. Obergaulinger et al. "Semi-global simulations of the magneto-rotational instability in core collapse supernovae." In: *Astron. Astrophys.* 498.1 (Apr. 2009), pp. 241–271. DOI: 10.1051/0004-6361/200811323. arXiv: 0811.1652 [astro-ph].

[428] R. Oechslin, H. T. Janka, and A. Marek. "Relativistic neutron star merger simulations with non-zero temperature equations of state. 1. Variation of binary parameters and equation of state." In: *Astron. Astrophys.* 467 (2007), p. 395. DOI: 10.1051/0004-6361:20066682. arXiv: astro-ph/0611047.

[429] R. Oechslin, S. Rosswog, and F.-K. Thielemann. "Conformally flat smoothed particle hydrodynamics application to neutron star mergers." In: *Phys. Rev. D* 65.10, 103005 (May 2002), p. 103005. DOI: 10.1103/PhysRevD.65.103005. arXiv: gr-qc/0111005 [gr-qc].

[430] M. Oertel, A. F. Fantina, and J. Novak. "Extended equation of state for core-collapse simulations." In: *Phys. Rev. C* 85.5, 055806 (May 2012), p. 055806. DOI: 10.1103/PhysRevC.85.055806. arXiv: 1202.2679 [nucl-th].

[431] M. Oertel et al. "Equations of state for supernovae and compact stars." In: *Reviews of Modern Physics* 89.1, 015007 (Jan. 2017), p. 015007. DOI: 10.1103/RevModPhys.89.015007. arXiv: 1610.03361 [astro-ph.HE].

[432] G. I. Ogilvie. "On the dynamics of magnetorotational turbulent stresses." In: *MNRAS* 340.3 (Apr. 2003), pp. 969–982. DOI: 10.1046/j.1365-8711.2003.06359.x. arXiv: astro-ph/0212442 [astro-ph].

[433] A. Oron. "Relativistic magnetized star with poloidal and toroidal fields." In: *Phys. Rev. D* 66.2, 023006 (July 2002), p. 023006. DOI: 10.1103/PhysRevD.66.023006.

[434] C. D. Ott et al. "One-armed Spiral Instability in a Low-T/|W| Postbounce Supernova Core." In: *Astrophys. J. Lett.* 625.2 (June 2005), pp. L119–L122. DOI: 10.1086/431305. arXiv: astro-ph/0503187 [astro-ph].

[435] S. Ou and J. E. Tohline. "Unexpected Dynamical Instabilities in Differentially Rotating Neutron Stars." In: *Astrophys. J.* 651.2 (Nov. 2006), pp. 1068–1078. DOI: 10.1086/507597. arXiv: astro-ph/0604099 [astro-ph].

[436] C. Palenzuela. "Modelling magnetized neutron stars using resistive magnetohydrodynamics." In: *MNRAS* 431.2 (May 2013), pp. 1853–1865. DOI: 10.1093/mnras/stt311. arXiv: 1212.0130 [astro-ph.HE].

[437] C. Palenzuela et al. "Beyond ideal MHD: towards a more realistic modelling of relativistic astrophysical plasmas." In: *MNRAS* 394.4 (Apr. 2009), pp. 1727–1740. DOI: 10.1111/j.1365-2966.2009.14454.x. arXiv: 0810.1838 [astro-ph].

[438] C. Palenzuela et al. "Electromagnetic and Gravitational Outputs from Binary-Neutron-Star Coalescence." In: *Phys. Rev. Lett.* 111.6, 061105 (Aug. 2013), p. 061105. DOI: 10.1103/PhysRevLett.111.061105. arXiv: 1301.7074 [gr-qc].

[439] C. Palenzuela et al. "Effects of the microphysical equation of state in the mergers of magnetized neutron stars with neutrino cooling." In: *Phys. Rev. D* 92.4, 044045 (Aug. 2015), p. 044045. DOI: 10.1103/PhysRevD.92.044045. arXiv: 1505.01607 [gr-qc].

[440] C. Palenzuela et al. "Turbulent magnetic field amplification in binary neutron star mergers." In: *Phys. Rev. D* 106.2, 023013 (July 2022), p. 023013. DOI: 10.1103/PhysRevD.106.023013. arXiv: 2112.08413 [gr-qc].

[441] Y. Pan et al. "Inspiral-merger-ringdown waveforms of spinning, precessing black-hole binaries in the effective-one-body formalism." In: *Phys. Rev. D* 89.8, 084006 (Apr. 2014), p. 084006. DOI: 10.1103/PhysRevD.89.084006. arXiv: 1307.6232 [gr-qc].

[442] J. Papaloizou and J. E. Pringle. "Gravitational radiation and the stability of rotating stars." In: *MNRAS* 184 (Aug. 1978), pp. 501–508. DOI: 10.1093/mnras/184.3.501.

[443] E. N. Parker. "Hydromagnetic Dynamo Models." In: *Astrophys. J.* 122 (Sept. 1955), p. 293. DOI: 10.1086/146087.

[444] V. Paschalidis. "General relativistic simulations of compact binary mergers as engines for short gamma-ray bursts." In: *Class. Quantum Grav.* 34.8, 084002 (Apr. 2017), p. 084002. DOI: 10.1088/1361-6382/aa61ce. arXiv: 1611.01519 [astro-ph.HE].

[445] V. Paschalidis and S. L. Shapiro. "A new scheme for matching general relativistic ideal magnetohydrodynamics to its force-free limit." In: *Phys. Rev. D* 88.10, 104031 (Nov. 2013), p. 104031. DOI: 10.1103/PhysRevD.88.104031. arXiv: 1310.3274 [astro-ph.HE].

[446] V. Paschalidis et al. "One-arm spiral instability in hypermassive neutron stars formed by dynamical-capture binary neutron star mergers." In: *Phys. Rev. D* 92.12, 121502 (Dec. 2015), p. 121502. DOI: 10.1103/PhysRevD.92.121502. arXiv: 1510.03432 [astro-ph.HE].

[447] A. Passamonti and N. Andersson. "The intimate relation between the low T/W instability and the corotation point." In: *MNRAS* 446.1 (Jan. 2015), pp. 555–565. DOI: 10.1093/mnras/stu2062. arXiv: 1409.0677 [astro-ph.SR].

[448] F. Pedregosa et al. "Scikit-learn: Machine Learning in Python." In: *J. Machine Learning Res.* 12 (2011), pp. 2825–2830. arXiv: 1201.0490 [cs.LG].

[449] B. Peres, M. Oertel, and J. Novak. "Influence of pions and hyperons on stellar black hole formation." In: *Phys. Rev. D* 87.4, 043006 (Feb. 2013), p. 043006. DOI: 10.1103/PhysRevD.87.043006. arXiv: 1210.7435 [astro-ph.HE].

[450] M. E. Pessah. "Angular Momentum Transport in Protoplanetary and Black Hole Accretion Disks: The Role of Parasitic Modes in the Saturation of MHD Turbulence." In: *Astrophys. J.* 716.2 (June 2010), pp. 1012–1027. DOI: 10.1088/0004-637X/716/2/1012. arXiv: 0908.1791 [astro-ph.HE].

[451] M. E. Pessah and C.-k. Chan. "Viscous, Resistive Magnetorotational Modes." In: *Astrophys. J.* 684.1 (Sept. 2008), pp. 498–514. DOI: 10.1086/589915. arXiv: 0801.4570 [astro-ph].

[452] M. E. Pessah, C.-K. Chan, and D. Psaltis. "Local Model for Angular-Momentum Transport in Accretion Disks Driven by the Magnetorotational Instability." In: *Phys. Rev. Lett.* 97.22, 221103 (Dec. 2006), p. 221103. DOI: 10.1103/PhysRevLett.97.221103. arXiv: astro-ph/0610565 [astro-ph].

[453] M. E. Pessah, C.-K. Chan, and D. Psaltis. "The signature of the magnetorotational instability in the Reynolds and Maxwell stress tensors in accretion discs." In: *MNRAS* 372.1 (Oct. 2006), pp. 183–190. DOI: 10.1111/j.1365-2966.2006.10824.x. arXiv: astro-ph/0603178 [astro-ph].

[454] M. E. Pessah, C.-k. Chan, and D. Psaltis. "Angular Momentum Transport in Accretion Disks: Scaling Laws in MRI-driven Turbulence." In: *Astrophys. J. Lett.* 668.1 (Oct. 2007), pp. L51–L54. DOI: 10.1086/522585. arXiv: 0705.0352 [astro-ph].

[455] M. E. Pessah and J. Goodman. "On the Saturation of the Magnetorotational Instability Via Parasitic Modes." In: *Astrophys. J. Lett.* 698.1 (June 2009), pp. L72–L76. DOI: 10.1088/0004-637X/698/1/L72. arXiv: 0902.0794 [astro-ph.HE].

[456] J. Pétri. "General-relativistic force-free pulsar magnetospheres." In: *MNRAS* 455.4 (Feb. 2016), pp. 3779–3805. DOI: 10.1093/mnras/stv2613. arXiv: 1511.01337 [astro-ph.HE].

[457] C. Pilgrim. "piecewise-regression (aka segmented regression) in Python." In: *The Journal of Open Source Software* 6.68, 3859 (Dec. 2021), p. 3859. DOI: 10.21105/joss.03859.

[458] A. Piórkowska-Kurpas and M. Biesiada. "Testing Quantum Gravity in the Multi-Messenger Astronomy Era." In: *Universe* 8.6 (2022), p. 321. DOI: 10.3390/universe8060321.

[459] T. Piran. "The physics of gamma-ray bursts." In: *Reviews of Modern Physics* 76.4 (Oct. 2004), pp. 1143–1210. DOI: 10.1103/RevModPhys.76.1143. arXiv: astro-ph/0405503 [astro-ph].

[460] A. L. Piro, B. Giacomazzo, and R. Perna. "The Fate of Neutron Star Binary Mergers." In: *Astrophys. J. Lett.* 844.2, L19 (Aug. 2017), p. L19. DOI: 10.3847/2041-8213/aa7f2f. arXiv: 1704.08697 [astro-ph.HE].

[461] J. A. Pons and U. Geppert. "Magnetic field dissipation in neutron star crusts: from magnetars to isolated neutron stars." In: *Astron. Astrophys.* 470.1 (July 2007), pp. 303–315. DOI: 10.1051/0004-6361:20077456. arXiv: astro-ph/0703267 [astro-ph].

[462] J. A. Pons et al. "Evolution of Proto-Neutron Stars." In: *Astrophys. J.* 513.2 (Mar. 1999), pp. 780–804. DOI: 10.1086/306889. arXiv: astro-ph/9807040 [astro-ph].

[463] J. A. Pons et al. "Toward a Mass and Radius Determination of the Nearby Isolated Neutron Star RX J185635-3754." In: *Astrophys. J.* 564.2 (Jan. 2002), pp. 981–1006. DOI: 10.1086/324296. arXiv: astro-ph/0107404 [astro-ph].

[464] A. Y. Potekhin. "Atmospheres and radiating surfaces of neutron stars." In: *Physics Uspekhi* 57.8, 735-770 (Aug. 2014), pp. 735–770. DOI: 10.3367/UFNe.0184.201408a.0793. arXiv: 1403.0074 [astro-ph.SR].

[465] J. Poutanen et al. "The effect of accretion on the measurement of neutron star mass and radius in the low-mass X-ray binary 4U 1608-52." In: *MNRAS* 442.4 (Aug. 2014), pp. 3777–3790. DOI: 10.1093/mnras/stu1139. arXiv: 1405.2663 [astro-ph.HE].

[466] J. Powell et al. "Three dimensional magnetorotational core-collapse supernova explosions of a 39 solar mass progenitor star." In: *MNRAS* 522.4 (July 2023), pp. 6070–6086. DOI: 10.1093/mnras/stad1292. arXiv: 2212.00200 [astro-ph.HE].

[467] M. Prakash et al. "Composition and structure of protoneutron stars." In: *Phys. Rep.* 280 (Jan. 1997), pp. 1–77. DOI: 10.1016/S0370-1573(96)00023-3. arXiv: nucl-th/9603042 [nucl-th].

[468] M. Punturo et al. "The Einstein Telescope: a third-generation gravitational wave observatory." In: *Class. Quantum Grav.* 27.19, 194002 (Oct. 2010), p. 194002. DOI: 10.1088/0264-9381/27/19/194002.

[469] D. Radice. "General-relativistic Large-eddy Simulations of Binary Neutron Star Mergers." In: *Astrophys. J. Lett.* 838.1, L2 (Mar. 2017), p. L2. DOI: 10.3847/2041-8213/aa6483. arXiv: 1703.02046 [astro-ph.HE].

[470] D. Radice. "Binary Neutron Star Merger Simulations with a Calibrated Turbulence Model." In: *Symmetry* 12.8 (July 2020), p. 1249. DOI: 10.3390/sym12081249. arXiv: 2005.09002 [astro-ph.HE].

[471] D. Radice, S. Bernuzzi, and C. D. Ott. "One-armed spiral instability in neutron star mergers and its detectability in gravitational waves." In: *Phys. Rev. D* 94.6, 064011 (Sept. 2016), p. 064011. DOI: 10.1103/PhysRevD.94.064011. arXiv: 1603.05726 [gr-qc].

[472] D. Radice and I. Hawke. "Turbulence modelling in neutron star merger simulations." In: *Living Reviews in Computational Astrophysics* 10.1, 1 (Feb. 2024), p. 1. DOI: 10.1007/s41115-023-00019-9. arXiv: 2402.03224 [astro-ph.HE].

[473] D. Radice et al. "Dynamical mass ejection from binary neutron star mergers." In: *MNRAS* 460.3 (Aug. 2016), pp. 3255–3271. DOI: 10.1093/mnras/stw1227. arXiv: 1601.02426 [astro-ph.HE].

[474] D. Radice et al. "Binary Neutron Star Mergers: Mass Ejection, Electromagnetic Counterparts, and Nucleosynthesis." In: *Astrophys. J.* 869.2, 130 (Dec. 2018), p. 130. DOI: 10.3847/1538-4357/aaf054. arXiv: 1809.11161 [astro-ph.HE].

[475] D. Radice et al. "A new moment-based general-relativistic neutrino-radiation transport code: Methods and first applications to neutron star mergers." In: *Mon. Not. Roy. Astron. Soc.* 512.1 (2022), pp. 1499–1521. DOI: 10.1093/mnras/stac589. arXiv: 2111.14858 [astro-ph.HE].

[476] C. Raithel, V. Paschalidis, and F. Özel. "Realistic finite-temperature effects in neutron star merger simulations." In: *Phys. Rev. D* 104.6 (2021), p. 063016. DOI: 10.1103/PhysRevD.104.063016. arXiv: 2104.07226 [astro-ph.HE].

[477] C. A. Raithel, F. Özel, and D. Psaltis. "Tidal Deformability from GW170817 as a Direct Probe of the Neutron Star Radius." In: *Astrophys. J. Lett.* 857.2, L23 (Apr. 2018), p. L23. DOI: 10.3847/2041-8213/aabcbf. arXiv: 1803.07687 [astro-ph.HE].

[478] C. A. Raithel and V. Paschalidis. "Detectability of Finite-Temperature Effects From Neutron Star Mergers with Next-Generation Gravitational Wave Detectors." In: *arXiv e-prints* (Dec. 2023), arXiv:2312.14046. DOI: 10.48550/arXiv.2312.14046. arXiv: 2312.14046 [astro-ph.HE].

[479] V. Ravi and P. D. Lasky. "The birth of black holes: neutron star collapse times, gamma-ray bursts and fast radio bursts." In: *MNRAS* 441.3 (July 2014), pp. 2433–2439. DOI: 10.1093/mnras/stu720. arXiv: 1403.6327 [astro-ph.HE].

[480] R. Raynaud et al. "Magnetar formation through a convective dynamo in protoneutron stars." In: *Science Advances* 6.11 (Mar. 2020), eaay2732. DOI: 10.1126/sciadv.aay2732. arXiv: 2003.06662 [astro-ph.HE].

[481] J. S. Read et al. "Constraints on a phenomenologically parameterized neutron-star equation of state." In: *Phys. Rev.* D79 (2009), p. 124032. DOI: 10.1103/PhysRevD.79.124032.

[482] J. S. Read et al. "Measuring the neutron star equation of state with gravitational wave observations." In: *Phys. Rev. D* 79.12, 124033 (June 2009), p. 124033. DOI: 10.1103/PhysRevD.79.124033. arXiv: 0901.3258 [gr-qc].

[483] J. S. Read et al. "Matter effects on binary neutron star waveforms." In: *Phys. Rev. D* 88.4, 044042 (Aug. 2013), p. 044042. DOI: 10.1103/PhysRevD.88.044042. arXiv: 1306.4065 [gr-qc].

[484] A. Reboul-Salze et al. "A global model of the magnetorotational instability in protoneutron stars." In: *Astron. Astrophys.* 645, A109 (Jan. 2021), A109. DOI: 10.1051/0004-6361/202038369. arXiv: 2005.03567 [astro-ph.HE].

[485] A. Reboul-Salze et al. "MRI-driven $\alpha\Omega$ dynamos in protoneutron stars." In: *Astron. Astrophys.* 667, A94 (Nov. 2022), A94. DOI: 10.1051/0004-6361/202142368. arXiv: 2111.02148 [astro-ph.HE].

[486] T. Regimbau and J. A. de Freitas Pacheco. "Population synthesis of pulsars: Magnetic field effects." In: *Astron. Astrophys.* 374 (July 2001), pp. 182–188. DOI: 10.1051/0004-6361:20010710. arXiv: astro-ph/0105254 [astro-ph].

[487] T. Rembiasz et al. "On the maximum magnetic field amplification by the magnetorotational instability in core-collapse supernovae." In: *MNRAS* 460.3 (Aug. 2016), pp. 3316–3334. DOI: 10.1093/mnras/stw1201. arXiv: 1603.00466 [astro-ph.SR].

[488] T. Rembiasz et al. "Termination of the magnetorotational instability via parasitic instabilities in core-collapse supernovae." In: *MNRAS* 456.4 (Mar. 2016), pp. 3782–3802. DOI: 10.1093/mnras/stv2917. arXiv: 1508.04799 [astro-ph.SR].

[489] T. Rembiasz et al. "Termination of the MRI via parasitic instabilities in core-collapse supernovae: influence of numerical methods." In: *Journal of Physics Conference Series*. Vol. 719. Journal of Physics Conference Series. May 2016, 012009, p. 012009. DOI: 10.1088/1742-6596/719/1/012009. arXiv: 1605.05200 [astro-ph.SR].

[490] L. Rezzolla and K. Takami. "Gravitational-wave signal from binary neutron stars: A systematic analysis of the spectral properties." In: *Phys. Rev. D* 93.12, 124051 (June 2016), p. 124051. DOI: 10.1103/PhysRevD.93.124051. arXiv: 1604.00246 [gr-qc].

[491] L. Rezzolla et al. "Accurate evolutions of unequal-mass neutron-star binaries: properties of the torus and short GRB engines." In: *Class. Quantum Grav.* 27.11, 114105 (June 2010), p. 114105. DOI: 10.1088/0264-9381/27/11/114105. arXiv: 1001.3074 [gr-qc].

[492] L. Rezzolla et al. "The Missing Link: Merging Neutron Stars Naturally Produce Jet-like Structures and Can Power Short Gamma-ray Bursts." In: *Astrophys. J. Lett.* 732.1, L6 (May 2011), p. L6. DOI: 10.1088/2041-8205/732/1/L6. arXiv: 1101.4298 [astro-ph.HE].

[493] T. E. Riley et al. "A NICER View of PSR J0030+0451: Millisecond Pulsar Parameter Estimation." In: *Astrophys. J. Lett.* 887.1, L21 (Dec. 2019), p. L21. DOI: 10.3847/2041-8213/ab481c. arXiv: 1912.05702 [astro-ph.HE].

[494] T. E. Riley et al. "A NICER View of the Massive Pulsar PSR J0740+6620 Informed by Radio Timing and XMM-Newton Spectroscopy." In: *Astrophys. J. Lett.* 918.2, L27 (Sept. 2021), p. L27. DOI: 10.3847/2041-8213/ac0a81. arXiv: 2105.06980 [astro-ph.HE].

[495] G. Rivieccio et al. "Gravitational-wave imprints of nonconvex dynamics in binary neutron star mergers." In: *Phys. Rev. D* 109.6, 064032 (Mar. 2024), p. 064032. DOI: 10.1103/PhysRevD.109.064032. arXiv: 2401.06849 [astro-ph.HE].

[496] L. F. Roberts et al. "The influence of neutrinos on r-process nucleosynthesis in the ejecta of black hole-neutron star mergers." In: *MNRAS* 464.4 (Feb. 2017), pp. 3907–3919. DOI: 10.1093/mnras/stw2622. arXiv: 1601.07942 [astro-ph.HE].

[497] S. Rosswog. "The dynamic ejecta of compact object mergers and eccentric collisions." In: *Philosophical Transactions of the Royal Society of London Series A* 371.1992 (Apr. 2013), pp. 20120272–20120272. DOI: 10.1098/rsta.2012.0272. arXiv: 1210.6549 [astro-ph.HE].

[498] M. Ruffert, H. T. Janka, and G. Schaefer. "Coalescing neutron stars - a step towards physical models. I. Hydrodynamic evolution and gravitational-wave emission." In: *Astron. Astrophys.* 311 (July 1996), pp. 532–566. DOI: 10.48550/arXiv.astro-ph/9509006. arXiv: astro-ph/9509006 [astro-ph].

[499] M. Ruffert et al. "Coalescing neutron stars - a step towards physical models. II. Neutrino emission, neutron tori, and gamma-ray bursts." In: *Astron. Astrophys.* 319 (Mar. 1997), pp. 122–153. DOI: 10.48550/arXiv.astro-ph/9606181. arXiv: astro-ph/9606181 [astro-ph].

[500] M. Ruiz, V. Paschalidis, and S. L. Shapiro. "Pulsar spin-down luminosity: Simulations in general relativity." In: *Phys. Rev. D* 89.8, 084045 (Apr. 2014), p. 084045. DOI: 10.1103/PhysRevD.89.084045. arXiv: 1402.5412 [astro-ph.HE].

[501] M. Ruiz and S. L. Shapiro. "General relativistic magnetohydrodynamics simulations of prompt-collapse neutron star mergers: The absence of jets." In: *Phys. Rev. D* 96.8 (2017), p. 084063. DOI: 10.1103/PhysRevD.96.084063. arXiv: 1709.00414 [astro-ph.HE].

[502] M. Ruiz, S. L. Shapiro, and A. Tsokaros. "Multimessenger Binary Mergers Containing Neutron Stars: Gravitational Waves, Jets, and γ-Ray Bursts." In: *Frontiers in Astronomy and Space Sciences* 8, 39 (Apr. 2021), p. 39. DOI: 10.3389/fspas.2021.656907. arXiv: 2102.03366 [astro-ph.HE].

[503] M. Ruiz, A. Tsokaros, and S. L. Shapiro. "Jet launching from merging magnetized binary neutron stars with realistic equations of state." In: *Phys. Rev. D* 104.12 (2021), p. 124049. DOI: 10.1103/PhysRevD.104.124049. arXiv: 2110.11968 [astro-ph.HE].

[504] M. Ruiz et al. "Binary Neutron Star Mergers: A Jet Engine for Short Gamma-Ray Bursts." In: *Astrophys. J. Lett.* 824.1, L6 (June 2016), p. L6. DOI: 10.3847/2041-8205/824/1/L6. arXiv: 1604.02455 [astro-ph.HE].

[505] D. Ryu, T. W. Jones, and A. Frank. "The Magnetohydrodynamic Kelvin-Helmholtz Instability: A Three-dimensional Study of Nonlinear Evolution." In: *Astrophys. J.* 545.1 (Dec. 2000), pp. 475–493. DOI: 10.1086/317789. arXiv: astro-ph/0008084 [astro-ph].

[506] S. Sachdev et al. "The GstLAL Search Analysis Methods for Compact Binary Mergers in Advanced LIGO's Second and Advanced Virgo's First Observing Runs." In: (Jan. 2019). arXiv: 1901.08580 [gr-qc].

[507] S. Sachdev et al. "An Early-warning System for Electromagnetic Follow-up of Gravitational-wave Events." In: *Astrophys. J. Lett.* 905.2 (2020), p. L25. DOI: 10.3847/2041-8213/abc753. arXiv: 2008.04288 [astro-ph.HE].

[508] I. Sagert et al. "Signals of the QCD Phase Transition in Core-Collapse Supernovae." In: *Phys. Rev. Lett.* 102.8, 081101 (Feb. 2009), p. 081101. DOI: 10.1103/PhysRevLett.102.081101. arXiv: 0809.4225 [astro-ph].

[509] M. Saijo and S. Yoshida. "Low T/|W| dynamical instability in differentially rotating stars: diagnosis with canonical angular momentum." In: *MNRAS* 368.3 (May 2006), pp. 1429–1442. DOI: 10.1111/j.1365-2966.2006.10229.x. arXiv: astro-ph/0505543 [astro-ph].

[510] M. Saijo et al. "Dynamical Bar Instability in Rotating Stars: Effect of General Relativity." In: *Astrophys. J.* 548.2 (Feb. 2001), pp. 919–931. DOI: 10.1086/319016. arXiv: astro-ph/0010201 [astro-ph].

[511] T. Sano and S.-i. Inutsuka. "Saturation and Thermalization of the Magnetorotational Instability: Recurrent Channel Flows and Reconnections." In: *Astrophys. J. Lett.* 561.2 (Nov. 2001), pp. L179–L182. DOI: 10.1086/324763. arXiv: astro-ph/0110125 [astro-ph].

[512] T. Sano et al. "Angular Momentum Transport by Magnetohydrodynamic Turbulence in Accretion Disks: Gas Pressure Dependence of the Saturation Level of the Magnetorotational Instability." In: *Astrophys. J.* 605.1 (Apr. 2004), pp. 321–339. DOI: 10.1086/382184. arXiv: astro-ph/0312480 [astro-ph].

[513] N. Sarin and P. D. Lasky. "The evolution of binary neutron star post-merger remnants: a review." In: *General Relativity and Gravitation* 53.6, 59 (June 2021), p. 59. DOI: 10.1007/s10714-021-02831-1. arXiv: 2012.08172 [astro-ph.HE].

[514] V. Savchenko et al. "INTEGRAL Detection of the First Prompt Gamma-Ray Signal Coincident with the Gravitational-wave Event GW170817." In: *Astrophys. J. Lett.* 848.2, L15 (Oct. 2017), p. L15. DOI: 10.3847/2041-8213/aa8f94. arXiv: 1710.05449 [astro-ph.HE].

[515] C. Schaab and M. K. Weigel. "Quasi-periodic oscillations in low-mass X-ray binaries and constraints on the equation of state of neutron star matter." In: *MNRAS* 308.3 (Sept. 1999), pp. 718–730. DOI: 10.1046/j.1365-8711.1999.02743.x. arXiv: astro-ph/9904211 [astro-ph].

[516] G. Schäfer and P. Jaranowski. "Hamiltonian formulation of general relativity and post-Newtonian dynamics of compact binaries." In: *Living Reviews in Relativity* 21.1, 7 (Aug. 2018), p. 7. DOI: 10.1007/s41114-018-0016-5. arXiv: 1805.07240 [gr-qc].

[517] M. B. Schäfer et al. "First machine learning gravitational-wave search mock data challenge." In: *Phys. Rev. D* 107.2, 023021 (Jan. 2023), p. 023021. DOI: 10.1103/PhysRevD.107.023021. arXiv: 2209.11146 [astro-ph.IM].

[518] P. Schmidt. "Gravitational Waves From Binary Black Hole Mergers: Modeling and Observations." In: *Front. Astron. Space Sci.* 7 (2020), p. 28. DOI: 10.3389/fspas.2020.00028.

[519] A. S. Schneider, L. F. Roberts, and C. D. Ott. "Open-source nuclear equation of state framework based on the liquid-drop model with Skyrme interaction." In: *Phys. Rev. C* 96.6 (2017), p. 065802. DOI: 10.1103/PhysRevC.96.065802. arXiv: 1707.01527 [astro-ph.HE].

[520] B. F. Schutz. "Determining the Hubble constant from gravitational wave observations." In: *Nature* 323.6086 (Sept. 1986), pp. 310–311. DOI: 10.1038/323310a0.

[521] Y. Sekiguchi et al. "Gravitational waves and neutrino emission from the merger of binary neutron stars." In: *Phys. Rev. Lett.* 107 (2011), p. 051102. DOI: 10.1103/PhysRevLett.107.051102. arXiv: 1105.2125 [gr-qc].

[522] Y. Sekiguchi et al. "Dynamical mass ejection from the merger of asymmetric binary neutron stars: Radiation-hydrodynamics study in general relativity." In: *Phys. Rev. D* 93.12, 124046 (June 2016), p. 124046. DOI: 10.1103/PhysRevD.93.124046. arXiv: 1603.01918 [astro-ph.HE].

[523] P. A. Seoane et al. "Astrophysics with the Laser Interferometer Space Antenna." In: *Living Rev. Rel.* 26.1 (2023), p. 2. DOI: 10.1007/s41114-022-00041-y. arXiv: 2203.06016 [gr-qc].

[524] S. Setiawan, M. Ruffert, and H. T. Janka. "Three-dimensional simulations of non-stationary accretion by remnant black holes of compact object mergers." In: *Astron. Astrophys.* 458.2 (Nov. 2006), pp. 553–567. DOI: 10.1051/0004-6361:20054193. arXiv: astro-ph/0509300 [astro-ph].

[525] N. I. Shakura and R. A. Sunyaev. "Black holes in binary systems. Observational appearance." In: *Astron. Astrophys.* 24 (Jan. 1973), pp. 337–355.

[526] I. I. Shapiro. "Fourth Test of General Relativity." In: *Phys. Rev. Lett.* 13.26 (Dec. 1964), pp. 789–791. DOI: 10.1103/PhysRevLett.13.789.

[527] S. L. Shapiro and S. Zane. "Bar Mode Instability in Relativistic Rotating Stars: A Post-Newtonian Treatment." In: *Astrophys. J. Suppl. Ser.* 117.2 (Aug. 1998), pp. 531–561. DOI: 10.1086/313124. arXiv: gr-qc/9711050 [gr-qc].

[528] H. Shen et al. "Relativistic Equation of State for Core-Collapse Supernova Simulations." In: *Astrophys. J. Suppl.* 197 (2011), p. 20. DOI: 10.1088/0067-0049/197/2/20. arXiv: 1105.1666 [astro-ph.HE].

[529] S. Shibagaki et al. "A new gravitational-wave signature of low-T/|W| instability in rapidly rotating stellar core collapse." In: *MNRAS* 493.1 (Mar. 2020), pp. L138–L142. DOI: 10.1093/mnrasl/slaa021. arXiv: 1909.09730 [astro-ph.HE].

[530] M. Shibata et al. "Truncated Moment Formalism for Radiation Hydrodynamics in Numerical Relativity." In: *Progress of Theoretical Physics* 125.6 (June 2011), pp. 1255–1287. DOI: 10.1143/PTP.125.1255. arXiv: 1104.3937 [astro-ph.HE].

[531] M. Shibata. "Constraining Nuclear Equations of State Using Gravitational Waves from Hypermassive Neutron Stars." In: *Phys. Rev. Lett.* 94.20, 201101 (May 2005), p. 201101. DOI: 10.1103/PhysRevLett.94.201101. arXiv: gr-qc/0504082 [gr-qc].

[532] M. Shibata, T. W. Baumgarte, and S. L. Shapiro. "The Bar-Mode Instability in Differentially Rotating Neutron Stars: Simulations in Full General Relativity." In: *Astrophys. J.* 542.1 (Oct. 2000), pp. 453–463. DOI: 10.1086/309525. arXiv: astro-ph/0005378 [astro-ph].

[533] M. Shibata, S. Fujibayashi, and Y. Sekiguchi. "Long-term evolution of neutron-star merger remnants in general relativistic resistive magnetohydrodynamics with a mean-field dynamo term." In: *Phys. Rev. D* 104.6, 063026 (Sept. 2021), p. 063026. DOI: 10.1103/PhysRevD.104.063026. arXiv: 2109.08732 [astro-ph.HE].

[534] M. Shibata and K. Hotokezaka. "Merger and Mass Ejection of Neutron Star Binaries." In: *Annual Review of Nuclear and Particle Science* 69 (Oct. 2019), pp. 41–64. DOI: 10.1146/annurev-nucl-101918-023625. arXiv: 1908.02350 [astro-ph.HE].

[535] M. Shibata, K. Kiuchi, and Y.-i. Sekiguchi. "General relativistic viscous hydrodynamics of differentially rotating neutron stars." In: *Phys. Rev. D* 95.8, 083005 (Apr. 2017), p. 083005. DOI: 10.1103/PhysRevD.95.083005. arXiv: 1703.10303 [astro-ph.HE].

[536] M. Shibata and T. Nakamura. "Evolution of three-dimensional gravitational waves: Harmonic slicing case." In: *Phys. Rev. D* 52.10 (Nov. 1995), pp. 5428–5444. DOI: 10.1103/PhysRevD.52.5428.

[537] M. Shibata and Y.-i. Sekiguchi. "Three-dimensional simulations of stellar core collapse in full general relativity: Nonaxisymmetric dynamical instabilities." In: *Phys. Rev. D* 71.2, 024014 (Jan. 2005), p. 024014. DOI: 10.1103/PhysRevD.71.024014. arXiv: astro-ph/0412243 [astro-ph].

[538] M. Shibata and K. Taniguchi. "Coalescence of Black Hole-Neutron Star Binaries." In: *Living Reviews in Relativity* 14.1, 6 (Dec. 2011), p. 6. DOI: 10.12942/lrr-2011-6.

[539] M. Shibata, K. Taniguchi, and K. Uryū. "Merger of binary neutron stars with realistic equations of state in full general relativity." In: *Phys. Rev. D* 71 (2005), p. 084021. DOI: 10.1103/PhysRevD.71.084021. arXiv: gr-qc/0503119.

[540] M. Shibata and K. Uryū. "Simulation of merging binary neutron stars in full general relativity: Γ=2 case." In: *Phys. Rev. D* 61.6, 064001 (Mar. 2000), p. 064001. DOI: 10.1103/PhysRevD.61.064001. arXiv: gr-qc/9911058 [gr-qc].

[541] M. Shibata et al. "Magnetized Hypermassive Neutron-Star Collapse: A Central Engine for Short Gamma-Ray Bursts." In: *Phys. Rev. Lett.* 96.3, 031102 (Jan. 2006), p. 031102. DOI: 10.1103/PhysRevLett.96.031102. arXiv: astro-ph/0511142 [astro-ph].

[542] C.-W. Shu and S. Osher. "Efficient Implementation of Essentially Non-oscillatory Shock-Capturing Schemes." In: *Journal of Computational Physics* 77.2 (Aug. 1988), pp. 439–471. DOI: 10.1016/0021-9991(88)90177-5.

[543] D. M. Siegel et al. "Magnetorotational instability in relativistic hypermassive neutron stars." In: *Phys. Rev. D* 87 (12 June 2013), p. 121302. DOI: 10.1103/PhysRevD.87.121302. URL: https://link.aps.org/doi/10.1103/PhysRevD.87.121302.

[544] J. B. Simon, J. F. Hawley, and K. Beckwith. "Simulations of Magnetorotational Turbulence with a Higher-Order Godunov Scheme." In: *Astrophys. J.* 690.1 (Jan. 2009), pp. 974–997. DOI: 10.1088/0004-637X/690/1/974. arXiv: 0806.3969 [astro-ph].

[545] D. Skinner and L. Lindblom. "On the Viscosity-driven Secular Instability in Rotating Neutron Stars." In: *Astrophys. J.* 461 (Apr. 1996), p. 920. DOI: 10.1086/177113.

[546] J. Smagorinsky. "General Circulation Experiments with the Primitive Equations." In: *Monthly Weather Review* 91.3 (Jan. 1963), p. 99. DOI: 10.1175/1520-0493(1963)091<0099:GCEWTP>2.3.CO;2.

[547] A. F. M. Smith and D. J. Spiegelhalter. "Bayes Factors and Choice Criteria for Linear Models." In: *Journal of the Royal Statistical Society: Series B (Methodological)* 42.2 (1980), pp. 213–220. DOI: https://doi.org/10.1111/j.2517-6161.1980.tb01122.x. eprint: https://rss.onlinelibrary.wiley.com/doi/pdf/10.1111/j.2517-6161.1980.tb01122.x. URL: https://rss.onlinelibrary.wiley.com/doi/abs/10.1111/j.2517-6161.1980.tb01122.x.

[548] M. Soares-Santos et al. "The Electromagnetic Counterpart of the Binary Neutron Star Merger LIGO/Virgo GW170817. I. Discovery of the Optical Counterpart Using the Dark Energy Camera." In: *Astrophys. J. Lett.* 848.2 (2017), p. L16. DOI: 10.3847/2041-8213/aa9059. arXiv: 1710.05459 [astro-ph.HE].

[549] K. A. Sorathia, C. S. Reynolds, and P. J. Armitage. "Connections Between Local and Global Turbulence in Accretion Disks." In: *Astrophys. J.* 712.2 (Apr. 2010), pp. 1241–1247. DOI: 10.1088/0004-637X/712/2/1241. arXiv: 1002.3611 [astro-ph.HE].

[550] K. A. Sorathia et al. "Global Simulations of Accretion Disks. I. Convergence and Comparisons with Local Models." In: *Astrophys. J.* 749.2, 189 (Apr. 2012), p. 189. DOI: 10.1088/0004-637X/749/2/189. arXiv: 1106.4019 [astro-ph.HE].

[551] T. Soultanis, A. Bauswein, and N. Stergioulas. "Analytic models of the spectral properties of gravitational waves from neutron star merger remnants." In: *Phys. Rev. D* 105.4, 043020 (Feb. 2022), p. 043020. DOI: 10.1103/PhysRevD.105.043020. arXiv: 2111.08353 [astro-ph.HE].

[552] A. Spitkovsky. "Time-dependent Force-free Pulsar Magnetospheres: Axisymmetric and Oblique Rotators." In: *Astrophys. J. Lett.* 648.1 (Sept. 2006), pp. L51–L54. DOI: 10.1086/507518. arXiv: astro-ph/0603147 [astro-ph].

[553] L. Spitzer. *Physical processes in the interstellar medium.* 1978. DOI: 10.1002/9783527617722.

[554] H. C. Spruit. "Differential rotation and magnetic fields in stellar interiors." In: *Astron. Astrophys.* 349 (Sept. 1999), pp. 189–202. DOI: 10.48550/arXiv.astro-ph/9907138. arXiv: astro-ph/9907138 [astro-ph].

[555] I. H. Stairs et al. "Studies of the Relativistic Binary Pulsar PSR B1534+12. I. Timing Analysis." In: *Astrophys. J.* 581.1 (Dec. 2002), pp. 501–508. DOI: 10.1086/344157. arXiv: astro-ph/0208357 [astro-ph].

[556] A. W. Steiner, J. M. Lattimer, and E. F. Brown. "The Equation of State from Observed Masses and Radii of Neutron Stars." In: *Astrophys. J.* 722.1 (Oct. 2010), pp. 33–54. DOI: 10.1088/0004-637X/722/1/33. arXiv: 1005.0811 [astro-ph.HE].

[557] J. Steinhoff et al. "Dynamical tides in general relativity: Effective action and effective-one-body Hamiltonian." In: *Phys. Rev. D* 94.10, 104028 (Nov. 2016), p. 104028. DOI: 10.1103/PhysRevD.94.104028. arXiv: 1608.01907 [gr-qc].

[558] N. Stergioulas, T. A. Apostolatos, and J. A. Font. "Non-linear pulsations in differentially rotating neutron stars: mass-shedding-induced damping and splitting of the fundamental mode." In: *Mon. Not. Roy. Astron. Soc.* 352.4 (Aug. 2004), pp. 1089–1101. DOI: 10.1111/j.1365-2966.2004.07973.x. arXiv: astro-ph/0312648 [astro-ph].

[559] N. Stergioulas and J. L. Friedman. "Comparing Models of Rapidly Rotating Relativistic Stars Constructed by Two Numerical Methods." In: *Astrophys. J.* 444 (May 1995), p. 306. DOI: 10.1086/175605. arXiv: astro-ph/9411032 [astro-ph].

[560] N. Stergioulas and J. L. Friedman. "Nonaxisymmetric Neutral Modes in Rotating Relativistic Stars." In: *Astrophys. J.* 492.1 (Jan. 1998), pp. 301–322. DOI: 10.1086/305030. arXiv: gr-qc/9705056 [gr-qc].

[561] N. Stergioulas et al. "Gravitational waves and non-axisymmetric oscillation modes in mergers of compact object binaries." In: *Mon. Not. Roy. Astron. Soc.* 418.1 (Nov. 2011), pp. 427–436. DOI: 10.1111/j.1365-2966.2011.19493.x. arXiv: 1105.0368 [gr-qc].

[562] G. Strang. "On the Construction and Comparison of Difference Schemes." In: *SIAM Journal on Numerical Analysis* 5.3 (1968), pp. 506–517. DOI: 10.1137/0705041. eprint: https://doi.org/10.1137/0705041. URL: https://doi.org/10.1137/0705041.

[563] L. Sun et al. "Jet launching from binary neutron star mergers: Incorporating neutrino transport and magnetic fields." In: *Phys. Rev. D* 105.10 (2022), p. 104028. DOI: 10.1103/PhysRevD.105.104028. arXiv: 2202.12901 [astro-ph.HE].

[564] Y. Suwa et al. "Magnetorotational Collapse of Population III Stars." In: *Publ. Astron. Soc. Jpn* 59 (Aug. 2007), pp. 771–785. DOI: 10.1093/pasj/59.4.771. arXiv: 0704.1945 [astro-ph].

[565] K. Takami, L. Rezzolla, and L. Baiotti. "Constraining the Equation of State of Neutron Stars from Binary Mergers." In: *Phys. Rev. Lett.* 113.9, 091104 (Aug. 2014), p. 091104. DOI: 10.1103/PhysRevLett.113.091104. arXiv: 1403.5672 [gr-qc].

[566] K. Takami, L. Rezzolla, and L. Baiotti. "Spectral properties of the post-merger gravitational-wave signal from binary neutron stars." In: *Phys. Rev. D* 91.6, 064001 (Mar. 2015), p. 064001. DOI: 10.1103/PhysRevD.91.064001. arXiv: 1412.3240 [gr-qc].

[567] T. Takiwaki, K. Kotake, and T. Foglizzo. "Insights into non-axisymmetric instabilities in three-dimensional rotating supernova models with neutrino and gravitational-wave signatures." In: *MNRAS* 508.1 (Nov. 2021), pp. 966–985. DOI: 10.1093/mnras/stab2607. arXiv: 2107.02933.

[568] M. Tanaka and K. Hotokezaka. "Radiative Transfer Simulations of Neutron Star Merger Ejecta." In: *Astrophys. J.* 775 (2013), p. 113. DOI: 10.1088/0004-637X/775/2/113. arXiv: 1306.3742 [astro-ph.HE].

[569] M. Tanaka et al. "Systematic opacity calculations for kilonovae." In: *MNRAS* 496.2 (Aug. 2020), pp. 1369–1392. DOI: 10.1093/mnras/staa1576. arXiv: 1906.08914 [astro-ph.HE].

[570] K. Taniguchi and E. Gourgoulhon. "Quasiequilibrium sequences of synchronized and irrotational binary neutron stars in general relativity. III. Identical and different mass stars with γ=2." In: *Phys. Rev. D* 66.10, 104019 (Nov. 2002), p. 104019. DOI: 10.1103/PhysRevD.66.104019.

[571] N. R. Tanvir et al. "The Emergence of a Lanthanide-rich Kilonova Following the Merger of Two Neutron Stars." In: *Astrophys. J. Lett.* 848.2, L27 (Oct. 2017), p. L27. DOI: 10.3847/2041-8213/aa90b6. arXiv: 1710.05455 [astro-ph.HE].

[572] A. Taracchini et al. "Prototype effective-one-body model for nonprecessing spinning inspiral-merger-ringdown waveforms." In: *Phys. Rev. D* 86.2, 024011 (July 2012), p. 024011. DOI: 10.1103/PhysRevD.86.024011. arXiv: 1202.0790 [gr-qc].

[573] A. Taracchini et al. "Effective-one-body model for black-hole binaries with generic mass ratios and spins." In: *Phys. Rev. D* 89.6, 061502 (Mar. 2014), p. 061502. DOI: 10.1103/PhysRevD.89.061502. arXiv: 1311.2544 [gr-qc].

[574] R. J. Tayler. "The adiabatic stability of stars containing magnetic fields-I.Toroidal fields." In: *MNRAS* 161 (Jan. 1973), p. 365. DOI: 10.1093/mnras/161.4.365.

[575] C. Thompson and R. C. Duncan. "Neutron Star Dynamos and the Origins of Pulsar Magnetism." In: *Astrophys. J.* 408 (May 1993), p. 194. DOI: 10.1086/172580.

[576] K. S. Thorne. "Relativistic radiative transfer - Moment formalisms." In: *MNRAS* 194 (Feb. 1981), pp. 439–473. DOI: 10.1093/mnras/194.2.439.

[577] R. F. Tooper. "Adiabatic Fluid Spheres in General Relativity." In: *Astrophys. J.* 142 (Nov. 1965), p. 1541. DOI: 10.1086/148435.

[578] K. Topolski, S. D. Tootle, and L. Rezzolla. "Post-merger Gravitational-wave Signal from Neutron-star Binaries: A New Look at an Old Problem." In: *Astrophys. J.* 960.1, 86 (Jan. 2024), p. 86. DOI: 10.3847/1538-4357/ad0152. arXiv: 2310.10728 [gr-qc].

[579] D. Tsang. "Shattering Flares during Close Encounters of Neutron Stars." In: *Astrophys. J.* 777.2, 103 (Nov. 2013), p. 103. DOI: 10.1088/0004-637X/777/2/103. arXiv: 1307.3554 [astro-ph.HE].

[580] D. Tsang et al. "Resonant Shattering of Neutron Star Crusts." In: *Phys. Rev. Lett.* 108.1, 011102 (Jan. 2012), p. 011102. DOI: 10.1103/PhysRevLett.108.011102. arXiv: 1110.0467 [astro-ph.HE].

[581] K. W. Tsang, T. Dietrich, and C. Van Den Broeck. "Modeling the post-merger gravitational wave signal and extracting binary properties from future binary neutron star detections." In: *Phys. Rev. D* 100.4, 044047 (Aug. 2019), p. 044047. DOI: 10.1103/PhysRevD.100.044047. arXiv: 1907.02424 [gr-qc].

[582] S. Typel et al. "Composition and thermodynamics of nuclear matter with light clusters." In: *Phys. Rev. C* 81 (2010), p. 015803. DOI: 10.1103/PhysRevC.81.015803. arXiv: 0908.2344 [nucl-th].

[583] O. M. Umurhan, K. Menou, and O. Regev. "Weakly Nonlinear Analysis of the Magnetorotational Instability in a Model Channel Flow." In: *Phys. Rev. Lett.* 98.3, 034501 (Jan. 2007), p. 034501. DOI: 10.1103/PhysRevLett.98.034501. arXiv: astro-ph/0608374 [astro-ph].

[584] V. Varma et al. "Surrogate models for precessing binary black hole simulations with unequal masses." In: *Physical Review Research* 1.3, 033015 (Oct. 2019), p. 033015. DOI: 10.1103/PhysRevResearch.1.033015. arXiv: 1905.09300 [gr-qc].

[585] E. P. Velikhov. "Stability of an Ideally Conducting Liquid Flowing between Cylinders Rotating in a Magnetic Field." In: *Soviet Journal of Experimental and Theoretical Physics* 9.5 (Nov. 1959), pp. 995–998.

[586] D. Viganò et al. "Unifying the observational diversity of isolated neutron stars via magneto-thermal evolution models." In: *MNRAS* 434.1 (Sept. 2013), pp. 123–141. DOI: 10.1093/mnras/stt1008. arXiv: 1306.2156 [astro-ph.SR].

[587] D. Viganò, R. Aguilera-Miret, and C. Palenzuela. "Extension of the subgrid-scale gradient model for compressible magnetohydrodynamics turbulent instabilities." In: *Physics of Fluids* 31.10, 105102 (Oct. 2019), p. 105102. DOI: 10.1063/1.5121546. arXiv: 1904.04099 [physics.flu-dyn].

[588] D. Viganò et al. "General relativistic MHD large eddy simulations with gradient subgrid-scale model." In: *Phys. Rev. D* 101.12, 123019 (June 2020), p. 123019. DOI: 10.1103/PhysRevD.101.123019. arXiv: 2004.00870 [gr-qc].

[589] V. Villa-Ortega et al. "Self-consistent treatment of thermal effects in neutron-star post-mergers: observational implications for third-generation gravitational-wave detectors." In: *arXiv e-prints*, arXiv:2310.20378 (Oct. 2023), arXiv:2310.20378. arXiv: 2310.20378 [gr-qc].

[590] S. Wanajo et al. "Production of All the r-process Nuclides in the Dynamical Ejecta of Neutron Star Mergers." In: *Astrophys. J. Lett.* 789.2, L39 (July 2014), p. L39. DOI: 10.1088/2041-8205/789/2/L39. arXiv: 1402.7317 [astro-ph.SR].

[591] L. R. Weih, E. R. Most, and L. Rezzolla. "On the stability and maximum mass of differentially rotating relativistic stars." In: *MNRAS* 473.1 (Jan. 2018), pp. L126–L130. DOI: 10.1093/mnrasl/slx178. arXiv: 1709.06058 [gr-qc].

[592] L. R. Werneck et al. "Addition of tabulated equation of state and neutrino leakage support to illinoisgrmhd." In: *Phys. Rev. D* 107.4 (2023), p. 044037. DOI: 10.1103/PhysRevD.107.044037. arXiv: 2208.14487 [gr-qc].

[593] J. C. Wheeler et al. "Asymmetric Supernovae, Pulsars, Magnetars, and Gamma-Ray Bursts." In: *Astrophys. J.* 537.2 (July 2000), pp. 810–823. DOI: 10.1086/309055. arXiv: astro-ph/9909293 [astro-ph].

[594] T. Whittaker et al. "Using machine learning to parametrize postmerger signals from binary neutron stars." In: *Phys. Rev. D* 105.12, 124021 (June 2022), p. 124021. DOI: 10.1103/PhysRevD.105.124021. arXiv: 2201.06461 [gr-qc].

[595] M. Wijngaarden et al. "Probing neutron stars with the full premerger and postmerger gravitational wave signal from binary coalescences." In: *Phys. Rev. D* 105.10, 104019 (May 2022), p. 104019. DOI: 10.1103/PhysRevD.105.104019. arXiv: 2202.09382 [gr-qc].

[596] S. E. Woosley. "Gamma-Ray Bursts from Stellar Mass Accretion Disks around Black Holes." In: *Astrophys. J.* 405 (Mar. 1993), p. 273. DOI: 10.1086/172359.

[597] S. E. Woosley and J. S. Bloom. "The Supernova Gamma-Ray Burst Connection." In: *Annu. Rev. Astron. Astrophys.* 44.1 (Sept. 2006), pp. 507–556. DOI: 10.1146/annurev.astro.43.072103.150558. arXiv: astro-ph/0609142 [astro-ph].

[598] A. J. Wright and I. Hawke. "A resistive extension for ideal magnetohydrodynamics." In: *MNRAS* 491.4 (Feb. 2020), pp. 5510–5523. DOI: 10.1093/mnras/stz2779. arXiv: 1906.03150 [physics.plasm-ph].

[599] M.-R. Wu et al. "Production of the entire range of r-process nuclides by black hole accretion disc outflows from neutron star mergers." In: *MNRAS* 463.3 (Dec. 2016), pp. 2323–2334. DOI: 10.1093/mnras/stw2156. arXiv: 1607.05290 [astro-ph.HE].

[600] X. Xie et al. "Instabilities in neutron-star postmerger remnants." In: *Phys. Rev. D* 102.4, 044040 (Aug. 2020), p. 044040. DOI: 10.1103/PhysRevD.102.044040. arXiv: 2005.13696 [astro-ph.HE].

[601] Y. Xu and R. Goodacre. "On Splitting Training and Validation Set: A Comparative Study of Cross-Validation, Bootstrap and Systematic Sampling for Estimating the Generalization Performance of Supervised Learning." In: *Journal of Analysis and Testing* 2 (Oct. 2018). DOI: 10.1007/s41664-018-0068-2.

[602] K. Yagi and N. Yunes. "Approximate universal relations for neutron stars and quark stars." In: *Phys. Rep.* 681 (Apr. 2017), pp. 1–72. DOI: 10.1016/j.physrep.2017.03.002. arXiv: 1608.02582 [gr-qc].

[603] Z. Yuan, C. Xie, and J. Wang. "Deconvolutional artificial neural network models for large eddy simulation of turbulence." In: *Physics of Fluids* 32.11, 115106 (Nov. 2020), p. 115106. DOI: 10.1063/5.0027146. arXiv: 2007.14212 [physics.flu-dyn].

[604] F. Zappa et al. "Binary neutron star merger simulations with neutrino transport and turbulent viscosity: impact of different schemes and grid resolution." In: *MNRAS* 520.1 (Mar. 2023), pp. 1481–1503. DOI: 10.1093/mnras/stad107. arXiv: 2210.11491 [astro-ph.HE].

[605] N.-B. Zhang, B.-A. Li, and J. Xu. "Combined Constraints on the Equation of State of Dense Neutron-rich Matter from Terrestrial Nuclear Experiments and Observations of Neutron Stars." In: *Astrophys. J.* 859.2, 90 (June 2018), p. 90. DOI: 10.3847/1538-4357/aac027. arXiv: 1801.06855 [nucl-th].

[606] X. Zhuge, J. M. Centrella, and S. L. W. McMillan. "Gravitational radiation from coalescing binary neutron stars." In: *Phys. Rev. D* 50.10 (Nov. 1994), pp. 6247–6261. DOI: 10.1103/PhysRevD.50.6247. arXiv: gr-qc/9411029 [gr-qc].

[607] T. Zwerger and E. Mueller. "Dynamics and gravitational wave signature of axisymmetric rotational core collapse." In: *Astron. Astrophys.* 320 (Apr. 1997), pp. 209–227.